Thèse n° 10 224

Exploiting the chirality of intermetallic PdGa

Présentée le 8 juillet 2020

à la Faculté des sciences de base
Laboratoire de nanostructures superficielles
Programme doctoral en physique

pour l'obtention du grade de Docteur ès Sciences

par

Samuel Thomas STOLZ

Acceptée sur proposition du jury

Prof. H. M. Rønnow, président du jury
Prof. H. Brune, Dr R. Widmer, directeurs de thèse
Prof. K.-H. Ernst, rapporteur
Dr T. Kudernac, rapporteur
Prof. R. Beck, rapporteur

École
polytechnique
fédérale
de Lausanne

2020

Abstract

The intermetallic compound PdGa has recently attracted considerable interest for combining high catalytic activity with high reaction selectivity in symmetric heterogeneous catalysis, in particular semi-hydrogenation of acetylene and methanol steam reforming. However, its potential for asymmetric heterogeneous catalysis, for which its chiral bulk crystal structure predestines it, remained largely unexplored. The possibility to prepare clean, atomically well-defined, and bulk-truncated low Miller-index surfaces of chiral PdGa (Pd_1Ga_1) under ultra-high vacuum conditions paves the way to tackle several fundamental research questions in chemistry and physics under idealized conditions. In particular, the PdGa{111} surfaces and their unique properties are ideally suited to serve as model system to study ensemble (geometry) and ligand (electronic) effects and show the enormous potential of PdGa towards asymmetric heterogeneous catalysis.

In this work, the focus is on obtaining fundamental insights into chirality transfer of intrinsically chiral surfaces on the electronic structure and on each of the principal steps of a catalytic reaction pathway by experimental surface analytical tools, which constitute the basis for comparison with theoretical, *i.e.*, computational modelling. The main experimental characterization tools which were exploited within this PhD thesis have been angle-resolved photoemission spectroscopy (ARPES), temperature-programmed x-ray photoelectron spectroscopy (TP-XPS), low temperature scanning tunneling microscopy (LT-STM), and non-contact atomic force microscopy (nc-AFM).

With regard to the relation of the chiral crystal structure of PdGa and its electronic structure, crystals of the space group $P2_13$, such as PdGa, are predicted to exhibit peculiar symmetry-protected fermionic quasiparticles. Using ARPES, we were able to evidence such symmetry-protected fermionic quasiparticles in PdGa, to exhibit multifold band-crossings at the high-symmetry points Γ and R in the Brillouin zone. These band-crossings correspond to fermionic quasiparticles that carry a topological charge, also denoted as Chern number C, whose magnitude is proportional to the number of chiral surface Fermi-arcs. By using synchrotron-based ARPES measurements, we could demonstrate for the first time that these fermionic quasiparticles carry the maximal Chern number $|C| = 4$, owing to the capability to prepare high quality PdGa surfaces in combination with the large spin-orbit coupling of PdGa. Additionally, the sign of the Chern number at the high-symmetry points can be controlled via the deliberate choice of the PdGa enantiomorph.

The non-centrosymmetry of PdGa is not only manifested in the emergence of chiral Fermi-arcs, but its chirality governs also the interaction with molecules and its surfaces, which is expressed, for instance in unidirectional motion or enantioselective on-surface reactions. In particular, we have evidenced and induced directed rotation of isolated small, achiral acetylene (C_2H_2) molecules on Pd_3-terminated PdGa{111} surfaces by using LT-STM. This molecular motor is exceptionally small and consists of only 16 atoms, whereas 4 are provided by the C_2H_2 rotor, and the remaining 12 constitute the chiral PdGa cluster provided by the Pd_3-terminated PdGa{111} surface, which acts as stator. While the direction of rotation of this smallest molecular motor is solely dictated by the chirality of the stator, its rotation frequency can be controlled electronically and thermally. We have driven the C_2H_2/PdGa motor with a directionality of up to unprecedented 98% in the classical, but also in the unexpected quantum tunneling regime!

This strong chirality transfer from the substrate to the molecule is not only encountered in the directed motion of acetylene on chiral PdGa{111}, but also in enantiospecific interactions with prochiral molecules which is a prerequisite for enantioselective control in on-surface reactions, *i.e.*, asymmetric heterogeneous catalysis. With this focus, we have studied three different reactions on the two structurally different Pd_1- and Pd_3-terminated PdGa{111} surfaces with regard to enantiomeric excess and the relevance of ensemble effect (geometry) over the ligand effect (electronic structure):

(i) Enantioselective debromination of 5-Bromo-7Methylbenz(a)Anthracene (BMA)

(ii) Nearly enantiopure homocoupling of 9-Ethynylphenanthrene (9-EP)

(iii) Regio- and enantioselective azide-alkyne Huisgen cycloaddition between 3-(4-Azidophenyl)propionic azid (APA) and 9-EP

In particular, the debromination of prochiral BMA has been demonstrated to proceed enantioselectively with a reaction temperature difference of 35 K on the Pd_3- and even 46 K for the Pd_1-terminated surfaces, which corresponds to a debromination energy difference of about 35 meV and 60 meV, respectively, between the two enantiomers. Even though on both surfaces, the debromination process exhibits a high enantioselectivity, a remarkably strong ensemble effect has been encountered, which is expressed in the preferential debromination of the respectively opposite enantiomer on the two dissimilar PdGa{111} surface terminations of the same crystal enantiomorph.

On the other hand, 9-EP molecules, whose monomers have been reported to adsorb enantioselectively upon room-temperature (RT) deposition on the Pd_1-terminated PdGa{111} surface and to dimerize without enantiomeric excess at elevated temperatures, appear in a racemic mixture if deposited at RT on the Pd_3-terminated PdGa{111} surface. However, upon annealing the 9-EP racemic mixture on the Pd_3-terminated PdGa{111} surface to 500 K, they form almost enantiopure, homochiral 9-EP trimers, which again highlights the strong chiral recognition of the PdGa{111} surfaces.

Due to the highly enantiospecific interaction of 9-EP (alkyne) with the PdGa{111} surfaces and the copper-like d-band structure of PdGa{111}, we have conducted an azide-alkyne Huisgen cycloaddition, with APA as azide on these substrates. We have demonstrated that this azide-alkyne heterocoupling reaction proceeds not only regioselectively by forming 1,4-triazoles, but also enantioselectively on the Pd_1-terminated PdGa{111} surfaces. However on the Pd_3-terminated PdGa{111} surfaces the reaction does not take place at all. The vastly differing behavior identified for the 9-EP homocoupling as well as for the azide-alkyne Huisgen cycloaddition on the Pd_1- and Pd_3-terminated PdGa{111} surfaces underline once more the decisive influence of the ensemble effect on the overall reactivity.

Our results highlight the outstanding potential of intermetallic PdGa in numerous fields of research, specifically as a chiral topological material with non-trivial bandstructure, as stator for molecular motors, or as template for asymmetric heterogeneous catalysis. In particular, the strong manifestation of the PdGa{111} surface chirality in the molecule's dynamics demonstrates these substrate to be very promising candidates for the investigation, understanding, and realization of enantioselective on-surface synthesis of prochiral or even chiral molecules on the atomic scale and allows fundamental insights into asymmetric catalysis on the surfaces of intermetallic compounds.

Keywords

Scanning tunneling microscopy, non-contact atomic force microscopy, temperature-programmed x-ray photoelectron spectroscopy, angle-resolved photoemission spectroscopy, intermetallic compounds, PdGa, topological materials, molecular motor, heterogeneous catalysis, molecular adsorption, ensemble effect, enantioselectivity, azide-alkyne Huisgen cycloaddition, debromination

Zusammenfassung

Die intermetallische Verbindung PdGa kombiniert eine herausragende katalytische Aktivität mit einer hohen Selektivität in der Semi-Hydrogenierung von Acetylen und der Methanol-Dampfreformierung. Obwohl diese intermetallische Verbindung durch ihre Chiralität geradezu für asymmetrische heterogene Katalyse prädestiniert wäre, blieb dieser Aspekt bis zum heutigen Zeitpunkt grösstenteils unerforscht. Der Umstand, dass atomar glatte, wohldefinierte und volumenterminierte PdGa (Pd_1Ga_1) Oberflächen unter Ultrahochvakuumbedingungen präpariert werden können, eröffnet die Möglichkeit fundamentale wissenschaftliche Fragen der Chemie und Physik unter idealisierten Bedingungen zu untersuchen. Insbesondere die zwei unterschiedlich terminierten PdGa{111} Oberflächen bieten sich an, um das bereits erwähnte Potential von PdGa als enantioselektiver heterogener Katalysator aufzuzeigen. Gleichzeitig kann anhand dieser beiden Oberflächen der Einfluss des Ensemble- (geometrisch) vom Liganden- (elektrisch) Effekts in der asymmetrischen heterogenen Katalyse getrennt werden.

In der vorliegenden Doktorarbeit wird der Chiralitätstransfer intrinsisch chiraler Oberflächen zum einen auf deren elektronische Struktur, zum anderen auf einzelne Teilschritte des Reaktionspfads molekularer Oberflächenprozesse mittels experimenteller Oberflächenanalysemethoden untersucht. Die dadurch gewonnenen Einblicke bilden die Basis für einen detaillierten Vergleich mit analytischen und computergestützten Modellen.

Den Einfluss der chiralen Kristallstruktur von PdGa auf dessen elektronische Struktur haben wir mittels winkelaufgelöster Photoelektronenspektroskopie (ARPES) untersucht. Gemäss theoretischer Voraussagen weisen Kristalle, die zur Raumgruppe $P2_13$ gehören, wie beispielsweise PdGa, besondere symmetriegeschützte fermionische Quasipartikel auf. Dank der Möglichkeit der reproduzierbaren Präparation von qualitativ hochwertigen PdGa Oberflächen und einer ausgeprägten Spin-Bahn-Kopplung konnten wir nachweisen, dass diese Quasipartikel in PdGa vorkommen und sie mehrfach überkreuzende Bänder an den hochsymmetrischen Punkten Γ und R in der Brillouin-Zone aufweisen. Diese sich überkreuzende Bänder entsprechen fermionischen Quasipartikeln mit einer topologischen Ladung, welche auch Chern-Nummer genannt wird. Da die Anzahl der Oberflächenzustände, auch Fermi-Bögen genannt, proportional zur topologischen Ladung ist, konnten wir mittels Synchrotron basierten ARPES Messungen zum ersten Mal nachweisen, dass diese fermionischen Quasipartikel die maximal mögliche Chern Nummer $|C| = 4$ besitzen. Zusätzlich konnten wir das Vorzeichen der Chern-Nummer an den hochsymmetrischen Punkten durch eine spezifische Wahl des PdGa-Enantiomorphs kontrollieren.

Der Umstand, dass PdGa keine Zentrosymmetrie besitzt, manifestiert sich nicht nur in chiralen Fermi-Bögen, sondern beeinflusst auch die Wechselwirkung von Molekülen mit dessen Oberflächen. Dies kann zum Beispiel zu gerichteten Molekülbewegungen oder Enantioselektivität von Reaktionen auf diesen Oberflächen führen. Eine gerichtete Bewegung, konnten wir für isolierte achirale Acetylenmoleküle (C_2H_2) auf der Pd_3-terminierten PdGa{111} Oberfläche mittels Tieftemperatur Rastertunnelmikroskopie (LT-STM) beobachten und auch gezielt induzieren. Dieser spezifische molekulare Motor besteht aus insgesamt nur 16 Atomen, wobei 4 vom Acetylen-Rotor und die restlichen 12 vom chiralen PdGa-Stator beigetragen werden. Während die Richtung dieses molekularen Motors einzig durch die Chiralität des Stators diktiert wird, kann die Rotationsfrequenz thermisch und elektrisch kontrolliert werden. Dadurch konnten wir diesen C_2H_2/PdGa-Motor mit einer Rotation, die zu 99% gerichtet abläuft, sowohl im klassischen, als auch in einem unerwarteten quantenmechanischen Bewegungsbereich antreiben.

Der starke Chiralitätstransfer vom Substrat auf Moleküle ruft nicht nur die gerichtete Bewegung von Acetylen hervor, sondern zeigt sich auch deutlich in enantiospezifischen Wechselwirkungen mit prochiralen Molekülen. Letzteres ist eine grundlegende Voraussetzung für die Kontrolle der Enantioselektivität in Oberflächenreaktionen, und somit für asymmetrische heterogene Katalyse. Wir haben deshalb die folgenden drei Reaktionen auf den zwei unterschiedlich terminierten Pd_1- und Pd_3-PdGa{111} Oberflächen durchgeführt und im Hinblick auf den Enantiomerenüberschuss und die Relevanz des Ensemble- gegenüber dem Liganden-Effekt analysiert:

(i) Enantioselektive Debrominierung von 5-Bromo-7Methylbenz(a)Anthracene (BMA)

(ii) Quasi-enantiomerenreine Homokopplung von 9-Ethynylphenanthrene (9-EP)

(iii) Regio- und enantioselektive Azid-Alkin Huisgen Cycloaddition zwischen 3-(4-Azidophenyl)propionic azid (APA) und 9-EP

Wir konnten nachweisen, dass die Debrominierung von prochiralem BMA enantioselektiv abläuft. Dabei konnten wir eine Temperaturdifferenz zwischen der Debrominierung der Enantiomere von 35 K auf der Pd_3- und von sogar 46 K auf der Pd_1-terminierten

PdGa{111} Oberfläche bestimmen (was in etwa einer Energiedifferenz von etwa 35 meV, beziehungsweise 60 meV, entspricht). Obwohl die Reaktion auf beiden Oberflächen äusserst enantioselektiv abläuft, haben wir einen ausgeprägten Ensemble-Effekt festgestellt. Dieser manifestiert sich in der bevorzugten Debrominierung der jeweils entgegengesetzten BMA Enantiomere auf den zwei unterschiedlich terminierten {111} Oberflächen desselben PdGa Enantiomorphs.

Werden 9-EP Moleküle bei Raumtemperatur auf der Pd_1-terminierten PdGa{111} aufgedampft, kommen sie mit einem Enantiomerenüberschuss von 98% vor. Dieselbe Präparation resultiert hingegen in einem 9-EP Racemat auf der Pd_3-terminierten PdGa{111} Oberfläche. Auch die stabilen 9-EP Strukturen, die sich bei höheren Temperaturen bilden, unterscheiden sich deutlich auf diesen beiden Oberflächen. Auf Pd_1-terminierten PdGa{111} Oberflächen formieren sich stabile 9-EP Dimere ohne Enantiomerenüberschuss, während solche 9-EP Dimere auf den Pd_3-terminierten PdGa{111} Oberflächen nur Zwischenprodukte in der Bildung von stabilen, homochiralen und enantiomerenreinen 9-EP Trimeren darstellen.

Aufgrund der ausgeprägten enantiospezifischen Wechselwirkung von 9-EP (Alkin) mit den PdGa{111} Oberflächen und der kupferähnlicher d-Bandstruktur von PdGa{111} Oberflächen, bietet sich die Azid-Alkin Huisgen Cycloaddition als Reaktion auf diesen Substraten an. Wir konnten nachweisen, dass diese Azid-Alkin Heterokopplung auf den Pd_1-terminierten PdGa{111} Oberflächen sowohl regio- als auch enantioselektiv abläuft, auf den Pd_3-terminierten PdGa{111} Oberflächen jedoch nicht initiiert werden kann. Wir haben demnach deutliche Unterschiede zwischen Pd_1- und Pd_3-terminierten PdGa{111} Oberflächen in Bezug auf die Reaktionsprodukte in der 9-EP-Homokopplung und der Reaktivität in der Azid-Alkin Heterokopplung festgestellt. Diese Unterschiede können dem starken Einfluss des Ensemble-Effekts auf den gesamten Reaktionsprozess zugeordnet werden.

Das herausragende Potential der intermetallischen Verbindung sowohl als Material mit topologisch nicht trivialer Bandstruktur, als auch als Stator für molekulare Motoren, oder als Substrat für asymmetrische heterogene Katalyse wird durch unsere Resultate aufgezeigt. Der beeindruckende Chiralitätstransfer der PdGa{111} auf die Dynamik molekularer Prozesse belegt, dass diese Substrate ideale Kandidaten zur Erforschung von enantioselektiven Reaktionen auf atomarer Ebene und mittels Oberflächenreaktionen sind.

Schlüsselwörter

Rastertunnelmikroskop, Rasterkraftmikroskop im Nicht-Kontakt-Modus, Temperatur-programmierte Röntgenphotoelektronenspektroskopie, winkelaufgelöste Photoelektronenspektroskopie, intermetallische Verbindungen, PdGa, topologische Materialien, molekulare Motoren, heterogene Katalyse, Moleküladsorption, Ensemble Effekt, Enantioselektivität, Azid-Alkin Huisgen Cycloaddition, Debrominierung

Contents

Abstract .... **ii**

Zusammenfassung .... **iv**

Contents .... **vi**

List of Figures .... **viii**

List of Tables .... **xi**

List of Equations .... **xii**

1. Introduction **13**

1.1 PdGa – chiral topological material 14

1.2 PdGa – stator for molecular motors 14

1.3 PdGa – template for enantioselective heterogeneous catalysis 14

1.4 PdGa – Chiral intermetallic compound 16

2. Materials and methods **18**

2.1 Preparation of single crystal surfaces under UHV conditions 19

2.2 Low energy electron diffraction 20

2.3 Photoelectron spectroscopy 21

2.3.1 Fundamental aspects of the method 21

2.3.2 Experimental setup 22

2.3.3 Temperature-programmed x-ray photoelectron spectroscopy 24

2.3.4 Angle-resolved photoelectron spectroscopy 25

2.4 Scanning probe microscopy 26

2.4.1 Theoretical background of Scanning Tunneling Microscopy 27

2.4.2 Main STM components 28

2.4.3 Non-contact atomic force microscopy 29

2.5 Instrumentation 31

2.5.1 PEARL at the Swiss Light Source 31

2.5.2 ADRESS at the Swiss Light Source 31

2.5.3 I05 at the Diamond Light Source 31

2.5.4 Low temperature scanning probe microscopes at EMPA 31

3. PdGa – chiral topological material **32**

3.1 Symmetry protected fermionic excitations in condensed-matter systems 32

3.2 Publication (accepted in *Science*): "Observation and manipulation of maximal Chern numbers in the chiral topological semimetal PdGa" 34

3.2.1 Supporting Information for the publication "Observation and manipulation of maximal Chern numbers in the chiral topological semimetal PdGa" 40

4. PdGa – stator for molecular machines **43**

4.1 Molecular motors 43

4.1.1 Physical background of molecular motors 43

4.1.2 Artificial molecular motors 44

4.2 Publication (accepted in *PNAS*): "Molecular motor crossing the frontier of classical to quantum tunneling motion" 47

4.2.1 Supplementary Materials for the publication "Molecular motor crossing the frontier of classical to quantum tunneling motion" 54

5. PdGa – template for enantioselective heterogeneous catalysis 66

5.1 Asymmetric catalysis 66

5.2 Publication (in preparation): "Enantioselective debromination on chiral metal surfaces" 68

5.2.1 Supporting Information for the publication "Enantioselective debromination on chiral metal surfaces" 74

5.3 Publication (published in Angewandte Chemie): "Reversible dehalogenation in on-surface aryl-aryl coupling" 90

5.3.1 Supporting Information for the publication "Reversible dehalogenation in on-surface aryl-aryl coupling" 95

5.4 Publication (under Review in Angew. Chem. Int. Ed.): "Near-enantiopure trimerization of 9-Ethynylphenanthrene on a chiral metal surface" 103

5.4.1 Supporting Information for the publication "Near-enantiopure trimerization of 9-Ethynylphenanthrene on a chiral metal surface" 109

5.5 Publication (in preparation): "Asymmetric azide-alkyne Huisgen cycloaddition on chiral metal surfaces" 115

5.5.1 Supporting Information for the publication "Asymmetric azide-alkyne Huisgen cycloaddition on chiral metal surfaces" 120

6. Conclusion and outlook 126

6.1 PdGa – chiral topological material 126

6.2 PdGa – stator for molecular machines 126

6.3 PdGa – template for enantioselective heterogeneous catalysis 127

7. References 129

Curriculum Vitae 144

Acknowledgements 146

List of Figures

Figure 1.1| PdGa(100) surface characterization 16

Figure 1.2| PdGa{111} surfaces characterization 17

Figure 2.1 | LEED........ 20

Figure 2.2 | XPS spectrum of clean PdGa:A(-1-1-1)Pd_3........ 21

Figure 2.3 | Surface sensitivity of XPS........ 22

Figure 2.4 | Schematic of XPS setup 23

Figure 2.5 | Universal curve........ 23

Figure 2.6 | Information gained from TP-XPS 24

Figure 2.7 | Examples of STM experiments 26

Figure 2.8 | Sketch of the STM working principle. 27

Figure 2.9 | Principle of quantum tunneling between STM tip and sample surface 27

Figure 2.10 | Sketch of the main components required for an STM. 28

Figure 2.11 | Basics of non-contact Atomic Force Microscopy........ 30

Figure 2.12 | nc-AFM images of pentacene on NaCl 30

Figure 3.1 | Surface Fermi-arcs of CoSi, RhSi, and PtAl........ 32

Figure 3.2 | Structural and electronic chirality in the two enantiomers of PdGa 36

Figure 3.3 | Electronic characterization of the bulk electronic structure of PdGa measured on the (100) surface of enantiomer A 37

Figure 3.4 | Surface electronic structure of the (100) surface of enantiomer A........ 38

Figure 3.5 | Comparison of the surface electronic structure of the (100) surface of enantiomer A (left) and enantiomer B (right) 39

Figure 3.6 | PdGa enantiomorphs and x-ray diffraction 41

Figure 4.1 | Chemically-driven molecular motors 44

Figure 4.2 | Light-driven molecular motors 45

Figure 4.3 | Electrically-driven molecular motors........ 45

Figure 4.4| Acetylene rotation on the PdGa:A(-1-1-1)Pd_3 surface 48

Figure 4.5| Parametric dependence of the rotation frequency and jump sequence 49

Figure 4.6| Parametric dependence of the nanomotor's directionality 50

Figure 4.7| Quantum tunnelling rotation of acetylene........ 51

Figure 4.8 | Overview STM image of C_2H_2 on Pd_3........ 54

Figure 4.9 | Rotation frequency dependence on tunnelling current in the tunnelling regime........ 54

Figure 4.10 | Positional dependence of signal amplitude sequence 55

Figure 4.11 | Schematics for the jump sequence map modelling........ 56

Figure 4.12 | Parametric influence in the jump sequence map modelling........ 56

Figure 4.13 | Reproducing experimental jump sequence maps 57

Figure 4.14 | Illustration of difficulties in automatized jump sequence map analysis........................57

Figure 4.15 | Residence times of the three rotation states 58

Figure 4.16 | Residence time as function of distance from rotation center 58

Figure 4.17 | Saw-tooth potential 59

Figure 4.18 | Modelling voltage dependence of rotation frequency..61

Figure 4.19 | Sketch of potential for tunnelling frequency determination..62

Figure 4.20 | C_2H_2 libration modes 63

Figure 4.21 | Position of C_2H_2 and its isotopes when determining their tunnelling frequency 64

Figure 4.22 | Analysis of relative tunnelling frequency 64

Figure 5.1 | Enantioselective decomposition reactions on chiral copper surfaces.............................66

Figure 5.2 | Complexity arising from molecule-molecule interactions...67

Figure 5.3 | Model systems for enantioselective debromination...69

Figure 5.4 | Enantiospecific BMA adsorption on PdGa:A(-1-1-1)Pd_3 70

Figure 5.5 | Enantiospecific BMA adsorption on PdGa:A(111)Pd_1..71

Figure 5.6 | Bromine detachment and desorption 72

Figure 5.7 | Enantioselectivity of BMA debromination 73

Figure 5.8 | Illustration of TP-XPS experiment...76

Figure 5.9 | BMA deposited at 165 K on Au(111) 77

Figure 5.10 |Trapezoid-shape of BMA on PdGa:A(-1-1-1)Pd_3..77

Figure 5.11 | Trapezoid-shape of BMA on PdGa:A(111)Pd_1 78

Figure 5.12 | DFT relaxed adsorption geometries of BMA on PdGa:A(-1-1-1)Pd_3 79

Figure 5.13 | BMA adsorption configurations on PdGa:A(111)Pd_1...80

Figure 5.14 | BMA trimer agglomerations on PdGa:B(-1-1-1)Pd_1...81

Figure 5.15 | Evidencing enantioselective debromination on PdGa:A(-1-1-1)Pd_3 with XPS 82

Figure 5.16 | HR-XPS of BMA during the debromination on PdGa:A(-1-1-1)Pd_3 and Au(111).............83

Figure 5.17 | Enantioselective debromination of BMA on PdGa:B(-1-1-1)Pd_1 84

Figure 5.18 | Adsorption configuration of debrominated S BMA on PdGa:A(111)Pd_1 85

Figure 5.19 | Debrominated R and S BMA on PdGa:A(111)Pd_1 86

Figure 5.20 | BMA dimer on Au(111)...86

Figure 5.21 | BMA dimer on PdGa:A(-1-1-1)Pd_3 87

Figure 5.22 | BMA dimer-like structures on PdGa:A(111)Pd_1...88

Figure 5.23 | NEB simulations of the BMA debromination on PdGa:A(-1-1-1)Pd_3 and PdGa:A(111)Pd_1...89

Figure 5.24 | Reaction mechanism 91

Figure 5.25 | Temperature evolution of DBTP on Cu(111) and Au(111)...92

Figure 5.26 | Temperature evolution of DBTP + Cl on Cu(111) 93

Figure 5.27 | Temperature evolution of DBTP + Cl on Au(111): Halogen exchange 93

Figure 5.28 | Kinetic model........94

Figure 5.29 | Length distribution of OM on Cu(111) and PPP on Cu(111) and Au(111)........96

Figure 5.30 | Metal contamination for AuCl and $CuCl_2$ deposition........97

Figure 5.31 | TP-XPS of Cl 2p doublet upon Cl deposition on Au(111)........97

Figure 5.32 | HR-XPS of multilayer and sub-monolayer Cl on Au(111)........98

Figure 5.33 | TP-XPS of Cl 2p doublet upon Cl deposition on Cu(111)........98

Figure 5.34 | HR-XPS and TP-XPS of C 1s core level for DBTP and DBTP+Cl on Au(111)........99

Figure 5.35 | STM of DBTP co-adsorbed with Cl........100

Figure 5.36 | Kinetic curves for polymerization on Cu(111)........102

Figure 5.37 | Polanyi-Wigner equation fit of kinetic curves for DBTP on Au(111)........102

Figure 5.38 | Baseline of 9-EP on PdGa:A(-1-1-1)Pd_3........104

Figure 5.39 | Temperature evolution of 9-EP on PdGa:A(-1-1-1)Pd_3........105

Figure 5.40 | Variety of 9-EP molecular structures on PdGa:A(-1-1-1)Pd_3........106

Figure 5.41 | From 9-EP racemic mixture to near-enantiopure, homochiral 9-EP trimer........107

Figure 5.42 | Bias voltage dependence of 9-EP trimers........109

Figure 5.43 | Deformation of 9-EP trimers........110

Figure 5.44 | Reaction pathway for the near-enantiopure, homochiral 9-EP trimerization........110

Figure 5.45 | Mobility of 9-EP structures........111

Figure 5.46 | 9-EP [2+2+2] cyclotrimerization........112

Figure 5.47 | Pd adatoms and their influence on 9-EP trimerization........112

Figure 5.48 | Ga adatoms and their influence on 9-EP trimerization........113

Figure 5.49 | carbon atoms as center of 9-EP trimers........114

Figure 5.50 | Model system for enantioselective on-surface azide-alkyne Huisgen cycloaddition...116

Figure 5.51 | Suppression of azide-alkyne Huisgen cycloaddition on PdGa:A(-1-1-1)Pd_3........117

Figure 5.52 | Alkyne and azide on Pd_1-terminated PdGa{111} surfaces........118

Figure 5.53 | Azide-alkyne Huisgen cycloaddition on Pd_1-terminated PdGa{111} surfaces........118

Figure 5.54 | Temperature evolution of APA on PdGa:B(-1-1-1)Pd_1........120

Figure 5.55 | XPS of APA on PdGa:A(-1-1-1)Pd_3, PdGa:A(111)Pd_1, and Cu(111)........121

Figure 5.56 | Abundance of 1,4-triazoles on PdGa:B(-1-1-1)Pd_1........123

Figure 5.57 | Abundance of 1,4-triazoles on PdGa:A(111)Pd_1........124

Figure 5.58 | Adsorption configuration of the 1,4-triazoles........124

List of Tables

Table 4.1 | Comparison of tunnelling parameters for different atoms and molecules 63

Table 4.2 | Tunneling parameters for C_2H_2 and its isotopes on Pd_3 63

Table 4.3 | Experimentally determined tunneling frequencies 65

Table 5.1 | Adsorption energies of BMA on PdGa:A(-1-1-1)Pd_3 79

Table 5.2 | Adsorption energies of BMA on PdGa:A(111)Pd_1 80

Table 5.3 | Fitting parameters for HR-XPS for DBTP on Au(111) 99

Table 5.4 | Fitting parameters for HR-XPS for sub-monolayer Cl on Au(111)....................................99

Table 5.5 | Fitting parameters for HR-XPS for multi-layer Cl on Au(111) 99

Table 5.6 | Fitting parameters for HR-XPS of DBTP+Cl on Au(111)..100

Table 5.7 | Fitting parameters for HR-XPS of DBTP+Cl on Cu(111)..100

Table 5.8 | Statistical analysis of the 1,4-triazoles on Pd_1-terminated PdGa{111} surfaces 119

Table 5.9 | Fitting parameters for XPS of APA on PdGa:A(-1-1-1)Pd_3...122

Table 5.10 | Fitting parameters for XPS of APA on PdGa:A(-1-1-1)Pd_1...122

Table 5.11 | Fitting parameters for XPS of APA on Cu(111)..122

Table 5.12 | 1,4-triazole reaction yield...125

List of Equations

Equation 2.1 | Einstein equation 21

Equation 2.2 | STM tunneling Current – distance dependence 27

Equation 2.3 | Tunneling current – density of states dependence 28

Equation 2.4 | Frequency shift in AFM 29

Equation 4.1 | Langevin equation 43

Equation 4.2 | thermal rotation frequency 49

Equation 4.3 | 1-dimensional Langevin rotational equation for a saw-tooth potential 58

Equation 5.1 | Chemical equation for dehalogenative aryl-aryl coupling 93

Equation 5.2 | Fitting equations of kinetic curves for DBTP on Au(111) 101

Equation 5.3 | Fitting equation of kinetic curves for DBTP on Cu(111) 101

1. Introduction

The word chirality (handedness) is derived from the Greek word, χειρ (kheir) for hand and denotes the property of an object that appears in two so-called enantiomers, each being the mirror image of one another that, however, cannot be superimposed by rotation and/or translation. In direct correspondence with the linguistic root of the word, one obvious example of chiral objects in our everyday life is our pair of hands. Of course, chirality is not at all limited to the macroscopic length scales, but is also encountered on the molecular level for organic and inorganic compounds, for instance, in biomolecules (*e.g.* amino acids, DNA, and sugars) or crystals (*e.g.* quartz). Biomolecules like proteins are composed almost exclusively of L-amino acids, while nucleic acids only contain D-sugars. Without this chiral asymmetry, prebiotic molecular complexity leading to the formation of biologically active polymers could probably not have evolved.[1,2] This very pronounced enantiospecifity of the active molecular species in biochemical processes have tremendous effects regarding their physiological expression.[3,4] Accordingly, the production of enantiopure chemicals is of highest technological relevance in the pharmaceutical, agro-chemical, and food industry. In this context, homogenous catalysis is the most widely employed synthesis methods.[5,6] It is, however, marred by tedious separation of product and catalyst, costly recycling and limited temperature accessibility. Asymmetric heterogeneous catalysis can partially alleviate these drawbacks, yet, as it commonly relies on organic chiral modifiers,[7–15] the temperature range it can be applied in remains limited and due to the complex structure dynamics,[5,16] the atomistic details of the chirality transfer in the four critical stages of the catalytic reactions are hard to follow and largely unknown. Specifically, these stages are: (i) Adsorption of the educts; (ii) their activation, (iii) the specific coupling of the educts to yield the product, and (iv) the product's adsorption properties.

Whereas the chirality of molecules is related to isolated singular objects, the chirality of crystalline materials is connected with translational periodicity. In this respect, quartz presents a prototypical material as it crystalizes in a truly chiral space group. Out of the 230 space groups, representing all possible, irreducible combinations of 3-dimensional symmetries, 65 are in fact chiral. This enables to follow a different approach for asymmetric heterogeneous catalysis based on exploiting the intrinsic crystalline chirality of bulk materials.[17] In contrast to chirality imparted by chiral modifiers, here, it is the intrinsically chiral surface structure which can induce enantioselectivity by transferring its chirality to the molecules in any of the four stages of catalytic reactions. In principle, the chirality is still conserved after fine grinding or surface etching these materials, which promotes them as prospectively interesting materials as industrial catalysts. This has been shown for chiral oxide crystals, however, their low activity usually limits their practical use as efficient catalysts and only for very particular reactions high enantiomeric excess (*ee*) was reported.[18]

Recently, the intermetallic compound PdGa was identified as an extraordinary selective catalysts for the semi-hydrogenation of acetylene ,[19–23] a key process in the polyethylene production and for methanol steam reforming.[24] Additionally, PdGa belongs to one of the 65 chiral space groups, namely $P2_13$ (no. 198), hence possesses no mirror axis and all its surfaces are intrinsically chiral.[25] PdGa combines high structural, thermal and chemical stability due to a crystal structure that has a partially covalent bond character with high catalytic activity and selectivity, as well as bulk chirality. For all these reasons, PdGa bears great potential for application as enantioselective catalyst. Furthermore, the low Miller index surfaces of PdGa are to date the only sufficiently well characterized substrates of a metallic, chiral crystal to allow the research towards enantioselective heterogeneous catalysis, which is envisioned in this work. It has been shown that the low index surfaces of PdGa can be prepared under ultra-high vacuum conditions (UHV) to exhibit large and regular monoatomic terraces which express the bulk stereoisomerism also at the surfaces.[26] Furthermore, highly enantioselective adsorption of 9-Ethynylphenanthrene has been demonstrated on a PdGa{111} surface.[26,27] Thereby the proof of concept has been given that chiral processes can be induced and studied on bare, chiral intermetallic surfaces. This bears the potential to establish a fundamental understanding of physico-chemical mechanisms involved in the structure/function relationship of chirality transfer in asymmetric heterogeneous catalysis.

In this PhD work the expression of the chirality of PdGa surfaces has been investigated in its relation to a range of different chemical and physical effects. This range covers the enantioselectivity in adsorption and reaction of molecules on chiral surfaces, the detailed study of a highly unidirectional molecular motors who's sense of rotation is solely defined by the substrate to the elucidation of exotic fermionic quasiparticles states that have no counterparts in particle physics because they are fundamentally related to specific symmetries of the crystalline material which hosts them. This work aims to deepen the understanding of how crystal bulk chirality is expressed on its surface and how strongly the surface chirality influences the dynamics and reactivity of achiral or prochiral molecules.

1.1 PdGa – chiral topological material

Crystals belonging to the non-centrosymmetric space group 198, such as PdGa, with large spin-orbit coupling are of special interest because they are expected to possess exotic chiral spin-3/2 fermions with the maximum topological charge, also denoted Chern number C, of magnitude 4,[28–31] as discussed in detail in chapter 3.1. The Chern number is proportional to the number of surface Fermi-arcs emerging on the {100} surfaces, which can be resolved with angle resolved photoemission spectroscopy (ARPES, chapter 2.3). However, the existence of fermions with |C| = 4 could not yet be evidenced because none of the investigated materials so far fulfilled the two prerequisites: (i) a large enough spin-orbit coupling which allowed the resolution of spin-split surface Fermi-arcs, and (ii) the possibility of preparing atomically well-defined chiral single-crystal metal surfaces.

As PdGa meets these requirements, we perfomed ARPES measurement in combination with ab-initio calculation to determine the Chern number magnitude and as such the number of Fermi-arcs, which are directly proportional. By simply counting the number of surface Fermi-arc states of PdGa resolved by ARPES, therefore allows the determination of the Chern number magnitude. As is discussed in the preprint of the publication *Observation and manipulation of maximal Chern numbers in a chiral topological semimetal* accepted in Science and presented in 3.2, we not only succeed in resolving the chiral surface Fermi-arcs, but also in proving that these surface Fermi-arcs exhibit a spin-orbit splitting. Additional to the disclosure of the Chern number of magnitude |C|=4, we evidence that the sign of this Chern number for nodes at different high-symmetry points in the Brillouin zone can be controlled by the deliberate choice of the crystal enantiomorph.

1.2 PdGa – stator for molecular motors

The non-centrosymmetry of PdGa is not only expressed in the electronic structure by its chiral surface Fermi-arcs, but we encountered an unexpected manifestation of chirality transfer in the dynamical behavior of single achiral molecules adsorbed on its surfaces. We observed a highly unidirectional rotation of these molecules at low temperatures thus representing a molecular motor as introduced in chapter 4.1. Such an artificial molecular motor is of considerable interest, as it might ultimately result in energy harvesting on molecular scales.

In chapter 4.2 the characterization of an artificial molecular motor that consists of a single C_2H_2 molecule adsorbed on a chiral PdGa cluster provided by the Pd_3-terminated PdGa{111} surface is presented in detail as a manuscript, which has been accepted in Proceedings of the National Academy of Sciences of the United States of America. The rotational motion of this molecular motor is tracked by STM and turns out to be highly directed. Although several artificial molecular motors have been reported, our acetylene on PdGa motor is unique in several aspects. First, it reverses the common concept applied for all other reported molecular motors, which always consist of a complex chiral rotor. In contrast, our molecular motor is built of an achiral rotor, being a simple acetylene molecule that is adsorbed on top of a chiral stator. This stator solely defines the rotor's unique sense of rotation. Second, the whole motor consists of an unprecedented low number of maximum 16 atoms involved, of which only 4 are contributed by the rotor. This low number of atoms in the rotor results in, third, the motor to be able to operate in the quantum tunneling regime with an exceptional directionality of 98%. Fourth, this motor can be further powered unidirectionally by a single, continuous source of energy, specifically electrons. Finally, the highly directed rotational motion in combination with its relatively low frequency allows not only a far more detailed qualitative description, but for the first time also an experimental quantification of all parameters influencing the motion.

1.3 PdGa – template for enantioselective heterogeneous catalysis

In the previous chapters, details on the electronic structure being at the origin of many physical properties of a material and the enantiospecific dynamics of single achiral molecules on PdGa were outlined. Thus setting the stage for the next step, which aims to unravel the potential applicability of PdGa as template for enantioselective catalytic reactions. As outlined in chapter 5.1, asymmetric heterogeneous catalysis is of utmost biological relevance as biological macromolecules, such as amino acids, sugars, enzymes and receptors in the living system, occur in one single enantiomeric form only, which indicates that chirality is an indispensable element of life.

In view of their enantioselective catalytic reactivity, the three-fold symmetric PdGa{111} surfaces were investigated on three different aspects of molecular on-surface reactions:

1. Enantioselective debromination, being the first step in the most versatile and widely applied on-surface reaction, the dehalogenative aryl-aryl coupling.
2. Near-enantiopure trimerization of 9-Ethynylphenanthrene (9-EP), representing a homocoupling on-surface reaction.
3. Azide-alkyne Huisgen cycloaddition between 9- Ethynylphenanthrene (alkyne) and 3-(4-Azidophenyl)propionic azid (azide), which is a prototypical heterocoupling reaction in the field of click chemistry.

Using on-surface chemical reactions, not only small molecular structures (few unit oligomers) may be created, but also extended 1D and 2D carbon based nanomaterials.[32] A large variety of reactions has been successfully realized and scrutinized on various surfaces with the help of surface science techniques in combination with theoretical calculations. Among all reactions, Ullmann-like coupling reactions are the most widely used reactions in on-surface synthesis, resulting in the homocoupling of aryl halides. By linking aromatic units through CC bonds, it has been widely employed to build up all sorts of carbon-based scaffolds on coinage surfaces, from dimers,[33,34] 1D polymer chains[35–41] to 2D covalently linked organic networks.[34,42,43] Dehalogenation always represents the first step to initiate Ullmann coupling and to the best of our knowledge has not yet been investigated with regard to enantioselectivity. In chapter 5.2, the pivotal dehalogenation step for enantiopure dehalogenative aryl-aryl coupling on the chiral PdGa{111} surfaces is investigated for prochiral 5-Bromo-7-Methylbenz(a)anthracene (BMA) by combining temperature-programmed x-ray photoelectron spectroscopy (TP-XPS, chapter 2.3) and scanning tunneling microscopy (STM, chapter 2.4). Striking evidence for enantioselective BMA debromination are reported in the manuscript *Enantioselective debromination on chiral metal surfaces*, which is planned to be submitted to Advanced Materials.

Thorough analysis of the TP-XPS data for BMA on PdGa{111} has been hampered initially because no dedicated mathematical model has been established for on-surface synthesis processes under UHV conditions. A good estimation of the mean debromination temperature for each BMA enantiomer was achieved by the simplest approach of assuming the amount of BMA debrominating per temperature interval to follow a Gaussian distribution. Thereby, the debromination temperature differences between the two BMA enantiomers of 36 K for the Pd_3- and 46 K for the Pd_1-terminated PdGa{111} could be determined. Nevertheless, the respective debromination energy barriers could only be derived based on the well-founded kinetic rate laws applied in solution chemistry, which we valiadated to hold true for UHV on-surface synthesis as well. These rate laws presume reversibility of certain reaction steps, which has not yet been demonstrated under UHV conditions. For simplicity, we verified this reversibility on the model surface Au(111) via a halogen exchange reaction for a bromine containing molecule, where bromine is replaced by chlorine, which has been co-deposited on the surfacein chapter 5.3 by the manuscript *Reversible dehalogenation in on-surface aryl-aryl coupling*, which has been published in Angewandte Chemie.[44] This proof of reversibility also for on-surface reactions is expected to entail a paradigm shift. First, because until recently, chemical processes in on-surface synthesis were assumed to be irreversible. Second, since it establishes TP-XPS as a powerful tool to extract reaction kinetics, and thus to develop strategies for improving reaction conditions.

After having establishied high enantioselectivity of PdGa{111} surfaces for a decomposition reaction, i.e., debromination, we discuss the chirality transfer from the PdGa{111} surfaces onto a homocoupling reaction. This topic has already been addressed in a previous publication by Prinz *et al.* for 9-EP on the Pd_1-terminated surfaces, where they could not establish any enantioselectivity for 9-EP dimerization.[27] Complementary to this work, we focus on the Pd_3-terminated PdGa{111} surfaces, where we achieved the formation of almost enantiopure and homochiral 9-EP trimers.[26] As presented in chapter 5.4 by the manuscript *Near-enantiopure trimerization 9-Ethynylphenanthrene on a chiral metal surface* under review in to Angewandte Chemie, the formation of these enantiopure trimers from an initially racemic mixture of prochiral 9-EP at room temperature is in stark contrast to their behavior on the Pd_1-terminated surfaces. Therefore, we encounter again a significant ensemble effect (impact of geometric arrangement of catalytically active sites on the overall catalytic activity) in the PdGa system[45,46]. The specific bonding configuration of the homochiral trimers on the Pd_3-terminated surfaces remains unclear, although we examined all plausible binding centers for these homochiral trimers either experimentally or theoretically.

In the study addressing the enantioselective on-surface reactivity studies on the PdGa{111} surfaces, we investigate the heterocoupling between the alkyne molecule 9-EP and the azide 3-(4-Azidophenyl)propionic azid (APA), which represents an alkyne-azide Huisgen cycloaddition. Usually, such click reactions are Cu-catalyzed in solution, but an alkyne-azide Huisgen cycloaddition was demonstrated to run on Cu(111) surfaces also under UHV conditions with 9-EP as alkyne and 4-azidobiphenyl (ABP) as azide.[47] Based on the strong enantioselectivity of 9-EP on the PdGa{111} surfaces and the copper-like d-band structure of PdGa,[48,49] the focus is put on the feasibility to run this reaction on PdGa{111} with special emphasis on the ensemble effect. Again, the ensemble effect turned out to be substantial, as the azide-alkyne Huisgen cycloaddition can enantioselectively be performed on Pd_1-terminated PdGa{111} surfaces with high regioselectivity forming exclusively 1-4 triazoles, but does not proceed at all on the Pd_3-terminated PdGa{111} surfaces. On the Pd_3-surfaces only enantiopure molecular assemblies consisting of two 9-EP and one APA molecule are created. Compared to the study on Cu(111), we encounter the drawback that other than ABP, APA possesses apart from the azide a second functional group, a carboxylic group. On Cu(111), the detachment of carboxylic group is a promising route for the creation of CC bonds.[50–52] However, this process might be the origin why azide-alkyne Huisgen cycloaddition is hampered on the PdGa{111} surfaces. The results are reported in the manuscript *Asymmetric azide-alkyne Huisgen cycloaddition on chiral metal surfaces*, which is to be submitted to the Journal of the American Chemical Society.

1.4 PdGa – Chiral intermetallic compound

Investigating the research questions outlined in the chapters 1.1-1.3 necessitates the fulfillment of several requirements regarding the substrate material: it must (i) belong to the a chiral space group, if possible to P2$_1$3, and (ii) be a catalytically active single crystal, whose (iii) bulk-truncated surfaces can be prepared atomically flat and well-defined. In fact, the intermetallic compound Palladium-Gallium with a 1:1 stoichiometry (PdGa) is currently the only material, which is characterized well enough to confidently satisfy all these criteria[19–22,25,48,53,54] and will thus be the material investigated throughout this work.

Within the crystal structure of PdGa, the Pd atoms are spatially separated by Ga atoms from each other and their position is well defined up to temperatures close to the melting point (1045° C) by the stability of its crystalline phase. The minimal Pd-Pd distance in PdGa is about 10% larger as compared to the elemental Pd bulk crystal. This separation of the Pd atoms is maintained and, depending on the crystal direction of the surface, even increased on the PdGa surfaces which have been shown to yield high catalytic activity in conjunction with high reaction selectivity for symmetric heterogeneous catalysis, in particular the semi-hydrogenation of acetylene.[19–22,53] However, its potential for asymmetric heterogeneous catalysis remained largely unexplored.

Owing to its non-centrosymmetric P2$_1$3 space group, PdGa appears in two enantiomeric forms, denoted as PdGa:A and PdGa:B, and all its bulk-truncated surfaces are chiral.[54] By recording the intensity dependence of the energy of low energy electron diffraction spots (LEED-I(V), chapter 2.2) in combination with scanning tunneling microscopy (STM, chapter 2.4), Prinz *et al.* determined the surface termination for several low Miller-index PdGa surfaces, such as the (100), (110), (210), (111), and (-1-1-1) surfaces.[26,48] In the following, the structural properties of the PdGa surfaces used throughout this work, specifically the PdGa{100} and PdGa{111} surfaces, are introduced.

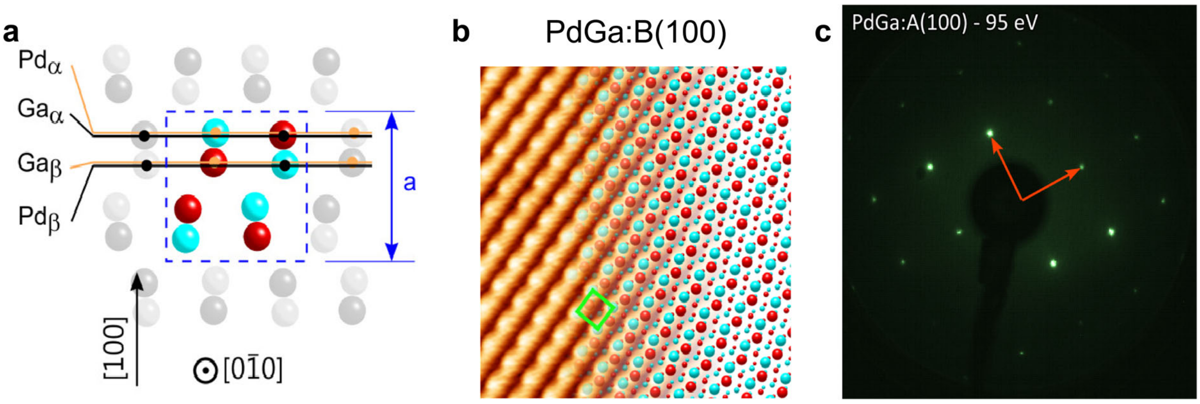

Figure 1.1| PdGa(100) surface characterization

a Stacking order of PdGa in the [100]-driection. The surface unit cell is indicated by a dashed rectangle. **b** LEED of the PdGa:A(100) surface recorded at an electron energy of 95 eV. **c** STM image (6x6 nm^2; 8 mV; 100 nA) with atomic resolution of the clean PdGa:B(100)Pd$_\alpha$ surface partially overlayed with the atomic structure model. In all presented PdGa models cyan represents Pd atoms, red Ga atoms. Figures adapted from Ref.[26]

In [100]-direction, PdGa possesses a 2$_1$ screw axis. Therefore, of the 8 atoms constituting the bulk-truncated PdGa(100) surface unit cell, the 4 atoms in the upper half of the unit cell are repeated in the lower half, but rotated by 180°. Hence, PdGa consists of 4 non-equivalent atomic layers in the [100]-direction, as presented in Figure 1.1a, of which only one, denoted as Pd$_\alpha$, is identified to terminate the rectangular (100) surface (Figure 1.1b). Moreover, due to the 2$_1$ screw axis, LEED patterns (as well as ARPES maps as discussed in 3.2) of the PdGa(100) surface exhibit a 2-fold rotational symmetry (Figure 1.1c), although the bulk-truncated surface does not possess neither mirror nor rotation symmetries.[26]

As for the [100]-direction, PdGa exhibits 4 non-equivalent atomic planes in the [111]-direction, as illustrated in Figure 1.2a, leading to structurally different, three-fold symmetric (111) and (-1-1-1) surfaces.[48,54] While one of the two surfaces is terminated by single, isolated Pd atoms, further denoted as Pd$_1$ (specifically PdGa:B(-1-1-1)Pd$_1$ and PdGa:A(111)Pd$_1$ for the two enantiomorphs), the top layer of the other surface consists of spatially separated Pd trimers, referred to as Pd_3 (Figure 1.2b, PdGa:B(111)Pd_3 and PdGa:A(-1-1-1)Pd_3).[48] Despite their dissimilar surface structure, the Pd_1 and Pd_3 surface share similar electronic properties, identical symmetry group, and the same surface lattice-structure and –parameters.[48,54] Therefore, PdGa{111} surfaces are ideal to disentangle the influence of geometric and electronic effects, *i.e.*, the ensemble and ligand effects in surface reactions.[45]

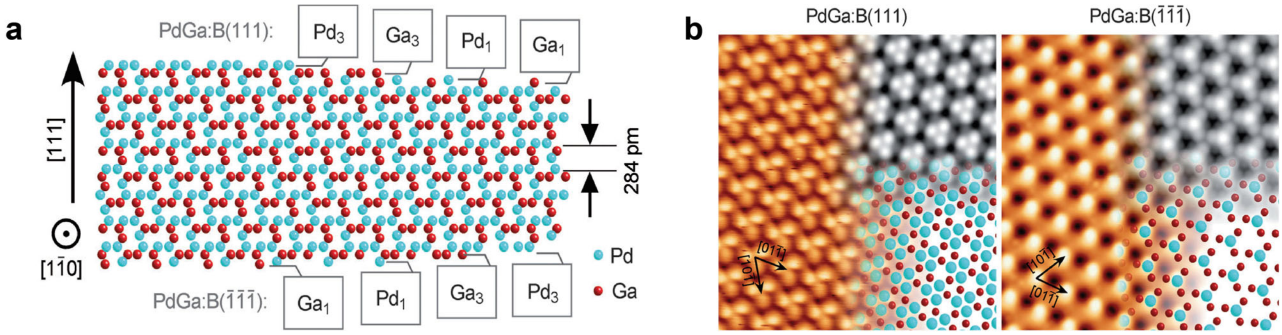

Figure 1.2| PdGa{111} surfaces characterization

a Stacking order of PdGa in the [111]-direction. **b** STM images of PdGa:B(111)Pd_3 (left, 6x6 nm^2; 80 m,V; 730 pA) and PdGa:B(-1-1-1)Pd_1 (right, 6x6 nm^2; 100 mV; 400 pA). Both experimental STM images are overlaid by simulated ones (top right) and the atomic surface structure (bottom right). In all atomic PdGa structures, Pd is colored cyan and Ga red. Figures adapted from Ref.[48]

The impact of the ensemble effect has already been investigated for the adsorption properties of achiral molecules like CO, C_2H_2, C_2H_4, and H_2.[45,46] For CO the ensemble effect is expressed in differences in the coverage dependence of the adsorption sites on the two structurally inequivalent PdGa{111} surfaces.[45] In particular, the Pd_1-terminated PdGa{111} surface provides only one on-top adsorption site for CO, independent of the coverage, while on the Pd_3-terminated PdGa{111} surface, CO prefers hollow-site adsorption at low coverages, but moves to on-top sites at high coverages. This results in different maximum loading capacities of one and three CO molecules per surface unit cell for Pd_1- and Pd_3-terminated PdGa{111} surfaces, respectively.[45] On the other hand, C_2H_2 molecules occur in two different adsorption sites on the Pd_1-terminated PdGa{111} surfaces - on top of a single top-layer Pd atom or in the center of three occupied on-top sites - but only in one on the Pd_3-terminated PdGa{111} surfaces, being on top of a top-layer Pd trimer.[46]

2. Materials and methods

As outlined in chapter 1, chirality can manifest itself in several different physical and chemical processes and effects, where the surfaces of the intermetallic PdGa allow to investigate those we have outlined in chapters 1.1-1.3. In the following the experimental techniques which have been employed for the investigation of (i) the topologically protected band-crossings at high symmetry points and surface Fermi-arcs, (ii) the dynamics of an electrically driven molecular motor, and (iii) asymmetric on-surface synthesis are discussed.

The *sine qua non* requirement in order to be able to address any of the outlined research is that the crystal surfaces must be prepared in a fashion such that each time the same, clean, bulk-truncated surfaces are obtained (chapter 2.1). The overall surface quality and symmetry properties are established and optimized with low energy electron diffraction, as introduced in chapter 2.2.

In order to experimentally corroborate the predicted symmetry-protected band-crossings at high symmetry points in PdGa and the presence of surface Fermi-arcs originating from the materials bulk electronic band structure (topic (i)), Angle-Resolved Photoemission Spectroscopy (ARPES), presented in chapter 2.3, has been used with synchrotron-light as excitation source.

Photoemission spectroscopy has also been employed to investigate (iii). Here, Temperature-Programmed X-Ray Photoemission Spectroscopy (TP-XPS) using synchrotron radiation (chapter 2.3) has allowed to elucidate the dynamics of chemical reactions on the PdGa surface by following the temperature dependence of characteristic core-level peaks with high energy and temperature resolution. On the other hand, to get a real-space structural insight into (iii) asymmetric on-surface reactions in terms of enantioselectivity, reaction mechanism, or created reaction products, the adsorption configuration and enantiomeric form of all reactants, intermediates, and reaction products have to be visualized with locally probing methods such as scanning tunneling microscopy (STM) or non-contact atomic force microscopy (both techniques are discussed in chapter 2.4). STM has furthermore been employed to (ii) investigate the dynamics of an electrically driven molecular motor.

2.1 Preparation of single crystal surfaces under UHV conditions

The indispensable requirement for a successful execution of this project, is the preparation of clean, atomically well-defined, and specific bulk-truncated PdGa(100) and PdGa{111} surfaces prepared under ultra-high vacuum (UHV; pressure < 5×10^{-10} mbar) conditions. It has been established by Widmer and co-workers, that the low Miller-index (100), (110), (210), (111), and (-1-1-1) surfaces of PdGa are largely unreconstructed, bulk-truncated terminations when prepared by repeated sputtering-annealing cycles in UHV.[26,48] Moreover, no indications for segregation has been found for temperatures below 870 K.[54] The standard procedure used throughout this work consists of Argon or Neon ion sputtering with 1 kV acceleration voltage, followed by heating to 870 K ± 20 K. The temperature is recorded with an optical Raytek pyrometer with its emissivity set to 0.1. Such prepared PdGa surfaces could be used for experiments over a period of several days, or even weeks without a significant amount of adsorbed contaminants if the base pressure of the analysis chamber was in the low 10^{-11} mbar regime.

For the Au(111) and Cu(111) surfaces, the preparation consists of the same sputter-annealing procedure as for the PdGa surfaces, apart from the annealing temperature, which was 730 K ± 20 K for Cu(111) and Au(111).

2.2 Low energy electron diffraction

Low energy electron diffraction (LEED) is a particularly surface sensitive method due to the short inelastic mean free path of electrons in the 20-500 eV range, which are diffracted by the periodic atomic and/or molecular arrangements on the surface.[55] LEED is routinely applied for the determination of the atomic surface structure in terms of symmetry, lattice parameters, reconstructions, and quality. A schematic sketch of the LEED working principle is presented in Figure 2.1. The sample is bombarded under normal incidence with nearly mono-energetic electrons, which are generated on a cathode in the electron gun, then accelerated to a fixed energy and collimated. The diffracted electrons are then accelerated to a fluorescent screen where the LEED pattern (examples in Figure 2.1b,c) can usually be directly observed. The grids in the experimental setup act as filters for inelastically scattered electrons, therefore allowing only the elastically scattered electrons of interest to reach the fluorescent screen.

In the preceding work by Prinz and co-workers, the intensity evolution of single LEED spots with electron energy was acquired for several low Miller-index PdGa surfaces.[26,48] The corresponding spot specific energy-intensity profiles have been matched to surface structure models by means of LEED-I(V) simulations. The LEED-I(V) method has been pivotal in the unambiguous determination of the terminating layer of the (111), $(\bar{1}\bar{1}\bar{1})$, (100), (110) and (210)PdGa surfaces. In this work, LEED was mainly used in the photoemission spectroscopy related works to verify the crystal enantiomer and check the surface quality.

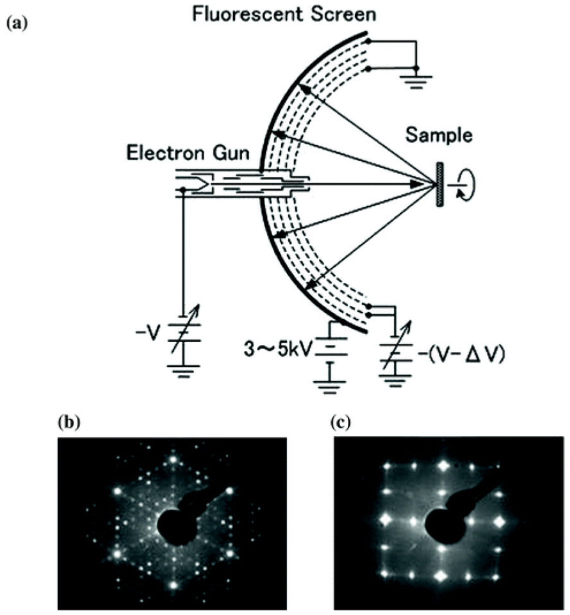

Figure 2.1 | LEED

a Schematics of a LEED with a four grid display system (dashed curved lines: grids; solid curved line: fluorescent screen). LEED pattern of **b** Si(111) 7x7 reconstruction and **c** Si(001) 2x1 reconstruction; both recorded with 50 eV electron energy. (Figure adapted from Ref.[55])

2.3 Photoelectron spectroscopy

2.3.1 Fundamental aspects of the method

Photoelectron spectroscopy (PES) is based on the photoelectric effect, *i.e.*, by illumination of a sufficiently conductive sample with nearly monochromatic photons of energy $h\nu$, the photon energy is transferred to the sample's electrons which are then emitted with a kinetic energy E_{kin}. The electrons emitted from the sample are detected in an energy-resolved fashion to yield an intensity-energy spectrum. For elastically emitted electrons, by knowing the photon energy $h\nu$, the kinetic energy E_{kin} can be related to the original binding energy E_{Bin} of the electron to the sample via the Einstein equation

$$E_{Bin} = h\nu - E_{kin} - \phi$$

Equation 2.1 | Einstein equation

where ϕ corresponds to the electrostatic potential where the kinetic energy is measured and therefore usually corresponds to the work function of the analyzer.

The correlation expressed by Equation 2.1 between kinetic energy of the elastically emitted electrons and the binding energy (*i.e.*, the initial state energy) of the electrons allows to access different aspects of the electronic structure of the material under investigation. For instance, when choosing photon energies in the ultra-violet range (ultra-violet photoelectron spectroscopy (UPS)) the material's valence bands are resolved with high intensity. Higher energy x-rays, *i.e.*, x-ray photoelectron spectroscopy (XPS) on the other hand, allow the detection of core-level electrons with element and chemical state dependent characteristic energies from which the quantitative elemental composition of a sample can be determined. Figure 2.2 shows an XPS spectrum of clean PdGa with the emission peaks labeled according to their elemental and orbital origin.

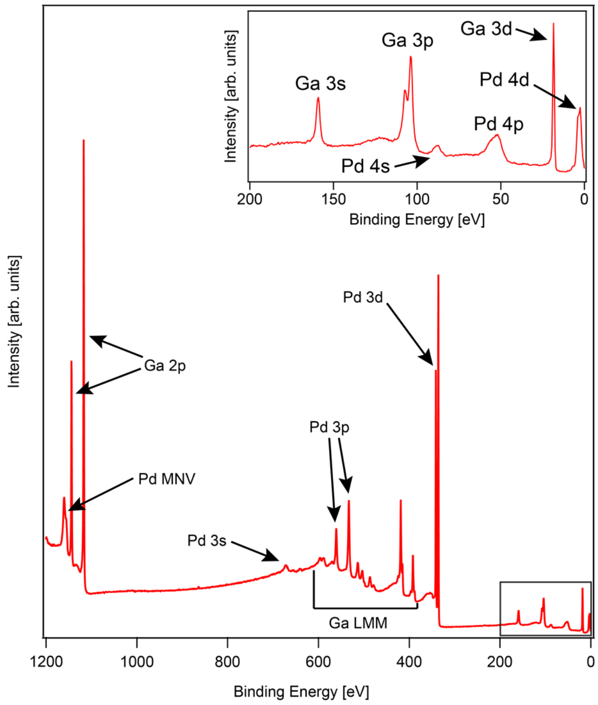

Figure 2.2 | XPS spectrum of clean PdGa:A(-1-1-1)Pd_3

XPS spectrum of a PdGa:A(-1-1-1)Pd_3, recorded with monochromatic Al K_α. All core level and Auger peaks are labelled. The inset is a close-up of the part of the spectrum indicated by a rectangle.

If an electron is emitted from a core level, a positively charged hole remains in the material. This hole can be filled by electrons from the outer shell with lower binding energy in a non-radiative recombination, transferring the thus released energy to a second electron, denoted Auger electron, which is then emitted. Because the transferred energy is independent of the excitation by the photon, these Auger electrons possess a constant kinetic energy, which is in contrast to the constant binding energy of the core level electrons. As a consequence, by varying the photon energy, core level electrons can be distinguished from Auger electrons.

The precise energy position of the core level peaks depends on the chemical environment of the corresponding atomic species and, therefore, can lead to multicomponent peaks if the same element is present in different chemical configurations. Measuring the relative weighting of such components with different chemical shifts under different conditions, for instance by varying the photon energy and thus the electron's mean free path (discussed in chapter 2.3.2), allows for example the identification of the contribution of individual layers for the Be(0001) surface to the overall XPS signal (Figure 2.3).[56]

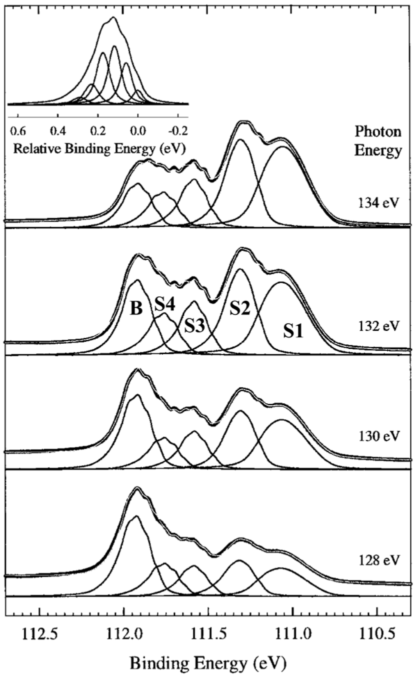

Figure 2.3 | Surface sensitivity of XPS

XPS spectrum of the Be 1s core level of the Be(0001) surface recorded with different photon energies. The chemical shift of the top (S1), second (S2), third (S3), and fourth (S4) layer with respect to the bulk (B) contribution are well resolved at all energies. The photon dependence of the weighting of the different contributions arises from changes in the electron mean free path. Figure adapted from Ref.[56]

In the context of this work, the possibility of using tunable, highly monochromatic, and intense synchrotron light offers particularly interesting experimental conditions. By tuning the photon energy a very high surface sensitivity can be achieved, which allows for fast acquisition of XPS spectra of adsorbed molecules which high energy resolution. This allows to measure thermally activated changes in chemical state of these molecules as discussed in more detail in chapter 2.3.3.

2.3.2 Experimental setup

A schematic illustration of the most important components of an experimental XPS setup is presented in Figure 2.4. These main components are (i) a photon source, (ii) the sample, which is fixed on a manipulator that can have several translational and/or rotational degrees of freedom, (iii) a hemispherical electrostatic electron energy filter and (iv) a detector. The combination of collection lenses, energy filter and detector constitute the electron analyzer.

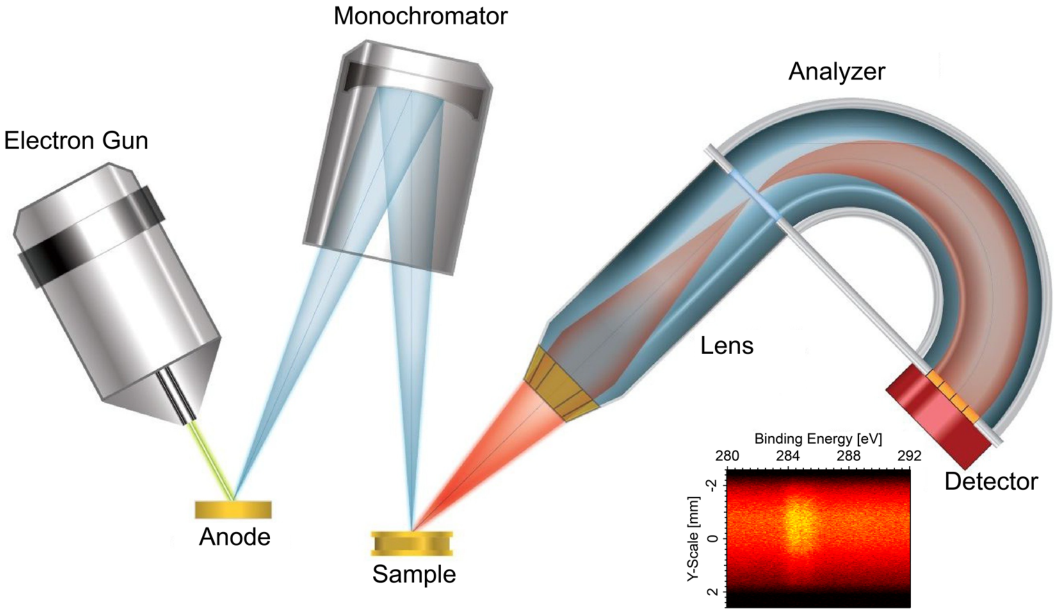

Figure 2.4 | Schematic of XPS setup

Schematics of a typical XPS setups, starting with an electron source, from which emitted electrons are accelerated onto the anode to generate X-rays. The emitted photons are then monochromatized, before they illuminate the sample. The photoelectrons emitted from the sample are focused onto the entrance slit of the hemispherical analyzer with electrostatic lenses. In the hemispherical analyzer the electrons are forced on a circular path with its radius depending to the electrons' kinetic energy. The electrons are then recorded with the detector in an energy-resolved fashion resulting in images as the exemplary one shown on the bottom right for a C 1s core level. Figure adapted from Ref.[57]

In order to unambiguously determine the electron's binding energy E_{Bin} in the material with Equation 2.1 (corresponding to the material's core level energy) from the measured kinetic energy E_{kin}, the photon energy $h\nu$ must be well-defined, *i.e.*, monochromatic. However, in experiments the energies of the photons emitted by the source are always distributed over a certain energy range, which should be as narrow as possible to optimize the energy resolution of the XPS signal. In laboratory based instruments, the x-ray sources are usually limited to Aluminum or Magnesium anodes. Both materials possess one dominant emission energy Al-K$_\alpha$ and Mg-K$_\alpha$, respectively, but both have a non-zero natural linewidth and also emit photons due to Bremsstrahlung and weaker characteristic emission lines. Therefore a Bragg-monochromator is often placed between photon source and sample to filter all signal besides the Al-K$_\alpha$ to achieve a narrower line-shape, and thus to improve the energy resolution of the XPS signal.

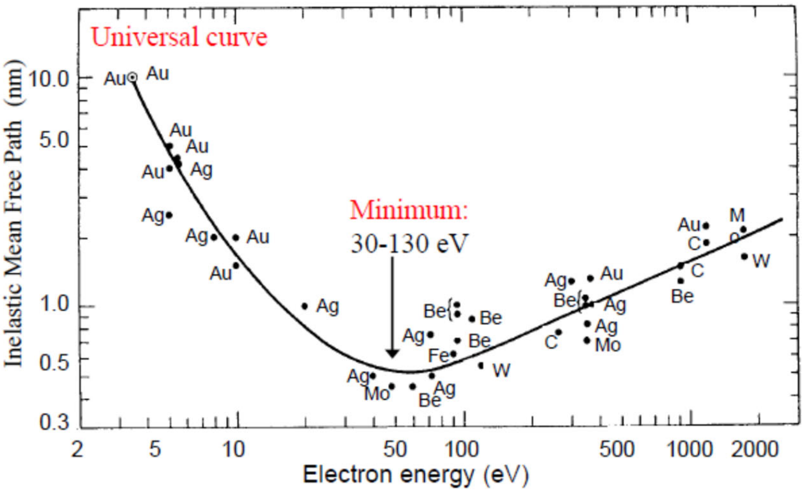

Figure 2.5 | Universal curve

Electron inelastic mean free path as a function of the electron's kinetic energy for several materials. The solid line represents the fitted universal curve with its minimum around 50 eV. The figure is adapted from Ref.[58]

The photoelectrons emitted by the sample under a certain angle are then collected and focused to the entrance of the hemispherical analyzer by the electron optical lens assembly. In the following, the electrons are selected according to their kinetic energies by the potential applied on the two concentric hemispheres before they are counted by the detector.

The limitation imposed by the element specific characteristic emission lines like Al-K_α or Mg-K_α can be surpassed by using monochromatic synchrotron radiation. At a synchrotron, a continuous, wide range of highly monochromatized photon energies are available. The selection of the initial photon energy at a synchrotron can be made according to (i) the desired surface or bulk sensitivity - which is defined by the mean free path length of the emitted electrons given by the universal curve in Figure 2.5 –, and (ii) the energy of Auger electrons, whose signal should not interfere with that of the core level electrons of interest.

2.3.3 Temperature-programmed x-ray photoelectron spectroscopy

Apart from the option to vary the photon energy, the signal to noise ratio is significantly enhanced at the synchrotron, owing to a high photon flux and narrow photon energy linewidth, compared to the Al-K_α or Mg-K_α laboratory x-ray sources. These two advantages allow the acquisition of high-resolution XPS spectra within a few seconds, as long as the molecules do not desorb or react due to the high flux, and thus to track the chemical evolution of each component of an element during a heating ramp with high time-, and accordingly, temperature-resolution. The described method has been established in the recent years and is generally referred to as temperature-programmed XPS (TP-XPS).[59–68] As an example, the temperature evolution of the Br $3d_{5/2}$ and $3d_{3/2}$ core level doublet for 4,4''-dibromo-*p*-terphenyl (DBTP) on Au(111) is shown in Figure 2.6b. Each horizontal pixel line of the TP-XPS map in Figure 2.6b consists of an individual XPS spectrum recorded over 5 s. The two possible chemical states of the Br atom, either covalently bonded to a carbon atom (Br-C) or physisorbed on the Au substrate (Br-Au), yield a distinct XPS spectrum (Figure 2.6a), where the temperature evolution of each state (Figure 2.6c) is extracted by fitting every XPS spectrum of the TP-XPS map by a weighted sum of the two distinct XPS spectra for the respective chemical state.

As TP-XPS allows tracking chemical processes with high temperature resolution, this method is used in chapter 5.2 to establish the enantioselective debromination of 5-Bromo-7-Methylbenz(a)Anthracene and to estimate the temperature difference for debromination between the two enantiomers. Moreover, this method allows the experimental determination of the energy barriers for several chemical processes. The mathematical model as well as the respective experimental evidence are discussed in chapter 5.3.

All (TP-)XPS experiments have been performed at the dedicated PEARL beamline at the Swiss Light Source, which is presented in chapter 2.5.1.

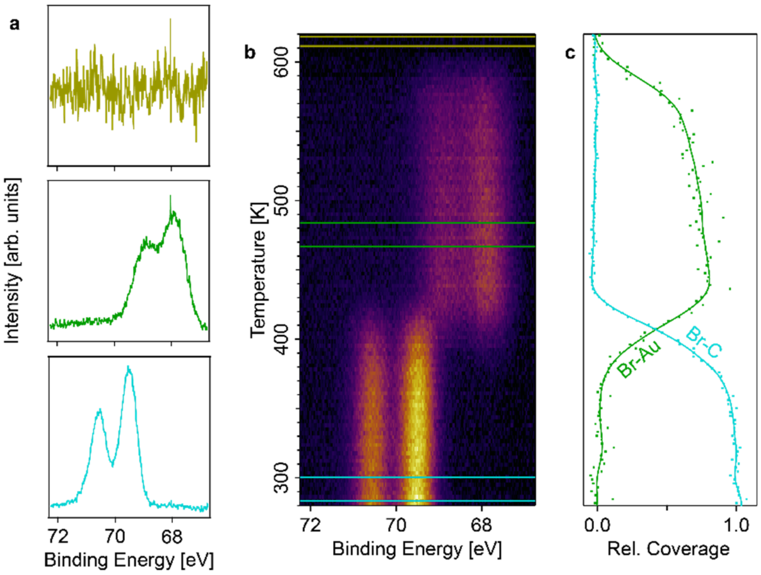

Figure 2.6 | Information gained from TP-XPS

a XPS spectra of the three chemical states of the bromine atoms, *i.e.*, attached to the DBTP molecules (bottom), adsorbed on the surface (center) and desorbed (top). The spectra in **a** are extracted from the TP-XPS map in **b** by averaging all spectra between the horizontal line with the respective color. In **c** the temperature evolution of the bromine's chemical states, *i.e.*, bromine attached to DBTP (Br-C) and bromine adsorbed on the surface (Br-Au).

2.3.4 Angle-resolved photoelectron spectroscopy

As shown in Figure 2.4, the sample can usually be rotated in two sometimes even three directions while being illuminated. These rotational degrees of freedom in combination with the angular resolution of modern electron-energy analyzers allow the acquisition of angle-resolved photoelectron data. Depending on the initial state of the photoelectron, the angular emission intensity distribution contains different information reflecting the crystal structure or the electronic band structure of the sample. If the intensity variation of a core level peak measured, the angular map is dominated by diffraction of the elastically emitted electrons at the surface crystal structure. The corresponding method is denoted x-ray photoelectron diffraction (XPD) and will not be detailed further. If, on the other hand, electrons from delocalized valence electronic states are measured, their angular emission intensity distribution is determined by the momentum $\hbar\boldsymbol{k}$ of the band state the electron is emitted from. In this case, the technique is called angle-resolved photoelectron spectroscopy (ARPES). For ARPES, the angular resolution in real space, translates into wave vector resolution $\boldsymbol{k}$ in the reciprocal space. This correspondence of emission angle in real space and wave vector $\boldsymbol{k}$ in reciprocal space is based on the conservation of the electron momentum parallel to the surfaces. Accordingly the polar emission angle θ and the azimuthal angle α are related to $\boldsymbol{k}_{||}$ by:

$$\hbar\boldsymbol{k}_{||} = \sqrt{2m_e E_{kin} sin^2(\theta)} \begin{pmatrix} \cos(\alpha) \\ \sin(\alpha) \end{pmatrix}$$

and assuming a free electron like final state of the electron in the bulk also k_z can be obtained using the inner potential V_0 of the material under investigation

$$hk_z = \sqrt{2m_e(E_{kin} cos^2(\theta) + V_0)}$$

ARPES not only resolves the bulk band structure of the investigated material, but, if present, also surface electronic states can be mapped. Contrary to bulk states, surface states are two dimensional states and hence localized in the z-direction, therefore they only disperse in the plane of the sample surface, *i.e.*, $\boldsymbol{k}_{||}$. As a concequence, by probing the dispersion perpendicular to the surface k_z via the variation of the photon energy, surface states can be distinguished from bulk states by their lack of k_z-dispersion, as realized in recent examples.[69–71]

In chapter 3.2, the bulk band structure of PdGa is probed by ARPES at the ADRESS beamline at the Swiss Light Source (SLS) by employing soft x-rays in the energy range between 350 eV-1000 eV (chapter 2.5.2), while the surface states are investigated with ARPES at the I05 Beamline at the Diamond Light Source (DLS) using VUV light with photon energy between 20-200 eV (chapter 2.5.3). ARPES measurements with photons in the lower energy range are more surface sensitive due to the decreased mean free inelastic pat length of the emitted electrons, as can be seen from the "universal curve" in Figure 2.5.

2.4 Scanning probe microscopy

Since its invention at IBM in Rüschlikon in 1982 by Binnig and Rohrer and the first real-space imaging of a 7x7 reconstructed Si(111) (Figure 2.7a) surface,[72,73] scanning tunneling microscopy (STM) evolved into an experimental technique widely applied in virtually all aspects of surface science. The particular strength of the STM technique is that it combines structural imaging with single atom or even intramolecular resolution (Figure 2.7b) with electron spectroscopy and atom/molecule manipulation. This unique combination of atomic-scale characterization and manipulation makes it one of the method of choice for the research of nanostructures. A striking illustration of the strength offered from this combination is shown in Figure 2.7c. where Nempkes *et al.* have created and characterized the quantum mechanical analogue of a Sierpiński triangle.[74] This has been achieved by STM induced manipulation and positioning of CO molecules on a Cu(111) surface in a controlled way, such that the surface state electrons are scattered such that the electronic analog of a Sierpiński triangle could be achieved. Using Scanning Tunneling Spectroscopy (STS) the higher order topologically protected corner states, predicted for this structure, were then spatially resolved.

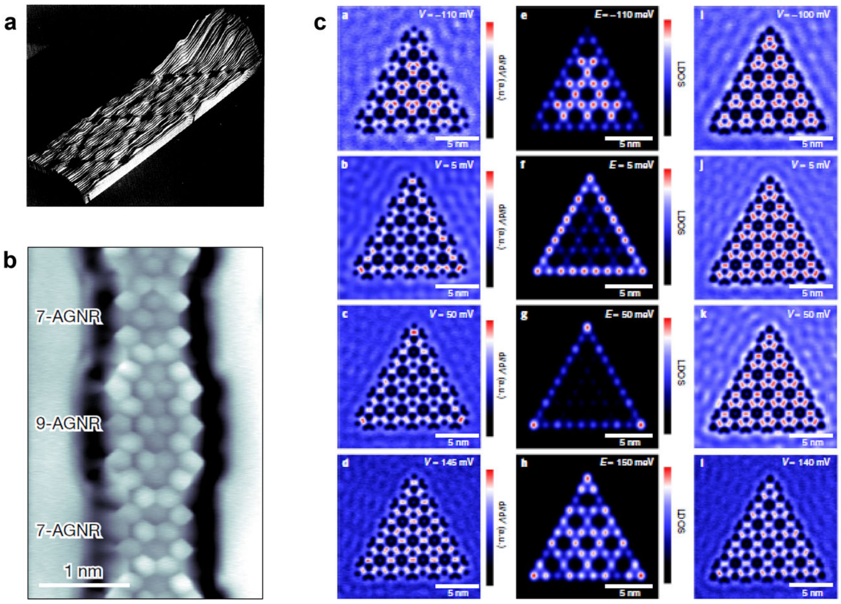

Figure 2.7 | Examples of STM experiments

a The first ever recorded STM image showing the spatially resolved 7x7 reconstruction of the Si(111) surface. **b** STM image with intramolecular structural resolution of a topological nanoribbon acquired with a CO terminated STM tip. **c** The electronic structure of a non-trivial breathing kagome lattice created by controlled manipulation of CO molecules on a Cu(111) surface with the STM tip. The images are adapted from Ref.[41,73,74]

In Figure 2.8 the basic working principle of the STM is schematically illustrated. As STM is based on the quantum mechanical tunneling current between two conductive electrodes, these electrodes, *i.e.*, an atomically sharp tip and the sample to be investigated, must be brought into close proximity (below 1 nm distance) to each other. Provided that the sufficiently small separation is established, upon application of a voltage between tip and sample, a finite current is generated. The magnitude of this tunneling current strongly depends (exponentially) on the separation distance of the electrodes. By laterally scanning the STM tip across the sample surface, 'topographical' maps are obtained. Such maps, generally referred to as STM images, are either recorded by keeping the STM tip at a constant height and detecting changes in the tunneling current, or by keeping the tunneling current constant while tracking changes of the tip height.

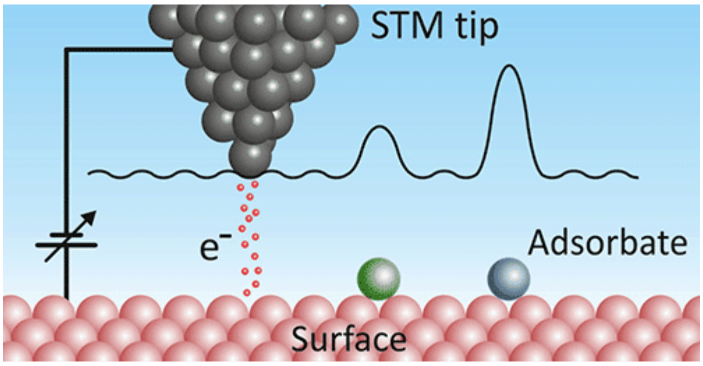

Figure 2.8 | Sketch of the STM working principle.

The recorded "topographical" information of the substrate is shown as solid black line for the case of the constant current scanning mode. (Image adapted from Ref.[75])

2.4.1 Theoretical background of Scanning Tunneling Microscopy

The operational principle of STM is primarily based on the quantum mechanical tunneling of electrons between two electrodes in close proximity. In the following, for simplicity, the tunnel junction resulting from the complex tip-sample geometry is assumed to be one-dimensional. Quantum mechanical tunneling generally refers to the situation, that even though the energy of a particle is lower than the potential energy barrier by which it is confined, the particle can still cross this barrier with a non-zero probability by 'tunneling' through it. In the case of an STM, these particles are electrons situated near the Fermi energy in the two conductive electrodes, which are the sample and STM tip respectively. The potential energy barrier is created by the work functions of STM tip ϕ_{Tip} and sample $\phi_{Surface}$ and its shape depends on the applied bias voltage V_{Bias} and the tip-sample distance z (Figure 2.9). When the bias voltage V_{Bias} is applied between STM tip and sample, a net tunneling current I_T according to:[76]

$$I_T(z) \propto V_{Bias} \exp(-\kappa z)$$

Equation 2.2 | STM tunneling Current – distance dependence

$$\kappa = \frac{\sqrt{2m_e\phi}}{\hbar}; \qquad \phi = \frac{\phi_{Tip}+\phi_{Surface}-eV_{Bias}}{2}$$

is generated, where m_e is the electron mass. The value of κ in the exponential is typically of the order of 1 Å^{-1}, *i.e.*, a variation of z by 2.3 Å results in change of a factor 10 in the current. As a consequence of the fast decrease of the current with z the STM tip must be brought in a controlled way within a few Ångström distance to the sample surface to measure a current in the order of a few pico- to nanoampères.[77,78] On the other hand, this exponential $I_T(z)$ relation allows very precise control over the STM tip – sample distance z by measuring the tunneling current I_T.

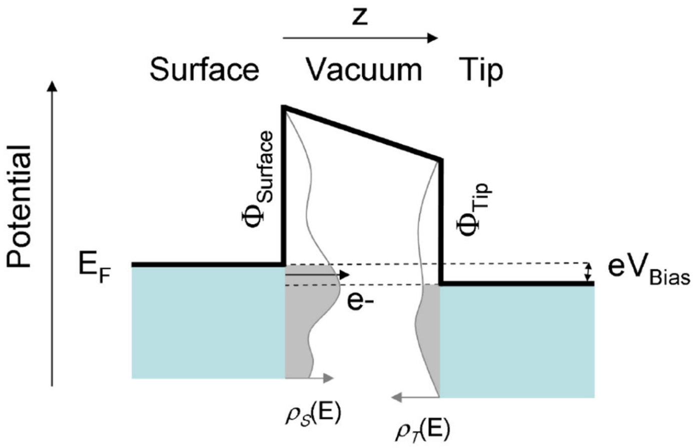

Figure 2.9 | Principle of quantum tunneling between STM tip and sample surface

Illustration of the energy potential landscape for an STM tip in proximity of a surface with a bias voltage V_{Bias} applied between them. Figure adapted from Ref.[79]

In the derivation of Equation 2.2, constant electronic densities of states for the STM tip $\rho_T(E)$, and the sample $\rho_S(E)$ have been assumed, which is not fulfilled in any material. The more complete physical description of the tunneling current between STM tip and sample considering non-constant densities of states for both is shown in Equation 2.3 and has been developed by Tersoff and Hamann:[80]

$$I_T \propto \int_{-\infty}^{\infty} [f(E_F - eV_{Bias} + \varepsilon) - f(E_F + \varepsilon)] \times \rho_S(E_F - eV_{Bias} + \varepsilon)\rho(E_F + \varepsilon)|M|^2 d\varepsilon$$

Equation 2.3 | Tunneling current – density of states dependence

In Equation 2.3, the probability for an electron to tunnel from an electronic state in the STM tip to one in the sample, hence the dependence of the tunneling current on the tip-sample separation in Equation 2.2, is included in the tunnel matrix M. Moreover, the occupation of the electron density of states in both, STM tip and sample, are assumed to obey the Fermi-Dirac distribution $f(E) = \frac{1}{1+\exp(\frac{E}{k_B T})}$ at finite temperature T.[77,78] To minimize this thermal broadening of the electron density of states, the electronic properties of the sample should be measured at cryogenic temperatures.

The tunneling current arises due to an induced offset of the sample's density of states by eV_{Bias} with respect to those of the tip. Depending on the polarity of the bias voltage the Fermi energy of the STM tip is either shifted above that of the sample, such that valence electrons of the tip in the energy range between $E_{F,Tip}$ and $E_{F,Tip} - eV_{Bias}$ tunnel to the conduction band of the sample in the range between $E_{F,Sample}$ and $E_{F,Sample} + eV_{Bias}$, or vice-versa. Therefore, the tunneling current I_T is a convolution of the density of states of STM tip and sample which are shifted with respect to each other by the applied bias voltage V_{Bias}. In order to deconvolute the electronic properties of the sample from those of the tip, the density of states of the tip material should be close to constant in an as wide range around Fermi energy as possible. This is usually achieved by choosing either metallic tungsten or platinum-iridium as STM tip material.

2.4.2 Main STM components

From the theoretical treatment of the operational principle of the STM in the previous chapters several challenges regarding the technical implementation of a working STM can be identified, such as (i) tip positioning with ideally sub-picometer accuracy, (ii) the capability to measure currents with a sensitivity below 1 pA and sufficient bandwidth, or (iii) the need for atomically sharp STM tips. In Figure 2.10 the key components of the STM to technologically address these obstacles are schematically sketched.

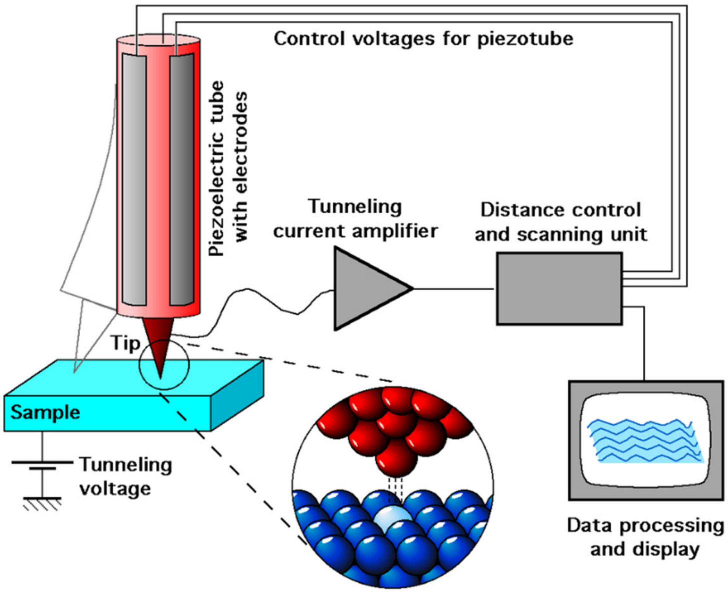
Control voltages for piezotube
Piezoelectric tube with electrodes
Tunneling current amplifier
Distance control and scanning unit
Tip
Sample
Tunneling voltage
Data processing and display

Figure 2.10 | Sketch of the main components required for an STM.
(Figure adapted from Ref.[81])

The required precision in the relative positioning of the tip and sample is achieved by making use of piezoelectric materials, which respond to the application of an external electric field with internal mechanical strain. Here, translation in all 3-axis of space can be achieved with a typical sensitivity of the order of 1 Å/V of the scanner piezo-tube. The positioning accuracy, made possible by the piezoelectric actuator, is however compromised by electronic noise, mechanical vibration and thermal drift all of which need to be reduced as best as possible. To reduce mechanical noise, the STM scan head can actively and passively be decoupled from the environment via spring suspensions in combination with eddy current damping. To further decrease mechanical noise, the entire UHV system can be pneumatically damped. The electronic noise is minimized by pre-amplifying the tunneling current signal in as close proximity to the instrument as possible, thus also overcoming the technical challenge (ii).

The spatial resolution of an STM is maximized if the whole contribution of the tunneling current signal is primarily passing through a single atom at the STM tip apex. Such atomically sharp tips can be obtained, *e.g.*, by electrochemical etching of a tungsten or platinum-iridium wire according to Ref.[82,83] before transferring it to the ultrahigh vacuum (UHV) STM system. In case, that the tip is blunted or picks up an unwanted contamination, it can be *in-situ* modified either by indentations into the metallic substrate, or with field emission. In both cases the metallic tips are reformed and might become atomically sharp. If a STM tip terminated by a single metallic atom is achieved, it can be optimized even further by picking up one CO molecule from the substrate, allowing intramolecular resolution as shown in Figure 2.7b.

To achieve such intramolecular resolution, both, the molecule on the substrate and the CO molecule on the STM tip have to be stabilized by reducing thermal fluctuations. This can be accomplished by performing the experiments at cryogenic temperatures. To reach and stabilize cryogenic temperatures, good thermal, *i.e.*, mechanical, contact of the STM tip/sample assembly to the cryostat is required without coupling in mechanical noise. This difficulty is overcome by pressing the STM tip/sample assembly to the cryostat for cool-down, then releasing it to a suspended configuration for the experiments. In the suspended mode, STM tip and sample are decoupled from mechanical noise, while still being cooled via a bunched wire connection to the cryostat. To maintain stable and low temperatures during the experiment, the STM tip/sample assembly is shielded from thermal radiations.

2.4.3 Non-contact atomic force microscopy

Non-contact atomic force microscopy (nc-AFM) is closely related to STM in terms of components required for the tip-sample positioning, but differs in the physical effect that delivers the signal, based on which the tip-sample distance can be determined.[84] Instead of probing the local electronic properties as in STM, nc-AFM probes the local forces acting between tip and sample with an ideally atomically sharp tip mounted on a cantilever, as illustrated Figure 2.11a, which is actively oscillating with a constant amplitude at its unperturbed resonance frequency f_0. When the cantilever is brought in proximity of the surface, the tip surface interaction force F_{ts} causes a resonance frequency shift of Δf which, in the small amplitude limit, is proportional to the force gradient $\frac{\partial F}{\partial y}$ that is reflecting the tip-sample interaction potential as shown in Figure 2.11b:[77,78,84]

$$\Delta f \propto -\frac{\partial F}{\partial y}$$

Equation 2.4 | Frequency shift in AFM

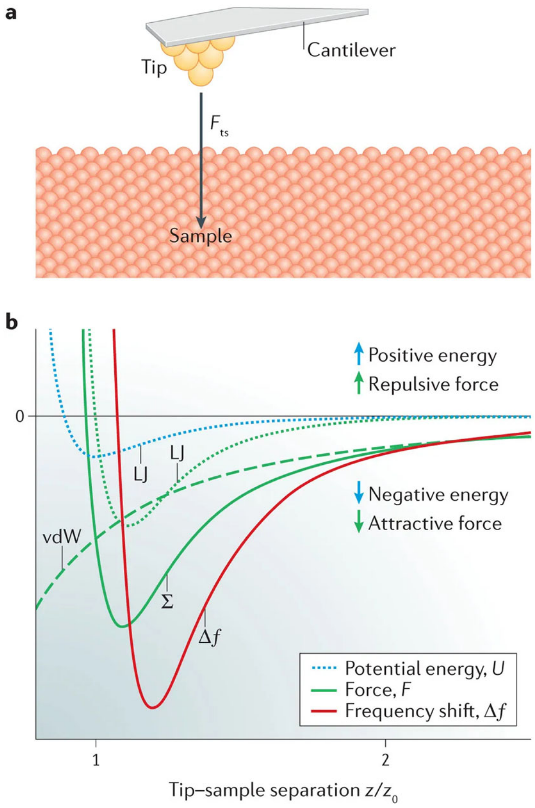
a
Cantilever
Tip
F_{ts}
Sample
b
Positive energy
Repulsive force
0
LJ
LJ
Negative energy
Attractive force
vdW
Σ
Δf
Potential energy, U
Force, F
Frequency shift, Δf
1
2
Tip–sample separation z/z0

Figure 2.11 | Basics of non-contact Atomic Force Microscopy

a Schematic illustration of a nc-AFM tip mounted on a cantilever experiencing the force F_{ts} arising from its interaction with the sample. **b** The overall interaction force (green solid), consisting of the force arising from the Lenard-Jones potential (green/blue dotted) and the one from van der Waals interactions (green dashed). The frequency shift induced by the overall force is depicted as red solid line. The figure is depicted from Ref.[85]

Contrary to STM, which relies on the detection of a tunneling current, nc-AFM is sensitive to the local forces and therefore also applicable for the investigation of insulating samples. Achieving atomic resolution in nc-AFM is challenging as the signal is very sensitive on the tip shape because the force does not exponentially depend on the tip – sample distance.[78,84,86] This is one reason why intra-molecular features can usually not be resolved with a standard metallic tip (Figure 2.12a). Ultra high-resolution nc-AFM has been made possible by recent advances in tuning fork based nc-AFM[87,88] and CO tip functionalization.[86,89–91] Only upon functionalizing the tip with a single molecule - commonly with CO - the intramolecular structure can be visualized as illustrated in Figure 2.12.[86] Today, the structures of molecules adsorbed on different atomic substrates are frequently confirmed or even determined using nc-AFM with CO terminated tips,[36,40,86,89–94] which are oftentimes conductive to allow simultaneous STM operation.

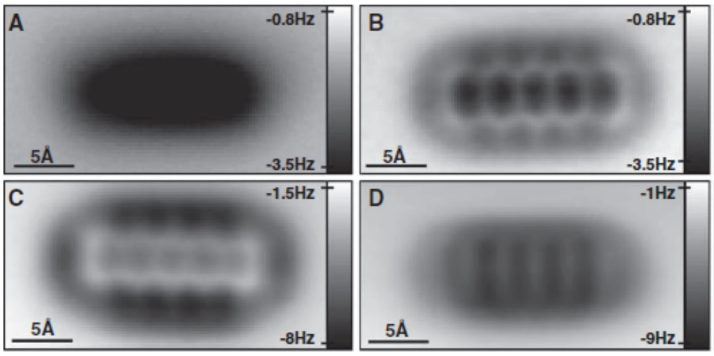
A
-0.8Hz
5Å
-3.5Hz
B
-0.8Hz
5Å
-3.5Hz
C
-1.5Hz
5Å
-8Hz
D
-1Hz
5Å
-9Hz

Figure 2.12 | nc-AFM images of pentacene on NaCl

Constant-height nc-AFM image of pentacene on NaCl(2ML)/Cu(111) acquired with **A** Ag, **B** CO, **C** Cl, and **D** pentacene terminated tip. (Figure adapted from Ref.[86])

2.5 Instrumentation

In the following, basic information of the three mentioned beamlines at which the (TP-)XPS and ARPES experiments have been performed are outlined. All three endstations are operated under ultra-high vacuum conditions with pressures in the low 10^{-10} mbar range and can be cooled to cryogenic temperatures of 10 K. Additionally, the equipment available in the nanotech@surfaces Laboratory at Empa is briefly reported.

The recorded data were mainly processed and analyzed with the Wavemetrics Igor Pro software. Specifically, the TP-XPS and ARPES data was mainly analyzed with Lab internal Wavemetrics Igor Pro based procedures, and the STM data with the matrixfilereader package from Thomas Braun (www.byte-physics.de).

2.5.1 PEARL at the Swiss Light Source

The PhotoEmission and Atomic Resolution Laboratory (PEARL) endstation is dedicated to the investigation of local atomic and electronic structures by combining global probing photoemission spectroscopy and diffraction techniques, such as XPS, ARPES, and XPD, with a locally probing low-temperature STM (LT-STM) from Omicron. The photoemission station is equipped with a 'Carving 2.0' six-axis manipulator and a Scienta EW4000 hemispherical electron analyzer. The endstation is operated in the energy range between 60 eV and 2000 eV with a resolving power of $E/\Delta E \geq 7'000$, where ΔE is the energy resolution. At this endstation the photon beam is focused to a spot size of 170 × 73 μm^2.[95]

2.5.2 ADRESS at the Swiss Light Source

The ADvanced RESonant Spectroscopy (ADRESS) hosts two endstations, one for ARPES and one for Resonant Inelastic X-ray Scattering. This high-performance soft-X-ray undulator beamline is operated in the energy range E from 300 eV to 1600 eV with circular and 0-180° linear polarized light. The ARPES endstation is equipped with a Carving manipulator and a PHOIBIOS 150 analyzer from specs. the photon beam is concentrated onto a spot of 10 × 74 µm2 on the sample with a resolving power of $E/\Delta E \geq 33'000$.[96]

2.5.3 I05 at the Diamond Light Source

The I05 consists of two ARPES endstations, the high-resolution branch and the nano-branch. All experiments within this work were performed at the high-resolution branch with an energy resolution of 5 to 10 meV in its core operating range of 18 to 80 eV photon energy. At this endstation, an R4000 analyzer from Scienta and the photon beam is focused to a spot size of 50 × 50 μm^2.[97]

2.5.4 Low temperature scanning probe microscopes at EMPA

The experimental equipment in the nanotech@surfaces Laboratory at Empa consists of one variable-temperature STM, one LT-STM, and one LT-STM with integrated nc-AFM capabilities (LT-STM/Qplus). The latter is furthermore connected to a second instrument which is devoted to PES-based techniques. Therefore, samples can be transferred in between these two systems without exposing them to air.

All experiments performed at Empa within this project have been executed either on the LT-STM or the LT-STM/Qplus, both of which are normally operated at liquid helium temperatures (4 K).

3. **PdGa – chiral topological material**

3.1 Symmetry protected fermionic excitations in condensed-matter systems

In the past decade, the field of topological electronic materials has considerably matured, where several classes of topological materials evolved from being exotic to well-studied. Topological materials are characterized by unique electronic properties arising from symmetry-protected surface or interface states.[98] For instance, in the case of topological insulators, the crystal bulk behaves like an insulator, whereas the surface hosts time-reversal symmetry protected conducting states.[99–101] These conducting states arise from the band inversion of the bulk, which is most commonly induced by large spin-orbit coupling (SOC). The class of topological materials has by now been expanded to materials that host fermionic quasiparticles that have been predicted in particle physics, such as Majorana, Dirac, and Wely fermions.[102–109] Contrary to particle physics, the fermionic quasiparticles in solid state systems are not restricted by Poincaré symmetry, but must only obey the respective crystal symmetry. Therefore, condensed-matter systems offer the potential for crystal symmetry-protected free fermionic excitations such as massless spin-1 and spin-3/2 fermions carrying non-trivial topological charges, without the requirement that their counterpart exist in the standard model of particles.[28–31]

All these fermionic excitation exhibit specific energy dispersions, which give rise to protected band-crossings at high-symmetry points of the Brillouin zone that can be obtained from the symmetry of the crystal's space groups (SG). Specifically, the family of SG 198 with significant SOC, to which intermetallic PdGa belongs to, is predicted to exhibit a six-fold band crossing at the R point of its Brioullin zone, which is realized from a doubling of spin-1 excitations with a topological charge, also denoted as Chern number C, of magnitude 4. Moreover, the same crystals are expected to have a four-fold band crossing, which represents a spin-3/2 Rarita-Schwinger-Weyl (RSW) chiral fermions with |C| = 4, at the center of their Brillouin zone.[29,30] Because the Chern number is, among others, proportional to the number of emerging surface Fermi-arcs at their {100} surfaces,[29,30,110] several of these transition metal silicides have been measured with angle-resolved photoemission spectroscopy ARPES (chapter 2.3.4). In particular, APRES experiments of CoSi and RhSi {100}-surfaces evidenced the existence of long, chiral surface Fermi-arcs (Figure 3.1a-e). However, they could only deduce a chiral topological charge, thus Chern number, of magnitude 2 as only two Fermi-arcs could have been resolved due to surface quality issues.[69,70]

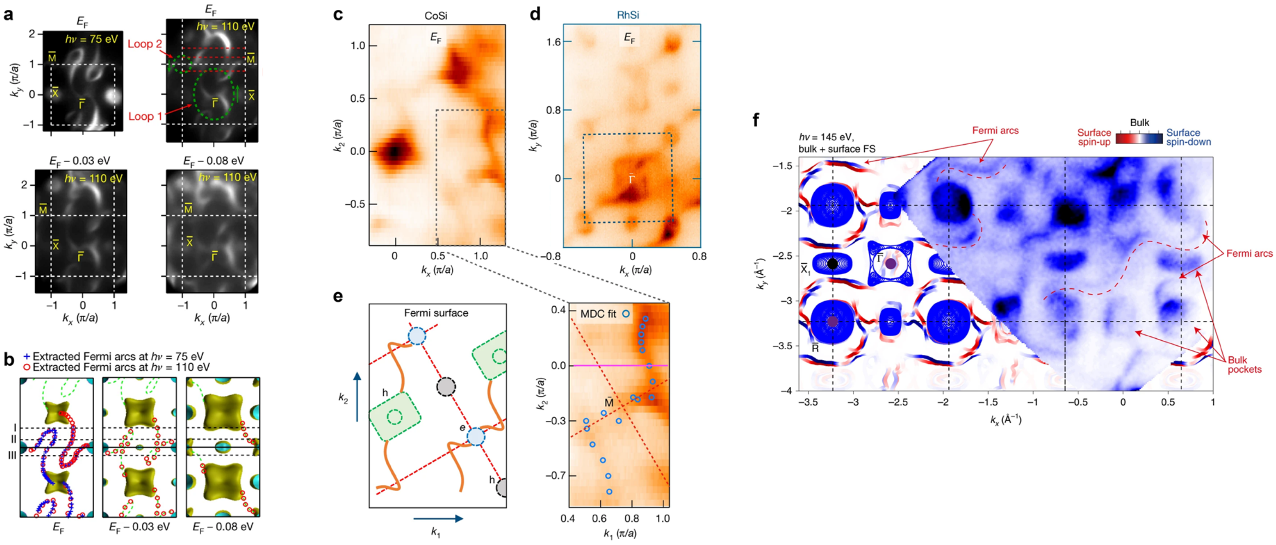

Figure 3.1 | Surface Fermi-arcs of CoSi, RhSi, and PtAl

a ARPES of CoSi recorded with a photon energy of 75 eV (top left) and 110 eV (top right) at Fermi energy E_F. Bottom: ARPES of CoSi recorded with photon energy of 110 eV at E_F-0.03 eV (left) and E_F-0.08 eV (right). **b** The experimental course of the surface Fermi-arcs overlaid with the simulated ones at E_F (left), E_F-0.03 eV (center), and E_F-0.08 eV (right). **c-d** ARPES of CoSi and RhSi at E_F recorded with a photon energy of 50 eV and 82 eV, respectively. **e** left: simulated surface Fermi-arcs for CoSi; right: course of the experimental surface Fermi-arcs. **F** ARPES of PtAl recorded with a photon energy of 145 eV overlaid with the trend and simulations of the surface Fermi-arcs. (Fig. **a-b** adapted from Ref.[70], **c-e** from Ref.[69], and **f** from Ref.[71])

Due to the facts that (i) experiments with crystals of the transition metal silicide family did not confirm the expected chiral topological charge $|C| = 4$, and (ii) the magnitude of this chiral topological charge is an intrinsic property of all crystals belonging to SG 198, the search for $|C| = 4$ materials has been extended to other candidates, such as PtAl. Although chiral surface Fermi-arcs could be detected also for PtAl (Figure 3.1f), but due to the inability to resolve their splitting, their predicted topological charge of magnitude 4 could not unambiguously be determined.[71]

Therefore, for all three investigated materials, Chern number of magnitude 4 could not be experimentally verified, because the spin splitting due to SOC of the surface Fermi-arcs could not be resolved, either owing to a small SOC or because of difficulties in preparing clean and atomically-flat bulk-truncated surfaces. PdGa presents and ideal candidate to confirm the Chern number of magnitude 4 as it is the only member of space group 198 for which a sputter-annealing process has been established to achieve the required high surface quality.

3.2 Publication (accepted in *Science*): "Observation and manipulation of maximal Chern numbers in the chiral topological semimetal PdGa"

Preprint version of article; also available on https://arxiv.org/abs/1907.08723

My contribution to this publication consisted of performing all ARPES and LEED measurements in collaboration with Niels B. Schröter, assisting in the analysis of the experimental data, and contributing to the writing of the manuscript.

Observation and manipulation of maximal Chern numbers in a chiral topological semimetal

Niels B.M. Schröter[1]*, Samuel Stolz[2,3], Kaustuv Manna[4], Fernando de Juan[5,6] , Maia G. Vergniory[5,6], Jonas A. Krieger[1,7,8], Ding Pei[9], Thorsten Schmitt[1], Pavel Dudin[10] , Timur K. Kim[10], Cephise Cacho[10], Barry Bradlyn[11], Horst Borrmann[4], Marcus Schmidt[4] , Roland Widmer[2], Vladimir N. Strocov[1], and Claudia Felser[4]* .

[1]*Swiss Light Source, Paul Scherrer Institute, CH-5232 Villigen PSI, Switzerland*

[2]*EMPA, Swiss Federal Laboratories for Materials Science and Technology, 8600 Dübendorf, Switzerland*

[3]*Institute of Condensed Matter Physics, Station 3, EPFL, 1015 Lausanne, Switzerland*

[4]*Max Planck Institute for Chemical Physics of Solids, Dresden, D-01187, Germany*

[5]*Donostia International Physics Center, 20018 Donostia-San Sebastian, Spain*

[6]*IKERBASQUE, Basque Foundation for Science, Maria Diaz de Haro 3, 48013 Bilbao, Spain*

[7]*Laboratory for Muon Spin Spectroscopy, Paul Scherrer Institute, CH-5232 Villigen PSI, Switzerland*

[8]*Laboratorium für Festkörperphysik, ETH Zurich, CH-8093 Zurich, Switzerland*

[9]*Clarendon Laboratory, Department of Physics, University of Oxford, Oxford OX1 3PU, United Kingdom*

[10]*Diamond Light Source, Didcot, OX110DE, United Kingdom*

[11]*Department of Physics and Institute for Condensed Matter Theory, University of Illinois at Urbana-Champaign, Urbana, IL, 61801-3080, USA*

*niels.schroeter@psi.ch

*Claudia.Felser@cpfs.mpg.de

Topological semimetals feature protected nodal band degeneracies characterized by a topological invariant known as the Chern number. While formally the Chern number C can take any integer value, nodal band crossings with linear dispersion are expected to have at most $|C|=4$, which sets an upper limit to the magnitude of many topological phenomena in these materials. However, such large Chern numbers have never been observed or manipulated experimentally. Here we show that the chiral crystal PdGa displays multifold band crossings, which are connected by exactly four surface Fermi-arcs, thus proving that they carry the maximal Chern number magnitude of 4. Furthermore, by comparing two enantiomers (crystals with mirrored structure that do not coincide), we observe a reversal of their Fermi-arc velocities, which demonstrates that the handedness of chiral crystals can be used as a tuning parameter to manipulate the sign of their Chern numbers. Our findings establish structural chirality as an important control parameter for topological phenomena in chiral crystals.

Topological invariants are mathematical objects that can be used to classify Hamiltonians, which have found widespread applications in physics, chemistry, and materials science. One of the most celebrated topological invariants in condensed matter physics is the Chern number, which in band theory language is the flux of Berry curvature through a closed two-dimensional surface. If this surface is taken to be the whole Brillouin zone, the Chern number classifies insulators in two dimensions, as first used in the context of the quantum Hall effect by Thouless and co-workers[111,112] in the 1980. More recently, Chern numbers have also been used to classify topological nodal semimetals,[110] where point-like energy degeneracies in their bulk electronic structure act as sources and sinks of quantized Berry flux through any local isoenergy surface enclosing the node. For the simplest case of a linear touching of two bands, which can occur in any non-centrosymmetric or magnetic material and is called a Weyl point, the magnitude of the Chern number C is limited to |C|=1. However, there is no reason preventing mor complicated nodal crossings from having larger Chern numbers, which has important consequences for many of the exotic phenomena predicted for topological semimetals, which are often directly proportional to their Chern number, such as the number of their topological Fermi-arc surface states,[110,113] the number of chiral Landau levels influencing magnetotransport phenomena related to the chiral anomaly,[114,115] the magnitude of the quantized rate of photocurrents in the quantized circular photogalvanic effect,[116–118] and many more.[119–121]

It has recently been predicted that in chiral crystals, which possess neither mirror nor inversion symmetries, more complex band crossings can be pinned at high symmetry lines and points that feature larger Chern numbers than Weyl semimetals. For example, twofold crossings with quadratic or cubic dispersion are predicted to host |C|=2 or |C|=3.[122,123] In materials with negligible spin-orbit coupling (SOC), three-fold and fourfold crossings can be found with |C|=2 per spin, while the combination of non-symmorphic symmetries and significan spin-orbit coupling gives rise to protected fourfold and sixfold degeneracies with Chern numbers up to magnitude 4. The symmetry classification is exhaustive for linear crossings[28–31,117,124] and predicts that |C|=4 only occurs due to SOC and is the highest possible Chern number achievable for a multifold node in chiral topological semimetals.

The family of chiral semimetals in space group 198, including RhSi, CoSi, AlPt, and PdBiSb, is expected to display these type of maximal |C|=4 crossings, realized as a fourfold spin S=3/2 crossing at the Γ point and a sixfold crossing the the R point of the Brillouin zone. Despite several recent angle-resolved photoelectron spectroscopy (ARPES) experiments on all these candidates,[69–71,125,126] the absolutemagnitude of the Chern number, measured by counting the number of Fermi-arcs, has not yet been observed due to two main roadblocks. The first is that SOC in some of these materials is low and spin-split Fermi arcs cannot be resolved, effectively leading to only two observable arcs. Most photoemission studies to date[69,70,125] in fact classify these nodes as having |C|=2, whilst recent all-optical measurements[127] find a Chern number close to 4. The second is the preparation of clean and flat surfaces by cleaving or sputtering and annealing, which has resulted in rough or nonstoichiometric surfaces for all previously examined candidates, causing band broadening that can wash out signatures of spin-split bands due to SOC. In this work, we overcome both obstacles by investigating a new chiral topological semimetal candidate PdGa from space group 198, which has substantial SOC and can be prepared with flat, clean, and well-ordered surfaces by polishing and subsequent sputtering and annealing in ultrahigh vacuum.[26,48,54] Employing ARPES and ab-initio calculations, we can clearly resolve the presence of multifold crossings in the bulk electronic structure of PdGa, as well as four topological Fermi-arcs on its surface, thus observing for the first time an experimental realization of the maximal Chern number |C|=4. Interestingly, PdGa is known as an important catalyst, for instance for the semi-hydrogenation of acetylene,[21] and shows potential for enantioselective catalytic reactions of chiral molecules,[27] which could be enhanced due to the large surface electronic density of states of the Fermi-arcs discovered in this work.

Besides the first observation of the largest possible Chern number in topological semimetals, we also describe here how to manipulate its sign by changing the handedness of their crystal structure. This has striking consequences for their physical properties, since in these materials, the directions of their chiral Fermi-arcs, chiral Landau levels, and quantized photocurrents are tied directly to the sing of the Chern number associated with the multifold nodes at the Fermi level. By measuring Fermi-surface maps for two enantiopure samples of PdGa with opposite handedness, we can detect the reversal of the Fermi velocity of their topological edge states when the sign of the Chern number is flipped. Manipulation of the Chern number sign by engineering of the crystal structure will become an important control parameter in future experiments that probe the topological properties of chiral crystals.

The PdGa samples used in this study crystallize in the cubic space group 198 with a lattice constant of a=4.896 Å. The chiral motif in their structure is the helical arrangement of Pd and Ga atoms along the (111) direction, which is displayed in Figure 3.2A. Upon a mirror operation, these helices reverse their handedness, which can be used to distinguish the two enantiomers of PdGa. We grew two enantiopure specimen of PdGa with opposite chirality via a self-flux method with a chiral seed crystal (see methods and supplementary for further details). The chirality of the crystal structure can also be observed from the intensity distribution of low energy electron diffraction (LEED) patterns of the (100) surface[26] at an electron energy of E_{kin}=95 eV, which we show in Figure 3.2B. As can be expected, the S-shaped intensity distribution is mirrored when comparing the two enantiomers. The crystals used for the LEED study were prepared by the same sputter-annealing recipe as for the subsequent ARPES experiments, which is well knwon to produce clean and stoichiometric surfaces of PdGa.[54] In Figure 3.2C, we display the results of an ab-initio bulk band structure calculation, which shows fourfold and sixfold band crossings at the Γ and R points, respectively. Such band crossings in space group 198 were predicted to carry a Chern number of magnitude 4, with opposite sings at the Γ and R points.[28–31] Since the Berry curvature is a pseudovector, a mirror operation will reverse the sign of the Chern number associated with the nodes at the high symmetry points. Such a mirror operations also leads to a reversal of the propagation direction of the Fermi-arcs, as is illustrated in Figure 3.2D. Any gapped 2D slice in the 3D Brillouin zone between the Γ and R points can be understood as a quantum Hall subsystem due to the Chern number of magnitude 2 that is associated with it. The two edge states of this quantum Hall state reverse their direction when the flux of Berry curvature is flipped, which also leads to a reversal of the velocity of the Fermi-arcs that are formed by the ensemble of all 2D slices in the 3D Brillouin zone.

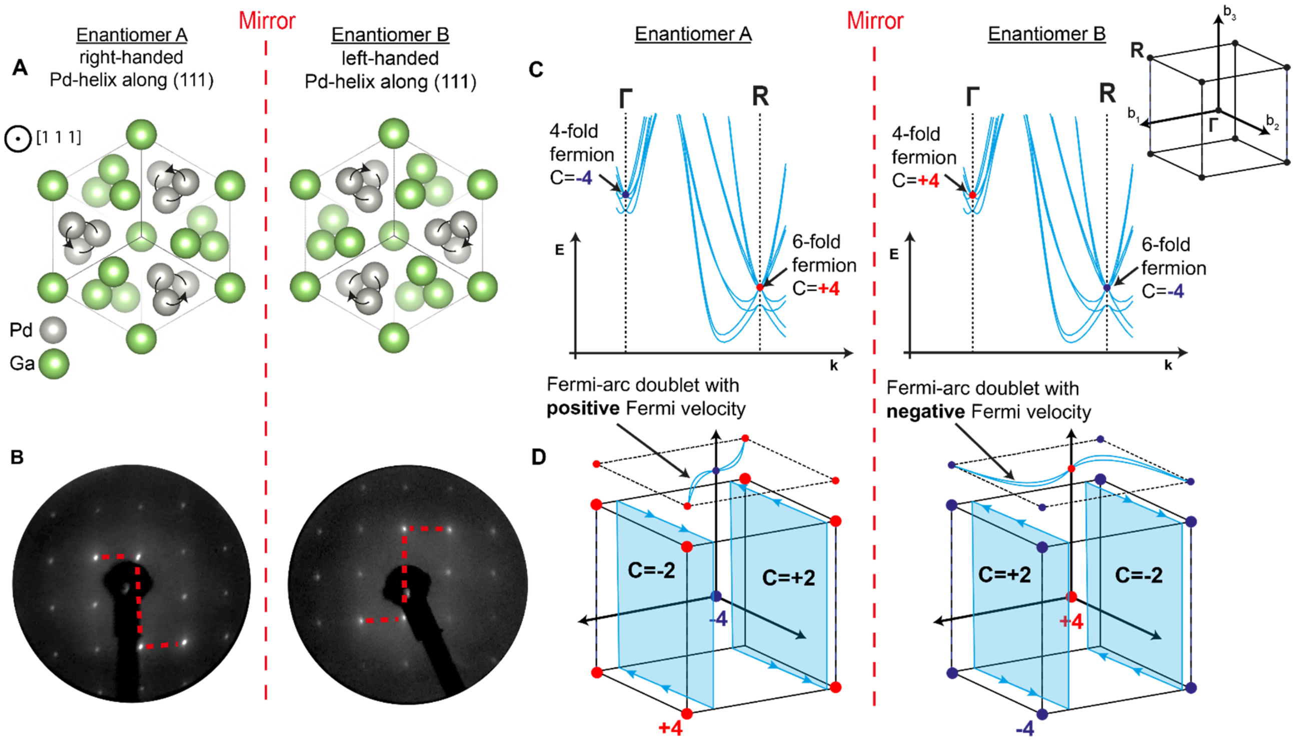
A
Enantiomer A
right-handed
Pd-helix along (111)
Mirror
Enantiomer B
left-handed
Pd-helix along (111)
[1 1 1]
Pd
Ga
B
C
Enantiomer A
Mirror
Enantiomer B
Γ
R
4-fold
fermion
C=-4
6-fold
fermion
C=+4
E
k
Γ
R
4-fold
fermion
C=+4
6-fold
fermion
C=-4
E
k
R
Γ
b3
b1
b2
Fermi-arc doublet with
positive Fermi velocity
Fermi-arc doublet with
negative Fermi velocity
D
C=-2
C=+2
-4
+4
C=+2
C=-2
+4
-4

Figure 3.2 | Structural and electronic chirality in the two enantiomers of PdGa

(A) Illustration of the crystal structure of two enantiomers of PdGa with opposite handedness.

(B) Low energy electron diffraction patterns for two samples with opposite chirality, measured with an electron energy of E_{kin}=95 eV. The S-shaped intensity distribution of the diffraction spots (highlighted by red dashed lines as guide for the eye) reflects the handedness of the crystal structure.

(C) Ab-initio calculations of the band structure in PdGa, showing fourfold and sixfold band crossings at the Γ and R points. The Chern numbers associated with the crossings are of magnitude 4 and flip their sign upon a mirror operation. This reverses the direction of Berry flux that is flowing from the crossing with positive Chern number towards the crossing with negative Chern number. Inset shows the cubic Brillouin zone with high symmetry point Γ at the zone center and R at the zone corner.

(D) Illustration of the position of sources and sinks of Berry curvature in the Brillouin zone. Blue shaded squares indicate 2D quantum Hall subsystems that are associated with a Chern number of magnitude 2. The signs of these Chern numbers depend on the direction of the Berry flux, which is reversed between the two enantiomers.

We performed bulk sensitive soft X-ray ARPES measurements on the (100) surface of our PdGa samples to investigate their bulk electronic structure, the results of which are displayed in Figure 3.3. We find that multifold crossings predicted at the R- and Γ-points are indeed present (see Figure 3.3A-C), and that our ab-initio calculations are in good agreement with the observed band dispersions. This agreement can also be observed from the Fermi surfaces for different high-symmetry planes displayed in Figure 3.3D-E.

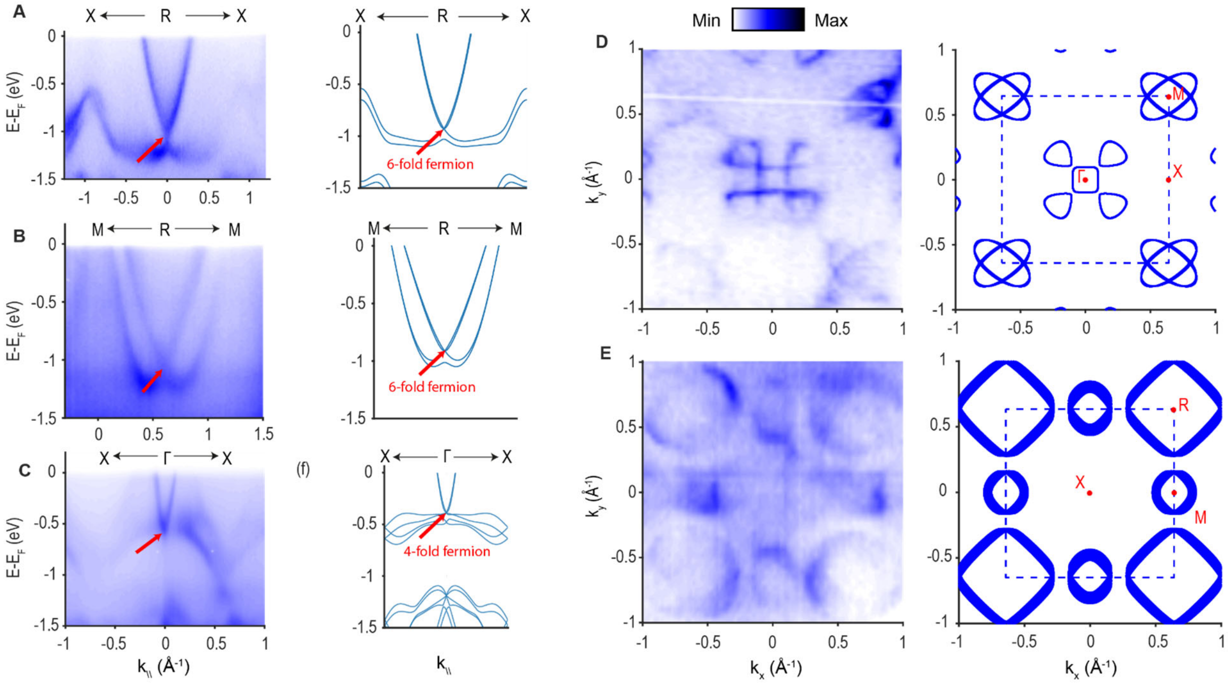

Figure 3.3 | Electronic characterization of the bulk electronic structure of PdGa measured on the (100) surface of enantiomer A

(A-C) Comparison between ARPES spectra (lef) and ab-initio calculations (right) along high symmetry lines that pass through the Γ and R points. Multifold fermions are indicated by red arrows. Spectra were measured at hv=550 eV, 552 eV, and 620 eV, respectively, all with linear-vertical (LV) polarization.

(D-E) Comparison between experimental Fermi surface (left) and ab-initio calculations (right). (D) shows the Fermi surface in the high symmetry plane containing the Γ point (measured with hv=620 eV, LV polarization), whilst (E) contains the plane including the R point (measured with hv=540 eV, LV polarization). The blue dashed lines indicate the boundary of the bulk Brillouin zone. Ab-initio calculations include k_z broadening of 0.1 Å^{-1}.

After establishing the existence of multifold band crossings in PdGa, we will now investigate the topological character of these crossings via surface sensitive ARPES of the (100) surface of enantiomer A at low photon energies (hv<150 eV), as well as ab-initio slab calculations. By comparing the calculated and experimental Fermi surfaces in Figure 3.4A-B, we can identify the existence of Fermi arc surface states (indicated by red arrows) that thread through the projected bulk band gap (white areas between projected bulk pockets that are represented by blue lines in Figure 3.4A), thereby connecting the pockets at $\bar{\Gamma}$ and $\bar{R}$, respectively. By performing photon energy dependent ARPES along the $\bar{R} - \bar{\Gamma} - \bar{R}$ direction, we confirm experimentall that these Fermi-arcs are indeed surface states without noticeable dispersion along the k_z direction (perpendicular to the sample surface), as can be seen from Figure 3.4C. Interestingly, we also find additional surface states that overlap with the projected bulk pocket at $\bar{\Gamma}$ (indicated by purple arrows). Due to the sizable SOC in PdGa and high quality of our ARPES data, we are furthermore able to resolve a spin-splitting in the surface Fermi-arcs (see Figure 3.4D-F, and the calculation in Figure 3.4A for comparison), which is the first experimental confirmation of the maximum Chern number magnitude 4 for multifold crossings in a topological semimetal due to four Fermi-arcs connecting $\bar{\Gamma}$ and $\bar{R}$ points. We find that the SOC splitting of the Fermi-arcs close to the Fermi level is ~0.015 Å^{-1} and ~60 meV. Since these multifold crossings are a generic feature of many chiral topological semimetals, we expect that our finding will also hold for other compounds from the same material family.

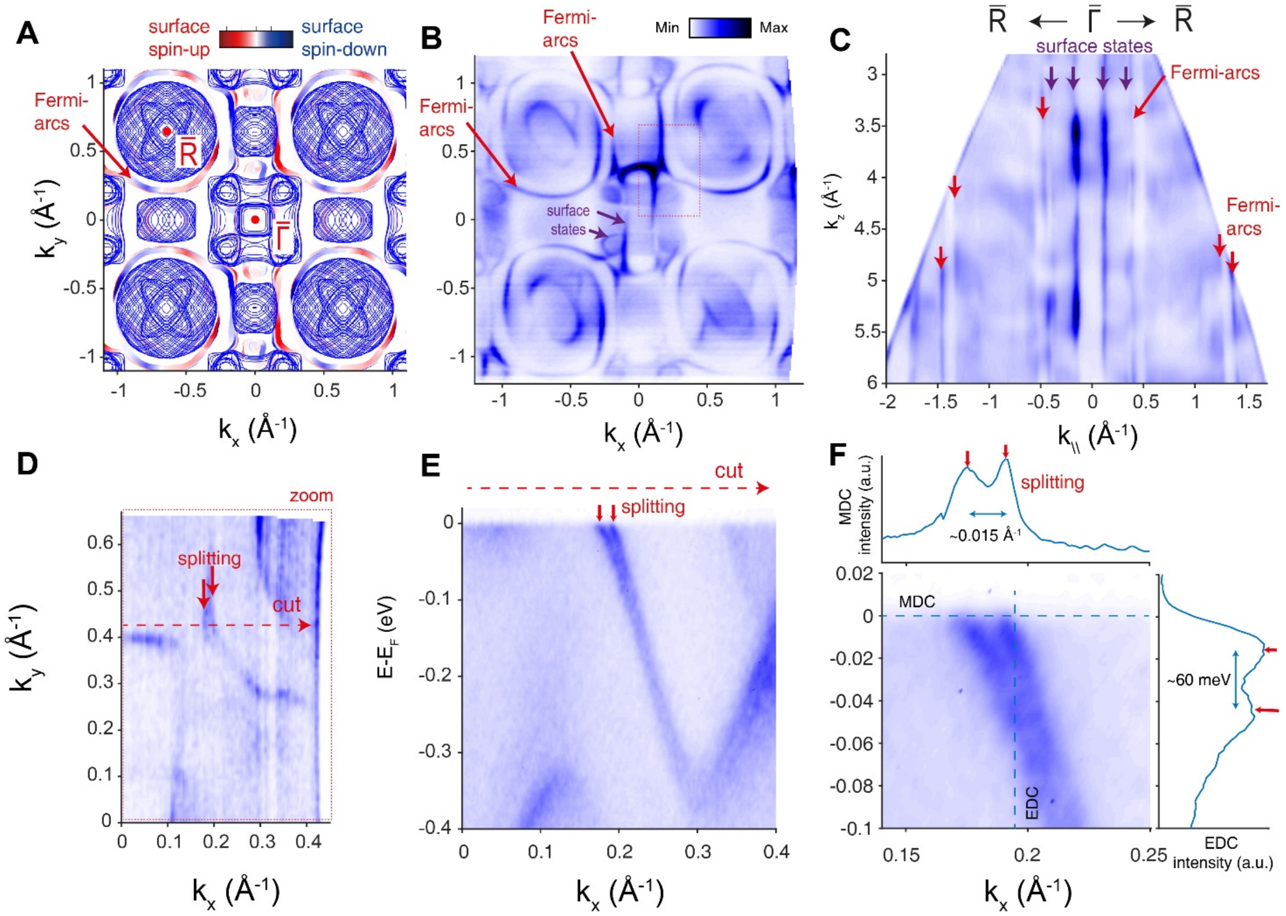

Figure 3.4 | Surface electronic structure of the (100) surface of enantiomer A

(A) Ab-initio slab calculations of the Fermi surface in the (100) plane (*i.e.*, k_x vs k_y plane) showing surface Fermi-arcs (indicated by a red arrow), superimposed by projected bulk band structure calculations (solid blue lines).

(B) Experimental Fermi surface measured with hv=60 eV and linear-horizontal (LH) polarization. Red arrows indicate Fermi-arcs, whilst purple arrows indicate additional surface states that overlap with the projected bulk states at $\bar{\Gamma}$.

(C) Experimental Fermi surface perpendicular to the sample surface (*i.e.*, k_y vs k_z plane), showing that the Fermi-arcs and surface states (indicated by red and purple arrows, respectively) show negligible dispersion along the k_z direction. Conversion from photon energy was performed within free-electron final state approximation with inner potential of V_0=12 eV.

(D) Magnified Fermi surface measured in the region of the red dotted rectangle shown in (B) with hv=30 eV and LH polarization. Red arrows indicate spin-splitting of Fermi-arcs.

(E) Band dispersion measured along the path in momentum space indicated by the dashed red arrow shown in (D) that is crossing the Fermi-arcs. Red arrows indicate their spin-splitting.

(F) Magnified version of (E), insets are momentum distribution curve (MDC) and energy distribution curve (EDC) along the dashed blue lines.

Next we investigate how the maximal Chern number in PdGa can be manipulated by tuning the handedness of its crystal structure. When comparing the Fermi-surfaces for enantiomers A and B as shown in Figure 3.5A, we see that the Fermi arcs wind around the bulk pocket at $\bar{R}$ in opposite directions. Due to the very high momentum resolution of the Fermi surface maps shown in Figure 3.5B we can cut an arbitrary path through the Brillouin zone that passes through the projected bulk band gap indicated by the red dashed line. By comparing the band dispersion of the Fermi-arcs between the two enantiomers along this path (as displayed in Figure 3.5C), we can see that the Fermi velocity of the edge states is indeed reversed, which implies that the Chern number signs are reversed between the two enantiomers. This observation constitutes the first experimental proof that the sign of the Chern numbers in topological semimetals can be manipulated by controlling the handedness of their crystal structure. We expect that this finding will serve as a control parameter in future experiments that investigate the response of topological semimetals to external perturbations, such as all-optical measurement of the quantized circular photogalvanic effect.[127] Here, a comparison of the nonlinear response between two enantiomers should give the same magnitude of the mesa-like plateau region in the photocurrent spectrum, albeit with a reversed sign. Similar arguments can also be applied to other experiments that attempt to probe topological properties proportional to the Chern number, which shows that our results establish a procedure to distinguis responses of topological origin from trivial ones.

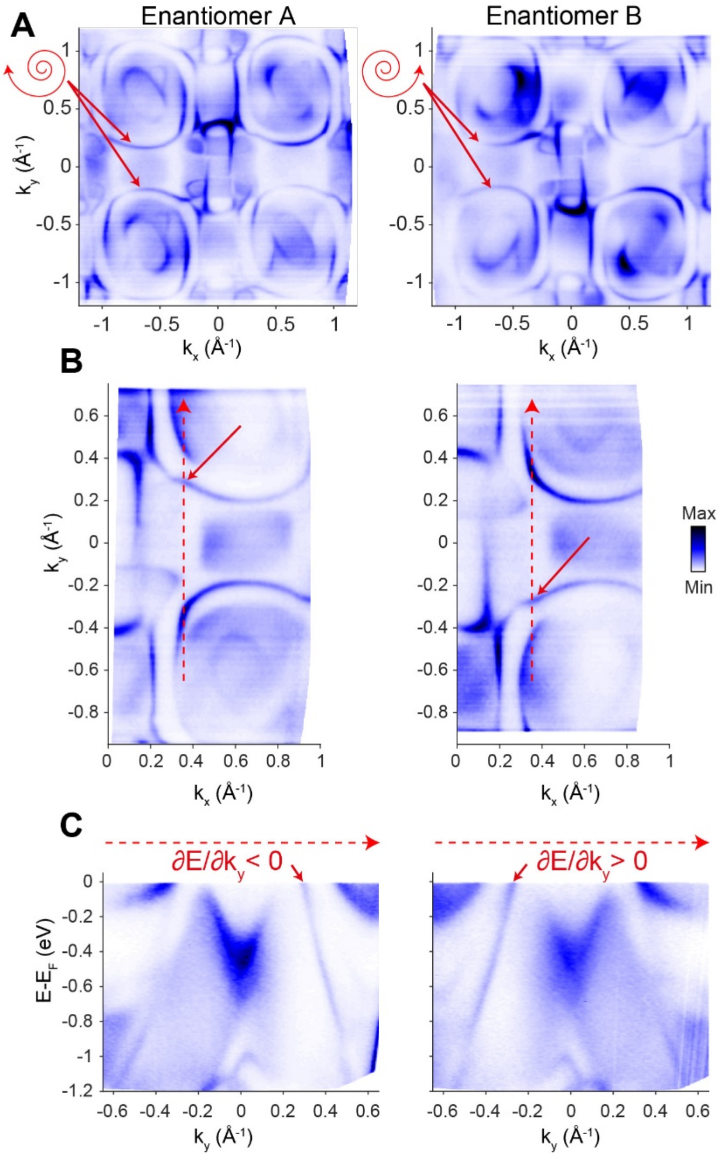

Figure 3.5 | Comparison of the surface electronic structure of the (100) surface of enantiomer A (left) and enantiomer B (right)

(A) Comparison of the Fermi surfaces for two enantiomers, measured with photon energy hv=60 eV and LH polarization. Red arrows indicate Fermi-arcs that reverse the direction along which they disperse around the $\bar{R}$ pocket under a mirror operation.

(B) Comparison of magnified Fermi surfaces measured with photon energy hv=30 eV and LH polarization. Red dashed line indicates momentum path shown in (C). Red solid arrows indicate Fermi-arcs that are crossing the projected bulk band gap that separates the projected bulk pockets at $\bar{\Gamma}$ and $\bar{R}$.

(C) Band dispersion along the path indicated by the red dashed line in (B). Red arrows indicate the Fermi-arcs that are crossing the projected bulk band gap. One can see that the components of the Fermi velocity along the k_y direction switches sign between the two enantiomers.

3.2.1 Supporting Information for the publication "Observation and manipulation of maximal Chern numbers in the chiral topological semimetal PdGa"

3.2.1.1 PdGa Crystal Growth and Structure Refinement

PdGa single crystals were grown from its melt using the self-flux technique. First, a polycrystalline ingot was prepared using arc melt technique with the stoichiometric mixture of high purity Pd and Ga metals. Then the crushed powder was filled in a bottom-cone shaped alumina crucible and finally sealed in a quartz tube. In order to control the structural chirality of the grown PdGa single crystals, we prepared the seeds of $Fe_{1-x}Co_xSi$ with Co doping $x = 0.08$ and $x = 0.25$.[128] Single crystals of $Fe_{1-x}Co_xSi$ [$x = 0.08$ and 0.25] were grown using the self-flux technique with melting the respective stoichiometric polycrystalline material at 1500 °C and followed by a slow cooling to 1200 °C with a rate of 5 °C/h. Then, in order to verify whether it is possible to transfer the details of structural chirality from the seed to another system, we cut small portion of the grown $Fe_{1-x}Co_xSi$ single crystals and used as a seed at the bottom of the alumina crucible. For both batches of PdGa single crystals, first the entire quartz ampoule was heated to 1100 °C, halted there for 12 h and then slowly cooled to 900 °C with a rate of 1.5 °C/h. Finally, the sample was cooled to 800 °C with a rate of 50 °C/h, annealed for 120 h and then cooled to 500 °C with a rate of 5 °C/h. For the growth of “form A” defined in Refs.[129,130] single crystal of $Fe_{1-x}Co_xSi$ with $x = 0.08$; and for the “form B”, $x = 0.25$ single crystals were used as a seed. High quality PdGa single crystals with average dimension of about 18 mm length and 6 mm diameter was obtained.

3.2.1.2 ARPES

Soft X-ray ARPES (SX-ARPES) measurements were performed at the SX-ARPES endstation[131] of the ADRESS beamline[96] at the Swiss Light Source, Switzerland, with a SPECS analyzer with an angular resolution of 0.07°. The photon energy varied from 350-1000 eV and the combined energy resolution was ranging between 50 meV to 150 meV. The temperature during sample cleaving and measurements was about 20 K and the pressure better than $1x10^{-10}$ mbars. The increase of the photoelectron mean free path in the soft-X-ray energy range results, by the Heisenberg uncertainty principle, in a higher k_z resolution of the ARPES experiment compared to measurements at lower photon energies,[132] which was critical to measure the new Fermions in the bulk band structure of PdGa.

VUV-ARPES measurements were performed at the high-resolution ARPES branch line of the beamline I05 at the Diamond Light Source, UK.[97] Measurements at the high-resolution branch were performed with a Scienta R4000 analyzer, and a photon energy range between 20 eV and 200 eV, at a temperature below 20 K. Measurements in the VUV-ARPES regime are more surface sensitive than SX-ARPES and therefore most suitable to image the Fermi-arcs in PdGa.

At both ARPES beamlines, the polished PdGa were sputtered with Ar-ions and annealed at T=870 K in UHV for multiple cycles, until clear LEED spots became visible.

3.2.1.3 Ab-initio calculations

We employed density functional theory (DFT) as implemented in the Vienna Ab Initio Simulation Package (VASP),[133,134] as well as Wien2k[135] (the latter only for Figure 3.3D-E).

For the VASP calculations, the exchange correlation term is described according to the Perdew-Burke-Ernzerhof (PBE) prescription together with projected augmented-wave pseudopotentials.[136] For the autoconsistent calculations, we used a 6x6x6 k-points mesh for the bulk and 6x6x1 for the slab calculations. The kinetic energy cut off was set to 520 eV. We calculated the surface states by using a slab geometry along the (001) direction. In order to achieve a negligible interaction between the surface states from both sides of the slab and reduce the overlap between top and bottom surface states, we considered a slab of 10-unit cells and 1 nm vacuum thickness. For the energy cuts, we used a 100x100 grid of K points.

The Wien2k calculations employed a full-potential linearized augmented plane-wave and local orbitals basis, as well as the PBE prescription of the exchange correlation term. The plane-wave cutoff parameter RMTKMAX was set to 7 and the irreducible Brillouin zone was sampled by 97,336 k-points. Spin-orbit coupling was included via a second variational procedure.

The crystal structure plotted in Figure 3.2 were generated with VESTA.[137]

3.2.1.4 PdGa Crystal Growth and Structure Refinement

Single crystallinity was first checked with a white beam backscattering Laue X-ray setup at room temperature. Then we performed rigorous single crystal X-ray diffraction experiments to analyze the structural chirality of the grown two batches of PdGa single crystals. Small pieces picked from different parts of the grown crystals were considered to truly reflect the structural properties of the entire sample. The selected crystallites were mounted on Kapton loops with aid of a trace of Apiezon H grease and used in diffraction experiments on a Rigaku AFC7 four-circle diffractometer with a Saturn 724+ CCD-detector applying graphite-monochromatized Mo-

Kα radiation. A total of five crystals were fully characterized, complete crystallographic information and final results are compiled in standard cif format. In any case, the determination of the absolute structure via refinement of Flack's parameter confirmed single domain crystals without any significant contribution from twinning by inversion.[138] This fully confirms the proper assignment of hand as expected from crystal growth. Even more, one among three crystallites originating from the right handed crystal showed diffraction images of rather fair quality; however, absolute structure refinement gave excellent results, thus reflecting the robustness of the procedure.

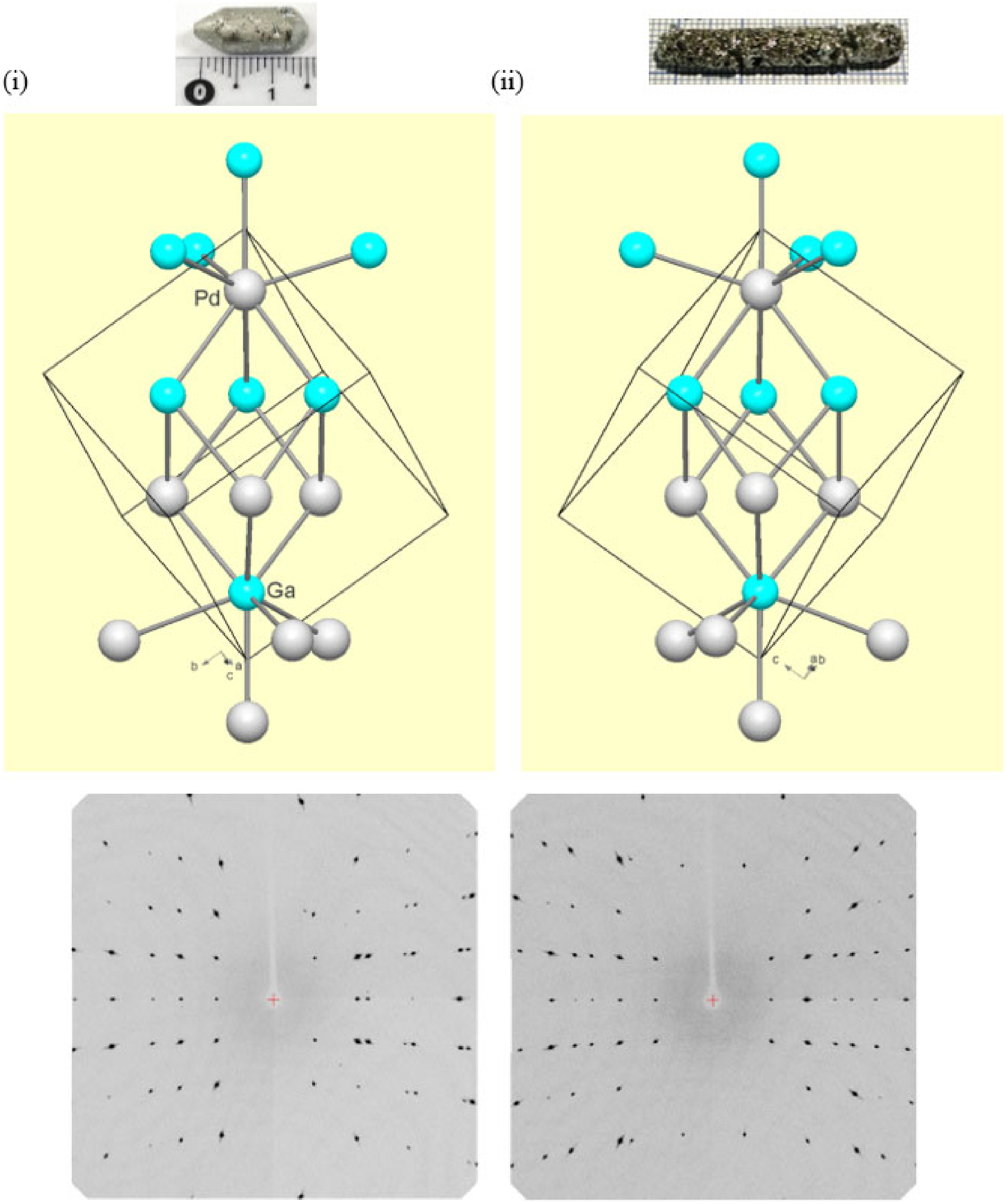

Figure 3.6 | PdGa enantiomorphs and x-ray diffraction

Basic structural unit for the PdGa crystals with the refined structural parameters. (i): right handed or A-form crystal in ref.[129] [Pd at x = 0.14246(4), Ga at x = 0.84301(6)] and (ii): left-handed or B-form crystal in ref.[129] [Pd at x = 0.85758(3), Ga at x = 0.15694(5)]. The corresponding top picture shows the grown PdGa single crystal. Below are the oscillation images about a main axis for both PdGa single crystals reflecting the excellent crystalline quality.

4. **PdGa – stator for molecular machines**

4.1 Molecular motors

Many processes of living organisms require directed motion and transport on the molecular level,[139–141] which is generally provided by highly specialized protein machines. In most cases, these protein machines like myosins, kinesins, or dynein convert the energy released by ATP hydrolysis into mechanical work like muscular contraction, ciliary beating, and organelle transport.[141–144] Owing to the wide range of fundamental tasks performed by these miniature machines, a lot of effort has been invested to understand the underlying physics and to devise artificial molecular machines.

Before reviewing the underlying physics and development of molecular motors in detail, the terminology of molecular machines, switches, and motors shall be clarified based on Refs.[145,146]. Specifically, in case of a 'molecular machine' a stimulus induced controlled motion of one molecular or submolecular unit with respect to another is accomplished. 'Molecular switches' are molecular machines that transits between two stable states, while in contrast a 'molecular motor' is a molecular machine that cycles unidirectionally through more than two stable states.

4.1.1 Physical background of molecular motors

In the following, we consider basic conditions under which directional molecular motion can arise from a non-directed, stochastic energy source. First and foremost, the motion will be defined by the energy potential $U(\vec{x})$ landscape of the molecule interacting with the surroundings; with $\vec{x}$ being an arbitrary configurational position in the energy potential. For the directional motion, expected from a molecular motor, additional restrictions on the energy potential landscape $U(\vec{x})$ are imposed, because the motion must be (i) repetitive and (ii) directed, but driven by stochastic processes. (i) implies $U(\vec{x})$ to be periodic in $\vec{x}$ with a periodicity $\Delta\vec{x}$, *i.e.*, $U(\vec{x}) = U(\vec{x} + \Delta\vec{x})$, and (ii) requires breaking the spatial reversal symmetry of $U(\vec{x})$, as is the case for the chiral, bunk-truncated surface of PdGa.

Biological molecular motors operate under comparably harsh conditions, appropriately described by the note of Astumian that saying molecular motors must "swim in molasses and walk in a hurricane".[147] Practically speaking, molecular motors function in an environment where viscous forces of the type $m\nu\frac{d\vec{x}}{dt}$ (where ν denotes the viscous dissipation coefficient) dominate inertia, and where thermal noise $\vec{f}(t)$ power exchange between the motor and environment exceeds the power provided by the fuel. Providing fuel, *i.e.*, free energy, to the system is crucial to achieve directed motion, as it can only operate out of thermal equilibrium. Thermodynamic out-of-equilibrium condition is a prerequisite for directed motion, as, according to the 2nd law of thermodynamics, entropy must be maximized at thermal equilibrium. Hence, the 2nd law of thermodynamics directly implies the forward motion and the backward motion to occur with the same likelihood under equilibrium conditions.

The artificial molecular motor, which will be presented in chapter 4.2 operates under ultra-high vacuum conditions and at low and stable temperatures. Therefore the thermal noise is assumed to be negligible, which in practice means, that the motion of our molecular motor can be mathematically described by the following Langevin equation[148,149]

$$m\frac{d^2\vec{x}}{dt^2} = -\nabla \mathrm{U}(\vec{x}) - m\nu\frac{d\vec{x}}{dt}$$

Equation 4.1 | Langevin equation

In the Langevin equation, energy dissipation is introduced as a velocity dependent force component and is a prerequisite to perform entropy decreasing directed motion. This Langevin equation will be applied in polar coordinates in chapter 4.2 to determine the viscous dissipation coefficient from the experiments on the electrically driven artificial motor represented by the rotation of acetylene on PdGa:A(-1-1-1)Pd_3 surfaces.

4.1.2 Artificial molecular motors

With the ever increasing insight into possible operation principles of molecular motors, more and more sophisticated artificial molecular machines were designed and experimentally realized and characterized. Additionally, also an increasing variety of energy sources to power such motors has been explored. In the following some of the most common processes to deliver the required energy input are outlined.

4.1.2.1 *Chemically-driven*

The first chemically-driven artificial molecular 'shuttles' were reported by Stoddart *et al.*[150] (Figure 4.1b) and can be classified as a rotaxane-based molecular switches (Figure 4.1a) whose states are controlled via changes in proton concentrations or electrical potentials. Following this seminal work, numerous such rotaxane-based molecular switches were reported, powered by a large variety of external chemical stimuli like redox processes, pH variations, or alternating solvent environments[145] Due to their molecular architecture, rotaxane molecules cannot be used to exhibit cyclic motions. Nevertheless, they have been employed to design artificial molecular pumps, thus transporting a molecular species against a concentration gradient until reaching an equilibrium state.[151]

In contrast to rotaxane-based molecular machines, catenane-based ones are designed to perform cyclic motions. They consist of at least one smaller ring-like molecule interlocked with and moving in discrete steps around a larger one (Figure 4.1a,c). This concept has first been exploited by Sauvage *et al.* for several systems, yet without accomplishing directed motion.[152] In 2003, Leigh and coworkers designed the first catenane-based molecular motor driven by light.[153] Such catenane-based molecular motors have then been continuously optimized over the years: First by achieving selective rotation in either direction via a sequence of chemical transformation,[154] then by developing a chemically-driven molecular motor that operates autonomously, *i.e.*, that executes directed rotation as long as unreacted fuel remains available.[155]

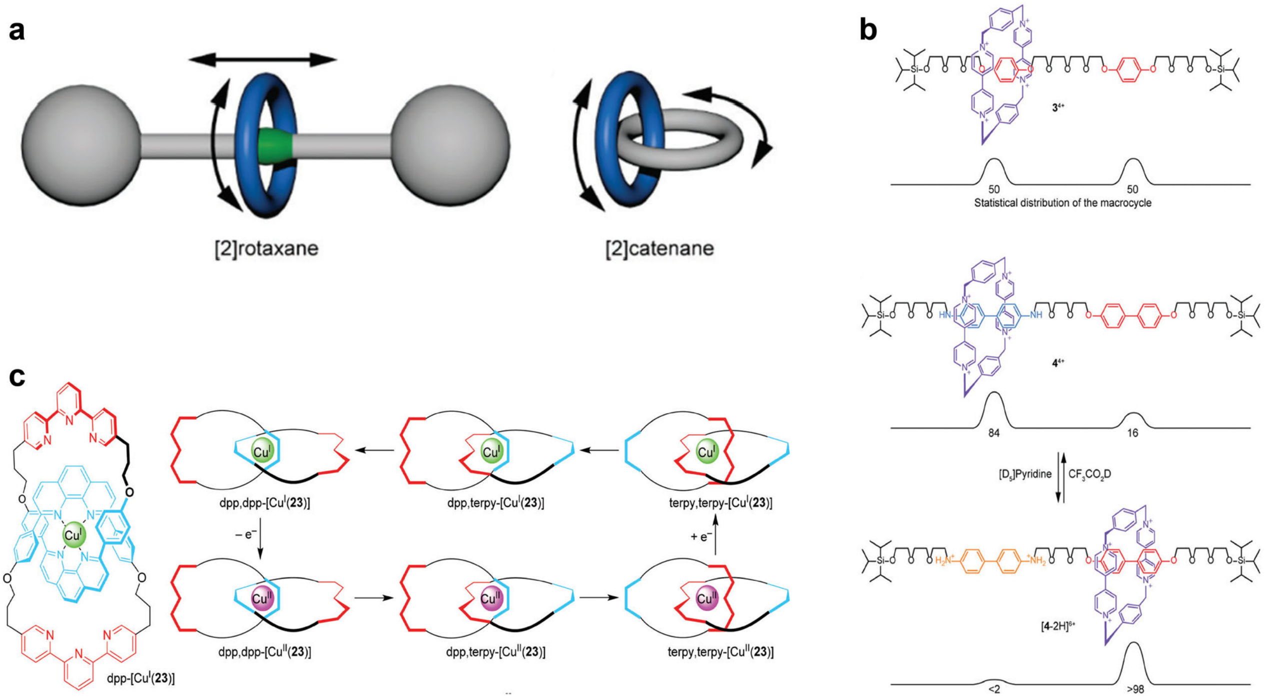

Figure 4.1 | Chemically-driven molecular motors

a Sketch of rotaxane- and catenane-based molecular machines. **b** the first stimuli-responsive rotaxane-based molecular shuttle, which switches between its two states in dependence of the pH-value. **c** Catenane-based molecular machine, which switches between three distinct conformations in dependence of the oxidation state. All Figures are adopted from Ref.[146]

4.1.2.2 *Light-driven*

The first ever reported light-driven artificial molecular motor by Feringa *et al.* completed repeated 360° rotations by cycling, alternating light and thermal activation, whereby the temperature required for the thermal activation had to be varied in dependence of the conformational changes (Figure 4.2a).[156] The obstacle of cycling different temperatures to achieve conformational changes was soon mastered by choosing a different stator molecular unit (Figure 4.2b) that continuously runs with light of the appropriate wavelength.[157] In the following years, light-driven molecular motors were further optimized regarding several aspects, namely: (i) control over rotation frequency by adapting the molecular rotor and stator,[158–160] (ii) change the sense of the motor's rotation via epimerization,[161] (iii) power molecular motor with visible light,[162,163] and (iv) reversible locking / unlocking of the motor.[164] Owing to all these advances, directed transport on the microscopic and even macroscopic scale was accomplished with light-driven molecular motors as illustrated in Figure 4.2c.[165–167] Further directions of optimizations are tackled by establishing well-defined arrangements to achieve controlled concerted motions.[168]

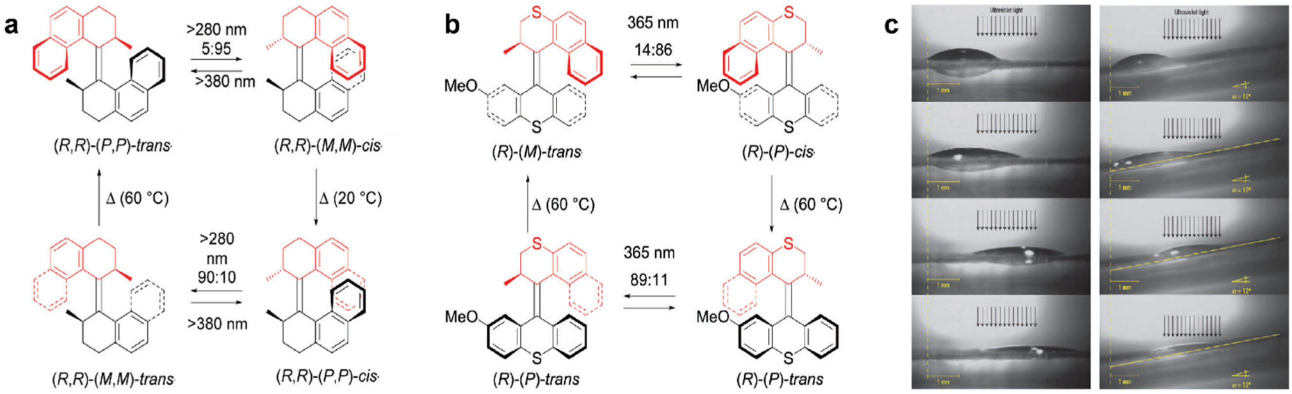

Figure 4.2 | Light-driven molecular motors

a-b light-driven molecular motors. The rotors are depicted in red, the stators in black. The conditions for each transformation are depicted in the respective figures. **c** Light induced lateral motion of a diiodomethane droplet with the arrows indicating the irradiated area. The left movie strip shows the droplet moving on a horizontal surface, the one on the right on a surface with 12° incline. The photographs were taken before irradiation, after 215 s, 370 s, and 580 s (from top to bottom). All Figures are adapted from Ref.[146]

4.1.2.3 Electrically-driven

Although there are numerous reports of electrically induced molecular motions,[169–186] the majority of them have been investigated and powered by the local electric field and electrical current present between the tip of a scanning tunneling microscope (STM) and the sample, only a few of these succeeded in directed motion.[169–173] Various concepts in directed, electrically powered lateral molecular motion were presented and competed against one another at the so-called nano-car race organized in 2017.[187]

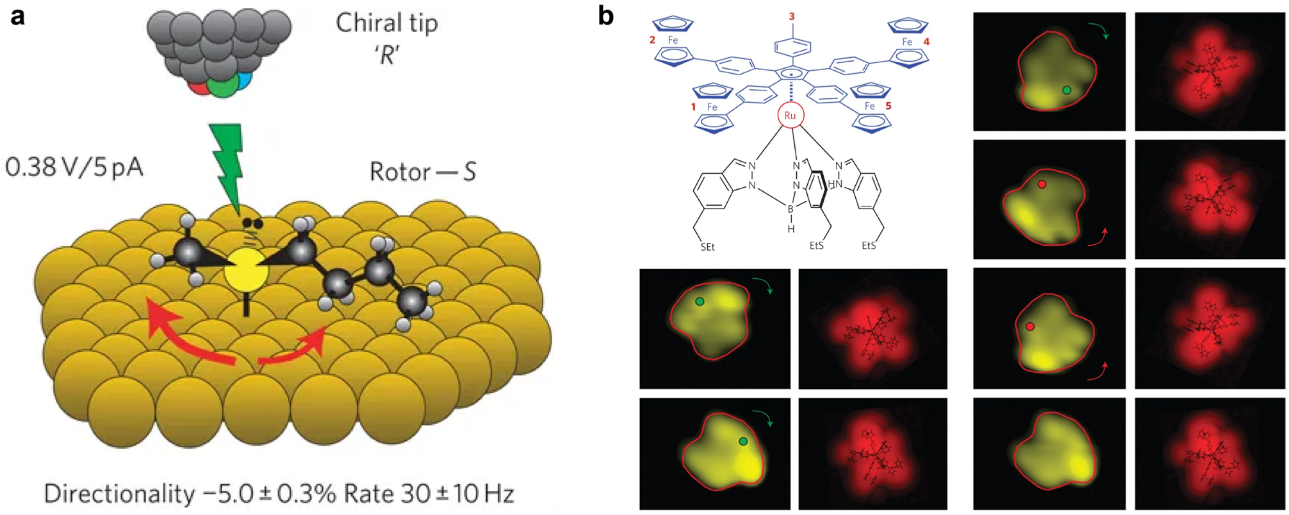

Figure 4.3 | Electrically-driven molecular motors

a Electrically powered butyl methyl sulphide (S enantiomer) rotation on Cu(111) with a directionality of up to 5% at a rotation frequency of 30 Hz. **b** Electrically induced motion of the molecule [η5-1-(4-tolyl)-2,3,4,5-tetra(4-ferrocenylphenyl) cyclopentadienyl hydrotris [((ethylsulphanyl)methyl)indazol-1-yl] borate ruthenium(π)] depicted in the top left corner. The direction of the molecular motion can be controlled by the STM tip position with respect to the molecule. Figure **a** is adapted from Ref.[169]; Figure **b** from Ref.[173]

However, for none of the operational concepts of these various nano-cars neither the relation of the non-uniformity of the electric field on the direction of motion, nor the dependence of its directionality or probability of performing a motion step on bias voltage, tunneling current, and temperature was investigated in detail. The reason for this situation is due to the fact that after each step of motion the position of the STM tip had to be placed anew to follow the translational motion of the molecular car. In this context, electrically-induced rotary motors have the potential to be explored far more precisely. Of the numerous reports of electrically-powered molecular rotations, only few succeeded to exert control on the direction of motion. In particular, Sykes *et al.* presented the electrically-driven rotation of chiral Butyl methyl sulphide anchored on Cu(111) (Figure 4.3a) to exhibit a small asymmetry of 5% between the number of clockwise and counterclockwise rotational events.[169] As this asymmetry was independent of the molecule's enantiomeric form, they concluded that the shape of the STM tip enforced this slight directed motion. Soon afterwards, Hla *et al.* succeeded in the controlled clock-wise or counter-clockwise rotation of a metal-organic stator-rotor complex shown in Figure 4.3b with an STM tip.[173] In this case, the direction of the rotation depended on the precise STM tip position. Several years later, Hla *et al.* succeeded in visualizing the directed rotation of an individual complex molecule on Au(111) while scanning with STM. As the motion of these motors could only be recorded during the lateral scanning, a detailed characterization was not possible.[171] On the other hand, a more detailed description in terms of directionality of motion was achieved for the rotation of chiral triazatruxene (TAT) molecules on Ag(111) very recently by Fonin and co-workers. They were even able to control the direction of rotation for TAT on Ag(111) via the magnitude of the STM bias voltage.[188]

In all the examples of molecular motors reported in literature, the spatial inversion symmetry has always been lifted by using chiral, and oftentimes very large molecules. If this task could be achieved via the substrate on which the directed molecular motion takes place, *i.e.*, if the substrate is chiral, the motion of small, achiral molecules might become directed. In chapter 4.2, a molecular motor consisting of the symmetric acetylene molecule adsorbed on the chiral, three-fold symmetric PdGa{111} is discussed and shown to allow deep insights into the working principle of molecular motors and into thermodynamic laws within the quantum mechanical limit.

4.2 Publication (accepted in *PNAS*): "Molecular motor crossing the frontier of classical to quantum tunneling motion"

My contribution to this work consisted of the acquisition and analysis of all experimental data. Additionally, I was involved in the planning of the experiments. The modeling of the molecular motor was shared between the authors, whereas I performed the simulations of the jump sequence maps, applied the Langevin model to the bias voltage dependence of the rotation frequency and directionality, and proved statistically that the directionality was independent of the tunneling current. I wrote the manuscript together with Oliver Gröning and with input from all co-authors.

Observation and manipulation of maximal Chern numbers in a chiral topological semimetal

Samuel Stolz[1,2], Oliver Gröning[1,*], Jan Prinz[1,2], Harald Brune[2], and Roland Widmer[1]

[1]*EMPA, Swiss Federal Laboratories for Materials Science and Technology, 8600 Dübendorf, Switzerland*

[2]*Institute of Condensed Matter Physics, Station 3, EPFL, 1015 Lausanne, Switzerland*

*oliver.groening@empa.ch

In 1959 Richard Feynman envisiioned downscaling of information storage and machines to atomic dimensions.[189] Both visions were eventually realized, by writing information via positioning single atoms on a nickel surface in 1990[190] and by devising the first artificial, light driven molecular machine in 1999.[156] However, most synthetic molecular machines, although driven by quantum processes, exhibit classical kinetics,[146,191] wheras operation by quantum tunneling motion is largely elusive.

We have realized and investigated a molecular motor applying scanning tunneling microscopy (STM), which consists of a single acetylene (C_2H_2) rotor anchored to a chiral atomic cluster provided by a PdGa(111) surace that acts as stator. By breaking spatial inversion symmetry, the stator defines the unique sense of rotation. While thermally activated motion is non-directed, inelastic electron tunneling triggers rotations, where the degree of directionality depends on the magnitude of the STM bias voltage. Below 17 K and 30 mV bias voltage, a constant rotation frequency is observed which bears the fundamental characteristics of quantum tunneling. The concomitantly high directionality, exceeding 97%, implicates the combination of quantum and non-equilibrium processes in this regime, being the hallmark of macroscopic quantum tunneling.[192]

The acetylene on PdGa(111) motor therefore pushes molecular machines to their extreme limits, not just in terms of size, but also regarding structural precision, degree of directionality, and crossover from classical motion to quantum tunneling. This ultra-small motor thus opens the possibility to investigate in-operando effects and origins of energy dissipation during tunneling events, and ultimately energy harvesting at the atomic scales.

Significance statement: Conversion of undirected energy inputs into directed motion on molecular scales is the basis for controlled movements in living organisms. In this context, fundamental insights can be obtained by investigating artificial molecular machines under well-defined conditions. We devised the currently smallest, atomically precise molecular machine, whose rotor (C_2H_2) consists of just 4 atoms and whose functioning we have tracked in detail employing scanning tunneling microscopy (STM). Unlike all other surface anchored rotors reported so far, ours is characterized by an extremely high degree of directionality which is independent on STM-tip conditions or position, therefore solely defined by the chiral support. Owing to its ultra-small size, our rotor's operation crosses the well-established classical to an unanticipated quantum tunneling kinetic regime without loss in directionality.

Inspired by molecular machines in biological systems,[139,141] substantial effort has been devoted to unravel their underlying physicochemical functioning,[148,149] and to create artificial molecular motors.[156,162,169–171,193–195] STM provides an ideal platform for investigating the dynamics of atoms and molecules on surfaces.[169–179] However, few studies were aimed at achieving controlled, STM tip position independent, directional motion requiring breaking of inversion symmetry, which is commonly achieved by adsorbing chiral molecules on achiral surfaces.[169–172] We reverse this concept by using the surface of non-centrosymmetric PdGa crystals as chiral stator. This relaxes the geometric constraints on the rotor molecule, and allows directed motion even for simple and symmetric molecules such as C_2H_2.

Starting point of our study is the creation of a well-defined chiral surface from a non-centrosymmetric single crystal, namely the intermetallic compound Palladium-Gallium with 1:1 stoichiometry (PdGa) exhibiting bulk terminated chiral surfaces.[54] The chiral structure of some of these surfaces manifests itself in pronounced enantioselective adsorption properties.[27] Here we choose the $(\bar{1}\bar{1}\bar{1})$ surface of the PdGa A enantiomorph.[54] Under appropriate ultra-high vacuum preparation, it terminates by a layer containing 3 Pd atoms per trigonal surface unit cell ($a_0 = 6.95$ Å) forming an equilateral triangle of 3.01 Å side length (Figure 4.8 and ref.[48]). The local inversion symmetry of this Pd trimer is lifted by coordination of the 6 second layer Ga atoms and furthermore by 3 Pd atoms in the third layer (Figure 4.4a-b). In the following we will denote this termination as Pd_3.

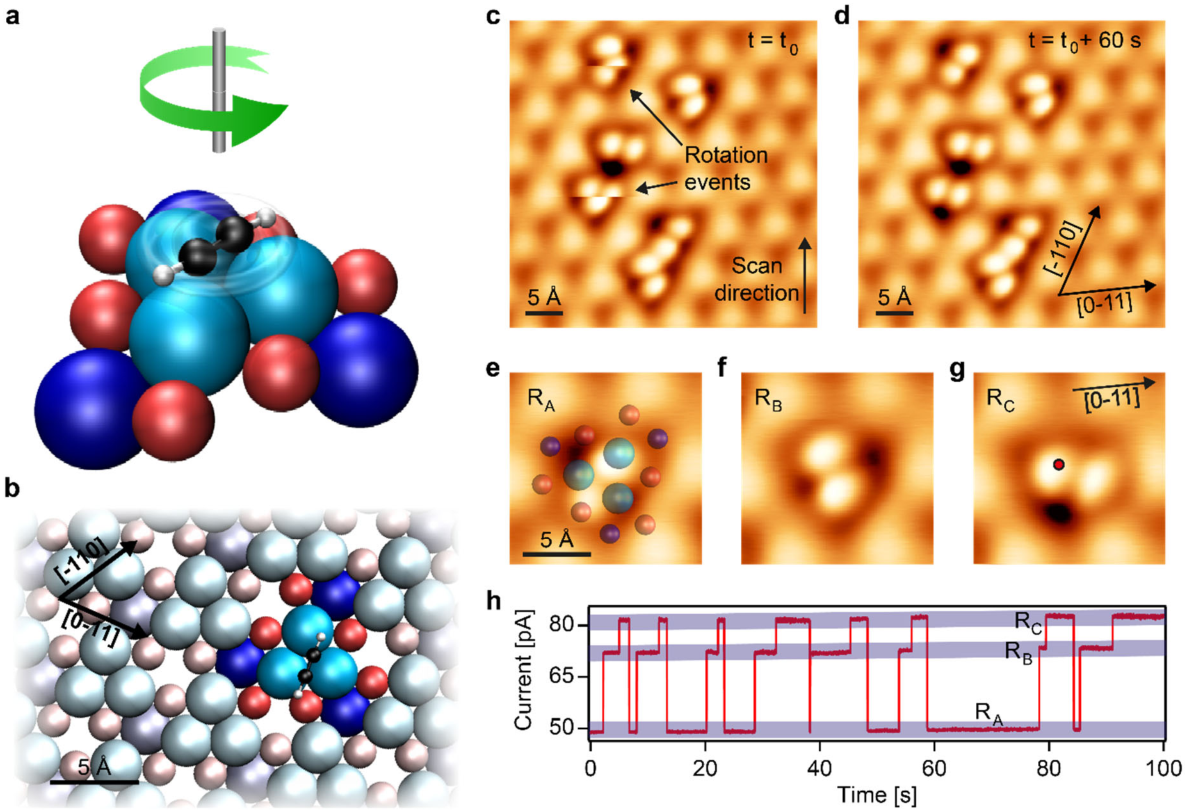

Figure 4.4| Acetylene rotation on the PdGa:A(-1-1-1)Pd_3 surface

a Sketch of the acetylene on Pd_3 motor. **b** Atomic structure of the PdGa:A(-1-1-1)Pd_3 surfaces with the PdGa cluster acting as stator highlighted in saturated colors. The acetylene (C_2H_2) rotor is depicted in one (R_a) of its three equivalent adsorption configurations R_a, R_b, R_c. In **a** and **b**, the top-layered Pd trimers ($z = 0$ Å) are depicted in bright blue, the second layer Ga trimers ($z = -0.85$ Å) in red and the third layered single Pd atoms ($z = -1.61$ Å) in dark blue. **c-g** Constant current STM images of C_2H_2 adsorbed on the Pd_3 surface ($T = 5\,K; V_G = 10\,mV; I_T = 50\,pA$). In **c** two rotating molecules are pointed out, whereas in **d**, recorded 60 s after **c**, no molecular rotation is observed. **e-g** STM images of the same acetylene molecule in its three rotational configurations. In **e** the underlying PdGa stator structure is superposed. **h** Constant height $I_T(t)$ time series ($\Delta t = 100$; $V_G = 25\,mV$; 1 ms time resolution) measured at the relative position to the C_2H_2 indicated by the red marker in **g**.

On Pd_3, acetylene molecules adsorb centered on the Pd trimers.[46] When imaged by STM at 5 K, they appear as dumbbells with lobe-to-lobe separation of about 3 Å in three 120°-rotated orientations (Figure 4.4e-g) between which they switch quasi instantaneously (Figure 4.4c-d). Acetylene molecules are firmly anchored to the trimer and usually dissociate before being dragged off the trimer by STM tip manipulation.

We have followed the rotation events by recording tunneling current time series $I_T(t)$ at a fixed tip position (Figure 4.4h), in analogy to the STM investigation of the rotation of chiral butyl-methyl-sulphide on Cu(111).[169] In the latter case, a weak (≤ 5%) asymmetry in the number of clockwise (CW) n_{CW} and counter-clockwise (CCW) n_{CCW} rotations was reported and tentatively attributed to chiral STM tips, as no correlation of the directionality with the molecule's enantiomeric form was found. The $I_T(t)$ of Figure 4.4h, recorded over 100 s, exhibits cyclic jump sequences between 3 levels (…R_A→R_B→B_C→R_A…) with $n_{CCW} = 23$ jumps in CCW direction and $n_{CW} = 0$ in CW, resulting in a frequency of 0.23 Hz and perfect directionality $dir = 100 * \frac{n_{CCW}-n_{CW}}{n_{CCW}+n_{CW}} = 100\%$. The movie SV1 shows a time lapse series of STM images evidencing the prevailing CCW rotation of the motor.

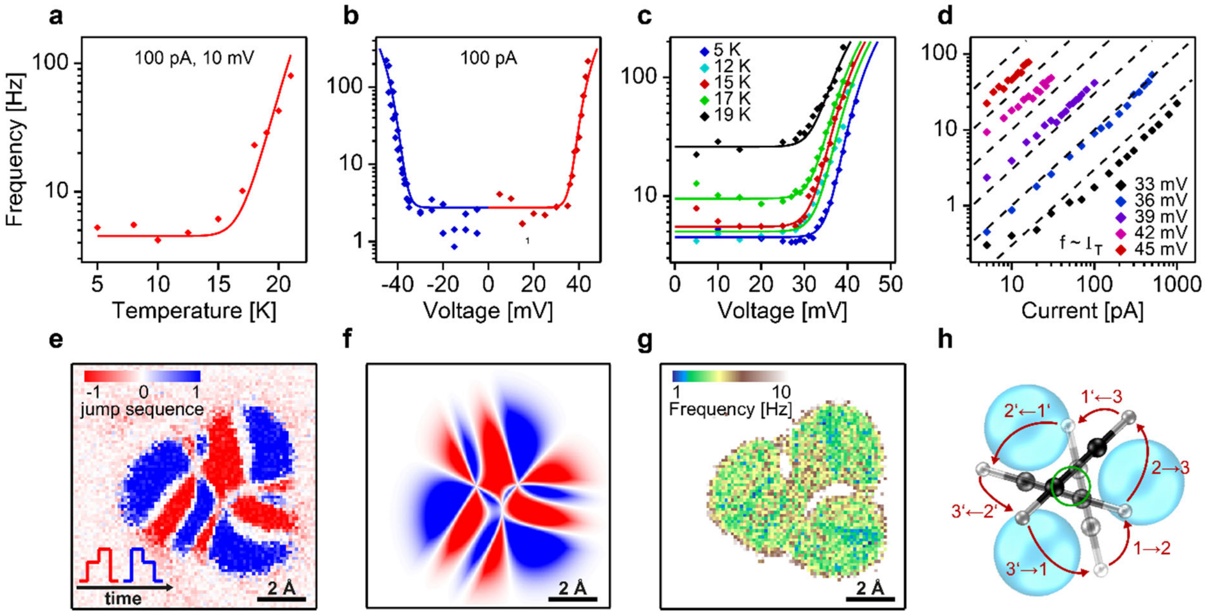

Figure 4.5| Parametric dependence of the rotation frequency and jump sequence

a Rotation frequency dependence on temperature ($V_G = 10\,mV$; $I_T = 100\,pA$), **b** on bias voltage for both polarities ($T = 5\,K$; $I_T = 100\,pA$), **c** on bias voltage at various temperatures between 5 K and 19 K ($I_T = 100\,pA$), and **d** on tunnelling current for different bias voltages between 33 mV and 45 mV at $T = 5\,K$. In **a-d**, the markers represent experimental data, while the solid lines are derived from the kinetic model (4.2.1.7). **e** Constant current jump sequence map ($js = 3 * \frac{n_{up}-n_{down}}{n_{up}+n_{down}} = sing(js) * |dir|$; $n_{up/down}$: number of jumps increasing/decreasing the tip height) generated from a 80x80 grid (1x1 nm^2) of individual $z_T(t)$ spectra, each recorded for 4 s (4000 points; $V_G = 10\,mV$; $I_T = 100\,pA$). **f** Simulated jump sequence map for 100% CCW rotation based on the motion pattern shown in **h**. **g** Frequency map of the C_2H_2 rotation extracted from the same experimental $z_T(t)$ grid of **e**. **h** Our best estimation of the tumbling acetylene rotation on Pd_3 for a full 360° rotation in six 60° steps indicated by tracking the motion of one H atom (1→2→3→1'→2'→3' with n and n' denoting indistinguishable C_2H_2 configurations) with the green circle indicating the motion of acetylene's center of mass.

Analyzing the parametric dependence of the rotation frequency (Figure 4.5a-c and Figure 4.9), shows that this molecular motor operates in two disting regimes; the *tunneling regime* (TR) where its rotation frequency ν_T is independent of temperature $T < 15\,K$, bias voltage $|V_G| < 30\,mV$, and current $I_T < 200\,pA$, and the *classical regime* (CR) where the frequency strongly depends on these parameters. Even though all experimental data presented in Figure 4.4 have been recorded in the TR, we first discuss the CR where C_2H_2 rotations can be selectively powered by thermal or electrical excitations. We find the temperature dependence of the rotation frequency at low bias (Figure 4.5a) to follow an Arrhenius characteristics (solid line in Figure 4.5a)

$$\nu(T) = \nu_T + \nu_A \exp\left(-\frac{\Delta E_B}{k_B T}\right)$$

Equation 4.2 | thermal rotation frequency

with $\nu_T = 4.5\,Hz, \nu_A = 10^{8.7\pm2.0}\,Hz$ (attempt frequency) and $\Delta E_B = 27.5 \pm 7.1\,meV$ (energy barrier for rotation). Above 30 mV the frequency increases exponentially with V_G, independent of polarity (Figure 4.5b-c). Under the same conditions, but at constant bias voltage, the power-law dependence $\nu \propto I_T^n$ with $n \approx 1$ (Figure 4.5d) identifies the electronically stimulated rotation as a single-electron process.[196] As we will discuss later, the parametric dependence of the rotation frequency and directionality with T, V_G and I_T is very well reproduced by a Langevin kinetic model (solid lines in Figure 4.5b-c).

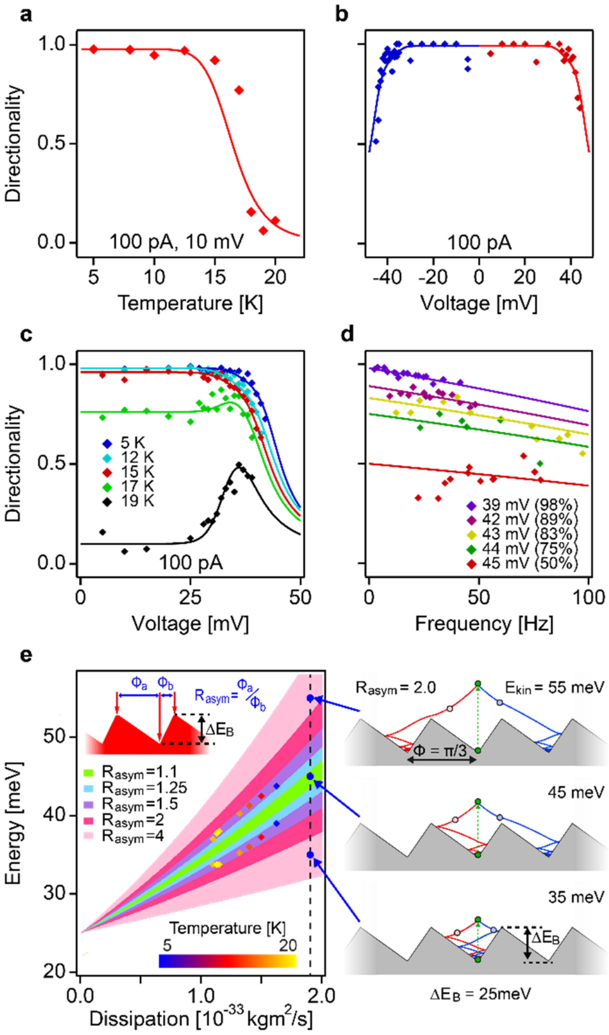

Figure 4.6| Parametric dependence of the nanomotor's directionality

a Dependence of the directionality on temperature ($V_G = 10\,mV;\ I_T = 100\,pA$), **b** bias voltage for both polarities ($I_T = 100\,pA;\ T = 5\,K$), **c** bias voltage at various temperatures between 5 K and 19 K ($I_T = 100\,pA$), and **d** rotation frequency controlled via varying I_T for several V_G. In **a-d** the markers represent experimental data, while the solid lines in **a-c** are derived from the kinetic model (4.2.1.7). The solid lines in **d** show simulated dependencies for constant directionality (given in brackets) with frequency considering finite time resolution of the experiment (4.2.1.8). **E** Schematic representation of the Langevin rotation dynamics derived for ratchet potentials with $\Delta E_B = 25\,meV$. On the left, the range of transferred kinetic energy E_{kin} for directed motion, i.e. $E_L < E_{kin} < E_R$, in dependence of energy dissipation is colored for several R_{asym}, as defined in the inset. The experimentally determined E_L and E_R are represented by two markers of the same color for several temperatures. On the right, the trajectories of the C_2H_2 60° rotation in a ratchet potential with $R_{asym} = 2.0$, $\lambda = 2 * 10^{-33}\,\frac{kgm^2}{s}$ and $\Delta E_B = 25\,meV$ are displayed as a function of E_{kin}. For $E_L < E_R < E_{kin}$ there is no unidirected motion, $E_L < E_{kin} < E_R$ results in directed motion by overcoming the steeper potential barrier, and $E_{kin} < E_L < E_R$ induces no rotation (from top to bottom).

Before we discuss the parametric dependence of the directionality, the influence of the STM tip, required for observing the motion, must be clarified. Particularly, we have to verify that breaking of the inversion symmetry due to the tip position (and possibly tip structure) in proximity to the motor does not prevail over the influence of the chiral substrate in determining the sense of rotation. To address this issue, we have measured 6400 constant current tip-height time series $z_T(t)$ on a grid of 80×80 equidistant points covering $1 \times 1\ nm^2$ in the vicinity of single acetylene molecules in the TR. Analysis of all these $z_T(t)$ series reveals an intricate, regular pattern with alternating, highly directional ascending (red) and descending (blue) jump sequences (Figure 4.5e). This pattern fully corroborates a tip position independent, unidirectional rotation of the molecule, which becomes apparent by modelling and mapping the position dependent jump sequence assuming a cyclic unidirectional CCW rotation of the molecule by 60° steps (Figure 4.10-Figure 4.13). After optimizing molecule configuration and tip-shape in the model, an excellent agreement of the simulated jump sequence map (Figure 4.5f) with the experiment is found. Hence, we conclude that, regardless of the tip position, the jump sequences always correspond to CCW rotations. Furthermore, as witnessed from Figure 4.5g and Figure 4.14-Figure 4.16, there is no pronounced dependence of v_T on the tip position. Although we investigated hundreds of molecules with tens of different tip modifications, we never observed any systematic CW rotations in the TR or CR evidencing that solely the stator dictates the direction and directionality of the rotation. Evaluating 1792 rotation events ($n_{CCW} = 1771$ and $n_{CW} = 21$) in the TR, we determine a directionality $dir \geq 96.7\%$ with 2σ confidence. By matching the simulated jump sequence map to the experiment we identify the C_2H_2 rotation to be best described as a tumbling rotor, whose center of mass moves on a circle with radius $r = 0.5 \pm 0.1$ Å and a moment of inertia $I_{C_2H_2} = 5.62 * 10^{-46} kgm^2$ (Figure 4.5h).

Having clarified the influence of the tip, we now turn to the discussion of the parametric dependencies of the directionality (Figure 4.6a-d). The temperature dependence shows a rapid drop in directionality once thermally activated rotations start to contribute significantly. The solid line in Figure 4.6a assumes that ν_T exhibits 98% directionality, whereas the thermally activatet jumps described by the Arrhenius Equation 4.2 are purely random. These random thermal rotation events are expected because substrate, STM tip, and hence molecule are in thermal equilibrium and accordingly, unidirectional rotation (which reduces entropy) is forbidden by the 2nd law of thermodynamics. At $T = 5\ K$ a decrease of directionality is also observed for bias voltages V_G beyond $\pm 35\ meV$ (Figure 4.6b). However, unlike thermal rotations, those induced by IET only become gradually non-directional. This is clearly observed in the regime where thermally and IET induced rotations coexist. As displayed in Figure 4.6c, the voltage independent directionality of only 10% at $T = 19\ K$ and $|V_G| < 30\ mV$ can be increased significantly at higher $|V_G|$ due to additional directed IET rotations. This increase is only effective in a narrow voltage window, above which the directionality rapidly decreases. By contrast, the I_T dependence of the directionality for a fixed voltage is weak (Figure 4.6d), where the slight decrease with increasing current, i.e. frequency, is attributed to the detection of two shortly successive CCW rotations as a single erroneous CW one (solid lines in Figure 4.6d). Hence we conclude that directionality stays above 95% for $|V_G| < 40\ mV$ even at high current.

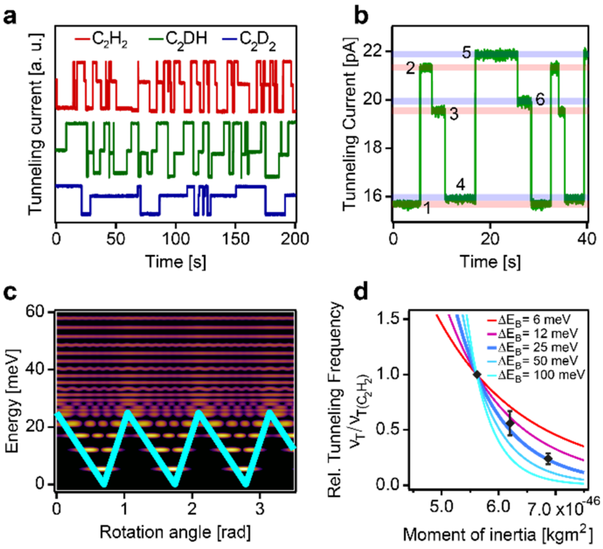

Figure 4.7| Quantum tunnelling rotation of acetylene

a $I_T(t)$ curves for C_2H_2, C_2DH, and C_2D_2, with a special focus on the six different current levels in a $I_T(t)$ curve of C_2DH in **b**. In **c** the ratchet potential is shown in turquois, based on which the C_2H_2 quantum states, energy levels and tunnelling frequencies are determined. The color (black to yellow) represents the probability density of the quantum states. The dependence of ν_T in the WKB approximation with the momentum of inertia, normalized to the ν_T at 5.62x10^{-46} kgm^2 (C_2H_2) is displayed as solid lines in **d** for several ΔE_B (see 4.2.1.9). The black markers represent the experimental ν_T for C_2H_2, C_2DH and C_2D_2, each normalized to the one of C_2H_2.

The observation of directional motion triggered from a non-cyclic, directionless, and position independent energy input stemming from a single IET event, prompts us to apply a variant of the biased Brownian motion concept proposed by Astumian and Hänggi for modelling the underlying mechanism.[148,149] Our model of IET induced rotation assumes a static, periodic, but asymmetric potential $U(\phi)$ ($\phi = [0,2\pi]$, with $\pi/_3$ periodicity), with the asymmetry of the potential, R_{asym}, defined in the inset in Figure 4.6e and Figure 4.17. A single IET event instantaneously excites the molecule from its ground state and its trajectory $\phi(t)$ is obtained from Langevin dynamics $I\ddot{\phi} = -\frac{\partial U(\phi)}{\partial \phi} - \lambda\dot{\phi}$, where I is the momentum of inertia and λ the viscous dissipation coefficient.[148,149] Depending on R_{asym} and λ, two dissimilar minimum kinetic energies E_L and E_R are required to overcome the barrier to the left (*i.e.* CW) and to the right (*i.e.* CCW), respectively. These energies are the basis for describing frequency and directionality by the kinetic model (see chapter 4.2.1.7).

Matching this kinetic model to our experimental data in Figure 4.5c and Figure 4.6c, allows determination of the temperature dependent $E_L(T)$ and $E_R(T)$ which are represented by colored markers in Figure 4.6e. From these values we deduce R_{asym} to be

$1.25 < R_{asym} < 1.5$ assuming $\Delta E_B = 25\ meV$. The reduction of the dissipation λ from about $1.6 * 10^{-33}\,\frac{kgm^2}{s}$ at 5 K to around $1.1 * 10^{-33}\,\frac{kgm^2}{s}$ at 20 K can be attributed to the less efficient coupling of the molecule to the substrate with increasing temperature.

Having successfully described the rich phenomenology of the over-the-barrier rotation processes in the CR, the unexpected, nearly perfect unidirectional rotation of C_2H_2 in the TR requires closer inspection. Tunneling, especially of hydrogen is a well-established phenomenon in chemistry[197] and surface science,[176] and plays a crucial role in numerous biological processes like enzyme catalyzed reactions.[198] The approximately exponential decrease of the tunneling rate with increasing mass, however, allows reasonably high tunneling rates of heavy atoms or molecules only for very small barrier heights and tunneling distances. Despite these restrictions, many tunneling transitions on surfaces involving heavy atoms like cobalt or small molecules are reported.[172,177,178,180]

In this respect, the tunneling of formaldehyde (CH_2O) between two adsorption configurations on Cu(110) reported by Chiang *et al.* Is very close to the C_2H_2 rotation in terms of ΔE_B, moment of inertia, and rotation angle and thus yields comparable frequencies ν_T.[180] In both cases ν_T is critically tip condition dependent and varies between 0.01 Hz and 0.1 Hz for CH_2O/Cu(110) and between 0.25 Hz and 5 Hz for C_2H_2/Pd_3. Thus, to evidence the strong isotopic dependence and corroborating quantum tunneling, we have paid attention that the ν_T for C_2H_2, fully (C_2D_2) and partially deuterated acetylene (C_2DH) are determined consecutively on the same sample with the same STM tip (Figure 4.21). Figure 4.7a shows the resulting $I_T(t)$ sequences for C_2H_2, C_2DH and C_2D_2 which reveal ν_T ratios (with respect to C_2H_2) of $1{:}\,0.56(11){:}\,0.24(5)$ (C_2H_2:C_2DH:C_2D_2), which we consistently observe with different tips (Table 4.3, Figure 4.22). This strong relative reduction of ν_T is contrasted by the comparatively small relative change of moment of inertia $1{:}\,1.08{:}\,1.2$ and thus indicative for quantum tunneling. Careful inspection of the $I_T(t)$ sequence of C_2DH with broken C_2-symmetry reveals that the rotation cycles through 6 rather than 3 current levels (Figure 4.7b), which proves that a full acetylene rotation indeed requires six CCW 60°-rotations. Comparison of the experimentally determined ν_T ratios to the corresponding WKB tunneling frequency (4.2.1.9) shows an excellent match for a barrier height of $\Delta E_B = 25\ meV$ (Figure 4.7d).

Quantum tunnelling rotations concomitant with high directionality of 97.7% allows for an estimation of the entropy change of a single tunnelling rotation from the experimental CCW and CW rotation probabilities, given by $\Delta S = -k_B \ln\left({}^{p_{CCW}}/_{p_{CW}}\right) \approx -k_B \ln\left({}^{100}/_{1}\right) \approx -0.4\,\frac{meV}{K}$. This implies that the directional rotation in the TR must be a non-equilibrium process with energy dissipation $\Delta Q > 2\ meV$ at 5 K and $\Delta Q > 6\ meV$ at 15 K per rotation. As these values of ΔQ are of the order of the energy difference of two frustrated rotation modes of C_2H_2 (*e.g.* $\hbar\omega_{10} - \hbar\omega_{00} = 6.8\ meV$; Figure 4.7c, Figure 4.20 and Table 4.2), one might assume that the reqired non-equilibrium tunneling proceeds via an excitation from the ground state to a bound rotational mode as proposed by Ch. Nacci *et al.*[178] We estimate a maximum power dissipation of 100 meV/s per motor, assuming 10 Hz tunnelling frequency as upper bound. On the other hand, the STM required for monitoring the rotation, locally dissipates at least $3\text{x}10^6$ meV/s even at the lowest settings of 1 pA tunneling current and 0.5 mV bias. Therefore, the STM tip is presumably critical in driving the system out of equilibrium also in the regime of tunneling motion.

In conclusion, the highly directional tumbling rotation of C_2H_2 on the chiral PdGa{111}Pd_3 surface exhibits a rich phenomenology, most prominently characterized by an unprecedentedly high directionality and small motor size. Its rotor (C_2H_2) and stator (Pd_3-Ga_6-Pd_3 cluster) shown in Figure 4.4a comprise just 16 atoms to form a unidirectional 6-state cyclic molecular motor (Figure 4.7b) through all of which it cycles ceaselessly, powered exclusively by single electrons. This contrasts reported motors driven by light or chemical reactions, since for the former concerted thermal and light driven activation is required. The latter usually requires a cycling of the chemical environment to complete one cycle. In the classical regime, we could establish a Langevin kinetic model of the motion describing frequency and directionality with temperature, STM bias voltage and tunneling current. The model provides robust values for the rotational potential asymmetry R_{asym} and the temperature dependence of the viscous dissipation coefficient $\lambda(T)$ relating the operation of this molecular machine to atomic friction. The negative entropy change associated with the high rotation directionality, also observed in the tunneling regime, challenges the understanding of this simple cyclic machine in terms of dissipative quantum tunneling dynamics. In the future it might be possible to convert energy via forced excitations, *e.g.* optical, by IET, into directional motion and thus investigating energy harvesting at the smallest possible length scale.

Materials and Methods

All experiments were performed under ultra-high vacuum (UHV) conditions with a base pressure below $5\text{x}10^{-11}$ mbar using an Omicron low-temperature STM operated at 5 K. The measurements were performed with different tips including 80:20 Pt/Ir tip, Tungsten STM and Tungsten Q+ Sensor tips. We have found no systematic difference in the experimental results obtained with different tips. The PdGa crystal surface was prepared by repeated sputter and annealing cycles (sputtering: Ar+, 1 keV; annealing: 20 min at 870 K).

Before dosing C_2H_2, which was purchased from PanGas with a purity of 99.6%, the gas line was precleaned by purging with the gas or by freeze-thaw cycling (77 K). In case of C_2D_2, purchased from CDN isotopes with 99% purity with C_2DH being the main impurity, no precleaning was performed, because the gas was in a bottle with atmospheric pressure. Both gases were dosed by chamber backfilling through a leak valve at a pressure of $2x10^{-9}$ mbar. By removing the sample from the STM stage at 5K and exposing it to the acetylene outside the cryostat for a short time (generally 10-20 s) the most effective exposure conditions were achieved.

4.2.1 Supplementary Materials for the publication "Molecular motor crossing the frontier of classical to quantum tunneling motion"

In the following, the PdGa:A(-1-1-1)Pd$_3$ surface, which is terminated by isolated Pd trimers, will just be referred to as Pd$_3$.

4.2.1.1 STM images of clean Pd$_3$ surface and with C$_2$H$_2$ adsorbed

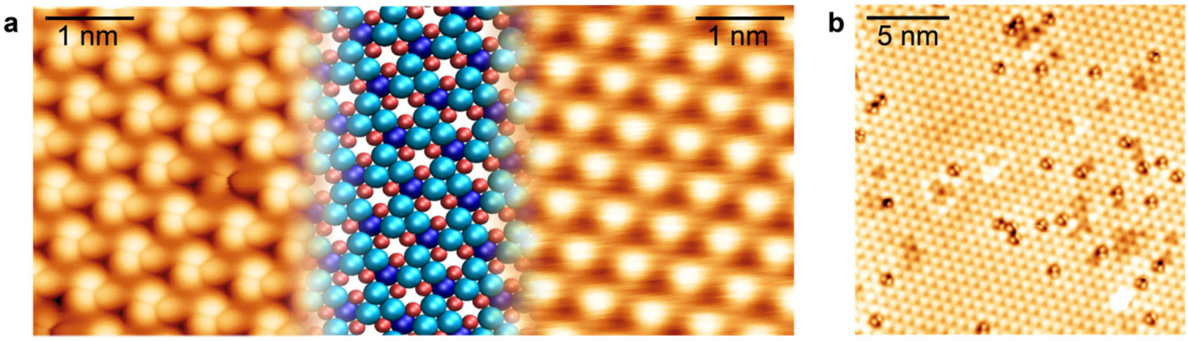

Figure 4.8 | Overview STM image of C$_2$H$_2$ on Pd$_3$

a STM images of the clean Pd$_3$ surface recorded at 5 K, 10 mV and 200 pA to resolve the Pd trimers in the top layer (left) partially overlaid by the atomic structure (center) and recorded at 77 K, -200 mV and 200 pA (right), representing the normal STM images taken. **B** 20 x 20 nm^2 STM image of C$_2$H$_2$ adsorbed on Pd$_3$, visualizing the usual coverage we worked with (5 K, 5 mV, 100 pA).

4.2.1.2 Voltage and current dependence of the rotation frequency in the tunneling regime

For temperatures $T < 15\ K$ and bias voltages $|V_G| \leq 30mV$ the rotation frequency ν_T shows a pronounced dependence on the tip condition and can vary between 0.1 Hz and 5 H, which is not uncommon for tunneling transition rates. When ν_T is high, we detect a rotation frequency, which is independent of voltage and only weakly dependent on the current. Such an example is depicted in Figure 4.9 for tip condition 1, where increasing from 2 pA to 200 pA only increases ν_T from 2 Hz to 5 Hz.

If the base frequency is low a transition from a voltage independent to a weakly current dependent region at low currents to a linear dependence and strong voltage dependence at higher currents can be observed as shown in Figure 4.9 for tip condition 2.

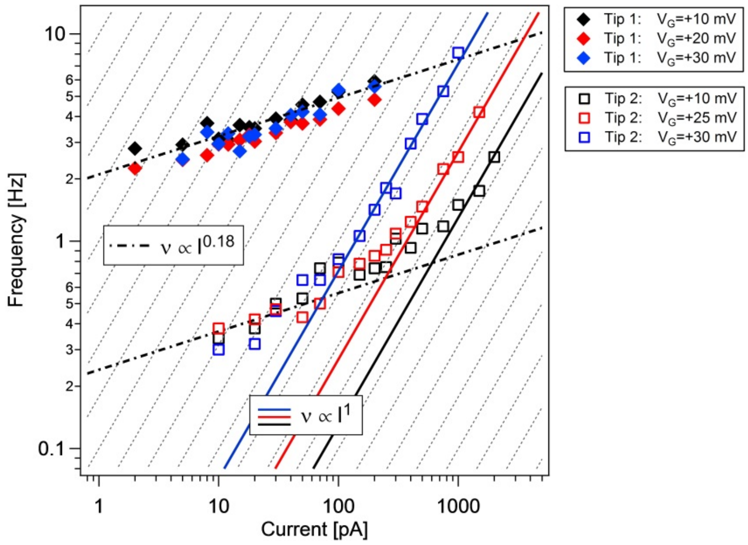

Figure 4.9 | Rotation frequency dependence on tunnelling current in the tunnelling regime

Experimentally measured rotation frequencies (markers) as a function of the current for different tip conditions and different STM bias voltages.

Such transitions are characteristic for vibrationally assisted tunneling (VAT) as proposed by Ueba *et al.*[199] The linear part corresponds to tunneling from excited vibrational states populated by energy transfer from inelastic electron tunneling. The weakly current dependent region would correspond to deep tunneling from the vibrational ground state. The fact that there is still a weak current dependence can be attributed to the fact that tunneling current and tip height cannot be varied independently, but are related via:

$$I_T(z) \propto e^{-\frac{2}{\hbar}\sqrt{2m_e\Phi z}} \approx e^{-2.3z[\text{Å}]}$$

For bias voltaes much smaller than the work function $\Phi = 5\ eV$. A variation of the tunnelling current over 2 orders of magnitude would therefore correspond to a change in the tip height of about 2 Å. It is plausible that the tip softens the potential energy landscape and thereby the tunnelling rate is increased.

With regards to the VAT mechanism, the theoretical tunnelling frequency for the vibrational ground state ($\hbar\omega_{00} = 3.58\ meV$, see 4.2.1.9) would be 12.95 MHz compared to 571.9 MHz (first excited vibration $\hbar\omega_{10} = 10.57\ meV$) and 10'150 MHz (second excited vibration $\hbar\omega_{20} = 16.54\ meV$).

4.2.1.3 Details of the rotational motion

Figure 4.10a shows a series of constant current STM topography images with the three rotation states in 1 to 3 observed for the acetylene molecule in the sequence of their motion from left to right. The atomic structure of the substrate has been superimposed to the STM images. As can be seen from Figure 4.10b the acetylene molecule does not simply rotate around the center of the Pd trimer, but performs a combination of rotation and translation, *i.e.*, tumbling rotation. 1 and 1' represent a 180° rotation of the C_2H_2 molecule which are indistinguishable due to the C_2 symmetry of the molecule.

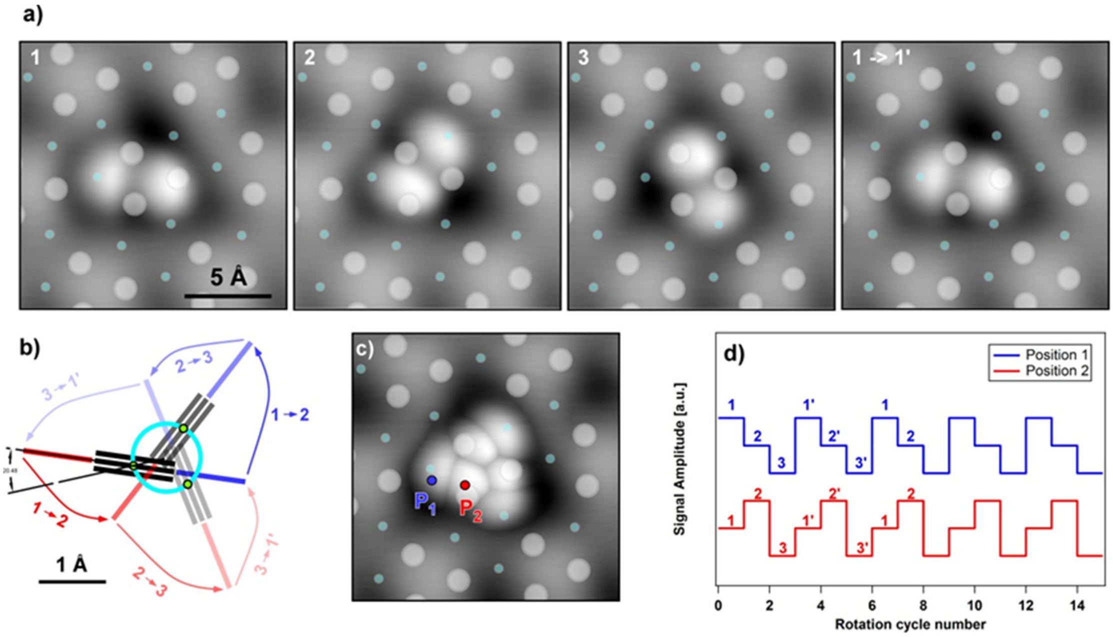

Figure 4.10 | Positional dependence of signal amplitude sequence

a Series of STM images of C_2H_2 on Pd_3 with the surface structure superimposed. 1-3 shows the acetylene's three distinguishable rotation states. **b** The assumed motion of acetylene on the Pd_3 surface. **c** Superposition ($z(x,y) = \max(z_1(x,y), z_2(x,y), z_3(x,y))$) of the three rotation states shown in **a**. **d** Schematic $I_T(t)$ spectra for the two accordingly colored tip positions marked in **c**.

4.2.1.4 Simulation of jump sequence maps

In order to compare the experimentally measured jump sequence maps with an idealized model of the acetylene motion, we describe the STM signal (current or height) by three amplitude functions $I_i(x,y), i = \{1,2,3\}$ for the three rotation states. The STM signal, for a given rotation state of the molecule, can be reasonably well approximated by the superposition of two ellipsoidal Gaussian peaks positioned at the two lobes of the acetylene molecule. This leads to the following approximation of the STM signature:

$$I_i(x,y) = \exp(\sigma_1(x-x_i)^2) + \sigma(y-y_i)^2) + \exp(\sigma_1(x+x_i)^2 + \sigma_2(y-y_i)^2)$$

The parameters σ_1 and σ_2 define the size and ellipticity of the lobes L_1 and L_2, separated by the distance d (Figure 4.11a). Variations in σ_1 and σ_2 are assumed to be due to changes in bluntness and symmetry of the STM tips only. Off-center positions and rotations are then realized by the appropriate translation and rotation operations on the coordinate system, as sketched in Figure 4.11a, where M_1 represents the center of the Pd trimer and M_2 the center of mass of C_2H_2. r corresponds to the distance between M_1 and M_2, while φ_1 is the angle between the vectors connecting M_1 to M_2 and M_1 to the center of a neighbouring Pd trimer. Finally φ_2 is the angle by which the molecule is tilted with respect to the vector $\overrightarrow{M_1M_2}$. The functions I_i, $i = \{1,2,3\}$, are related by a 3-fold rotation symmetry regarding the lobe positions. All variables, r, d, φ_1 and φ_2 are chosen, such that the resulting amplitude distribution of the lobes fit well with the experimental STM image of a single molecule as seen in Figure 4.11b. This way we determine $r = 0.55 \pm 0.1$ Å, $d = 3.25 \pm 0.2$ Å, $\varphi_1 = 5°$ and $\varphi_2 = 20°$.

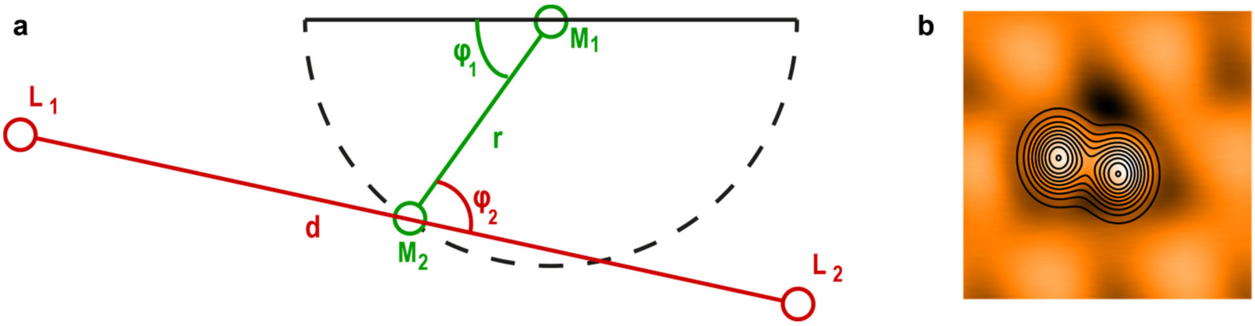

Figure 4.11 | Schematics for the jump sequence map modelling

a Sketch of the C_2H_2 on Pd_3 system and parameters used for the simulation of the jump sequence maps. **b** Simulated C_2H_2 STM image overlaid as contours on an experimental STM image.

With the synthetic model for the spatial current distribution in the three rotational configurations $I_i(x,y)$, $i = \{1,2,3\}$ the time sequence of current level $I_T(x,y,t)$ can be obtained for any tip position and any cycle sequence (in our case the CCW one $\ldots \rightarrow 1 \rightarrow 2 \rightarrow 3 \rightarrow 1\ (1') \rightarrow \ldots$) correspondingly the ascending (red) or descending current staircase (blue; see Figure 4.10d) can be determined at any position. It needs to be stressed that while the sequence can be determined in the model for arbitrarily small current jumps, in the experiment this is not the case. If the current variation between different rotational configurations becomes too small, *e.g.*, far away from the molecule or where two current levels become degenerate, the directionality goes to 0 in the experiment. In the model we have taken this into account by fading the directionality value when the smaller current jump is below 10% of the current amplitude ($\max(I_L, I_R)$).

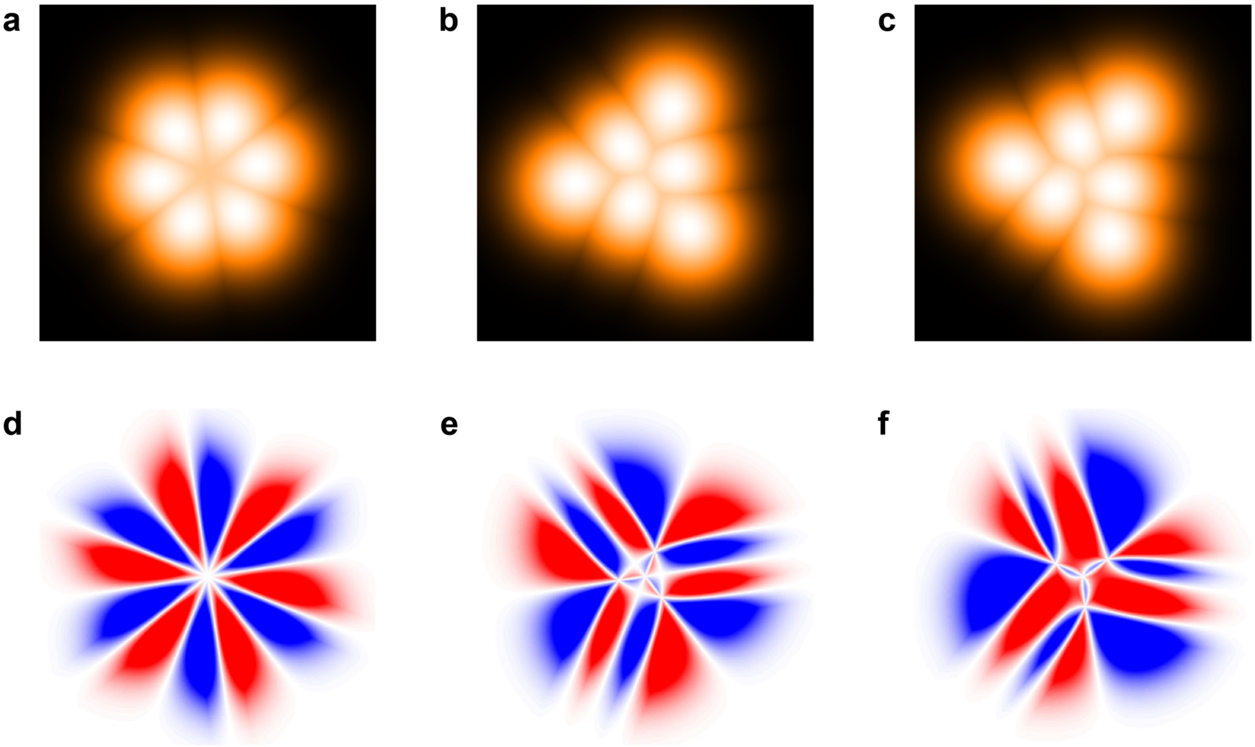

Figure 4.12 | Parametric influence in the jump sequence map modelling

a-c Simulated, superimposed current maps $I(x,y) = \max(I_1(x,y), I_2(x,y), I_3(x,y))$ for different rotational motions with the corresponding jump sequence maps shown in **d-f**.

The effect of the variables r and φ_2 on the superimposed current and jump sequence maps are demonstrated in Figure 4.12a-f. If the molecule would symmetrically rotate around its center of gravity (*i.e.* $r = 0$) the 6-fold symmetric pattern in Figure 4.12a and d would emerge. Allowing for an off-center rotation $r = 0.5$ Å but without tilt $\varphi_2 = 0$ the 3-fold symmetric pattern in Figure 4.12b and e result. Considering an off-center rotation with tilt $\varphi_2 = 20°$, shown in Figure 4.12c and f, reproduces well the slightly chiral pattern of the experiment.

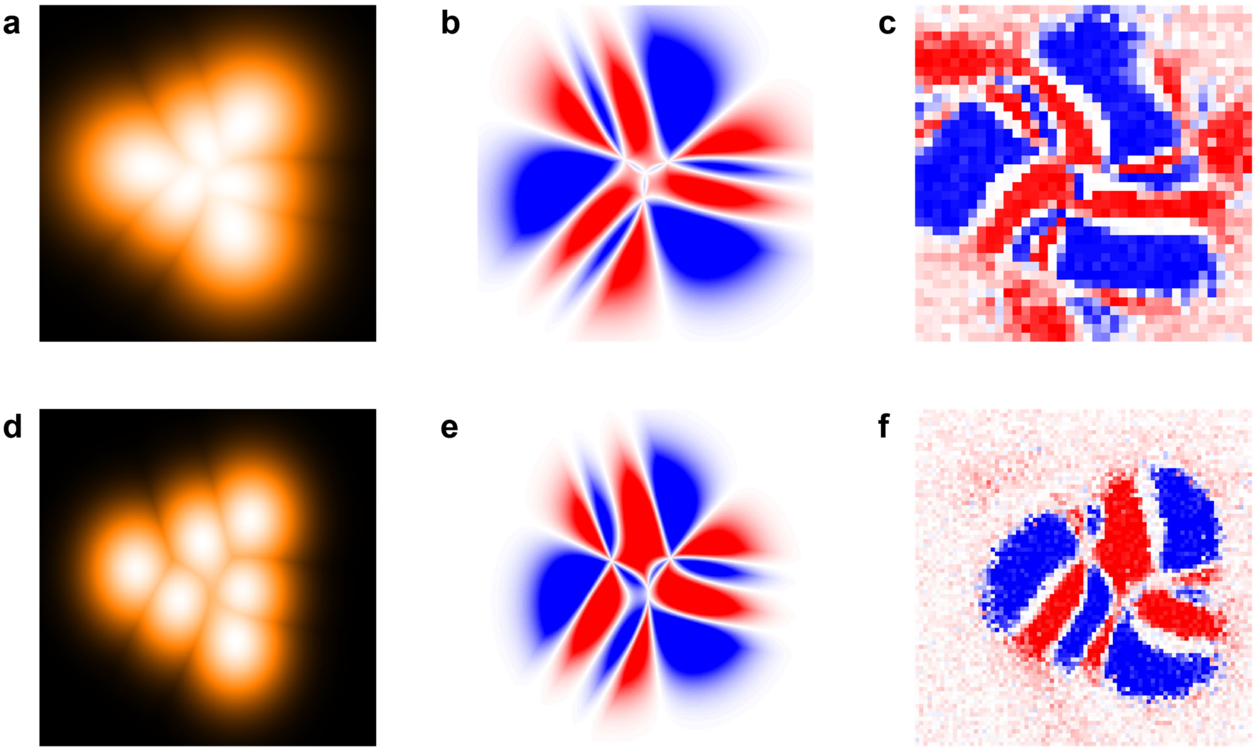

Figure 4.13 | Reproducing experimental jump sequence maps

Superimposed current maps in **a** and **d**, with the corresponding optimized simulated jump sequence maps in **b** and **e**, and the experimental jump sequence maps shown in **c** and **f** for two different STM tips and experimental conditions. (**c** 38x38 points equidistant grid, const. height map $25\ pA < I_T < 110\ pA$, $V_G = 10\ mV$; **f** 80x80 points equidistant grid, const. current map, $I_T = 100\ pA$, $V_G = 10\ mV$).

The jump sequence maps are very sensitive to the imaging conditions and can appear significantly different as illustrated in Figure 4.13. While the experimental jump sequence map in Figure 4.13c was recorded with a rather blunt, but symmetric tip described by $\sigma_1 = \sigma_2 = 0.25\ \text{Å}^{-1}$, the tip with which the experimental jump sequence map in Figure 4.13f was recorded was sharper, but asymmetric, best described with $\sigma_1 = 0.45\ \text{Å}^{-1}$ and $\sigma_2 = 0.35\ \text{Å}^{-1}$, respectively, resulting in an asymmetric jump sequence map.

4.2.1.5 Statistical analysis of the configurational residence times

Based on the grid of the 6400 z(x,y,t) time series, recorded with 10 mV and 100 pA, which is shown in Figure 4.13f and Figure 4.5e we have analyzed the residence times of the rotor in the different configurations. For this analysis we have considered all time series with directionality larger than 80% (a total of 1382) shown by the yellow markers in Figure 4.14a. The criterion on the directionality has been chosen to select $z_T(t)$ with sufficiently reliable automatic rotation detection.

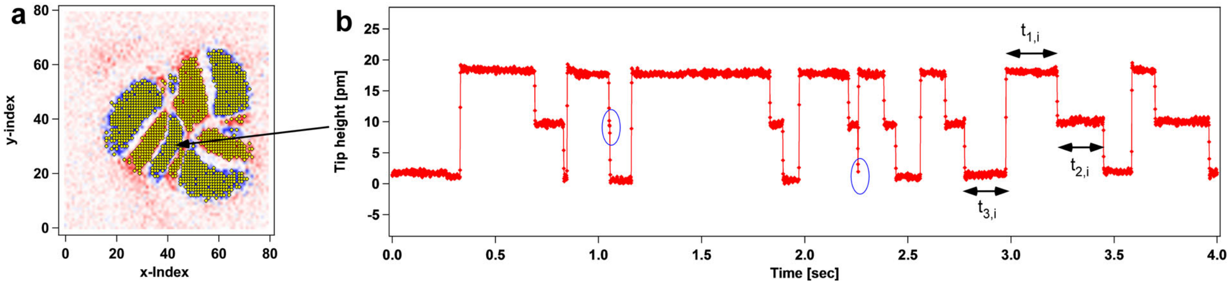

Figure 4.14 | Illustration of difficulties in automatized jump sequence map analysis

a Jump sequence map with the yellow markers denoting the positions of the $z_T(t)$ time series considered for the statistical analysis. **b** z(t) at the position marked by the arrow.

The $z_T(t)$ sequence shown in Figure 4.14b illustrates the difficulty of the automatic rotation detection. For this sequence the algorithm has detected 20 CCW and 2 CW jumps resulting in a directionality of 91%. However, closer inspection of the CW jumps, marked by the blue ellipses in Figure 4.14b, visualizes that these are very short double jumps in the CCW direction. This means there are in fact 24 CCW and 0 CW rotations with a directionality of 100%.

Analysis of the 26295 rotation events shows the following distribution of the residence time for the different rotation states.

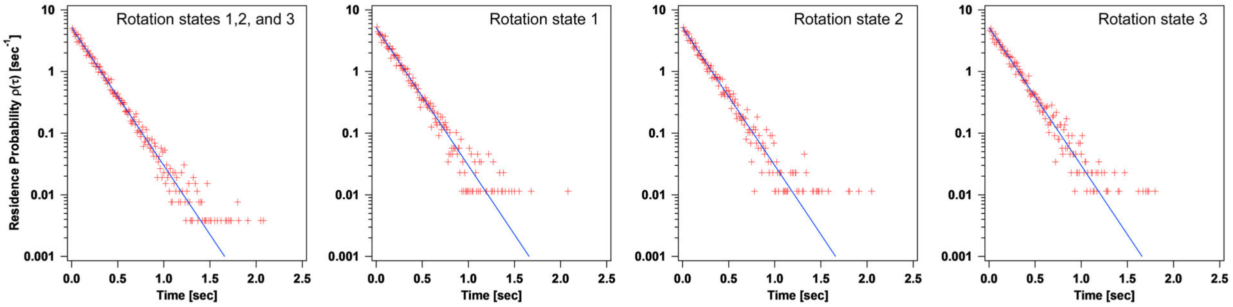

Figure 4.15 | Residence times of the three rotation states

Residence probability distribution for all rotation states combined and individual. The blue solid line in Figure 4.15 corresponds to $\rho(\tau) = \lambda^{-1}\exp(-\tau\lambda^{-1})$ with λ=0.194 sec denoting the rotation time constant

Figure 4.15 proves that the residence or persistence times in the different rotation states follow the same Poisson process distribution with the same time constant. The rotation events are therefore independent stochastic processes with a homogenous differential probability $d\rho = -\lambda^{-1}\rho d\tau$. The mean frequency for this tip condition is $\nu = \frac{1}{\lambda} = 5.15\ Hz$.

As shown in Figure 4.16, we find a weak dependence of the time constant with the tip position, where rotation frequency decreases from approx. 6.2 Hz in the center of the motor to 4.5 Hz at a distance of 4 Å from the center.

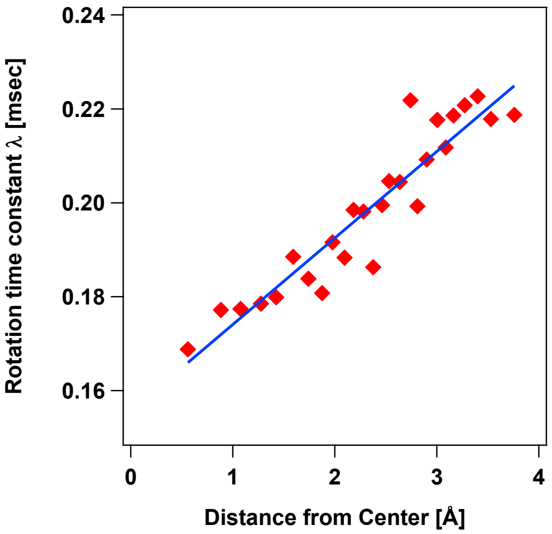

Figure 4.16 | Residence time as function of distance from rotation center

Rotation time constant λ as a function of the distance from the center.

4.2.1.6 Langevin dynamics of the rotation

To describe the motion of the C_2H_2 in the classical regime we rely on the Langevin rotational equation of motion in an asymmetric saw-tooth potential with a period of ${}^{\pi}/_{3}$.

$$I\ddot{\phi} = -T_n - \lambda\dot{\phi}$$

Equation 4.3 | 1-dimensional Langevin rotational equation for a saw-tooth potential

Where I denotes the moment of inertia ($I = 5.62 * 10^{-46}\ kgm^2$ for C_2H_2 in our case), T_n the restoration torque (with $n = \{CW, CCW\}$) and λ_v the dissipation coefficient.

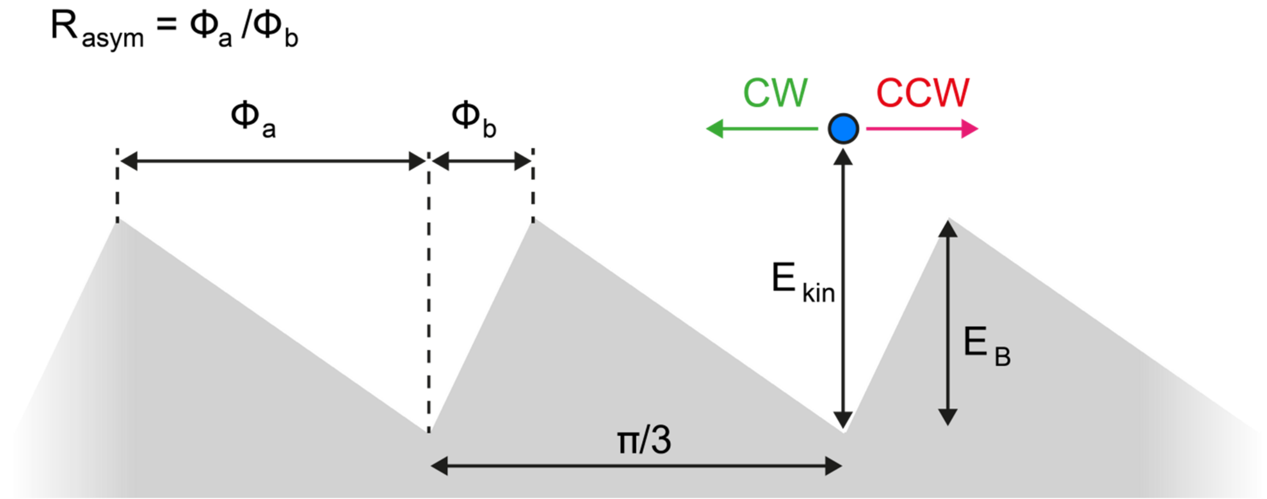

Figure 4.17 | Saw-tooth potential
Schematic representation of the rotational motion in an asymmetric saw-tooth potential.

Due to the asymmetry of the potential, the particle moving with a certain kinetic energy will experience a different restoration torque if it moves left or right, $T_{CW} = \frac{E_B}{\phi_a}$ and $T_{CCW} = \frac{E_B}{\phi_b}$, respectively. Equation 4.3 has the following general solution

$$\phi(t) = -\frac{A}{B}t + c_1\frac{\exp(Bt)}{B} + c\_2$$

With $A = -\frac{E_B}{\phi_a I}$ for moving left and $A = -\frac{E_B}{\phi_b I}$ for moving right and $B = -\frac{\lambda_v}{I}$.

For a given initial kinetic energy E_{kin} and assuming a starting position at rest in the minimum of the potential well $\phi(0) = 0$ we find $\dot{\phi}(0) = \sqrt{{2E_{kin}}/{I}}$, $c_1 = \dot{\phi}(0) + \frac{A}{B}$ and $c_2 = -\frac{c_1}{B}$.

The time of the molecule to travel to the extreme extend is then given by $\dot{\phi}(t_{ex}) = 0$ and yields

$$t_{ex} = \frac{1}{B}\ln(\frac{A}{Bc_1})$$

The condition that the particle will jump to the next well is then given by $\phi(t_{ex}) > \phi_a\ or\ \phi_b$. he relations $\phi\left(t_{ex}\left(E_{kin}^{CW}\right)\right) = \phi_a$ and $\phi\left(t_{ex}\left(E_{kin}^{CCW}\right)\right) = \phi_b$ yield the minimum initial kinetic energy for a clock-wise rotation E_{kin}^{CW} and counter-clockwise rotation E_{kin}^{CCW}. These energies depend on I, E_B, R_{asym} and λ_v as shown in Figure 4.6d.

4.2.1.7 Modelling the voltage-temperature dependent rotation frequency and directionality

Like for many other molecule manipulations using STM (several listed in Ref.[200]), we can induce rotations via inelastic tunneling electrons (IET), although we have no direct proof of C_2H_2 to exhibit any vibration or libration mode in the relevant energy range. Our model is similar to "action spectroscopy" proposed by Kim *et al*,[200] but they never discussed how this might lead to directed motion.

We simply assume, that the transferred energy from electron to molecule must be at least E_L to overcome the steeper potential barrier of the ratchet potential and $E_R > E_L$ to overcome the other potential barrier. We assume the probability to overcome the potential barrier on the steeper p_L or shallower p_R side to be an error function

$$p_{L/R}(V) = c * \left(\frac{1}{2} + \frac{1}{2}\text{erf}\left(\frac{|V| - E_{\frac{L}{R}}}{\alpha}\right)\right)$$

With α describing the broadening of the error function due to non-zero temperature or electric noise of the STM and c the probability that an IET transfers enough energy for a tunneling event to occur. The IET induced frequency ν_L and ν_R in either direction is determined by

$$\nu_{L/R}(V) = \int_0^V cN_{IET}\left(\frac{1}{2} + \frac{1}{2}\text{erf}\left(\frac{|V'| - E_{L/R}}{\alpha}\right)\right) dV'$$

Where N_{IET} is the number of electrons tunneling between tip and sample per second. In order to compare this model to the experimentally determined rotation ν_{exp} we assume all, tunneling frequency ν_{Tunnel}, thermally induced frequency ν_{Therm}, and IET activated frequencies $\nu_{R/L}$, to be additive

$$\nu_{Exp}(V,T) = \nu_{Tunnel} + \nu_{Therm}(T) + \nu_L(V,T) + \nu_R(V,T)$$

and the directionality dir to be described by

$$dir(V,T) = \frac{0.98\nu_{Tunnel} + \nu_L(V,T) - \nu_R(V,T)}{\nu_{exp}}$$

Considering the experiment series performed at different temperatures, but all with $I_T = 100\,pA$, thus $N_{IET} = 6.2 * 10^{11}\frac{e^-}{s}$, we find $c = 2.7 * 10^{-12}$ to be temperature independent, but α to increase from $\alpha_{5K} = 3.1\,meV$ at 5 K to $\alpha_{19K} = 3.6\,meV$ at 19 K. Furthermore, we determine $E_L = 39\,meV$ and $E_R = 43.75\,meV$ at 5 K, which, when compared to the Langevin dynamics for a ratchet potential barrier with $\Delta E_B = 25\,meV$ barrier height, results in a ratchet asymmetry $R_{asym} \approx 1.25$ and a dissipation $\lambda = 1.6 * \frac{10^{-33}kgm^2}{s}$. E_L and E_R decrease with increasing temperature, but while this leads to only marginal variations in R_{asym} for all temperatures between $1.25 < R_{asym} < 1.5$, λ decreases from $\lambda_{5K} = 1.6 * 10^{-33}\frac{kgm^2}{s}$ at 5 K to $\lambda_{20K} = 1.1 * 10^{-33}\frac{kgm^2}{s}$ at 20 K, as seen in Figure 4.6e.

4.2.1.7.1 Applying a modulation voltage

The presented model can further be extended to take into account a modulation voltage V_{mod}, which in our case is sinusoidal $V_{mod} = V_0 sin(f_{mod}t)$ with a modulation frequency f_{mod}. If we assume the $I_T(t)$ curve to be recorded for much longer times than $^1/_{f_{mod}}$, we can approximate the voltage distribution V_{dist} of V_{mod} to be

$$V_{dist}(V) = \sin^{-1}\frac{V}{V_0}$$

and the resulting voltage dependence of the rotation frequency $\nu_{mod_{L/R}}$ by the convolution of $V_{dist}(V)$ and $\nu_{R/L}$

$$\nu_{mod_{L/R}}(V) = \int V_{dist}(V') * \nu_{L/R}(V')dV'.$$

The model of how to treat the modulation voltage leads to a reasonable fit with experimental data as presented in Figure 4.18, and thus excluding electrical noise from STM to be driving the rotation in the tunneling regime.

Another, simpler approach to predict the influence around the onset of the IET induced rotation frequencies, is to take into consideration that V_{mod} around the onset only influences the rotation frequency if the absolute value of the total voltage $|V_{tot}| = |V_{Gap} + V_{mod}|$ increases. Therefore, estimating the mean value $\overline{V}_{mod}$ of all values of V_{mod} which increase $|V_{tot}|$ is enough to describe the influence of V_{mod} on the rotation frequency around the aforementioned onset (the onset is then shifted by $\overline{V}_{mod}$ towards lower bias voltages). In case of $V_0 = 10\ mV$ we find

$$\overline{V}_{mod} = \frac{\int_0^{\pi} \sin(\frac{V}{V_0}) dV}{\int_0^{\pi} dV} = \frac{2}{\pi} V_0 = 6.4 meV$$

corresponding well, to what we observe experimentally, as indicated by the black lines in Figure 4.18.

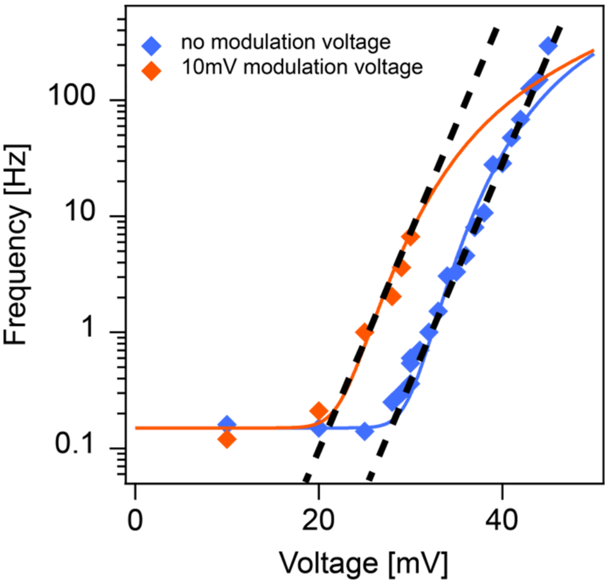

Figure 4.18 | Modelling voltage dependence of rotation frequency

Rotation frequency dependence on bias voltage if no modulation voltage (orange) or 10 mV sinusoidal modulation voltage (blue) is applied. The markers represent the experimentally determined rotation frequencies, while the solid lines are derived using equation for $\nu_{mod_{R/L}}$. The dashed lines indicate the increase of ν for each curve, which is shifted by 6.4 mV to lower bias voltage, if a 10 mV sinusoidal modulation voltage is applied.

4.2.1.8 *Influence of finite time resolution on the determination of the directionality*

The probability p_J of acetylene to perform a rotation within the time Δt, i. e. the experimental time resolution, is assumed (and shown in SI chapter 4) to be stochastic, thus independent of any previous events

$$p_J = \nu * \Delta t$$

with ν being the experimental rotation frequency.

We define the probability for a counter-clockwise (CCW) rotation as α, and thus can estimate the probability of a single CCW and clockwise (CW) rotation, p_{CCW} and p_{CW} respectively, within Δt to be $p_{CCW} = \alpha * p_J$ and $p_{CW} = (1-\alpha) * p_J$. The directionality, assuming no jumps missed due to limited time resolution, is given by $dir_0 = \frac{p_{CCW}-p_{CW}}{p_{CCW}+p_{CW}} = 2\alpha - 1$.

Due to the limited time resolution Δt, we cannot neglect the possibility of detecting two CCW rotations as one CW ($p_{2CCW} = \left(\alpha p_J\right)^2$) or vice versa ($p_{2CW} = \left(1-\alpha\right)^2 p_J^2$) and neither the one of detecting a CCW and a CW rotation as none ($p_{CCWCW} = \alpha\left(1-\alpha\right)p_J^2$). Due to all these undetected rotation events, the experimentally determined directionality dir_{exp} differs from dir_0 and can be estimated to be

$$dir_{exp} = \frac{(p_{CCW} - 2p_{2CCW} + p_{CW} - p_{CCWCW}) - (p_{CW} - 2p_{2CW} + p_{CCW} - p_{CCWCW})}{(p_{CCW} - 2p_{CCW} + p_{CW} - p_{CCWCW}) + (p_{CW} - 2p_{CW} + p_{CCW} - p_{CCWCW})} = dir_0 \frac{1-3p_J}{1-p_J(1+2\alpha-2\alpha^2)}$$

As expected, and shown in Figure 4.6d, the experimentally determined directionality decreases with increasing rotation frequency, since the likelihood of missing two jumps in the dominating direction, which are then recorded as one in the minor direction, is much higher than the reverse. In our experiment we find the time resolution to be about 1 ms, which is most likely limited by the feedback loop, needed for any constant current measurements.

The presented model holds true, as long as $\left(\alpha p_J\right)^3 \ll 1$ ($\left(\alpha p_J\right)^3 < 0.001$ in our experiments). If the frequency became larger, one would also have to consider the possibility of missing multiple rotation events.

4.2.1.9 *Determination of the tunnel splitting ΔE_T and the tunnelling frequency ν_{Th}*

For the calculation of the energy splitting of the ground state $|\Psi_{00}>$ we have used the WKB approximation for a double barrier.[201] For simplicity and comparability with the methyl tunnel rotation we have chosen a cosine line shape to represent the rotation potential $V(\phi) = \Delta E_B \cos^2(3\phi)$.

The ground state energy $E_{00} = \hbar\omega_{00}$ is obtained from the numerical solution of the Schrödinger equation of the rotational motion with $V(\phi)$ and the appropriate moment of inertia I. ϕ_a, ϕ_b and ϕ_c denote the angular position, where $V(\phi_i) = E_{00}$ as shown in Figure 4.19.

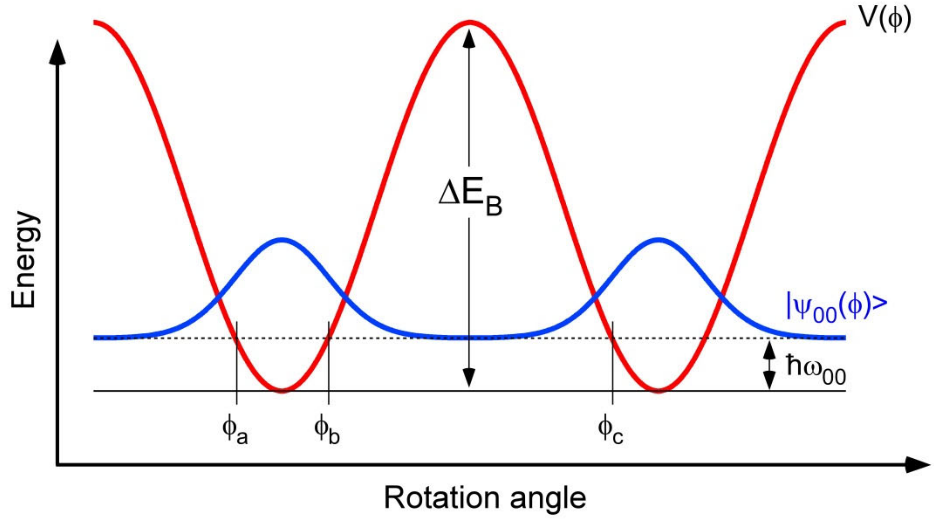

Figure 4.19 | Sketch of potential for tunnelling frequency determination
Schematic representation of the double well tunneling in a cos(f) potential. With the ground state wave function shown in blue.

With the period of oscillation in the ground state given by:

$$\tau_0 = 2I\int_{\phi_a}^{\phi_b} \frac{d\phi}{\sqrt{2I(E_{00} - V(\phi))}}$$

We find for the tunnel splitting:

$$\Delta E_T = \frac{2\hbar}{\tau_0} exp\left[-\frac{1}{\hbar}\int_{\phi_b}^{\phi_c} \sqrt{2I(V(\phi) - E_{00})}d\phi\right]$$

With the tunnel frequency given by: $\upsilon_T = \frac{\Delta E_T}{h}$

Table 4.1 gives the tunneling splitting ΔE_T and tunneling frequency ν_{Th} of the acetylene for its different isotopes and compares them to other systems of tunneling transitions reported in literature.

System	*I* [kgm^2] *m*[kg]	Tunneling distance d_T [Å] or [rad]	ΔE_B [meV]	E_{00} [meV]	ΔE_T [meV]	ν_{Th} [MHz]
C_2H_2 / PdGa	I=5.62e-46	π/3 rad	25	3.58	0.0536	12.96
C_2HD / PdGa	I=6.20e-46	π/3 rad	25	3.42	0.02704	6.538
C_2D_2 / PdGa	I=6.87e-46	π/3 rad	25	3.25	0.0129	3.12
$(CH_3)_6C_6$[63]	I=5.28e-47	2π/3 rad	86.5	10.9	0.0266	6.43
$(CH_3)_2C_2N_2S$[201]	I=5.28e-47	2π/3 rad	101	11.8	0.009	2.17
H/Cu(001)[176]	m=1.672e-27	2.55 Å	197	24.1	0.0355	8.59
D/Cu(001)[176]	m=3.344e-27	2.55 Å	194	17.1	5.22e-5	12.6e-3
H/Pt(111)[184]	m=1.672e-27	1.60 Å	190	36.7	20.8591	5.06e+3
Co/Cu(111)[177]	m=9.86e-26	1.55 Å	37	2.28	8.51e-10	0.2e-6

Table 4.1 | Comparison of tunnelling parameters for different atoms and molecules

Comparison of the tunnelling splitting and tunnelling frequency (assuming a cosine double well in all cases) for different tunnelling transitions.

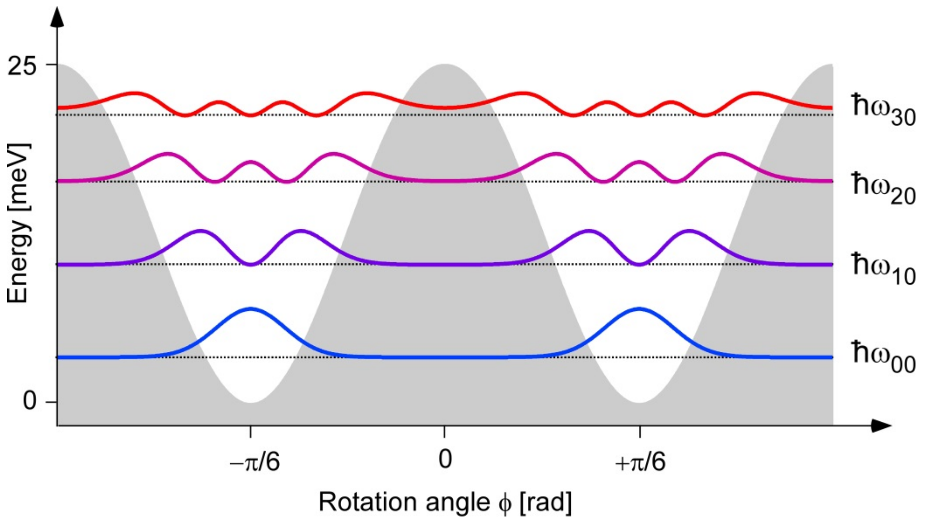

Figure 4.20 | C_2H_2 libration modes

Illustration of the 4 frustrated (bound) libration modes of the C_2H_2 with $\Delta E_B = 25\ meV$. The colored curves denote the probability density $\rho_n(\phi) = < \Psi_{n0}|\phi|\Psi_{n0} >$ of the states n=0,1,2,3.

System	*I* [kgm^2] *m*[kg]	Tunneling distance d_T [Å] or [rad]	ΔE_B [meV]	E_{n0} [meV]	ΔE_T [meV]	ν_{Th} [MHz]
C_2H_2 / PdGa	I=5.62e-46	π/3 rad	25	E_{00}=3.58	0.0536	12.96
C_2H_2 / PdGa	I=5.62e-46	π/3 rad	25	E_{10}=10.44	2.365	571.9
C_2H_2 / PdGa	I=5.62e-46	π/3 rad	25	E_{20}=16.54	43.70	10565
C_2H_2 / PdGa	I=5.62e-46	π/3 rad	25	E_{30}=21.44	327.92	79250

Table 4.2 | Tunneling parameters for C_2H_2 and its isotopes on Pd_3

Tunneling splitting and tunneling frequencies for C_2H_2 and $\Delta E_B = 25\ meV$ for the $n = 0,1,2,3$ frustrated libration modes.

4.2.1.10 Experimental isotope dependence of the tunneling frequency

In order to have an indication that directed tunneling could be the explanation for the observed constant rotation frequency ν_T for $|V_G| \leq 30\ mV$ and $T < 15\ K$, ν_T was determined for C_2D_2, C_2DH and C_2H_2. As discussed in the section "Voltage and current dependence of the rotation frequency in the tunneling regime", the STM tip has a considerable impact on ν_T, therefore a meaningful comparison of ν_T for the different isotopes requires them to be measured with the same tip conditions. Accordingly, all three isotopes had to be accessible within at most 10 nm in the same STM frame (Figure 4.21). Each color of Table Table 4.3 corresponds to one measurement without any tip change in between. While the absolute frequencies vary significantly, the ratios of ν_T is shown to be independent of the polarity of the applied bias voltage and condition of the STM tip (Figure 4.22).

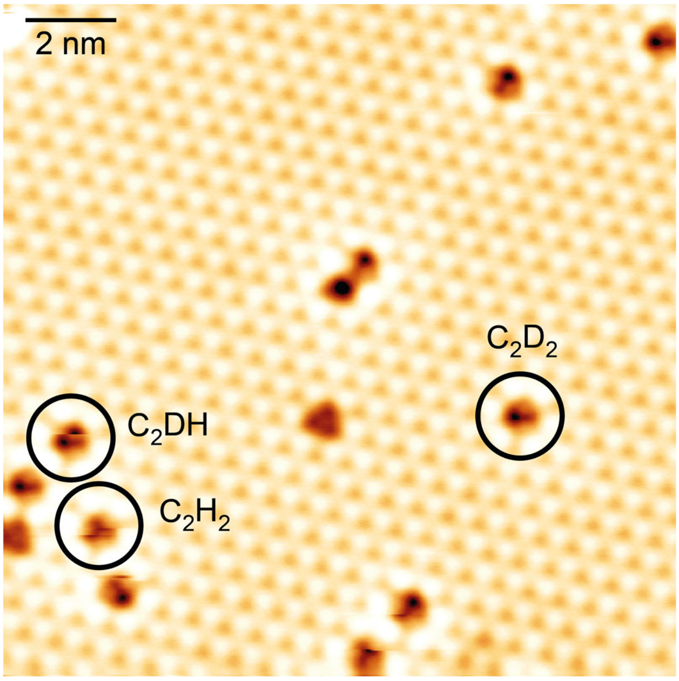

Figure 4.21 | Position of C_2H_2 and its isotopes when determining their tunnelling frequency

STM image of C_2H_2, C_2DH and C_2D_2 adsorbed on Pd₃ ($T = 5\,K, V_G = 20\,mV, I_T = 20\,pA$). The data marked blue in Table 4.3 has been recorded at these three molecules.

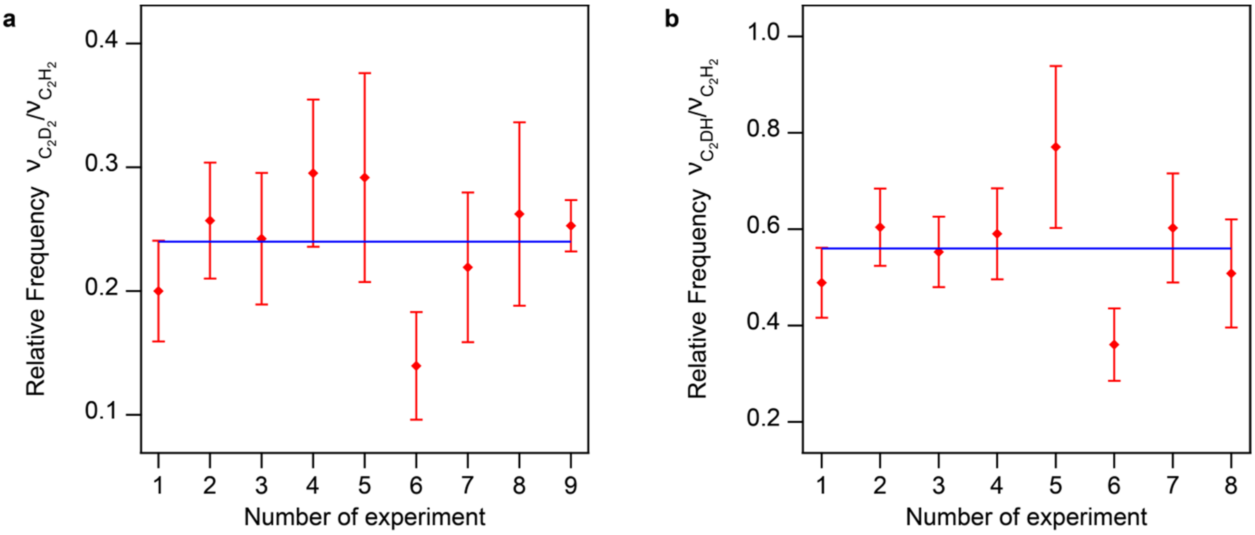

Figure 4.22 | Analysis of relative tunnelling frequency

Relative frequencies for each experiment (red markers) and their average (solid blue line) for both, **a** C_2D_2 and **b** C_2DH, compared to C_2H_2.

Bias	C_2D_2	C_2DH	C_2H_2	Time
-15 mV	0.054 ± 0.010 Hz	0.132 ± 0.016 Hz	0.270 ± 0.023 Hz	500 s
-5 mV	0.074 ± 0.012 Hz	0.174 ± 0.018 Hz	0.288 ± 0.024 Hz	500 s
+5 mV	0.078 ± 0.016 Hz Only 280 s	0.178 ± 0.019 Hz	0.322 ± 0.025 Hz	500 s
+15 mV	0.062 ± 0.011 Hz	0.124 ± 0.016 Hz	0.210 ± 0.020 Hz	500 s
-15 mV	0.028 ± 0.007 Hz	0.074 ± 0.012 Hz	0.096 ± 0.014 Hz	500 s
-5 mV	0.024 ± 0.007 Hz	0.062 ± 0.011 Hz	0.172 ± 0.019 Hz	500 s
+5 mV	0.032 ± 0.008 Hz	0.088 ± 0.013 Hz	0.146 ± 0.017 Hz	500 s
+15 mV	0.032 ± 0.008 Hz	0.062 ± 0.011 Hz	0.122 ± 0.016 Hz	500 s
+5 mV	0.108 ± 0.005 Hz	0.230 ± 0.010 Hz	NaN	5000 s (C_2D_2) 2500 s (C_2DH)
+ 10 mV	0.105 ± 0.006 Hz	0.259 ± 0.011 Hz	NaN	3000 s (C_2D_2) 2000s (C_2DH)
+5 mV	0.068 ± 0.005 Hz	NaN	0.269 ± 0.010 Hz	2500 s

Table 4.3 | Experimentally determined tunneling frequencies

Tunneling frequencies measured for all, C_2D_2, C_2DH and C_2H_2. The measurements taken without any change in the STM tip are marked with the same color in the most left column.

5. PdGa – template for enantioselective heterogeneous catalysis

5.1 Asymmetric catalysis

The homochiral structure of a large number of biomolecules like amino acids, sugars, or DNA, is a very pronounced feature of living systems and the origins of this chiral bias is still being unraveled.[7,202,203] Not surprisingly, the physiological consequences of this homochirality can be drastic if chiral biomolecules (*e.g.* olfactory proteins) interact with equally chiral molecules. As an everyday example, the odor perception of chiral limonene depends on its enantiomeric form. In particular, the enantiomeric form which is abundant in citrus oils and smells like oranges, whereas the other one appears in conifer needles and smells like turpentine.[204] Such enantiospecific physiological effects of chiral molecules are not just limited to flavors, but are of paramount relevance also, *e.g.*, in the pharmaceutical or agricultural industry and necessitate enantioselective synthesis.

Today, homogeneous catalysis is the most widely employed method to achieve such asymmetric synthesis, whereby the chirality of the catalyst is directly transferred form the catalyst's organic ligand(s) to the reactants. However, homogeneous catalysis entails tedious separation of the catalyst and the product being present in the same phase, elaborate recycling of the catalyst, and is restricted to a limited temperature range.[5,6,205] To alleviate these difficulties, different approaches based on heterogeneous catalysis have been designed, including metal organic frameworks, immobilized homogeneous catalysts, achiral metal surfaces rendered chiral by adsorbing enantiopure molecules, and intrinsically chiral metal surfaces.[5,6,205–209,8,9]

Despite these various approaches, heterogeneous asymmetric catalysis has been hampered because of the hitherto trial-and-error based approach used in their development. To overcome this obstacle, rational engineering of heterogeneous enantioselective catalysts requires a fundamental understanding of enantiospecific reaction mechanisms, kinetics, and interactions between catalyst, precursor molecules, intermediates, and reaction products. In order to achieve such insight into the fundamental processes, moving to idealized conditions, *i.e.*, using single crystal surfaces in ultra-high vacuum (UHV) can prove to be highly beneficial.[210,211]

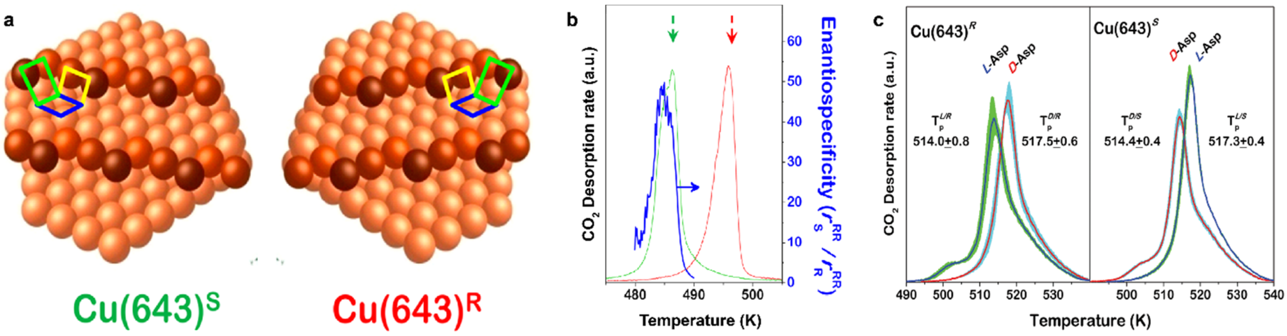

Figure 5.1 | Enantioselective decomposition reactions on chiral copper surfaces

a Atomic surface structure of the two enantiomorphs, R and S, of the Cu(643)^{R,S} surfaces. The chirality emerging from the kink sites is highlighted by green, blue, and yellow rectangles. **b** recorded CO$_2$ desorption arising from the decomposition of S,S-tartaric acid on the Cu(643)^S (green) and Cu(643)^R (red) surfaces. In blue, the enantiospecifity, *i.e.*, the ratio between the CO$_2$ desorption signal from the Cu(643)^S and Cu(643)^R of the reaction is depicted. **c** CO$_2$ desorption rate due to the decomposition of L- and D-aspartic acid (L-Asp and D-Asp, respectively) from the Cu(643)^R (left) and Cu(643)^S (right) surfaces. The Figures are adapted from Ref.[212,213]

In this respect, due to the largely unexplored realm of intrinsically chiral metal surfaces, most studies have focused on modifying achiral surfaces with enantiopure organic molecules.[7–14] However, low thermal stability of such systems in combination with increased complexity arising from the additional molecule-molecule interactions have limited the applicability of this approach to a few enantioselective decomposition reactions.[11–13] The complexity of these emerging molecule-molecule interactions was demonstrated by McBreen and co-workers by co-adsorbing one chiral modifier (1-(1-naphthyl)ethylamine (NEA)) and one prochiral reagent (2,2,2-trifluoroacetophenone (TFAP)) on a Pt(111) surface (prochiral molecules: achiral, but when confined to a planar orientation appears in two distinguishable surface enantiomers).[16] After co-adsorption of the two molecules, they identified five of the emerging eleven molecular assemblies consisting of exactly one of the chiral and one of the prochiral as the preferred molecular arrangements (Figure 5.2).

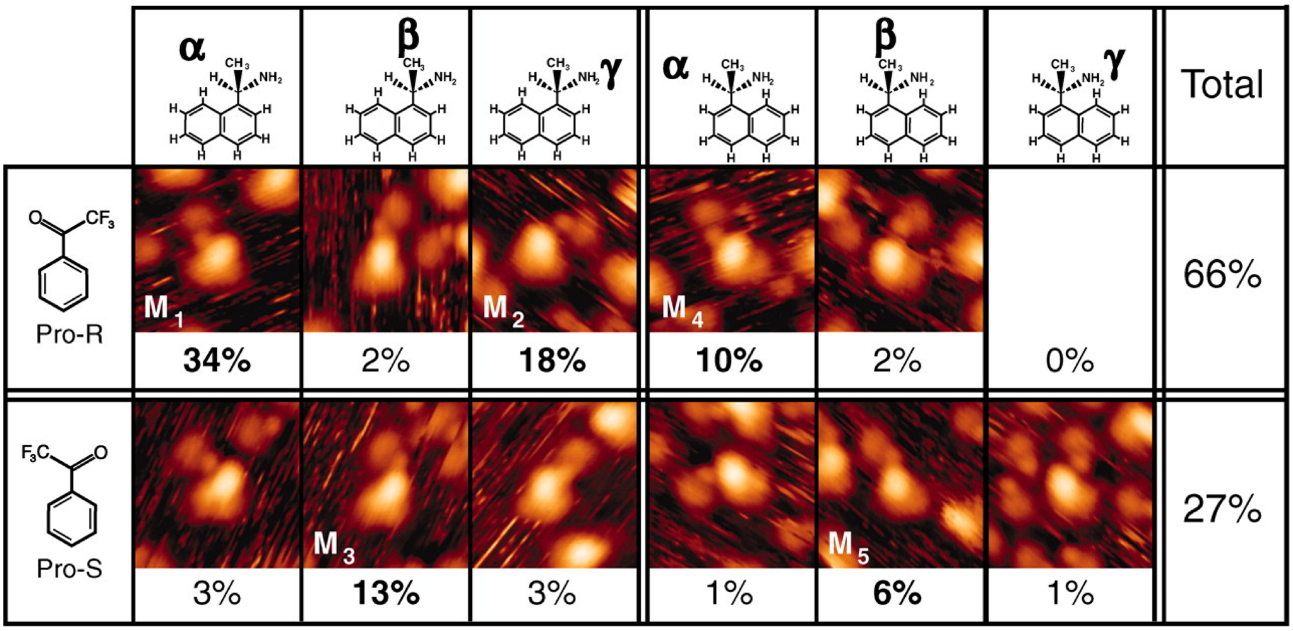

Figure 5.2 | Complexity arising from molecule-molecule interactions

The classification of modifier-substrate complexes formed by (R)-NEA and TFAP on Pt(111) at room temperature. The percentages represent the total complex population.

The application of chiral, well-defined metal surfaces to investigate the fundamental processes in enantioselective adsorption and reaction processes is promising to improve the thermal stability, while simultaneously decreasing the complexity of the interactions. A possibility to obtain such chiral surfaces from achiral crystals is cutting them along low-symmetry, *i.e.*, high Miller index directions.[214,215] The resulting surfaces possess chiral centers at the kink sites of their step-edges, as indicated in Figure 5.1a.[214,215] Although these terraced kinked surfaces exhibit a low density of chiral centers, Gellman and co-workers evidenced their chiral recognition to be strong enough for aspartic and tartaric acid to achieve enantioselective autocatalytic decomposition on Cu(643)$^{R/S}$ (Figure 5.1b-c).[212,213]

However, enantioselective on-surface synthesis has to our best knowledge not yet been reported so far. Even though there are reports of homochiral graphene nanoribbons, where these molecular structures were grown from achiral molecular precursors on achiral surfaces. As a consequence, the two enantiomers of such homochiral graphene nanoribbons were created with equal abundance.[216–218] The only enantioselective creation of prochiral molecules we are aware of has been achieved by Starý and co-workers by reducing the complexity of the enantiopure benzo[2,1-g:3,4-g']dichrysene (dibenzo[I,o]heptahelicene) (DBH) deposited on a Ag(111) surface from helical to planar chirality via a Diels-Alder [4+2] cycloaddition.[92]

A very significant limiting factor for the realization and in-depth investigation of asymmetric on-surface synthesis has been the lack of atomically-flat, bulk-truncated surfaces of intrinsically chiral metallic crystals. In this context, the surfaces of the non-centrosymmetric intermetallic compound PdGa constitutes a new opportunity to accomplish enantioselective coupling reactions. In the chapters 5.2, 5.4, and 5.5, three asymmetric reactions of different complexity, which have been performed on the PdGa{111} surfaces, are presented. In chapter 5.3, we discuss the analysis procedure of TP-XPS data that has been applied in chapter 5.2 by means of evidencing reversibility of the debromination process in aryl-aryl coupling on Au(111).

5.2 Publication (in preparation): "Enantioselective debromination on chiral metal surfaces"

I co-organized and supervised the measurements acquired at the PEARL beamline, which was a collaborative work of at least six people. Moreover, I designed and performed the STM and nc-AFM experiments and analyzed all experimental data. I wrote the manuscript with input from allco-authors.

Enantioselective debromination on chiral metal surfaces

Samuel Stolz,[†‡] Martina Danese,[†] Marco Di Giovannantonio,[†] José I. Urgel,[†] Qiang Sun,[†] Amogh Kinikar,[†] Max Bommert,[†] Shantanu Mishra,[†] Harald Brune,[‡] Oliver Gröning,[†] Daniele Passerone[†] and Roland Widmer*[†]

†Nanotech@surfaces Laboratory, Empa – Swiss Federal Laboratories for Materials Science and Technology, Überlandstrasse 129, CH -8600 Dübendorf, Switzerland

‡Institute of Physics, École Polytechnique Fédérale de Lausanne, CH-1015 Lausanne, Switzerland

* roland.widmer@empa.ch

Asymmetric heterogeneous synthesis requires enantiospecific modifications of the reaction kinetics that result, for instance, in the enantioselective dissociation of functional groups. Here, enantioselective dissociation has been studied by investigating the debromination reaction of 5-Bromo-7-Methylbenz(a)anthracene (BMA) on chiral PdGa{111} intermetallic surfaces under ultrahigh vacuum (UHV) conditions. We combine temperature programmed x-ray photoelectron spectroscopy, scanning probe microscopy and density functional theory to arrive at a detailed picture of the reaction kinetics. The BMA surface enantiomers are demonstrated to exhibit differences in their debromination temperatures of up to exceptional 46 K on the PdGa{111} surfaces. Moreover, we identify a significant ensemble effect in the PdGa system, which manifests itself in the preferential debromination of the opposite BMA enantiomeric form on the Pd_1- as compared to the Pd_3-terminated PdGa{111} surface of the same PdGa enantiomorph. These findings allow valuable insights into chiral recognition of BMA on the PdGa{111} surfaces and evidence enantiospecific control in the pivotal first reaction step for several on-surface reactions like dehalogenative aryl-aryl coupling, Sonogashira coupling, and Heck reaction. Hence, the possibility of highly enantioselective on-surface synthesis with prochiral reactants under UHV conditions can be envisioned.

On-surface synthesis under ultra-high vacuum (UHV) conditions emerged as valuable method to grow hitherto unattainable and atomically precise molecular structures in a bottom-up approach by profiting from a well-defined environment, dedicated molecular precursors and well-characterized single crystal surfaces.[219] In recent years, the variety of successfully demonstrated on-surface reactions increased significantly, whereof several include aryl halides.[219–222] In particular, dehalogenative aryl-aryl coupling emanated as the most controllable reaction with versatile applications ranging from dimerizations[33,34] to the growth of polymeric chains,[36,37,223] graphene nanoribbons,[38,40,41,219,224] and 2D organic frameworks.[34,225,226] However, none of these reports emphasizes the achievement of enantioselective coupling reactions, which are of utmost importance in, *e.g.*, pharmaceutics, agricultural, optical or food industry. Enantioselectivity in on-surface synthesis such as Ullmann-like coupling (dehalogenative aryl-aryl coupling), but also in Sonogashira coupling or Heck reaction can for instance be initiated via an enantiospecific dissociation of functional groups, particularly as dehalogenation, of reactants on a surface with chiral reaction centers.

Due to the lack of intrinsically chiral, catalytically active and well-characterized single crystal surfaces, considerable effort has been devoted to obtain chiral surfaces from achiral crystals. This is usually accomplished either by rendering or templating their surfaces chiral via the adsorption of enantiopure chiral molecules,[11–14] or by cutting them along low-symmetry directions.[214,215] Both techniques exhibit substantial drawbacks, most notably deficiency in thermal and chemical stability for the former, and low density of chiral centers in combination with a limited applicability primarily to basic research for the latter approach. Nonetheless, enantioselective decomposition reactions were achieved with both strategies.[12,212] To the best of our knowledge, the only attempt to achieve on-surface enantioselective dehalogenation was performed by Rampulla *et al.*[227,228] However, they could only indirectly deduce indications for enantioselective debromination of the chiral alkyl halides, S-1-bromo-2-methylbutane and R-2-bromobutane, on kinked Cu surfaces from a non-zero enantiomeric excess of up to 8% in the desorption of alkyls.[227,228]

Here, we make use of low-Miller index surfaces of the intrinsically chiral, catalytically active intermetallic compound PdGa with 1:1 stoichiometry to obtain enantioselective debromination.[25] Owing to its non-centrosymmetric space group $P2_13$, PdGa exists in two enantiomorphs PdGa:A and PdGa:B, and all its bulk-truncated surfaces are chiral.[54] We focus on the two structurally different, three-fold symmetric PdGa{111} surfaces: PdGa:A(-1-1-1)Pd_3 (denoted as A:Pd_3), which possesses isolated Pd timers as top layer (Figure 5.3a), and PdGa:A(111)Pd_1 (denoted as A:Pd_1), whose terminating layer consists of single, isolated Pd atoms (Figure 5.3b).[229] Owing to their structural dissimilarity, which is combined with an identical symmetry group, the same lattice parameter, and similar electronic properties, the PdGa{111} surfaces are excellent candidates to separate the impact of the geometric and electronic effects, *i.e.*, ensemble and ligand effect, in enantioselective heterogeneous catalysis.[45]

The chiral recognition of both PdGa{111} surfaces has been demonstrated to manifest itself in highly enantioselective adsorption or the near-enantiopure trimerization of 9-Ethynylphenanthrene (9-EP),[26,27] which, due to its prochirality, appears in two enantiomers R and S when confined to a surface.

Having established strong chiral recognition of 9-EP on the PdGa{111} surfaces, although expressed in two dissimilar manners, we progress by investigating and comparing the surfaces' enantioselective reactivity by means of thermally triggered debromination of prochiral 5-Bromo-7-Methylbenz(a)Anthracene (BMA; Figure 5.3c). Compared to 9-EP, BMA possesses a similar aromatic backbone but a different functional group (bromine vs. alkyne) and an additional methyl group. Like 9-EP, BMA is a prochiral molecule, and hence adsorbs in two discernible enantiomeric forms. Enantioselectivity in the thermally triggered dissociation of functional groups is experimentally expressed in different dissociation temperatures for the two surface enantiomers. We determine this temperature difference of the debromination of BMA by combining temperature programmed x-ray photoelectron spectroscopy (TP-XPS),[59,62,68] scanning tunneling microscopy (STM), non-contact atomic force microscopy (nc-AFM) with CO functionalized tips, and density functional theory (DFT) on chiral PdGa{111} and – as control experiment – on achiral Au(111), where no enantioselective debromination is expected.

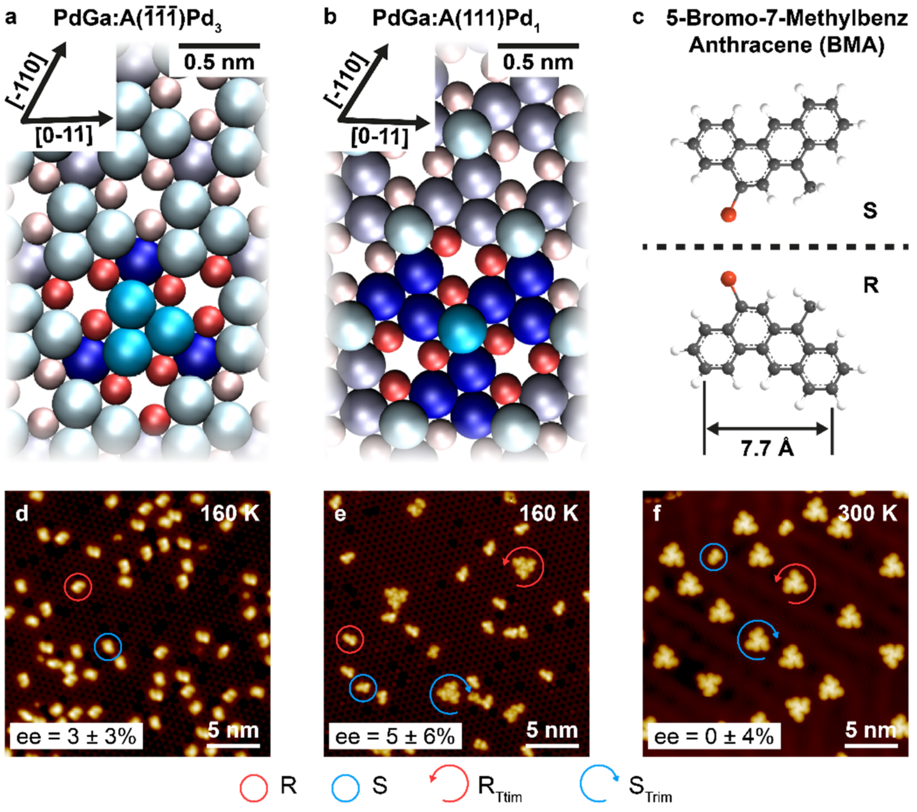

Figure 5.3 | Model systems for enantioselective debromination

Surface structure of **a** the PdGa:A(-1-1-1)Pd_3 surface (1st layer Pd_3 in bright blue: z = 0 pm; red 2nd layer Ga_3 in red: z = -85 pm; 3rd layer Pd_1 in dark blue: z = -161 pm) and **b** the PdGa:A(111)Pd_1 (1st layer Pd_1 in bright blue: z = 0 pm; 2nd layer Ga_3 in red: -57.4 pm ; 3rd layer Pd_3 in dark blue: -149.8 pm). The chirality of both surfaces is highlighted with one Pd trimer in case of PdGa:A(-1-1-1)Pd_3 and one Pd atoms for PdGa:A(111)Pd_1 and their neighboring Pd and Ga atoms in subjacent layer in saturated colors. **c** Molecular structure of BMA in its S (top) and R (bottom) surface enantiomeric form. STM images of BMA on **d** PdGa:A(-1-1-1)Pd_3 (V_{Bias} = 50 mV; I_T = 50 pA) , **e** PdGa:A(111)Pd_1 (V_{Bias} = -50 mV; I_T = 100 pA) and **f** Au(111) (V_{Bias} = -50 mV; I_T = 200 pA) deposited on the substrate held at the temperature indicated in the top right corner.

Before discussing the debromination process in detail, we want to clarify the conditions under which BMA remains intact, *i.e.*, brominated, and determine the corresponding enantiomeric excess ($ee_{Mono} = 100\% * \frac{|\#R - \#S|}{\#R + \#S}$) in the brominated state. Specifically, BMA molecules deposited on Au(111) between 160 K and 300 K remain brominated and mainly assemble without enantiomeric excess into homochiral trimers, which appear in same amounts with a clockwise and counter-clockwise sense of rotations (Figure 5.3f, Figure 5.9). On the other hand, BMA has to be deposited below 160 K on the Pd_3- and Pd_1-terminated PdGa{111} surfaces to avoid debromination (Figure 5.3d-e).

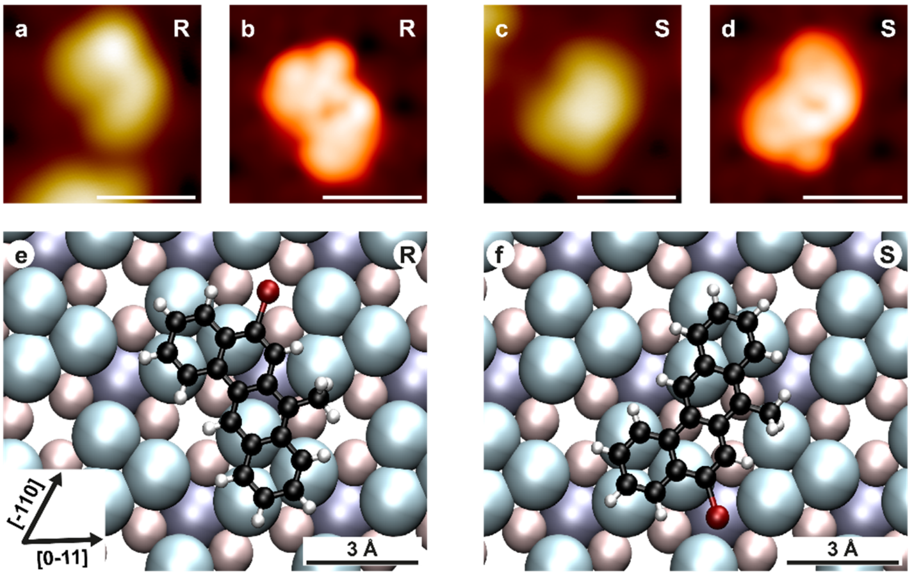

Figure 5.4 | Enantiospecific BMA adsorption on PdGa:A(-1-1-1)Pd_3

Experimental STM image (V_{Bias} = -50 mV, I_T = 200 pA) of **a** R and **c** S BMA/PdGa:A(-1-1-1)Pd_3 surface enantiomers with the respective DFT simulated STM images in **b** and **d** and the adsorption configurations in **e**-**f**. The experimentally determined adsorption configurations are in agreement with the most stable ones from DFT. All scale bars correspond to 1 nm if not labelled differently.

On the Pd_3-terminated PdGa{111} surfaces, BMA molecules deposited at 160 K appear solely as monomers (Figure 5.3d). They adsorb in two distinct configurations, which are present in three rotationally symmetric equivalent geometries. The STM signature of both BMA configurations resembles a trapezoid, which is mirrored for one configuration with respect to the other (Figure 5.10). Consequently, the two configurations are assigned to R and S enantiomers, which is corroborated with DFT based STM simulations (Figure 5.4). The two BMA surface enantiomers form a racemic mixture, *i.e.*, $ee_{Mono} = 3\% \pm 3\%$ (Figure 5.3d), although their adsorption geometries strongly differ with respect to the atomic layers subjacent to the Pd_3 top layer. The experimental adsorption site was determined from the STM images by extrapolating the atomic corrugation of the PdGa surface to the molecule position. In particular, the bromine atom of R BMA/A:Pd_3 is located in the hollow site of a second layer Ga trimer and benz(a)anthracene covers a Pd atom of the third layer, as displayed in Figure 5.4e. In contrast, for S BMA/A:Pd_3 the bromine atom is situated atop a third layer Pd atom and benz(a)anthracene covers a second layer Ga trimer, as shown in Figure 5.4f. These two strongly dissimilar adsorption geometries are the energetically most stable ones, also according to DFT simulations, yielding their adsorption energies to be E_{Ads_R} = -2.827 eV and E_{Ads_S} = -2.866 eV for the R and S enantiomers, respectively (Figure 5.12, Table 5.1).

On the Pd_1-terminated PdGa{111} surfaces, BMA molecules deposited at 160 K appear in seven different configurations, five of which are isolated BMA monomers that occur in three rotationally symmetric equivalent geometries, and two are homochiral BMA assemblies appearing as trimers (Figure 5.3e). Here, we focus on the discussion of the two experimentally most frequent monomer configurations (Figure 5.5), whose cumulative abundance amounts to 75%. The remaining BMA configurations are discussed in the Supporting Information. Similarly to the Pd_3-terminated PdGa{111} surfaces, the two most abundant BMA monomers on the Pd_1-terminated PdGa{111} surfaces exhibit a trapezoid-like shape, with opposing chirality, when imaged with STM (Figure 5.11). Accordingly, the two configurations are again assigned to R and S enantiomers, which is consistent with comparison to DFT simulations and corroborated by nc-AFM measurements (Figure 5.5a-h). Like on Au(111) and A:Pd_3, R and S BMA enantiomers are present in a racemic mixture ($ee_{Mono} = 5\% \pm 6\%$, Figure 5.3e) on A:Pd_1. For both, R and S enantiomers, the bromine atom lies atop a top-layer Pd atom and the benz(a)anthracene moiety above a second layer Ga trimer (Figure 5.5i-j). Due to the surface chirality, the position of the outermost phenyl rings of the benz(a)anthracene unit slightly differ with respect to the second layer Ga and third layer Pd trimers. According to DFT calculations, the adsorption energy of the R and S BMA enantiomers (E_{Ads_R} = -2.375 eV and E_{Ads_S} = -2.363 eV) differ by only 12 meV. Furthermore, DFT identifies four additional, isoenergetic adsorption configurations for BMA monomers. Of these four configurations, we only observe three with STM with low frequency, which is a discrepancy between experiment and DFT calculations that probably arises from the limited accuracy of the non-local corrections in DFT, which have been reported to decisively influence the adsorption energies of molecules adsorbed on the Pd_1-terminated PdG{111} surfaces.[230]

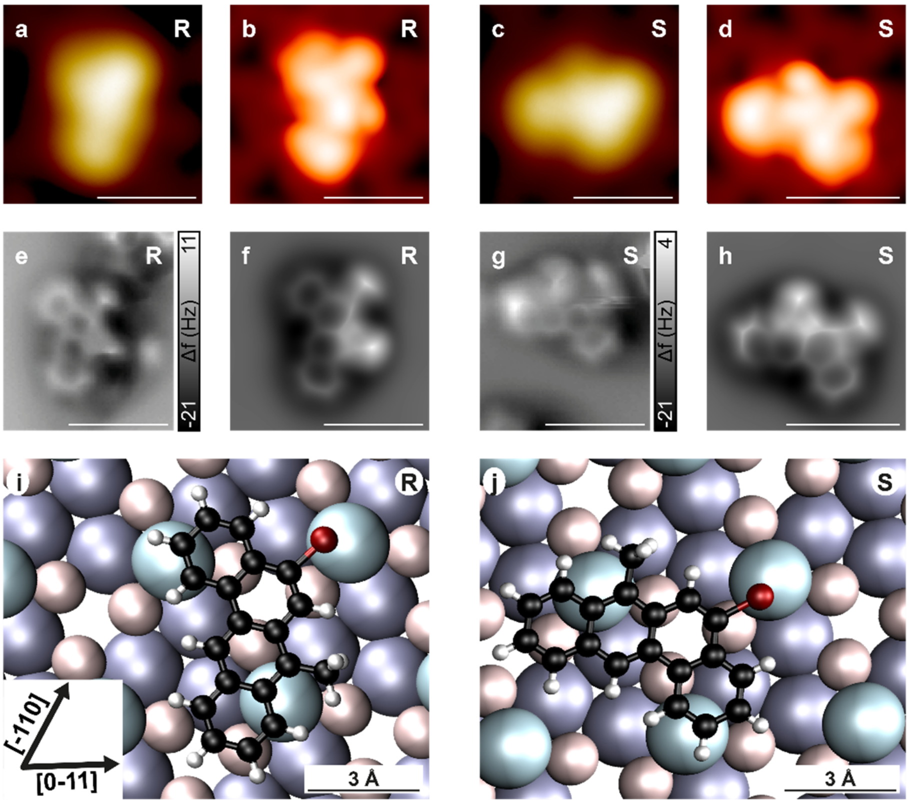

Figure 5.5 | Enantiospecific BMA adsorption on PdGa:A(111)Pd_1

Experimental STM image (V_{Bias} = -50 mV, I_T = 200 pA) of the most abundant **a** R and **c** S BMA/PdGa:A(111)Pd_1 enantiomers with the corresponding nc-AFM images in **e** and **g**. DFT simulated STM images of **b** R and **d** S BMA/PdGa:A(111)Pd_1 enantiomers and the respective simulated nc-AFM images in **f** and **h**. **i, j** The relaxed adsorption configurations for the R and S BMA enantiomers on Pdga:A(111)Pd_1, which correspond to the experimentally determined ones. All scale bars correspond to 1 nm if not labelled differently.

Having established BMA to appear as racemic mixture on all three surfaces, the dynamics of BMA debromination is investigated using TP-XPS by gradually increasing the temperature for a molecule coverage close to one monolayer. The chemical transformations of BMA reflected in the TP-XPS maps in Figure 5.6a-c are the same for all three substrates. First, bromine detaches from the molecule and chemisorbs on the substrate, expressed in a distinct chemical shift of the Br 3d doublet to lower binding energies. Second, bromine desorbs, resulting in an overall intensity decrease of the Br 3d signal. Highlighted by the kinetic curves (Figure 5.6d; derived from the respective TP-XPS map as described in Figure 5.8) for both chemical states of bromine - bromine attached to molecule (Br-C) and bromine chemisorbed to the substrate (Br-Au / Br-Pd) – the temperature range for the two transitions strongly varies between the three investigated surfaces. Specifically, on Au(111) BMA debromination occurs between 310 K and 410 K, but already between 190 K and 290 K and between 200 K and 300 K for the Pd_3- and Pd_1-terminated PdGa{111} surfaces, respectively. Conversely, bromine has entirely desorbed at 470 K from Au(111), while on PdGa{111} this process is just initiated at this temperature and completed at 550 K.

Because the mathematical model to describe the debromination process is still under debate, in particular di Giovannantonio *et al.* neglect any possibility of reversibility of the reaction,[59] which is considered by Fritton *et al.*, but merely under thermal equilibrium conditions,[68] we assume the number of molecules that debrominate at a given temperature T in the ramp to follow a Gaussian distribution $n_R(T, T_{Deb_R}, \sigma_R)$ centered at T_{Deb_R} and having the width σ_R for the R enantiomer (T_{Deb_S} and σ_S for the S enantiomer). Hence, the fraction of intact BMA molecules (BrC) is given by

$$\mathrm{BrC}(T) = 1 - \int_0^T n_R(T') + n_S(T') dT' = \frac{1}{2} - \frac{1}{4}\mathrm{erf}\left(\frac{T - T_{Deb_R}}{\sigma_R\sqrt{2}}\right) - \frac{1}{4}\mathrm{erf}\left(\frac{T - T_{Deb_S}}{\sigma_S\sqrt{2}}\right) \qquad (1)$$

where erf is the error function and the concentration of R and S are the same. For each surface and temperature rate, the factors $\sigma_{R/S}$ are used to take into account the different reaction speeds for each BMA surface enantiomer.

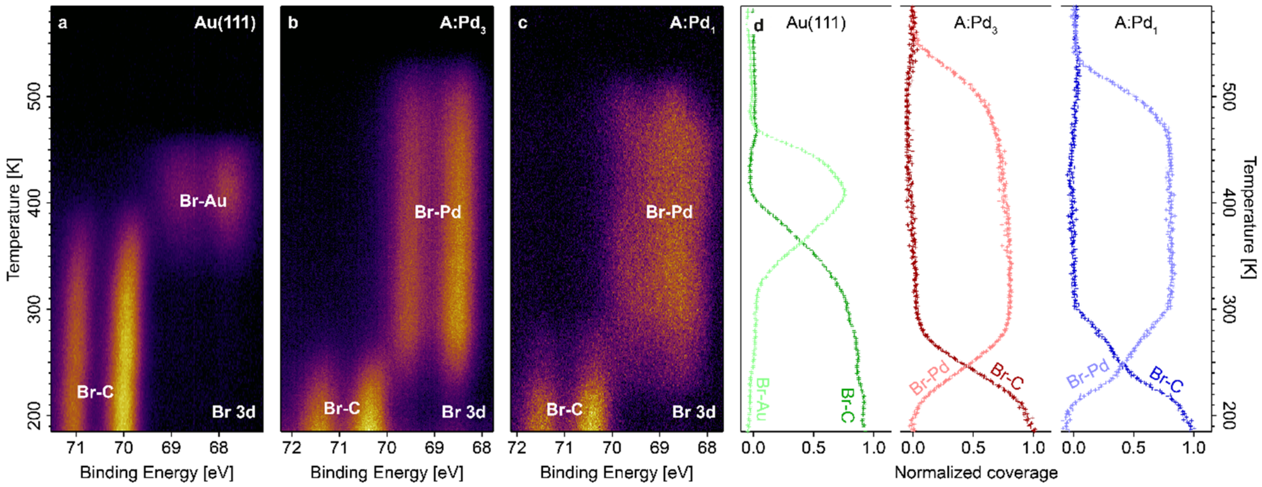

Figure 5.6 | Bromine detachment and desorption

TP-XPS maps of the Br 3d core level doublet for BMA adsorbed on **a** Au(111) **b** PdGa:A(-1-1-1)Pd$_3$ and **c** PdGa:A(111)Pd$_1$. **d** Temperature dependence of the Br-C and Br-Au / Br-Pd components extracted from the Br 3d TP-XPS maps normalized to the initial bromine signal for Au(111) (left), PdGa:A(-1-1-1)Pd$_3$ (center) and PdGa:A(111)Pd$_1$ (right).

In the following, we focus on the dynamics of the BMA debromination process on the three investigated substrates based on the Br-C traces of the TP-XPS experiments by fitting the Br-C traces with equation (1) (Figure 5.7a,e,j, which are a zoom-ins into the Br-C curves in Figure 5.6d). The conclusions from TP-XPS profiles are cross-checked by STM investigations, thereby resolving, identifying and quantifying all BMA configurations at very specific debromination states, which are highlighted with arrows in the Br-C traces (cf. Figure 5.7).

On Au(111), the Br-C profile decreases in a continuous, sigmoidal shape with no particularly apparent kink. Fitting this Br-C profile with (1) which yields $T_{DebR} = T_{DebS} = 366$ K, therefore indicating the expected absence of enantioselectivity in the BMA debromination process (Figure 5.7a). This is indeed corroborated by STM, as brominated BMA molecules appear with no enantiomeric excess neither before (300 K) nor after partial debromination at 350 K (Figure 5.7b-c). Also the BMA dimers (denoted RR or SS if containing only R or S, respectively, and RS if consisting of one R and S dehalogenated BMA, Figure 5.20) formed at 350 K, which are predominantly homochiral, exhibit no enantiomeric excess $ee_{Dimer} = 100\% \frac{|\#RR-\#SS|}{\#RR+\#RS+\#SS} = 5\% \pm 5\%$. After annealing to 400 K, coupling of a varying number of homochiral BMA dimers occurs; a structure of four merged dimers is indicated by a white arrow in Figure 5.7d.

Contrary to Au(111), the Br-C temperature profile of BMA on A:Pd$_3$ decreases in a continuous, yet rather linear shape (Figure 5.7e). This non-sigmoid profile can be fitted by (1) only by assuming two dissimilar debromination temperatures for the two enantiomers, $T_{DebR} = 220$ K and $T_{DebS} = 255$ K, indicating an enantioselective debromination of BMA. This interpretation is supported by the observation that the Br-C intensity only decreases to about 50% of its initial value if the temperature is kept constant at a value slightly above the onset of the debromination process (Figure 5.15, Figure 5.16). Indeed, STM investigations reveal that of the initial racemic mixture of BMA deposited on A:Pd$_3$ at 160 K (Figure 5.7f) only R BMA molecules debrominate and subsequently dimerize in numerous different configurations, some of which are shown in Figure 5.21, while the S BMA molecules persist unaltered upon annealing to 250 K (Figure 5.7g). Therefore, at this temperature, the coverage of S BMA enantiomers relative to all BMA derived molecular structures remains at 50% (Figure 5.7i). Upon further heating to 300 K, the S BMA/A:Pd$_3$ also debrominate and dimerize, as shown in Figure 5.7h.

In contrast to the Br-C profiles of BMA on Au(111) (sigmoid) and A:Pd$_3$ (near linear), the one on A:Pd$_1$ exhibits a clear double-sigmoid shape with a pronounced discontinuity at 50% of the initial intensity, which is again indicative for enantioselective BMA debromination (Figure 5.7j). The derived debromination temperatures for the two enantiomers on A:Pd$_1$ amount to $T_{DebR} = 274$ K and $T_{DebS} = 228$ K. STM also confirms this enantioselective debromination, as of the initial racemic mixture of BMA deposited on A:Pd$_1$ at 160 K (Figure 5.7k) only S BMA molecules debrominate while the R enantiomers stay mostly brominated between 225 K and 250 K with a coverage relative to all BMA of almost 50% (Figure 5.7l,n). In contrast to debrominated BMA molecules on the A:Pd$_3$ surface, the debrominated BMAs remain rather isolated (Figure 5.7l, Figure 5.18, Figure 5.19) on the A:Pd$_1$ surface and scarcely form dimer-like structures (Figure 5.7i,n; Figure 5.22). However, the few dimer-like structures appear enantioselectively with an $ee_{Dimer} = 75\%^{+17\%}_{-25\%}$ in favor of SS dimers at 250 K. Upon annealing to 300 K, the R BMA molecules debrominate and sometimes form dimer-like RS and RR structures (Figure 5.7m).

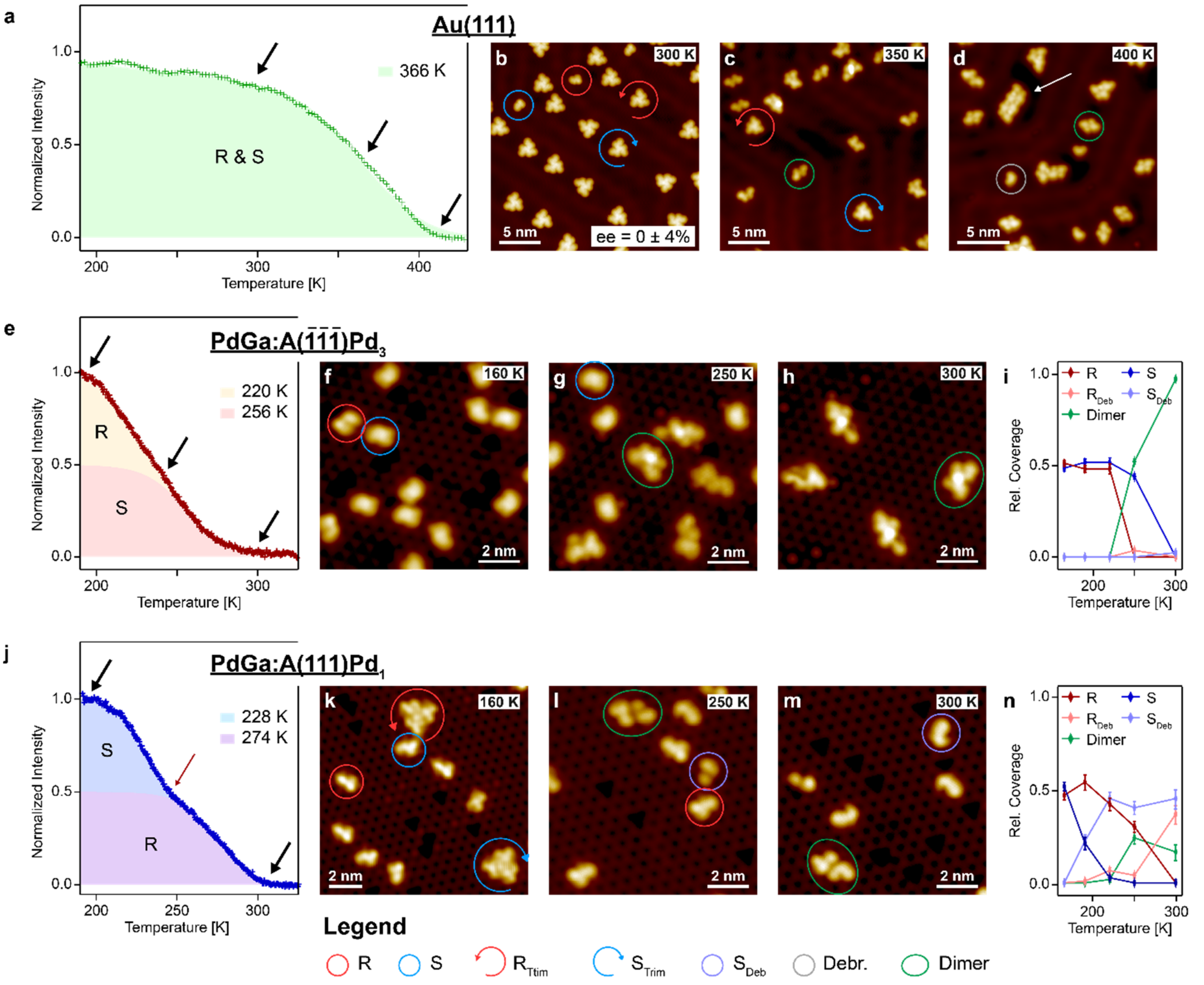

Figure 5.7 | Enantioselectivity of BMA debromination

Br-C intensity extracted from the Br 3d core level TP-XPS maps for the **a** Au(111), **e** PdGa:A(-1-1-1)Pd_3, and **j** PdGa:A(111)Pd_1 (bottom) surfaces. The shaded areas beneath each intensity curve corresponds to a fitting with equation (1), and separated for R and S BMA surface enantiomers. The temperatures at which half of the respective surface enantiomer debrominated are given in the legend. The arrows indicate the state of debromination visualized in the STM images in **b-d, f-h, k-m**, which have been recorded at 5 K. STM images of BMA on Au(111) deposited at **b** 300 K and after subsequent heating at **c** 350 K and at **d** 400 K. STM images of BMA on PdGa:A(-1-1-1)Pd_3 deposited at **f** 165 K and after subsequent heating to **g** 250 K and to **h** 300 K. **i** The abundance of BMA species on PdGa:A(111)Pd_1, which has been determined based on STM images that have been recorded after annealing to a certain temperature. STM images of BMA on PdGa:A(-1-1-1)Pd_3 deposited at **k** 165 K and after subsequent annealing to , **l** 250 K and **m** 300 K. **n** The abundance of BMA species on PdGa:A(111)Pd_1, which has been determined based on STM images that have been recorded after annealing to a certain temperature. The STM parameters have been **b-d, k-m** V_G = -50 mV, **f-h** V_G = +50 mV; **b, d, f, k, m** I_T = 200 pA, **c, l** I_T = 20 pA and **g-h** I_T = 50 pA.

In summary, by combining TP-XPS and STM we could clearly evidence the debromination process of prochiral BMA molecules to proceed in the temperature range of 300 K to 400 K and without enantioselectivity on achiral Au(111). On the other hand, the BMA debromination is highly enantioselective on the PdGa{111} surfaces and occurs between 190 K and 290 K on the Pd_3-terminated, and between 200 K and 300 K on the Pd_1-terminated PdGa{111} surfaces. This enantioselectivity could be evidenced by TP-XPS due to a strikingly different trend in the Br-C trace for the PdGa{111} surfaces as compared to the one for Au(111) (cf. Figure 5.7a,e,j). In particular, the sigmoid trend of the Br-C trace for Au(111) turns into a rather linear one for A:Pd_3 where we determined a temperature difference of 35 K between the two enantiomers, and even into double-sigmoidal trend for the A:Pd_1 surface where this temperature difference even amounts to 46 K. STM investigations of the process, at specific annealing temperatures determined from the TP-XPS, could corroborate the enantioselectivity and differentiate between the more and less stable enantiomeric form of the BMA.

Generally, the onset temperatures for the debromination process on the catalytically active PdGa{111} surfaces are significantly lower than the one on more inert Au(111), but correspond well to those reported for Cu(111)[44,231] Because the PdGa{111} surfaces have a similar d-band center as Cu(111),[49,229] they are expected to have a similar catalytic activity.[232] However, debromination processes on Cu(111) surfaces occur over a significantly narrower temperature range than the debromination of BMA on PdGa{111} surfaces.[44,231] Such increased temperature ranges for the debromination have been attributed to a reversible process,[44,68] whereas the reversibility is suppressed on Cu(111) owing to the formation of a stable organometallic phase. Employing the model proposed in Ref.[44] to fit the Br-C profiles for the PdGa{111} surfaces, we can estimate an energy difference necessary to justify the observed debromination temperature differences between R and S debromination of about 35 meV and 60 meV on Pd_3- and Pd_1-surfaces, respectively.

In order to obtain a deeper insight into the enantioselectivity of the debromination on the PdGa{111} surfaces, we performed nudged elastic band (NEB) simulations that, starting from the optimization of the minimum energy path between two stable states, allow to determine the nature of the transition state and the corresponding barrier height (Figure 5.23). NEB simulations result in a reasonable energy barrier of 0.99 eV for S BMA on the A:Pd_3 surface and even in a significantly lower one of 0.85 eV for the R BMA. However, the energy barrier for the BMA debromination derived for the A:Pd_1 surface is unreasonably high, as based on the experimental evidence it should be expected to be of the same order as the energy barrier determined for A:Pd_3. For the moment, NEB simulations could therefore not unravel the origin of the enantioselective debromination. Nevertheless, we gain valuable insight into the mobility of BMA and its debrominated counterpart on the PdGa{111} surfaces. In particular, on A:Pd_3, NEB simulations show a peak in energy when the bromine is dissociated from BMA, but a very shallow energy potential afterwards, when the debrominated BMA moves towards an energetically stable adsorption configuration (Figure 5.23a). On the other hand, on A:Pd_1, the energy increases upon bromine detachment and remains increased when the debrominated BMA moves to a stable adsorption configuration (Figure 5.23b). This implies a reduced mobility of debrominated BMA on A:Pd_1, which might be the reason for the low number of dimer-like structures formed on this surface as compared to A:Pd_3.

In conclusion, we have experimentally demonstrated the BMA debromination process to be remarkably enantioselective on both the PdGa{111} surfaces (Pd_1 and Pd_3) with an unprecedented high difference in debromination temperatures between the two enantiomers, which amounts up to 35 K on Pd_3- and even 46 K on Pd_1-terminated PdGa{111}. Even though the debromination process proceeds enantioselective on both PdGa{111} surfaces, the opposite BMA enantiomer debrominates first on PdGa:A(-1-1-1)Pd_3 as compared to PdGa:A(111)Pd_1. This disparity for the two structurally different PdGa{111} surfaces evidences a strong ensemble effect and emphasize the significance of the investigation of molecule-substrate interactions on the atomic level. Moreover, the reported enantioselective debromination further evidences the strong chiral recognition of the PdGa{111} surfaces and promises enantioselective control in on-surface synthesis.

5.2.1 Supporting Information for the publication "Enantioselective debromination on chiral metal surfaces"

5.2.1.1 Methods

5.2.1.1.1 Sample preparation and XPS experiments

The PdGa{111} and Au(111) single crystal surfaces were cleaned by repeated sputtering and annealing cycles (sputtering: Ar+, 1 keV; annealing PdGa{111}: 870 K; annealing Au(111): 750 K). BMA molecules were thermally evaporated onto the clean metal surfaces from a quartz crucible heated to 350 K.

5.2.1.1.2 STM / nc-AFM

A commercial low-temperature STM/AFM (ScientaOmicron) was used for in situ characterization at 5 K under ultrahigh vacuum conditions with a base pressure below $2x10^{-10}$ mbar. STM images were acquired in constant-current mode with an etched tungsten tip. nc-AFM measurements were performed with a tungsten tip mounted on a qPlus tuning fork sensor.[233] The tip was functionalized with a single CO molecule at the tip apex picked up from the previously CO-dosed surface. The sensor was driven at its resonance frequency (27.005 kHz) and the frequency shift from resonance of the tuning fork was recorded in constant-height mode using Omicron Matrix electronics and HF2Li PLL by Zurich Instruments.

5.2.1.1.3 XPS

XPS measurements were performed at the X03DA beamline (PEARL endstation)[95] at the SLS synchrotron radiation facility (Villigen, Switzerland), using linearly polarized radiation with photon energy of 425 eV. XPS spectra were obtained in normal emission geometry, using a hemispherical electron analyzer (Scienta R4000) equipped with a multichannel plate (MCP) detector. High-resolution XPS were recorded in “swept” mode with 20 eV pass energy, whereas TP-XPS measurements were performed in “fixed” mode during heating of the sample with a constant heating rate (0.03 K/s for PdGa{111} and 0.1 K/s for Au(111)) acquiring each spectrum with 50 eV pass energy for 5 s (Br 3d and C 1s core levels; temperature resolution of 0.6 K for PdGa{111} and 1.9 K for Au(111). The interpretation and analysis of TP-XPS maps is illustrated in Figure 5.8. For coverage determination, a commercial low-temperature STM (ScientaOmicron) operated at 77 K and attached to the XPS chamber was used, allowing transfers from STM to XPS and vice-versa without breaking the vacuum.

5.2.1.1.4 DFT

We performed Geometry Optimizations with the conjugate gradient algorithm[234] in the AiiDA framework.[235] The minimum energy paths were estimated through 10-replicas nudged elastic band (NEB) calculations[236] optimized with conjugate gradient in the climbing image[237] protocol.

Both STM and AFM images were performed according to Aiida-Lab[235] Apps, in particular: (i) STM simulations were performed in the Tersoff-Hamann approximation,[238] and in order to correct the wrong decay of the charge density caused by the localized basis set, the orbitals were extrapolated to the vacuum region;[239] (ii) AFM images were obtained with a 2-points implementation of the Probe Particle model, where the two probe particles represent the carbon and the oxygen.[240,241]

The surface/adsorbate system was modeled within the periodic boundary condition scheme, with a slab of 4x2x2 unit cells and 40 Å of vacuum in order to decouple the system from its periodic replicas in the direction perpendicular to the surface.

All the calculations were performed with CP2K/6.1[242] code, relying on density functional theory (DFT)[243,244] within the general gradient approximation (GGA)[245] for the exchange and correlation functionals implemented in the Perdew-Burke-Ernzerhof (PBE)[136] functional scheme with Grimme's D3[246] dispersion correction. In order to take into account for the possible radical character of the system, Nudged Elastic Bands calculations were implemented with the Unrestricted Kohn and Sham[247–249] electronic description to account for possible spin polarization effects.

The Goedecker–Teter–Hutter pseudopotentials[250] were adopted for the atomic cores representation. The wavefunction was expanded in a localized Gaussian basis set. All calculations were performed according to the mixed *Gaussian and plane waves method*[251] and the wave function convergence criterion was set to 10^{-7} a.u. The wavelet Poisson solver[252] was always adopted.

5.2.1.2 Illustration of TP-XPS experiments

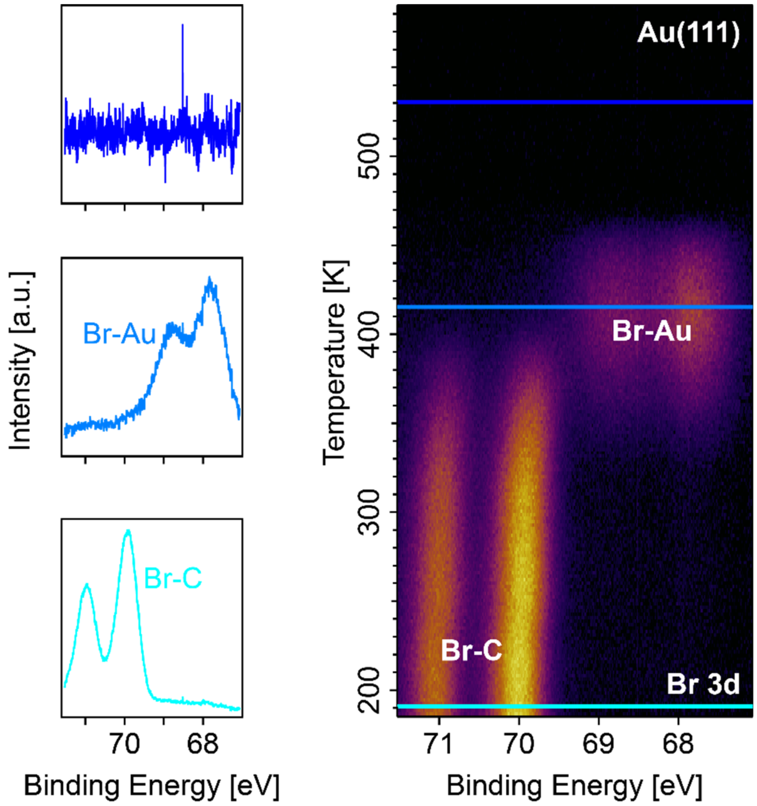

Figure 5.8 | Illustration of TP-XPS experiment

Horizontal cuts extracted from the TP-XPS map (right) of the Br 3d core level doublet, which show the XPS signal of bromine attached to the molecule (Br-C; left bottom), bromine adsorbed on Au(111) (Br-Au; left center) and after bromine desorption (left top)

As illustrated in Figure 5.8, each horizontal pixel line of TP-XPS maps corresponds to one XPS spectrum of the Br 3d core level doublet (Br $3d_{5/2}$ and Br $3d_{3/2}$) recorded during any heating ramp. For every pixel line, hence temperature step, the contribution of each of the chemical states (Br-C, Br-Au, Br desorbed) to the measured XPS spectrum is determined and yields the kinetic curves.

5.2.1.3 Deposition of BMA on Au(111) at 165 K

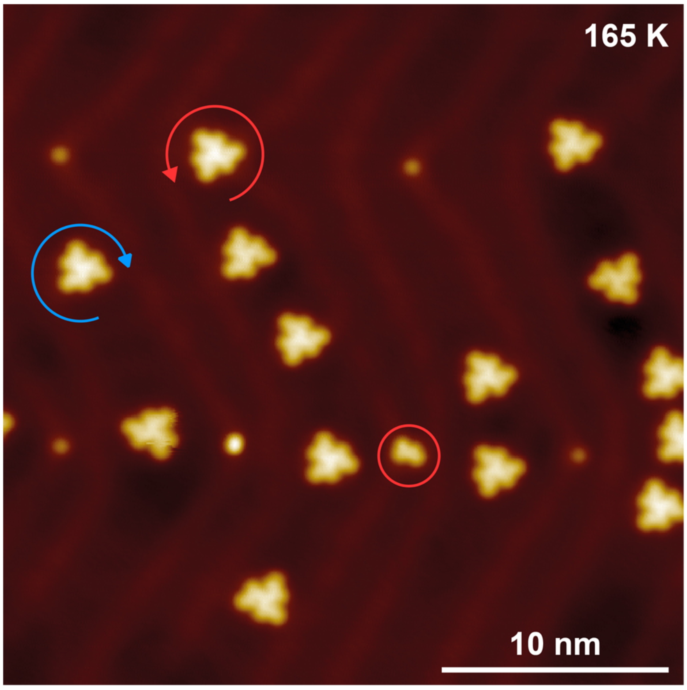

Figure 5.9 | BMA deposited at 165 K on Au(111)
STM image after BMA deposition on Au(111) at 165 K (V_B = 20 mV; I_T = 50 pA).

BMA molecules agglomerate to a significant amount in trimers already at 165 K, therefore BMA monomers must be mobile at this temperature. Moreover, because there are still BMA monomers present at 165 K, the BMA molecules in a trimer are only weakly bound. Therefore, this BMA agglomerations should not critically influence the debromination process. Especially not with regard to enantioselectivity, because both enantiomers of the propeller occur to the same amount.

5.2.1.4 Distinguishing R and S enantiomers with STM

5.2.1.4.1 PdGa:A(-1-1-1)Pd_3

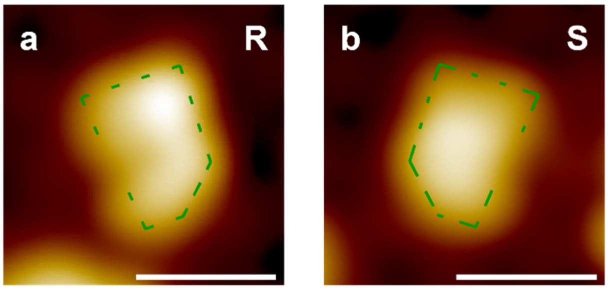

Figure 5.10 |Trapezoid-shape of BMA on PdGa:A(-1-1-1)Pd_3
STM images (V_B = -50 mV, I_T = 200 pA) of BMA monomers, each outlined with a trapezoid. The STM images show two different enantiomers being rotated such that the two overlaid trapezoids for each enantiomers are roughly the mirror images of one another.

5.2.1.4.2 PdGa:A(111)Pd_1

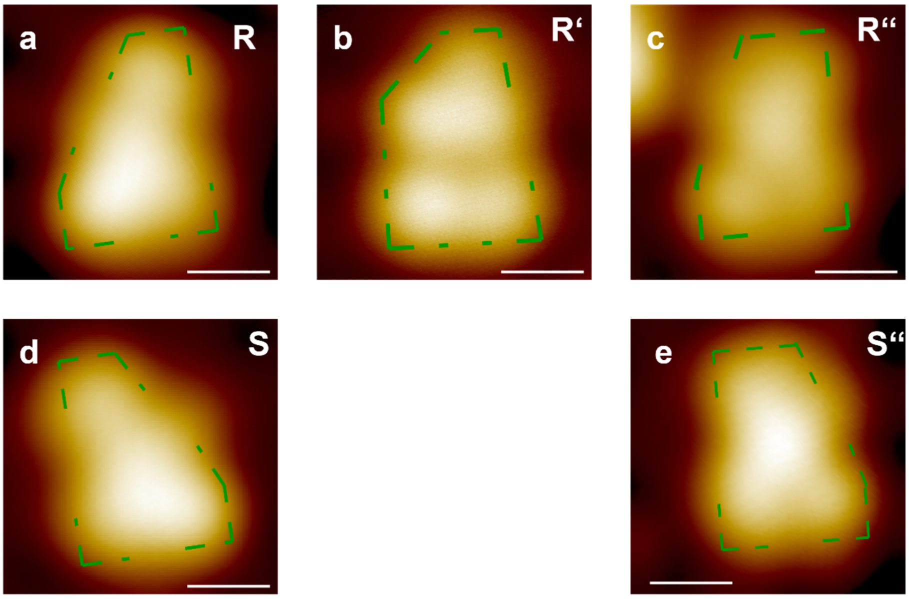

Figure 5.11 | Trapezoid-shape of BMA on PdGa:A(111)Pd_1

STM images (**a-d** V_G = -50 mV, I_T = 200 pA; **e** V_G = 50 mV, I_T = 200 pA) of BMA monomers, each delineate with a trapezoid. The STM images show different enantiomeric forms that have been rotated such that the two overlaid trapezoids for each enantiomers are roughly the mirror images of one another. All scale bars correspond to 5 Å.

BMA molecules adsorbed on PdGa:A(-1-1-1)Pd_3 and PdGa:A(111)Pd_1 always appear as trapezoids when resolved with STM. Depending on the handedness of these trapezoids, BMA can be categorized as R or S surface enantiomer.

When BMA is adsorbed on Pd_1-terminated PdGa{111} surfaces, its monomers occur in five adsorption configurations. For PdGa:A(111)Pd_1, three of these configurations are of the R enantiomer, two of the S. The configurations of the same enantiomeric form differ in their adsorption position on the surface, which is illustrated in Figure 5.13.

5.2.1.5 Density Functional Theory simulations of BMA on PdGa:A(-1-1-1)Pd_3

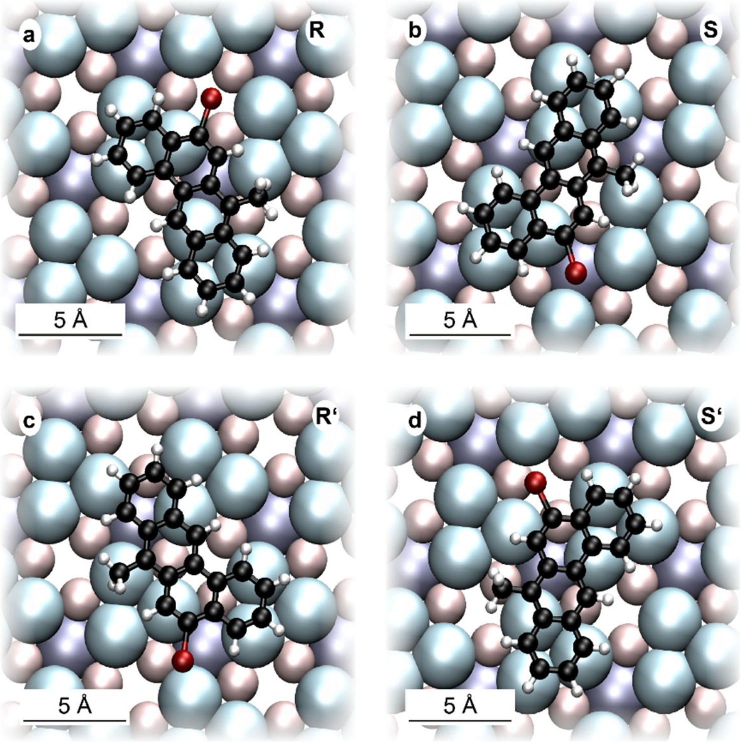

Figure 5.12 | DFT relaxed adsorption geometries of BMA on PdGa:A(-1-1-1)Pd_3

DFT relaxed adsorption geometries for the intact BMA species corresponding to the experimentally detected **a** R and **b** S, and the experimentally not observed **c** R' and **d** S'. While for R and S' the Br atom is situated above a second layer Ga trimer and the anthracene moiety covers a third layer Pd atom, the Br atom of S and R' is located above a third layer Pd atom and the anthracene moiety covered a second layer Ga trimer.

	VDW: D3	
Ads. Geometry	E_A [eV]	ΔE [meV]
R	-2.827	39
S	-2.866	0
R'	-2.781	85
S'	-2.690	176

Table 5.1 | Adsorption energies of BMA on PdGa:A(-1-1-1)Pd_3

Adsorption energy E_A and energy difference with respect to the S BMA/A:Pd_3 adsorption configuration derived from DFT simulations with the D3 van der Waals corrections.

The adsorption geometries denoted R and S are energetically the most stable and correspond to the geometries determined experimentally. Although an energy difference of almost 40 meV between R and S BMA surface enantiomers is determined, no enantiomeric excess could be established experimentally, due to suppressed R – S interconversion at temperatures below the debromination temperature.

5.2.1.6 *Adsorption configuration of BMA monomers on Pd_1-terminated PdGa{111} surfaces*

5.2.1.6.1 BMA monomers on PdGa:A(111)Pd_1

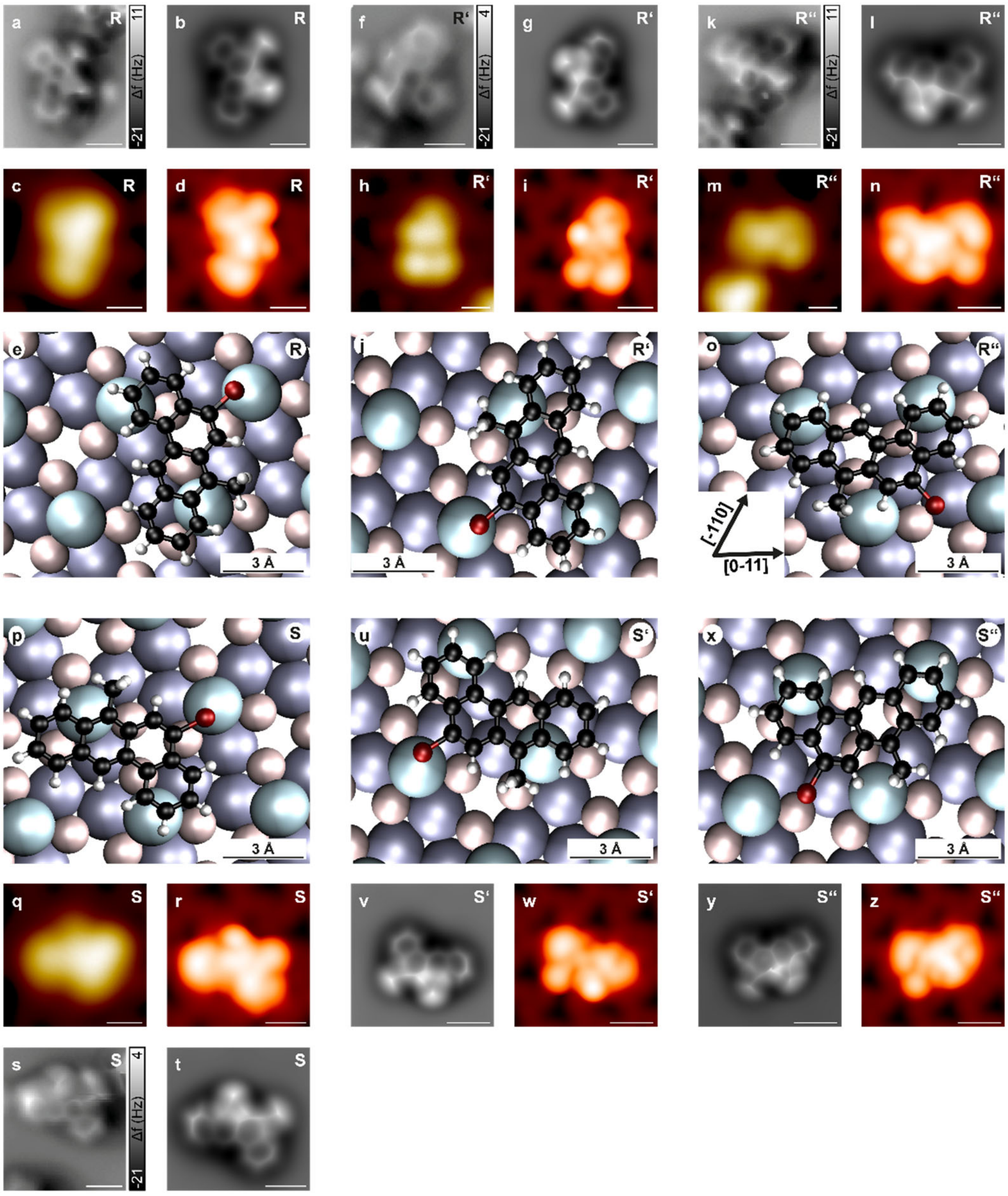

Figure 5.13 | BMA adsorption configurations on PdGa:A(111)Pd_1

Experimental (if available) and simulated nc-AFM and STM images, and the DFT relaxed adsorption geometry for **a-e** R, **f-j** R', **k-o** R'', **p-t** S, **u-v** S', and **w-x** S'' BMA on PdGa:A(111)Pd_1. The experimental nc-AFM are presented in **a, f, k, s** and the corresponding simulated nc-AFM in **b, g, l, t, v, y**. The experimental STM are shown in **c, h, m, q** and the respective simulated STM in **d, i, n, r, w, z**. All simulations are based on the DFT relaxed adsorption geometries displayed in **e, j, o, p, u, x**. All scale bars, if not mentioned differently in the figure, correspond to 5 Å. All STM images were recorded with V_G = -50 mV and I_T = 200 pA.

Ads. Geometry	E_A [eV]	ΔE [meV]
R	-2.375	0
S	-2.363	12
R'	-2.372	3
S'	-2.337	38
R''	-2.374	1
S''	-2.383	-8

Table 5.2 | Adsorption energies of BMA on PdGa:A(111)Pd_1

Adsorption energy E_A and energy difference with respect to the S BMA/A:Pd_1 adsorption configuration derived from DFT simulations with the D3 van der Waals correction.

Six stable BMA monomer configurations have been deduced on the PdGa:A(111)Pd$_1$ surface, and are referred to as R, R’, R’’, S, S’, and S’’ according to their surface enantiomeric form and displayed in Figure 5.13.

For the R, R’, S, and S’ configurations the bromine atom adsorbs on top of a top-layer Pd atom (Figure 5.13e,j,p,u). The R and S configurations differ from the R’ and S’ ones in terms of the benz(a)anthracene moiety, which covers a second-layer Ga trimer for R and S (Figure 5.13e,p), but above a third layer Pd trimer for R’ and S’ (Figure 5.13j,u). In case of the R’’ and S’’ adsorption geometry, the bromine atom is pointing towards a Ga of a second layer Ga trimer, while the benz(a)anthracene moiety covers another second layer Ga trimer.

The energies for the six DFT relaxed BMA/A:Pd$_1$ adsorption configurations in Table Table 5.2 barely differ from each other, although experimentally we observe mainly the configurations denoted R and S in Table ST2. In this context, Yakutovich *et al.* reported on the relevance of the implementation of non-local correction in DFT on the relative adsorption energies.[23] Therefore, performing DFT with another non-local correction might resolve this discrepancy. Nevertheless, the energy for the adsorption configuration denoted as S' is the highest, also for the employed additive Grimme D3 dispersion correction,[246] which is in agreement with experiments, where no S' monomers have been observed, even though we have categorized more than 250 BMA/A:Pd$_1$ S surface enantiomers.

5.2.1.6.2 BMA trimers and monomer moieties on PdGa:B(-1-1-1)Pd$_1$

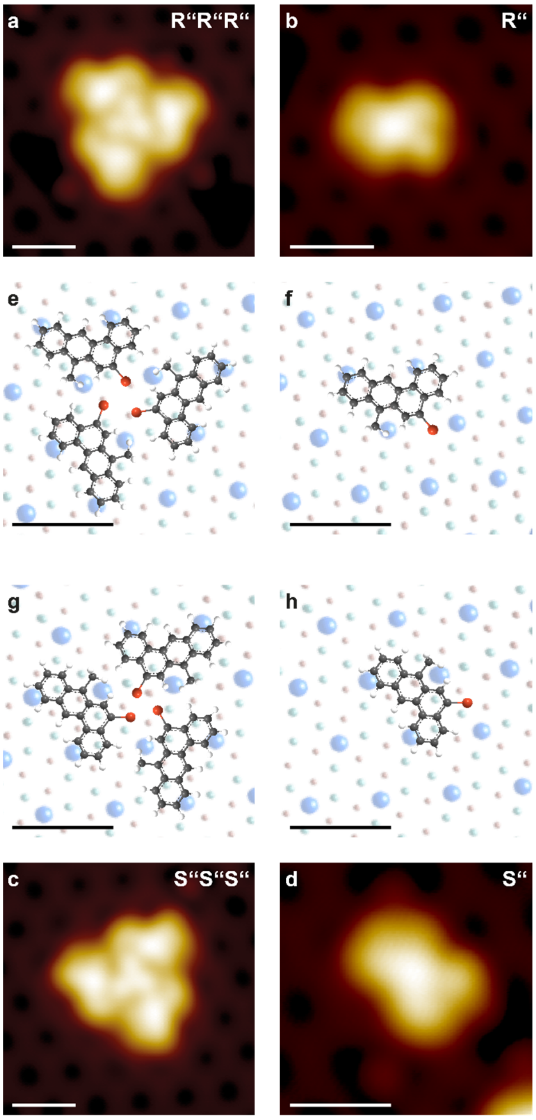

Figure 5.14 | BMA trimer agglomerations on PdGa:B(-1-1-1)Pd$_1$

STM image of **a** R’’R’’R’’ BMA trimer, **b** R’’ monomer, **c** S’’S’’S’’ trimer and **d** S’’ monomer on PdGa:B(-1-1-1)Pd$_1$ with the corresponding adsorption configuration in **e-h**. All STM images were recorded at V_B = 50 mV and I_T = 200 pA. All scale bars correspond to 1 nm.

BMA agglomerated in homochiral trimers on the Pd_1-terminated PdGa{111} surfaces always consist of three monomers in the adsorption geometry denoted as R'' and S'' in Figure 5.13, Figure 5.14 and Table 5.2.

5.2.1.7 XPS tracking of debromination at constant temperature of BMA on PdGa:A(-1-1-1)Pd_3 and Au(111)

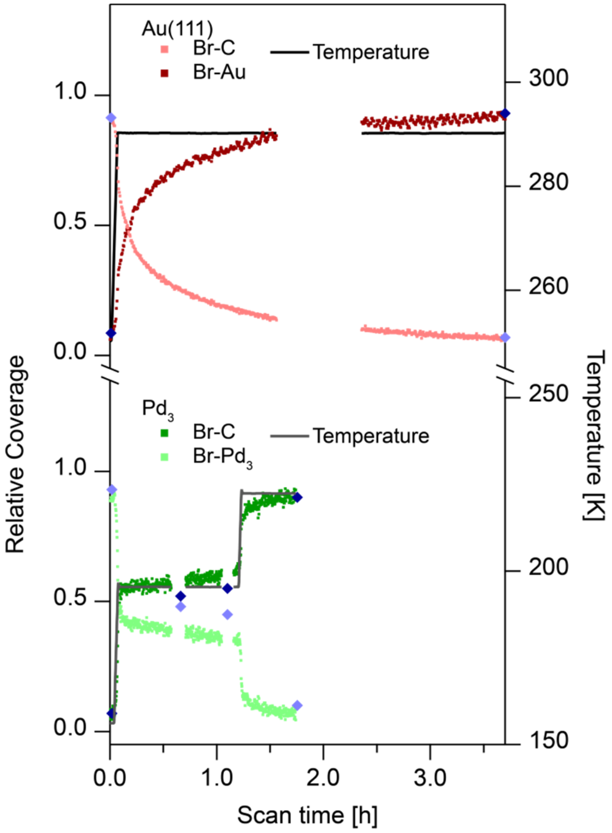

Figure 5.15 | Evidencing enantioselective debromination on PdGa:A(-1-1-1)Pd_3 with XPS

Br-C and Br-Au XPS signals of BMA on Au(111) and Pd_3 versus time, with constant, but increased temperature during a certain time interval. The blue markers represent the coverage determined from high-resolution XPS of the Br 3d signal shown in Figure 5.16.

The decrease (increase) of the Br-C (Br-Au) XPS signal exhibits an exponential decay towards full debromination on Au(111) upon temperature increase. Contrary, on Pd_3, the debromination process of the BMA/A:Pd_3 R enantiomer was completed when reaching the set temperature, while the debromination of the S surface enantiomer just started slowly. Hence, the coverage of debrominated BMA reached 52% after about 40 min and around 56% after 70 min (marker corresponding to the relative coverage determined from high-resolution XPS shown in Figure 5.16), which is an indication for enantioselective debromination of BMA on Pd_3.

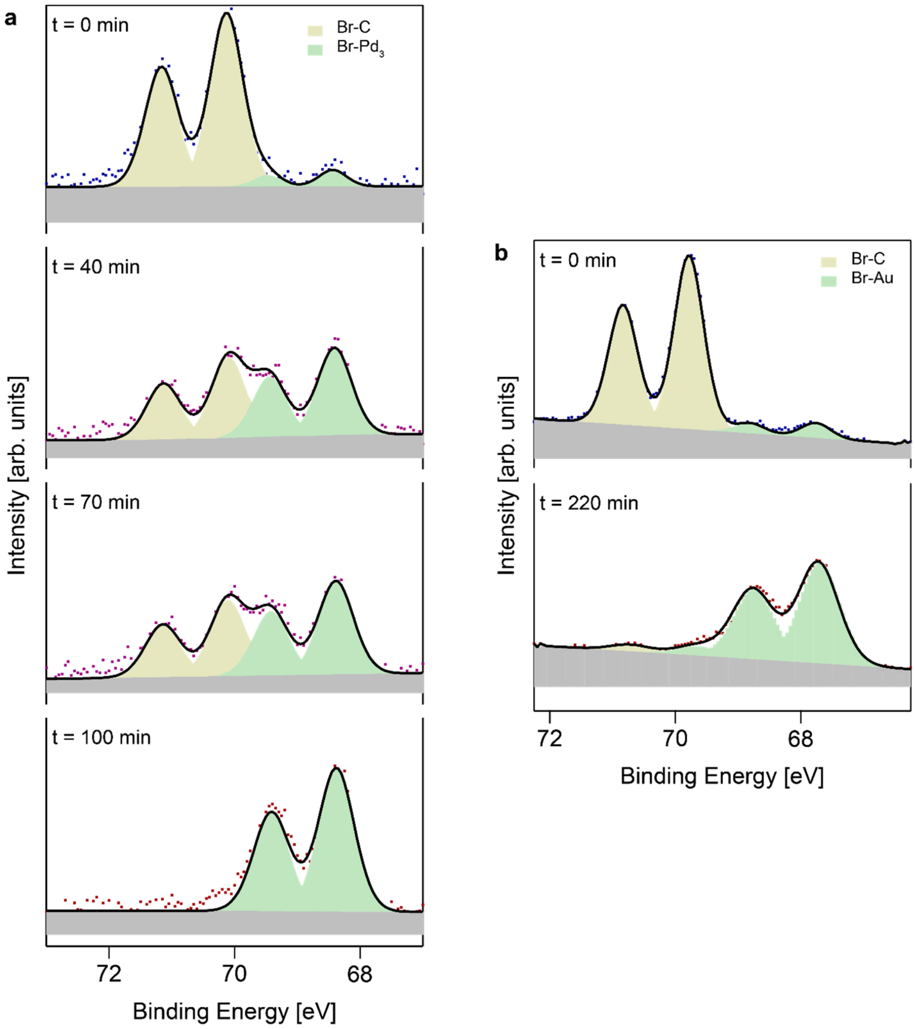

Figure 5.16 | HR-XPS of BMA during the debromination on PdGa:A(-1-1-1)Pd$_3$ and Au(111)

High-resolution XPS of Br 3d for BMA adsorbed on **a** A:Pd$_3$ and **b** Au(111). The topmost XPS in **a-b** were taken before any temperature ramp at 160 K for Pd$_3$ and 250 K for Au(111), while the lowest were after completion of all temperature ramps. For Pd$_3$, two XPS spectra were taken in between after 40 min and 70 min as labelled in **a**.

The experimental data is visualized with dots, while the fitted data is shown as shaded areas to illustrate the different core level components (colors) and background (black), resulting in the total fitted intensity represented by the black line.

5.2.1.8 BMA on PdGa:B(-1-1-1)Pd_1

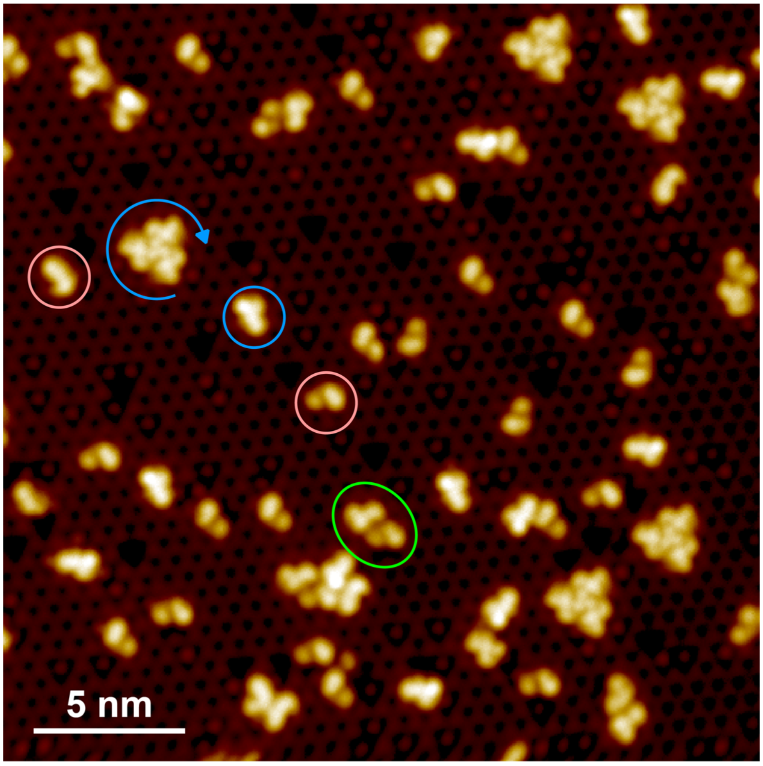

Figure 5.17 | Enantioselective debromination of BMA on PdGa:B(-1-1-1)Pd_1

STM image of BMA after deposition at 250 K on PdGa:B(-1-1-1)Pd_1 (V_{Bias} = -50 mV; I_T = 100 pA). The blue circular arrow indicates a trimer of intact S BMA/PdGa:B(-1-1-1)Pd_1, the blue circle an S BMA/PdGa:B(-1-1-1)Pd_1 monomer, red circles of debrominated BMA in two different configurations and the green circle a RR BMA dimer-like structures.

The main observations for BMA molecules on A:Pd_1 noted in the main text are corroborated by investigating BMA on the crystal surface with opposite chirality B:Pd_1. On B:Pd_1, enantioselectivity in BMA debromination and dimerization is observed as well. However the opposite BMA enantiomers as compared to A:Pd_1, specifically R BMA, debrominate first and form dimer-like structures with an $ee_{Dimer} = 69\%^{+11\%}_{-16\%}$ in favor of RR (Figure 5.17).

5.2.1.9 Debrominated BMA on PdGa:A(111)Pd$_1$

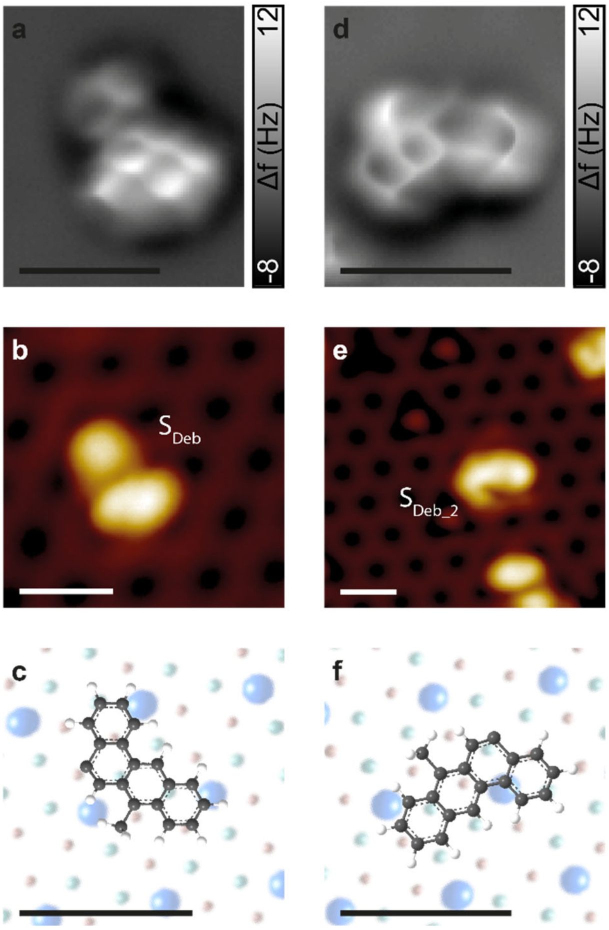

Figure 5.18 | Adsorption configuration of debrominated S BMA on PdGa:A(111)Pd$_1$

a, d nc-AFM with CO modified tip of two debrominated BMA S surface enantiomer species on PdGa:A(111)Pd$_1$ with STM images of the same molecule (V_{Bias} = 50 mV, **d** I_T = 5 pA, **g** I_T = 10 pA) in **d, g** and the determined adsorption configurations in **e, h**. All scale bars correspond to 1 nm.

Two dissimilar geometries of debrominated BMA molecules appear on the Pd$_1$-terminated PdGa{111} surfaces, as illustrated for the S enantiomer on the A:Pd$_1$ surface in Figure 5.18. The configuration presented in Figure 5.18a-c appears predominantly on A:Pd$_1$ at temperatures of 250 K or below, but vanishes upon annealing to 300 K. This configuration only occurs for one BMA enantiomer, as the debromination of the second does not take place in the relevant temperature range. The configuration in Figure 5.18d-f occurs as a minority of debrominated BMA at temperatures below 300 K, but becomes dominant at 300 K. At 300 K, both enantiomeric forms of debrominated BMA occur in the configuration in Figure 5.18d-f, as evidenced in Figure 5.19.

Based on STM and nc-AFM we cannot tell if the two molecular configurations in Figure 5.18 are structurally dissimilar or only differing in their adsorption geometry due to a limited mobility.

The adsorption geometries of the benz(a)anthracene moiety of debrominated S BMA does not coincide with the adsorption geometry of the same moiety for any of the energetically most stable BMA monomers.

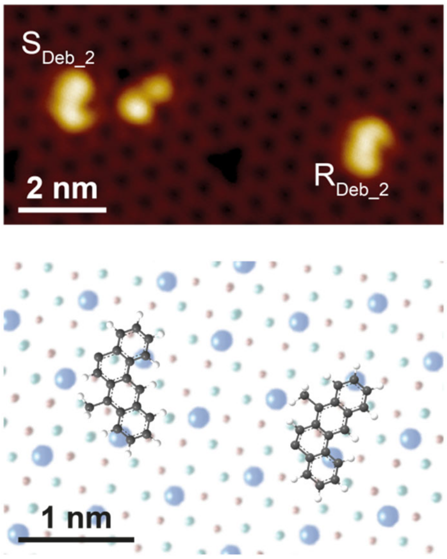

Figure 5.19 | Debrominated R and S BMA on PdGa:A(111)Pd_1

STM image (V_{Gap} = -50 mV; I_T = 200 pA) of debrominated BMA form R_{Deb2} and S_{Deb2} on PdGa:A(111)Pd_1 (top) and the corresponding adsorption configurations (bottom).

As S_{Deb_2} and R_{Deb_2} are hardly distinguishable under normal scanning conditions, they are assumed to appear 50% as R and 50% as S debrominated BMA.

5.2.1.10 BMA dimers

5.2.1.10.1 Au(111)

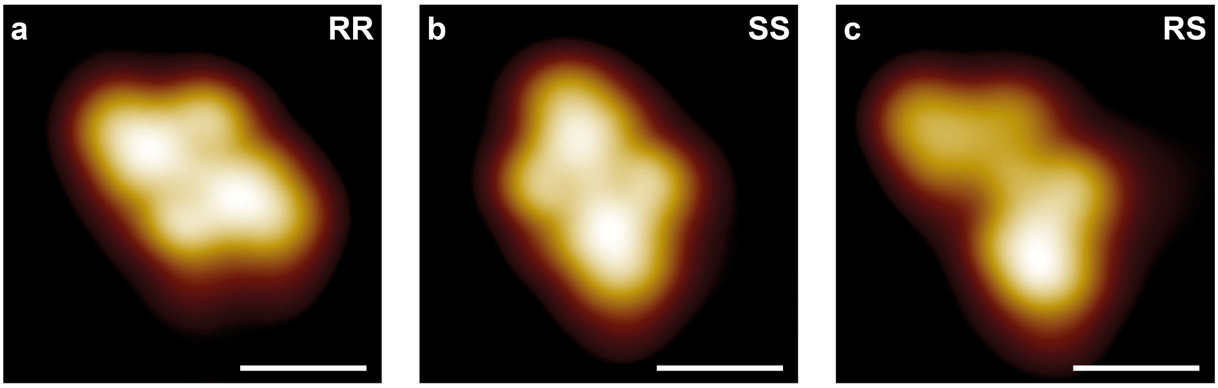

Figure 5.20 | BMA dimer on Au(111)

STM image of **a** RR, **b** SS and **c** RS BMA dimers formed on Au(111). All STM images were recorded at V_{Bias} = -50 mV and I_T = 200 pA. The scale bars all correspond to 0.5 nm.

We establish a preference for homochiral dimers over RS dimers (480:137, (RR+SS):RS; expected for a random distribution would have been a 1:1 ratio) with RR and SS dimers appearing to about the same amount (225:255, RR:SS). This preference for homochiral dimers originates from decreased steric hindrance as compared to heterochiral dimers.

5.2.1.10.2 PdGa:A(-1-1-1)Pd_3

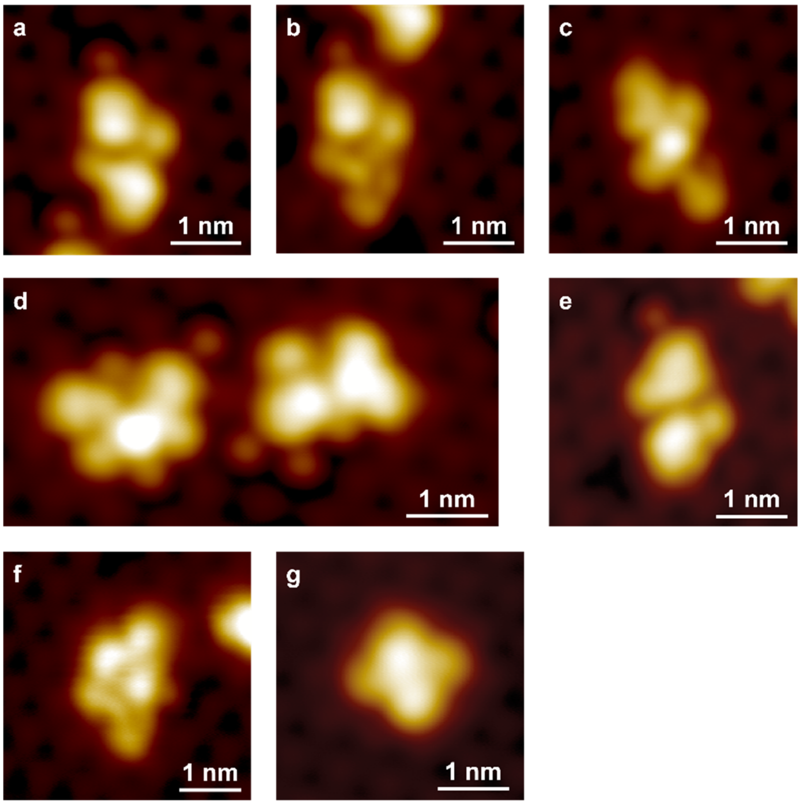

Figure 5.21 | BMA dimer on PdGa:A(-1-1-1)Pd_3

STM images of **a-c** three different RR dimers, **d** one RS dimer (left) and one SS dimer (right), **e** SS dimer and **f, g** of potentially fused BMA molecules. All STM images were recorded at V_{Bias} = 50 mV and I_T = 200 pA (**b** I_T = 50 pA).

The BMA dimers shown in Figure 5.21 represent a part of all dimer configurations generated on the PdGa:A(-1-1-1)Pd_3 surface. Due to the high variety of BMA dimers created on PdGa:A(-1-1-1)Pd_3, no statistical analysis was performed for this surface. While the BMA dimer in **a-e** are formed at 300 K, those in **f** are formed at 135 °C and those in **g** even at 175 °C.

5.2.1.10.3 PdGa:A(111)Pd$_1$

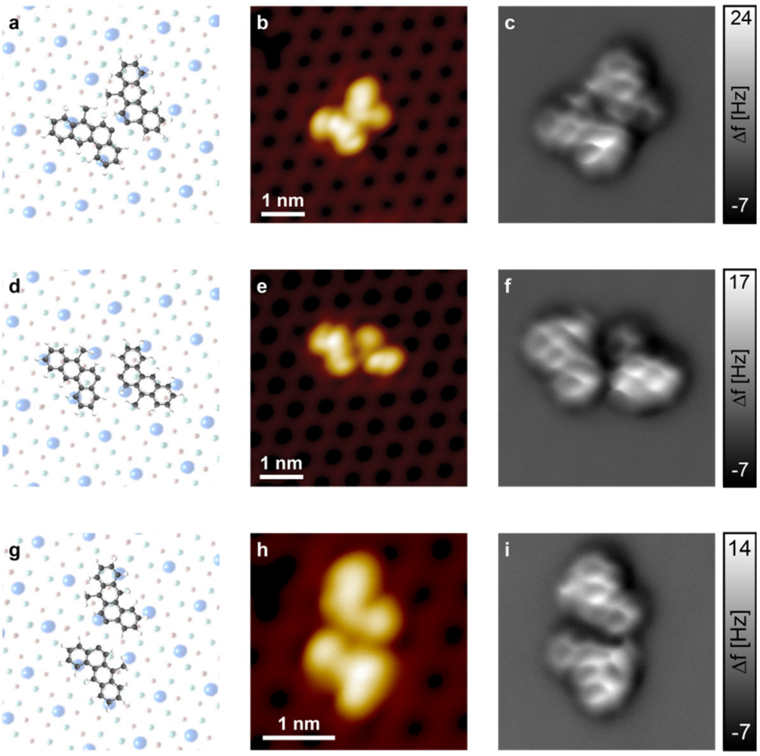

Figure 5.22 | BMA dimer-like structures on PdGa:A(111)Pd$_1$

STM images of **b** RS, **b** SS and **c** RR BMA dimer-like structures formed on PdGa:A(111)Pd$_1$. The corresponding adsorption configurations are in **a**, **d** and **g**, and the images recorded with nc-AFM with CO modified tip are in **c**, **f** and **i**. **a**, **g** and **h** were recorded at V_{Bias} = 50 mV, I_T = 500 pA, **b**, **i**, **k** and **l** at V_{Bias} = 50 mV, I_T = 200 pA

The dimer-like structures formed on Pd$_1$ are mainly homochiral, *i.e.*, RR or SS (Figure 5.22d-i), with a RR:SS ratio of 3:21 (5 unidentified dimers) on PdGa:A(111)Pd$_1$, but 25:3 (7 unidentified dimers) and 18:5 (13 unidentified dimers) on PdGa:B(-1-1-1)Pd$_1$. Compared to Au(111), BMA coupling is rare on Pd$_1$ surfaces, possibly due to reduced mobility.

5.2.1.11 NEBs simulation of the BMA debromination

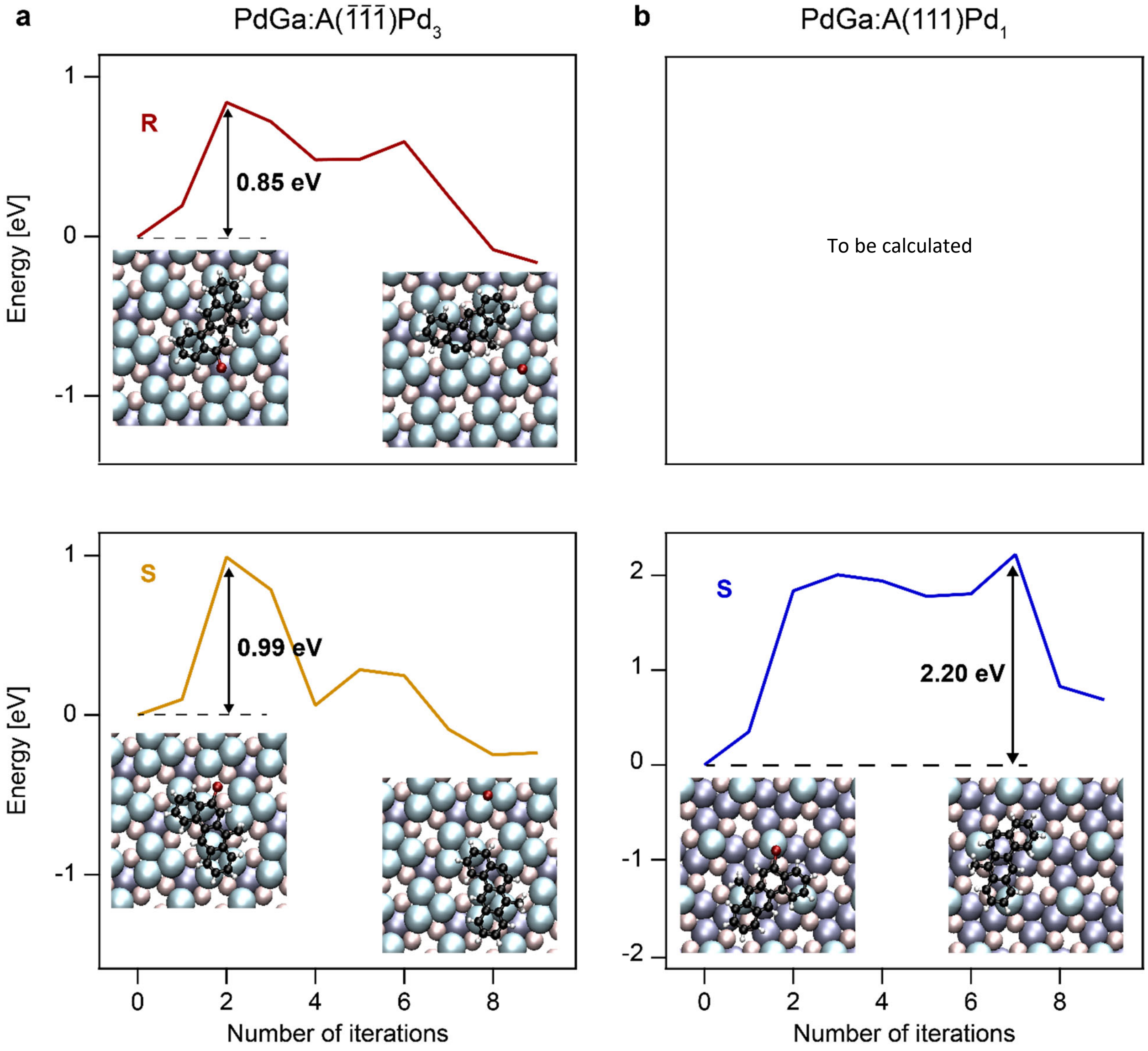

Figure 5.23 | NEB simulations of the BMA debromination on PdGa:A(-1-1-1)Pd_3 and PdGa:A(111)Pd_1

NEB simulations of the debromination process on the **a** PdGa:A(-1-1-1)Pd_3 surface and **b** PdGa:A(111)Pd_1 surface for each BMA surface enantiomer. (NEB of BMA debromination on A:Pd_1 is work in progress)

The NEB simulations for the BMA debromination on the A:Pd_3 surface indicate the experimentally observed enantioselective debromination with reasonable energy barriers.

However, in case of A:Pd_1, the energy barrier is significantly overestimated as compared to the expectations from experiments.

The NEB simulations indicate that the BMA molecule and its debrominated counterpart are more mobile on the A:Pd_3 surface than on the A:Pd_1 surface. This is because after the debromination of the molecule (which is the peak in energy), the debrominated BMA moves in a shallow potential, while on A:Pd_1, the debrominated BMA stays at elevated energies, which only drops when the debrominated BMA arrived at the stable adsorption configuration. This reduced mobility might be the reason for the limited number of dimer-like formations on Pd_1-terminated PdGa{111} surfaces.

5.3 Publication (published in Angewandte Chemie): "Reversible dehalogenation in on-surface aryl-aryl coupling"

Article available on: doi.org/10.1002/anie.202005443

I conceived and initiated this project in collaboration with Marco Di Giovannantonio, Roman Fasel, and Roland Widmer. The data recorded at the PEARL beamline was a collective work of at least six people, at which I co-organized and supervised the measurements. In addition, I performed the STM experiments and analyzed all experimental data. I wrote the manuscript together with Marco Di Giovannantonio with input from all co-authors.

Reversible dehalogenation in on-surface aryl-aryl coupling

Samuel Stolz,[1,2,†] Marco Di Giovannantonio,[1,†,*] Jose I. Urgel,[1] Qiang Sun,[1] Amogh Kinikar,[1] Gabriela Borin Barin,[1] Max Bommert,[1] Roman Fasel,[1,3,*] and Roland Widmer[1,*]

[1] EMPA, Swiss Federal Laboratories for Materials Science and Technology, 8600 Dübendorf, Switzerland

[2] Institute of Condensed Matter Physics, Station 3, EPFL, 1015 Lausanne, Switzerland

[3]Department of Chemistry and Biochemistry, University of Bern, 3012 Bern, Switzerland

[†]These authors contributed equally

*marco.digiovannantonio@empa.ch

*roman.fasel@empa.ch

*roland.widmer@empa.ch

In the emerging field of on-surface synthesis, dehalogenative aryl-aryl coupling is unarguably the most prominent tool for the fabrication of covalently bonded carbon-based nanomaterials. Despite its importance, the reaction kinetics are still poorly understood. Here we present a comprehensive temperature-programmed x-ray photoelectron spectroscopy investigation of reaction kinetics and energetics in the prototypical on-surface dehalogenative polymerization of 4,4''-dibromo-p-terphenyl into poly(para-phenylene) on two coinage metal surfaces, Cu(111) and Au(111). We find clear evidence for reversible dehalogenation on Au(111), which is inhibited on Cu(111) owing to the formation of organometallic intermediates. The incorporation of reversible dehalogenation in the reaction rate equations leads to excellent agreement with experimental data and allows extracting the relevant energy barriers. Our findings deepen the mechanistic understanding and call for its reassessment for surface-confined aryl-aryl coupling on the most frequently used metal substrates.

Keywords: aryl-aryl coupling, reversibility, dehalogenation, surface chemistry, reaction mechanisms.

Confining reactants onto a two-dimensional metallic surface is a powerful strategy for the synthesis of carbon-based nanomaterials that are elusive via wet chemistry.[32] In this context, thermally activated dehalogenative aryl-aryl coupling[253,254] has emerged as the most controllable and versatile on-surface reaction to covalently connect aryl halides under ultrahigh vacuum (UHV) conditions. Despite its extensive application to the on-surface synthesis of carbon nanostructures,[34,38,39,59,60,255] details of its reaction pathway are still lacking a comprehensive description.

Assessment of reaction pathways and products is usually performed employing scanning tunneling microscopy (STM) in combination with x-ray photoelectron spectroscopy (XPS), but neither of these techniques provide detailed time and temperature resolution of a dynamically evolving process. In this respect, temperature-programmed XPS (TP-XPS) is a unique tool to discern fundamental mechanistic aspects of thermally activated surface reactions that has also been applied to study dehalogenative aryl-aryl coupling reactions [61–68]. Such investigations have shown that the chemical transformations reflected in the halogen XPS signal are identical for many substrates, starting with the halogen's dissociation from the molecular precursor, accompanied by its chemisorption to the substrate, and its eventual desorption from the surface. Setting aside differences in the onset temperatures of these processes for different substrates and precursors, clear dissimilarities in the temperature evolution of the dehalogenation step are noted, *i.e.*, more rapid *versus* gradual temperature progressions with a temperature interval ranging from about 30 to 100 K.[61–63,66,68] These different behaviors have been attributed to two alternative reaction pathways: (i) the rapid formation of stable organometallic (OM) intermediates, and (ii) the radical stabilization by the substrate, followed by (more or less fast) covalent coupling.[68]

Here, we aim at unravelling the causes for such dissimilar dehalogenation dynamics and present a comparative study of 4,4''-dibromo-*p*-terphenyl (DBTP) as a model molecule undergoing dehalogenative homocoupling on Au(111) and Cu(111) surfaces (Figure 5.24).[37,256] The surface-assisted dehalogenative polymerization into poly(*para*-phenylene) (PPP) (Figure 5.24b,e) has been investigated by STM and TP-XPS. Our STM results reveal an average PPP length of 4.8 nm and 11.5 nm on Cu(111) and Au(111) respectively, as presented in Figure 5.29. We have designed an *ad hoc* experiment involving co-adsorbed chlorine atoms, which provides strong experimental evidence that debrominated DBTP radicals can be chlorinated on Au(111), thus implying a reversible dehalogenation mechanism on gold (Figure 5.24f). In contrast, such reversibility is not observed on Cu(111), where stable OM intermediates dominate after debromination (Figure 5.24c). Our results not only furnish a fundamental mechanistic insight into surface-confined aryl-aryl coupling but also set the basis for fine-tuning the dynamics of the product formation.

To study the dynamics of debromination in aryl-aryl coupling we have acquired TP-XPS maps (Figure 5.25) of a sub-monolayer coverage of DBTP deposited onto Au(111) and Cu(111) surfaces held at 300 K and 23 K (to avoid premature debromination), respectively. Each horizontal line of the maps shown in Figure 5.25a,d represents a single Br 3d core level doublet (Br $3d_{5/2}$ and Br $3d_{3/2}$) recorded during the 0.1 K/s heating ramp. With increasing temperature, a distinct chemical shift of the Br 3d doublet towards lower binding energy (BE) is observed. This chemical shift is due to debromination of the molecular precursor which occurs at different temperatures for Cu(111) (210 K) and Au(111) (350 K) according to their different catalytic activity. Polymerization and debromination happen simultaneously around 350 K on Au(111) (Figure 5.34b), whereas on Cu(111) the polymerization step is clearly distinct from the debromination one and occurs at 390 K (Figure 5.36), being preceded by the formation of a stable OM intermediate (Figure 5.24a). At high temperatures (above 600 K for Cu(111) and 550 K for Au(111)), a decrease in the overall Br 3d core level intensities is observed, which reflects bromine desorption from the surface. At the temperatures relevant for dehalogenation and polymerization, however, detached Br atoms remain adsorbed on both surfaces (Figure 5.24a,b,e), and we have not further studied Br desorption.

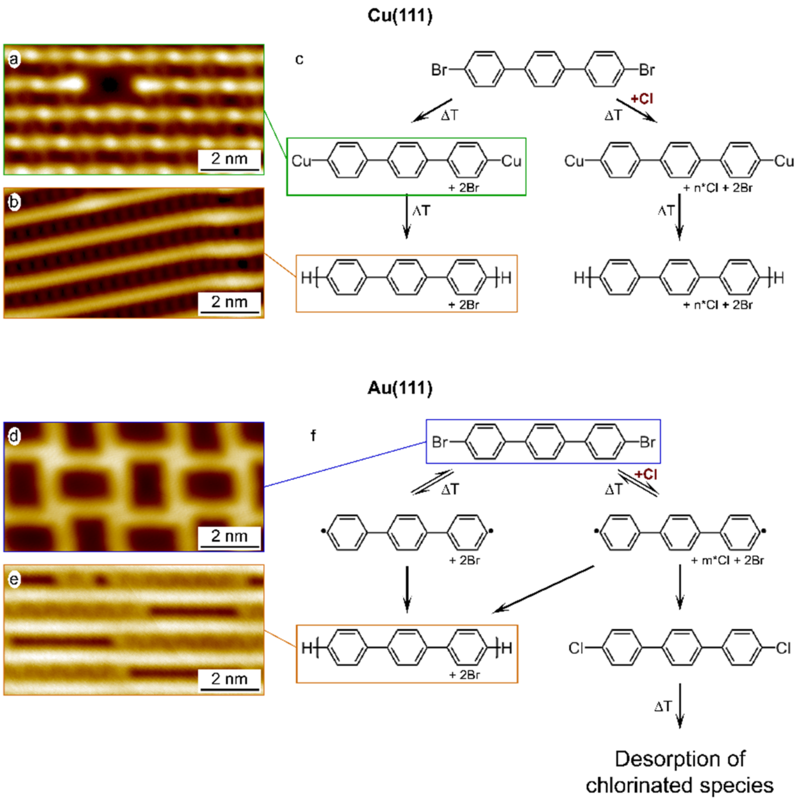

Figure 5.24 | Reaction mechanism

STM images of DBTP after 300 K deposition on **a** Cu(111) (V_G = 0.05 V; I_T = 100 pA), forming OM chains and **d** Au(111) (V_G = 0.05 V; I_T = 200 pA), on which DBTP remains intact. PPP chains are obtained after annealing to 450 K on **b** Cu(111) (V_G = 0.1 V; I_T = 200 pA) and **e** Au(111) (V_G = -1.0 V; I_T = 200 pA) with Br atoms lying in-between. Reaction schemes of DBTP and DBTP co-adsorbed with Cl on **c** Cu(111) and **f** Au(111).

A striking difference between the two substrates is seen in the thermal evolution of DBTP debromination, highlighted by the kinetic curves extracted from the corresponding TP-XPS maps (Figure 5.25b,c). Debromination takes place between 200-230 K on Cu(111) and between 300-420 K on Au(111); thus over an approximately four times larger temperature interval in case of Au(111). If such "slower" debromination was due to radical molecules that, apart from homocoupling, could also recombine with Br atoms, it should be possible to passivate some of them by offering another reaction path. Therefore, we have co-deposited chlorine (which has a higher dissociation enthalpy than bromine[257]) with DBTP on Au(111) and Cu(111), with the aim of assessing whether chlorinated molecules could be detected during the heating ramp.

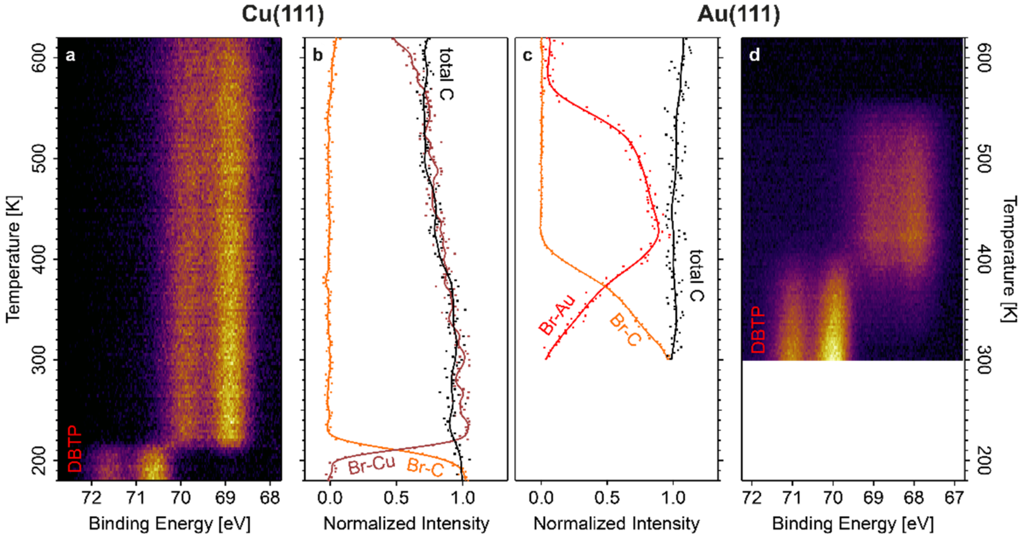

Figure 5.25 | Temperature evolution of DBTP on Cu(111) and Au(111)

TP-XPS maps of the Br 3d doublet during the annealing of DBTP on **a** Cu(111) and **d** Au(111). **b, c** Temperature dependence of the Br-C and Br-Metal signals extracted from these TP-XPS maps together with the total intensity of the C 1s signal, with the experimental data (dots) interpolated by a spline function (solid lines).

When chlorine is co-deposited with DBTP onto Cu(111) and the sample then annealed, no particular differences are observed in comparison to the standard growth of PPP from DBTP in absence of chlorine (Figure 5.26). In contrast, the growth of PPP on Au(111) presents distinct features in presence of co-deposited chlorine. In this case, the TP-XPS maps of simultaneously recorded Br 3d and Cl 2p (and C 1s) core levels in Figure 5.27a,b (and Figure 5.34c) reveal a clear chemical shift of the chlorine doublet (Cl $2p_{3/2}$ and Cl $2p_{1/2}$) to higher BE. As evidenced by the kinetic curves extracted from the Br 3d and Cl 2p TP-XPS maps (Figure 5.27c), the increase of the Cl-C and the simultaneous decrease of the Cl-Au component coincide with the bromine detachment from the molecules. This is also confirmed by high-resolution XPS spectra (Figure 5.27d, Figure 5.34d) acquired at 300 K and 450 K: after complete DBTP debromination, the Br $3d_{5/2}$ core level is shifted from 69.3 eV to 67.8 eV, while Cl $2p_{3/2}$ is partially shifted from 197.0 eV to 199.3 eV and the C 1s halogen component from 284.5 eV to 284.8 eV. After reaching a maximum at 450 K, the Cl-C intensity is reduced, concurrently with the total carbon amount, indicating desorption of chlorinated molecules from Au(111) to be more favorable than dechlorination (Figure 5.27c, Figure 5.35). All these observations clearly demonstrate that the radicals created at the carbon atoms upon debromination can again be attacked by halogens present on the surface. This provides unprecedented experimental evidence of reversible on-surface dehalogenation.

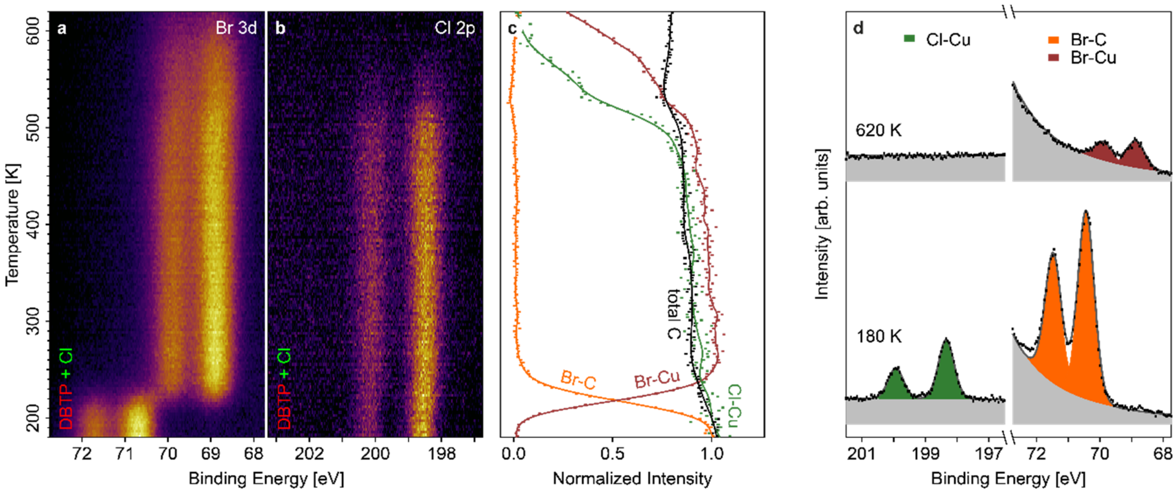

Figure 5.26 | Temperature evolution of DBTP + Cl on Cu(111)

TP-XPS maps of **a** Br 3d and **b** Cl 2p doublets during the annealing of DBTP + Cl on Cu(111). **c** Temperature dependence for all chemical states of Cl and Br, together with the total carbon coverage. The trend of each experimental curve (dots) is indicated with a spline (solid line). **d** High-resolution XPS for DBTP + Cl on Cu(111). Cl 2p (left) and Br 3d (right) doublets of the as prepared sample (bottom) and after almost complete halogen desorption (top).

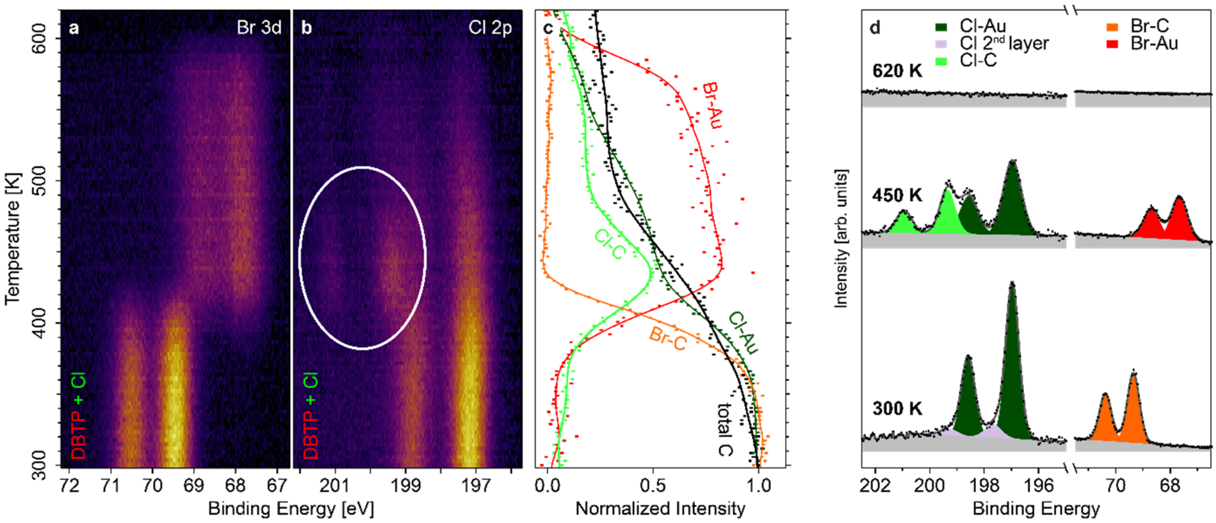

Figure 5.27 | Temperature evolution of DBTP + Cl on Au(111): Halogen exchange

TP-XPS maps of **a** Br 3d and **b** Cl 2p doublets during the annealing of DBTP + Cl on Au(111). The emergence of the Cl-C component is indicated with a white circle in **b**. **c** Temperature dependence for all chemical states of Cl and Br, together with the total carbon coverage. The trend of each experimental curve (dots) is indicated with a spline (solid line). **d** High-resolution XPS for DBTP + Cl on Au(111). Cl 2p (left) and Br 3d (right) doublets of the as prepared sample (bottom), after halogen exchange (center) and after halogen desorption (top).

Prompted by these findings, we included this so far neglected reversibility in the differential rate equations used to fit the experimental kinetic curves (*vide infra*). The relevant experimental kinetic curves extracted from the TP-XPS maps, *i.e.*, the Br-C and Br-Metal components for Cu(111) and additionally the C-C component for Au(111), are reported in Figure 5.28. The dehalogenative aryl-aryl coupling on both surfaces can be described by the following reaction pathway

$$A \underset{k_{-1}}{\overset{k_1}{\rightleftarrows}} B + X$$
$$2B \xrightarrow{k_2} C$$

Equation 5.1 | Chemical equation for dehalogenative aryl-aryl coupling

where A, B, X and C represent the intact DBTP precursor, the intermediate (OM on Cu(111), molecular radicals on Au(111)), the chemisorbed bromine atom and the covalently coupled product (*i.e.* PPP), respectively. k_1, k_{-1} and k_2 are the kinetic constants for each reaction step, *i.e.*, DBTP debromination, re-bromination of intermediate, and C-C coupling.

Owing to the high energetic stability of the OM on Cu(111), the re-bromination process is suppressed on this surface. Consequently, the rate equations describing DBTP debromination (polymerization) reduce to a first (second) order Polanyi Wigner equation,[258] well reproducing the corresponding experimental kinetic curves (Figure 5.28a, Figure 5.36).

In case of Au(111) the experimental kinetic curves cannot be successfully fit with a Polanyi-Wigner equation (Figure 5.37), instead we need the whole set of differential rate equations including reversibility of the dehalogenation (Figure 5.28a, see Supporting Information for further details). Our excellent fit confirms that the extended temperature range for debromination observed on Au(111) is associated to reversibility of this process, competing with the irreversible C-C bond formation, *i.e.*, polymerization.

Moreover, the fits performed in the two cases provide the activation energies for the involved processes (Figure 5.28b). Debromination of DBTP on Cu(111) requires 0.62 eV and the conversion of the OM assembly into polymers 1.08 eV to be initiated. In contrast, on Au(111) the energy barrier for debromination, 0.95 eV, is larger than the one on Cu(111) and the created molecular radicals are energetically unfavorable and hence immediately subject to two possible pathways (Figure 5.24): (i) back reaction towards the formation of intact DBTP (0.67 eV), or (ii) covalent coupling towards the formation of PPP chains (0.70 eV).

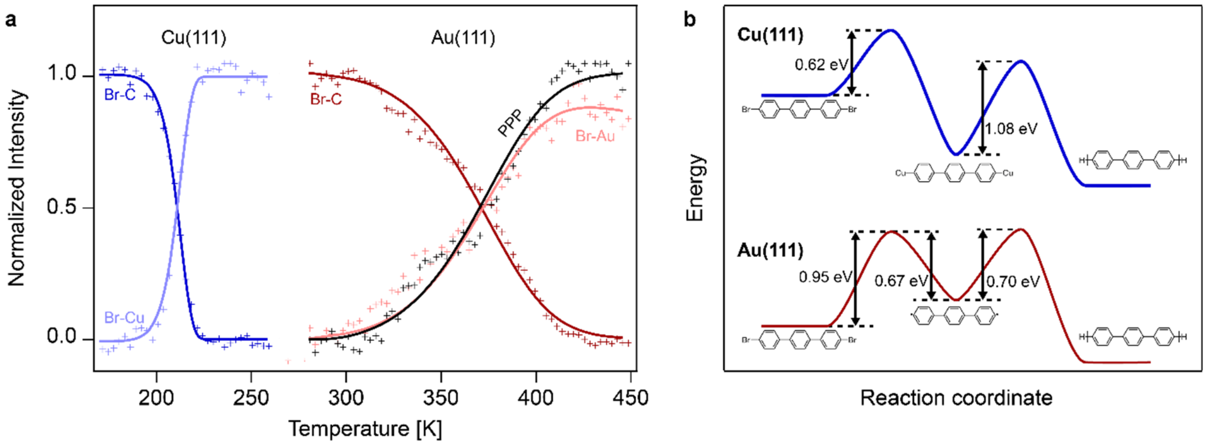

Figure 5.28 | Kinetic model

a Temperature evolution of Br-C, Br-Metal and PPP normalized signals extracted from the TP-XPS maps (markers) and fitted with the kinetic models for Cu(111) and Au(111) described in the text (solid lines). **b** Experimentally derived reaction profiles for the PPP formation from DBTP on the two substrates. The energy barriers have been obtained from fitting the kinetic curves in **a** and Figure 5.36.

Our experimentally determined energy barriers are in good agreement with those estimated using density functional theory (DFT).[68,259] In particular, for bromobenzene on Cu(111) Björk *et al.*[259] reported a bromine dissociation barrier of 0.66 eV yielding a surface bound radical that is about 0.7 eV more stable than the precursor, which suppresses re-bromination in accordance with our experimental results. On the other hand, the debromination barrier for bromobenzene on Au(111) is roughly 1 eV, resulting in a phenyl radical which is energetically about as stable as the precursor itself. Debrominated 1,3,5-tris(4-bromophenyl)benzene (TBB) was even found to be 0.25 eV less stable than the brominated TBB on Au(111).[68] Both simulations of the debromination process on Au(111) thus indicate re-bromination to be energetically possible, in agreement with our observation. The energy barrier for the covalent coupling towards PPP chains on Au(111) mainly arises from the diffusion energy barrier of debrominated DBTP. Our experimentally derived value of 0.70 eV for debrominated DBTP (which consists of 3 phenyl rings) is between the DFT-calculated diffusion barriers of debrominated bromobenzene (0.22 eV; 1 phenyl ring) and debrominated TBB (1.2 eV; 4 phenyl rings).

Such deeper insight into dehalogenative aryl-aryl coupling offers a better mechanistic understanding of this broadly exploited on-surface reaction and is a prerequisite for improving its efficiency and selectivity. In absence of stable OM formation the rate-limiting step for polymerization is the breaking of C-halogen bonds, whose temperature can be lowered with the choice of halogen functionalization, thus limiting undesired side reactions. On the other hand, the temperature range of the dehalogenation process extends in case of reversibility, increasing the likelihood of cross-talk with potential additional reactions occurring at higher temperature.[59] Therefore, to optimize polymer length, the halogens would ideally detach from the precursor molecule at as low temperature as possible and desorb from the surface right after, while the resulting radicals would immediately undergo polymerization. From a different perspective, however, such conditions could be detrimental to the growth of extended crystalline two-dimensional networks, which benefit from reversibility in the covalent coupling step.[260–262] Therefore, depending on the type of on-surface reaction and conditions at which it takes place, it is crucial to select the best catalyst/reagents combination to achieve a specific desired product.

5.3.1 Supporting Information for the publication "Reversible dehalogenation in on-surface aryl-aryl coupling"

5.3.1.1 Methods

5.3.1.1.1 Sample preparation and XPS experiments

The on-surface synthesis experiments were performed under ultrahigh vacuum (UHV) conditions with base pressure below 2×10^{-10} mbar. Cu(111) and Au(111) substrates (MaTeck GmbH) were cleaned by repeated cycles of Ar+ sputtering (1 keV) and annealing (470 ºC). DBTP molecules (Sigma Aldrich) were thermally evaporated onto the clean Cu(111) and Au(111) surfaces from quartz crucibles heated at 125 ºC. Similarly, $CuCl_2$ and AuCl (Sigma Aldrich) were used as sources of chlorine via thermal sublimation upon heating the quartz crucibles to 200 ºC and 70 ºC, respectively, to avoid cross-contamination of the single crystal substrates from the co-deposited metal (Figure 5.30). Chlorine is assumed to adsorb atomically on the two metal surfaces[263], and no significant chemical shift of the Cl 2p core level doublet (Cl $2p_{3/2}$ and Cl $2p_{1/2}$) is observed for sub-monolayer Cl coverages with TP-XPS up to the desorption temperature (above 600 K for Cu(111) and 580 K for Au(111)) (Figure 5.31 and Figure 5.33). Only upon deposition of a chlorine multilayer on Au(111), a second Cl 2p doublet emerges in XPS, shifted by 0.7 eV with respect to the component for Cl bound to the gold surface (Figure 5.31b and Figure 5.32).

XPS measurements were performed at the X03DA beamline (PEARL endstation)[95] of the SLS synchrotron radiation facility (Villigen, Switzerland) using linearly polarized radiation with photon energy of 425 eV. XPS spectra were obtained in normal emission geometry, using a Scienta R4000 hemispherical electron analyzer equipped with a multichannel plate (MCP) detector. TP-XPS maps were acquired during the heating of the sample (constant heating rate of 0.1 K/s) using the “fixed” mode (snapshots of the C 1s, Br 3d and Cl 2p core levels, 5 s per spectrum) with 100 eV pass energy. The samples (mounted on a double stack sample-holder) were heated by a built-in filament placed in close proximity to the back surface of the crystals. The sample temperature during each heating ramp was measured via a thermocouple positioned onto the top plate of the sample-holder, close to the sample surface. The TP-XPS maps have a resolution of 2.9 K in temperature and 29 s in time. XPS control experiments have been carried out in-house, using a monochromatized Al K_α X-ray radiation source equipped with a Scienta R3000 display analyzer. For the quantification of contamination or coverages, core levels of C 1s, Br 3d, Br 3p, Cl 2p, Au 4f and Cu 3p were fitted in CasaXPS with Voigt line shapes.

5.3.1.1.2 STM experiments

STM images were acquired with a low-temperature scanning tunneling microscope (Scienta Omicron) operated at 4 K, if not mentioned differently, in constant-current mode using an etched tungsten tip. Bias voltages V_B are given with respect to the sample.

5.3.1.2 Length distribution

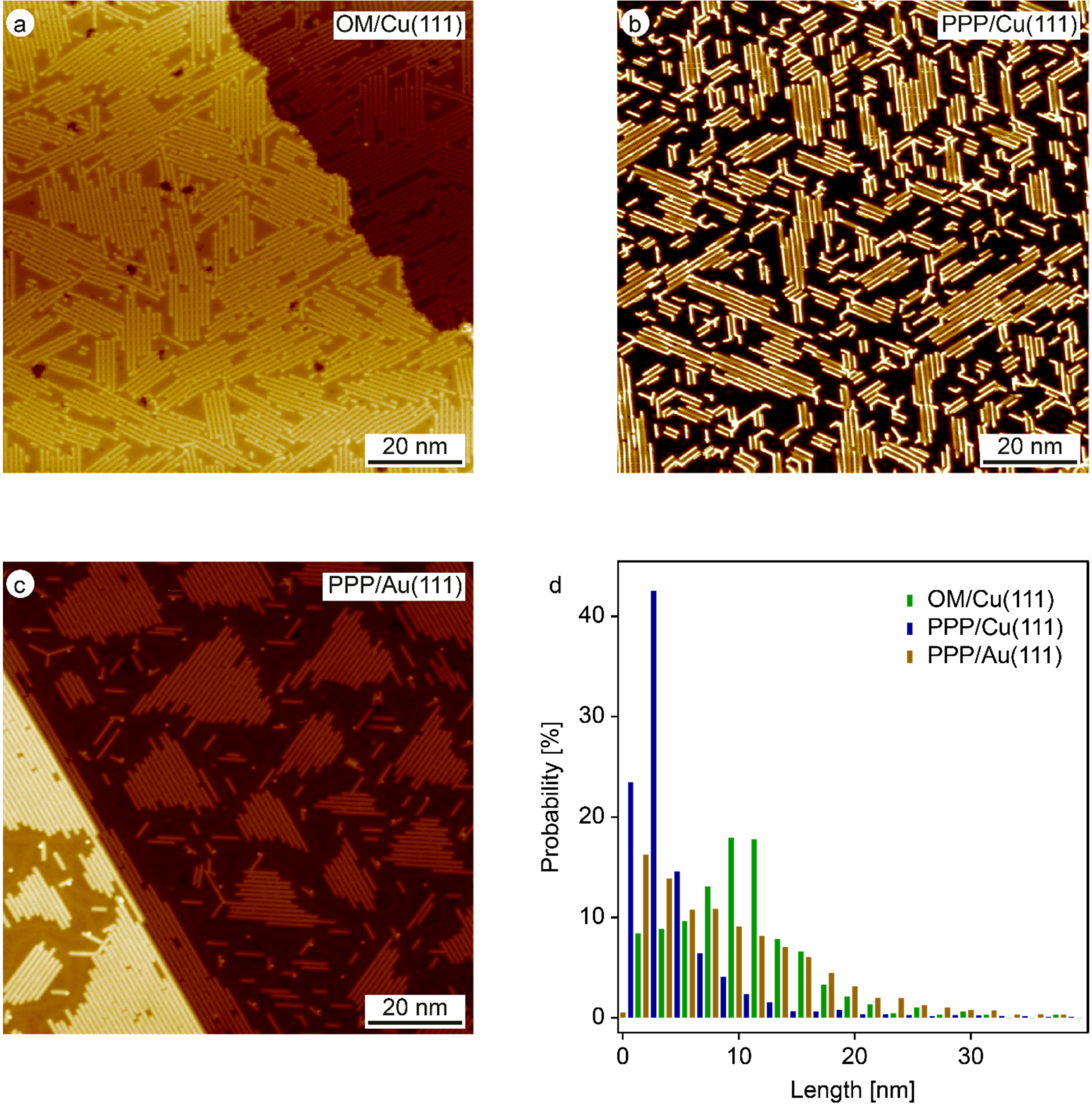

Figure 5.29 | Length distribution of OM on Cu(111) and PPP on Cu(111) and Au(111)

a Organometallic phase (OM) of DBTP formed on Cu(111) (V_B = -1.0 V; I_T = 30 pA). Poly(*para*-phenylene) (PPP) on **b** Cu(111) (V_B = 0.1 V; I_T = 30 pA) and **c** Au(111) (V_B = 1.0 V; I_T = 50 pA). **d** Length distribution of the organometallic phase of DBTP after RT deposition on Cu(111) (664 chains), PPP formed on Cu(111) (3545 polymers) and Au(111) (2508 polymers).

The average and median length of OM chains on Cu(111) are 9.4 nm and 9.1 nm, respectively. This average and median length are strongly reduced to 4.8 mm and 3.0 mm after annealing this sample to 450 K to form PPP. In contrast, the average length amounts to 11.5 nm and the median to 9.6 nm for PPP on Au(111).

5.3.1.3 Control Experiments: Metal co-deposition upon Cl deposition using AuCl and $CuCl_2$

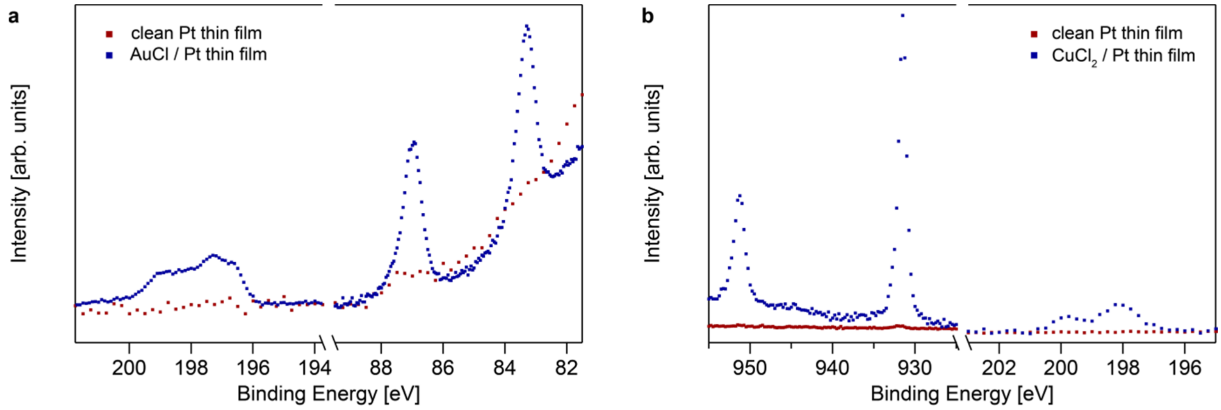

Figure 5.30 | Metal contamination for AuCl and $CuCl_2$ deposition

XPS spectra after depositing **a** AuCl and **b** $CuCl_2$ on a clean Pt thin film. Based on these spectra we assess a Cl:Au = 4:1 ratio when depositing AuCl and a Cl:Cu =1:1 ratio for $CuCl_2$.

5.3.1.4 Chlorine on Au(111)

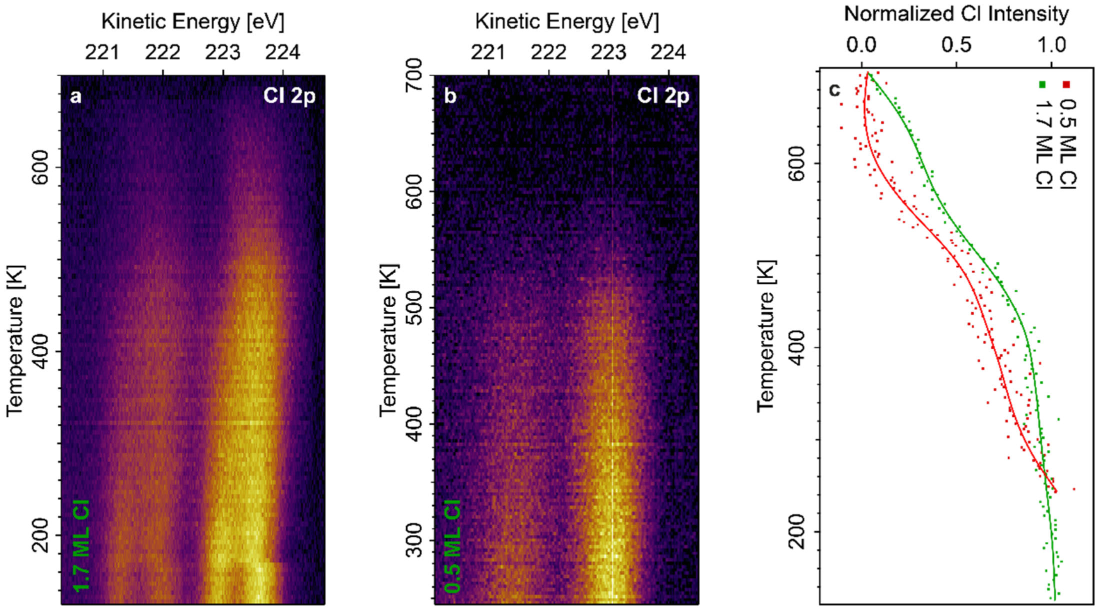

Figure 5.31 | TP-XPS of Cl 2p doublet upon Cl deposition on Au(111)

TP-XPS maps of Cl 2p core levels for Cl on Au(111) with an initial coverage of **a** 0.5 ML and **b** 1.7 ML with the corresponding Cl-Au kinetic curves for both initial coverages in **c**. The experimental data is presented by dots and their trend by solid lines.

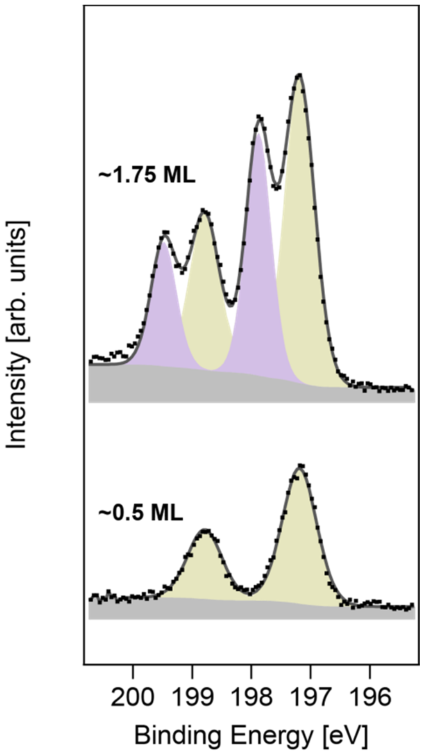

Figure 5.32 | HR-XPS of multilayer and sub-monolayer Cl on Au(111)
Cl 2p XPS signal for multilayer and sub-monolayer Cl coverage on Au(111) recorded at 100 K.

5.3.1.5 *Chlorine on Cu(111)*

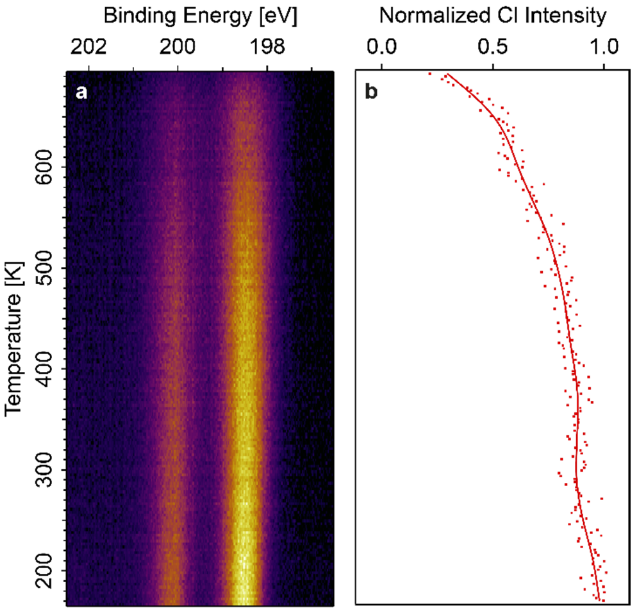

Figure 5.33 | TP-XPS of Cl 2p doublet upon Cl deposition on Cu(111)
a TP-XPS map of Cl 2p core levels for Cl on Cu(111) with an initial coverage of 0.7 ML with the corresponding Cl-Cu kinetic curve in **b**, whereas the experimental data is depicted as dots and the trend as solid line.

For Cu(111), chlorine desorption could not be completed owing to temperature limitations in the experimental setup.

5.3.1.6 HR-XPS and TP-XPS maps of C 1s core level for Au(111)

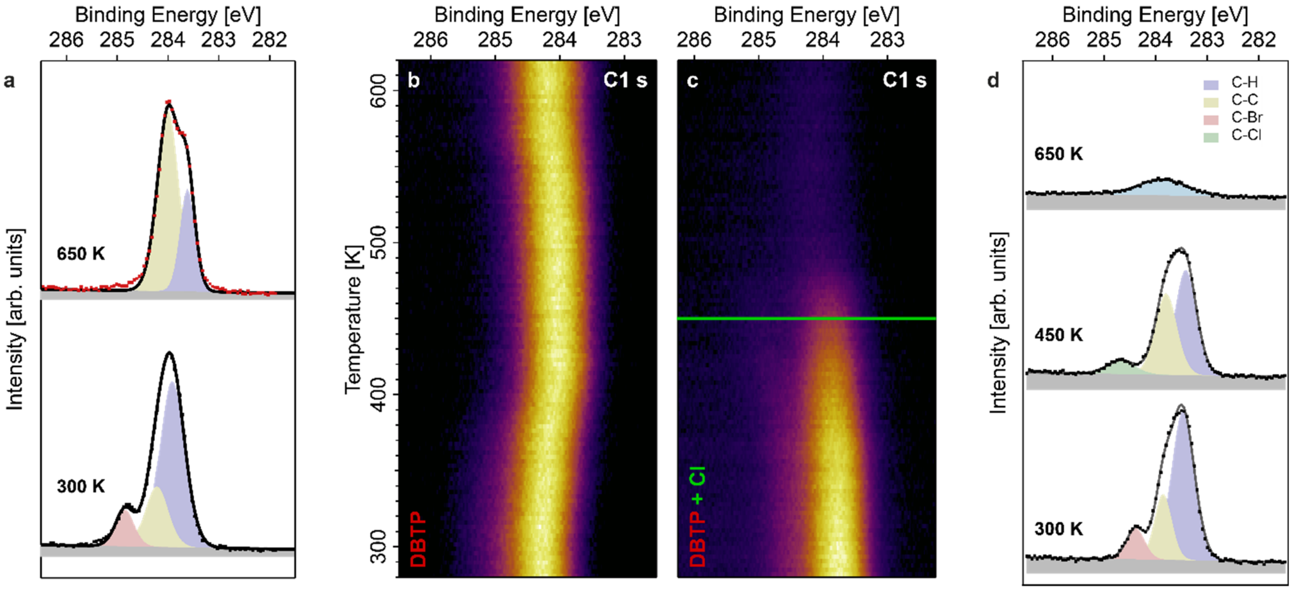

Figure 5.34 | HR-XPS and TP-XPS of C 1s core level for DBTP and DBTP+Cl on Au(111)

C 1s core level HR-XPS of **a** DBTP only and **d** DBTP co-adsorbed with Cl. C 1s core level TR-XPS of **b** DBTP only and **c** DBTP co-adsorbed with Cl. HR-XPS in **a** and **d** were recorded after annealing to the inscribed temperatures. The spectrum in **d** center, taken at the temperature indicated by a green line in **c**, the emergence of the C-Cl component is observed. In **a** and **d**, the shaded areas are background (gray), carbon components (colors), resulting in the overall intensity (solid line) were derived from fitting the experimental data (dots).

5.3.1.7 Fitting parameters for HR-XPS

5.3.1.7.1 DBTP on Au(111)

Component	Temperature [K]	Binding Energy [eV]	FWHM	Area	Concentration[%]
Br 3d Br-C	**300**	**69.78 / 70.81**	**0.559**	**5251**	**100**
C 1s C-Br	**300**	**284.90**	**0.432**	**2057**	**11.11**
C 1s C-C	**300**	**284.27**	**0.527**	**4115**	**22.22**
C 1s C-H	**300**	**283.96**	**0.576**	**12344**	**66.67**
C 1s C-C	**600**	**284.05**	**0.496**	**8675**	**71.91**
C 1s C-H	**600**	**283.67**	**0.342**	**3389**	**28.09**

Table 5.3 | Fitting parameters for HR-XPS for DBTP on Au(111)

5.3.1.7.2 Sub-monolayer Cl on Au(111)

Component	Temperature [K]	Binding Energy [eV]	FWHM	Area	Concentration[%]
Cl 2p Cl-Au	**300**	**197.24 / 198.84**	**0.689**	**5658**	**100**

Table 5.4 | Fitting parameters for HR-XPS for sub-monolayer Cl on Au(111)

5.3.1.7.3 1.7 Monolayer Cl on Au(111)

Component	Temperature [K]	Binding Energy [eV]	FWHM	Area	Concentration[%]
Cl 2p Cl-Au	**300**	**197.19 / 198.79**	**0.603**	**11181**	**59.83**
Cl 2p Cl-Cl	**300**	**197.89 / 199.49**	**0.511**	**7507**	**40.17**

Table 5.5 | Fitting parameters for HR-XPS for multi-layer Cl on Au(111)

5.3.1.7.4 DBTP and Cl on Au(111)

Component	Temperature [K]	Binding Energy [eV]	FWHM	Area	Concentration[%]
Cl 2p Cl-Cl	300	197.67 / 199.30	0.724	776	9.90
Cl 2p Cl-Au	300	196.97 / 198.60	0.577	7066	90.10
Cl 2p Cl-Au	450	196.97 / 198.57	0.777	4544	65.93
Cl 2p Cl-C	450	199.35 / 200.95	0.676	2348	34.07
Br 3d Br-C	300	69.35 / 70.38	0.524	3203	100
Br 3d Br-Au	450	67.66 / 68.68	0.686	2608	100
C 1s C- Br	300	284.49	0.414	1503	11.11
C 1s C-C	300	283.96	0.393	3005	22.22
C 1s C-H	300	283.57	0.525	9016	66.67
C 1s C-Cl	450	284.77	0.631	1016	8.71
C 1s C-C	450	283.90	0.492	4643	39.78
C 1s C-H	450	283.52	0.494	6011	51.51
C 1s remaining [a]	650	283.97	1.106	2047	100

Table 5.6 | Fitting parameters for HR-XPS of DBTP+Cl on Au(111)

[a] Fit of C 1s core level of the remaining unidentified molecular structures (Figure 5.35b) after desorption of all chlorinated species.

5.3.1.7.5 DBTP and Cl on Cu(111)

Component	Temperature [K]	Binding Energy [eV]	FWHM	Area	Concentration[%]
Br 3d Br-C	300	70.48 / 71.51	0.567	7333	100
Br 3d Br-Cu	650	68.91 / 69.94	0.622	1152	100
Cl 2p Cl-Cu	300	198.38 / 199.97	0.532	1960	100

Table 5.7 | Fitting parameters for HR-XPS of DBTP+Cl on Cu(111)

5.3.1.8 STM of DBTP co-adsorbed with chlorine

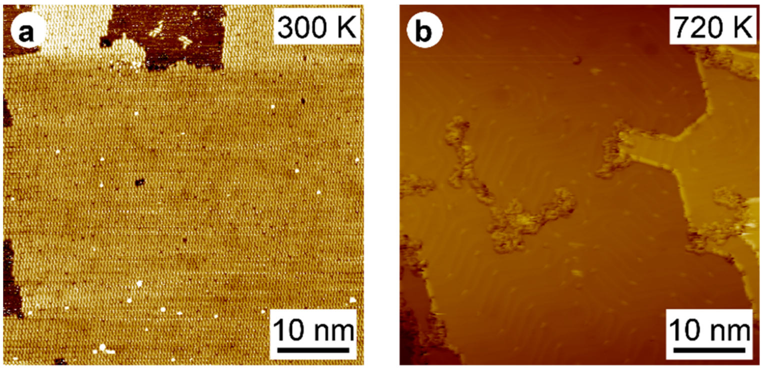

Figure 5.35 | STM of DBTP co-adsorbed with Cl

STM images of DBTP co-adsorbed with Cl on Au(111) after **a** RT deposition (V_{Bias} = -1 V; I_T = 15 pA) and **b** after the temperature ramp to 720 K (V_{Bias} = -1 V; I_T = 30 pA).

All images were recorded at 78 K.

The initially high DBTP coverage after RT deposition is reduced by about 85% after a temperature ramp to 720 K if co-deposited with Cl atoms, because of desorption of chlorinated molecular species.

5.3.1.9 Kinetic Models

The surface-assisted aryl-aryl coupling reaction consists of homolytic cleavage of the C-Br bond (debromination) and subsequent molecular radical addition, summarized by the reaction scheme in Equation 5.1. The kinetic constants are of the form $k_i = \nu \cdot e^{\frac{\Delta E_i}{k_B T}}$, where ν is the attempt frequency (set to 10^{13}), ΔE_i is the activation energy of the process, k_B is the Boltzmann constant, and T is the temperature.

This aforementioned reaction pathway is described by the following set of differential equations:

$$\begin{cases} \dfrac{d[A]}{dt} = -k_1[A] + k_{-1}[B][X] \\ \dfrac{d[B]}{dt} = k_1[A] - k_{-1}[B][X] - k_2[B]^2 \\ \dfrac{d[X]}{dt} = k_1[A] - k_{-1}[B][X] \\ \dfrac{d[C]}{dt} = k_2[B]^2 \end{cases}$$

Equation 5.2 | Fitting equations of kinetic curves for DBTP on Au(111)

As our experiments were performed with a constant heating rate α, the derivative with respect to time t can be replaced by one with respect to temperature T: $\frac{d}{dt} = \frac{1}{\alpha}\frac{d}{dT}$.

In case of DBTP/Cu(111), the intermediate corresponds to an energetically stable organometallic (OM) compound, hence the kinetic constant for re-bromination k_{-1} becomes negligibly small, reducing the rate equations to:

$$\begin{cases} \dfrac{d[A]}{dt} = -k_1[A] \\ \dfrac{d[B]}{dt} = k_1[A] - k_2[B]^2 \\ \dfrac{d[X]}{dt} = k_1[A] \\ \dfrac{d[C]}{dt} = k_2[B]^2 \end{cases}$$

Equation 5.3 | Fitting equation of kinetic curves for DBTP on Cu(111)

The first of these equations, describing DBTP debromination, corresponds to the Polanyi-Wigner equation for a first order reaction, while the fourth equation, depicting the polymerization, is a Polanyi-Wigner equation for a second order reaction.[258] As the debromination process is completed when the polymerization starts, both processes can be analyzed independently. The successful fitting of experimental data (Figure 5.28a, Figure 5.36) results in a debromination energy barrier of 0.62 eV and polymerization energy barrier of 1.08 eV.

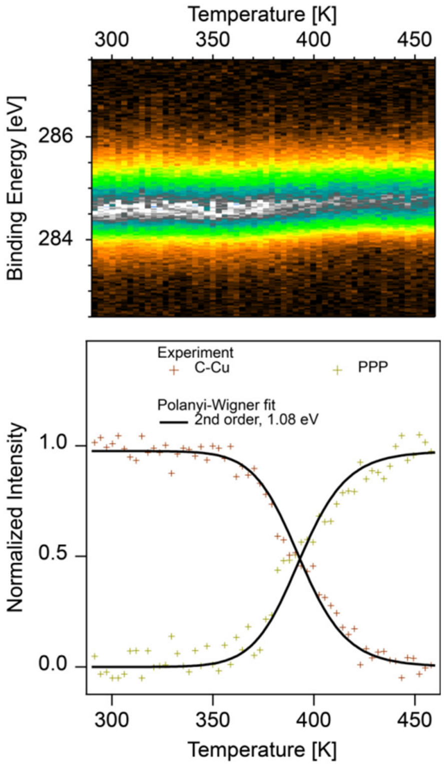

Figure 5.36 | Kinetic curves for polymerization on Cu(111)

C 1s TP-XPS map of DBTP on Cu(111) (top) and the extracted temperature evolution of the C-Cu and PPP signal (markers, bottom), fitted with a Polanyi-Wigner equation for a 2nd order reaction and 1.08 eV activation energy (solid line).

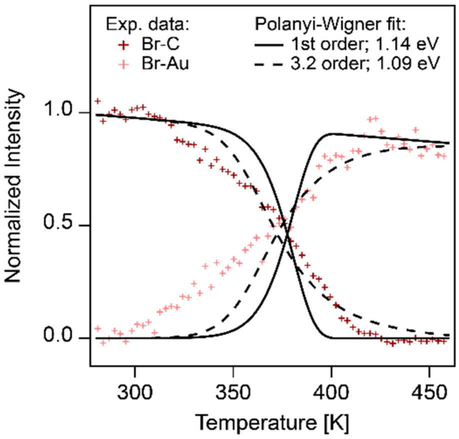

Figure 5.37 | Polanyi-Wigner equation fit of kinetic curves for DBTP on Au(111)

Temperature evolution of the Br-C and Br-Au signal for DBTP on Au(111) (markers) fitted with two different Polanyi-Wigner equations. The solid line represents a fit assuming a reaction order 1, analogous to Cu(111), whereas the reaction order was a fitting variable for the fit depicted by the dashed line.

While the Polanyi-Wigner equations describe DBTP debromination and polymerization on Cu(111) very accurately, they completely fail for Au(111) as displayed in Figure 5.37. Hence, reversibility of the dehalogenation step must be taken into account. Therefore, the full set of differential equations (Equation 5.2) was fitted to the Br-C, surface stabilized radicals (not observed, thus set to zero), Br-Au and PPP signal intensities extracted from the TP-XPS maps of Br 3d and C 1s (Figure 5.25d and Figure 5.34b, respectively), and the result of the fit is shown in Figure 5.28a.

5.4 Publication (under Review in Angew. Chem. Int. Ed.): "Near-enantiopure trimerization of 9-Ethynylphenanthrene on a chiral metal surface"

I was involved in the planning of the experiments, collected and analyzed the experimental data, and wrote the manuscript with input from all co-authors.

Near-enantiopure trimerization of 9-Ethynylphenanthrene on a chiral metal surface

Samuel Stolz,[§,‡] Aliaksandr V. Yakutovich,[§,†] Jan Prinz,[§,‡] Thomas Dienel,[§,⊥] Carlo A. Pignedoli,[§] Harald Brune,[‡] Oliver Gröning,[§] and Roland Widmer*[,§]

[§]nanotech@surfaces Laboratory, Empa – Swiss Federal Laboratories for Materials Science and Technology, Überlandstrasse 129, CH -8600 Dübendorf, Switzerland

[‡]Institute of Physics, École Polytechnique Fédérale de Lausanne, CH-1015 Lausanne, Switzerland

* roland.widmer@empa.ch

Enantioselectivity in heterogeneous catalysis strongly depends on the chirality transfer between catalyst surface and all reactants, intermediates, and the product along the reaction pathway. Here we report the first enantioselective on-surface synthesis of molecular structures from an initial racemic mixture and without the need of enantiopure modifier molecules. The reaction consists of a trimerization of prochiral 9-ethynylphenanthrene (9-EP) upon annealing to 500 K on the chiral Pd_3-terminated PdGa$\{111\}$ surface into essentially enantiopure, homochiral 9-EP propellers. The observed behavior is in stark contrast to the reaction of 9-EP on the chiral Pd_1-terminated PdGa$\{111\}$ surface; where 9-EP monomers that are in nearly enantiopure configuration, dimerize without particular enantiomeric excess. Our findings demonstrate strong chiral recognition and a significant ensemble effect in the PdGa system, hence highlighting the huge potential of chiral intermetallic compounds for enantioselective synthesis and underlining the importance to control the catalytically active sites at the atomic level.

The pronounced enantiospecific physiological effects of chiral molecules, requires enantioselective asymmetric synthesis, *e.g.*, in pharmaceutical or food industry. Homogeneous catalysis is most widely used to obtain enantioselective synthesis via chirality transfer directly from the catalyst's organic ligand(s) despite the fact that it involves tedious separation, elaborate recycling, and its restriction to a limited temperature range.[5,6] Difficulties in separation and recycling can be alleviated by moving from homogeneous to heterogeneous catalysis.

Rational engineering of such catalysts requires fundamental understanding of the enantiospecific reactant-catalyst interaction, reaction mechanism, and kinetics. This can be achieved by investigating the interaction of molecules (educts and products) with the catalyst's surface on the atomic and molecular level and under idealized conditions, *i.e.*, using single crystal surfaces in ultra-high vacuum (UHV).[210,211] For this purpose, achiral surfaces are commonly rendered chiral by using molecular modifiers.[7–15] This approach is marred by the need of enantiopure modifier molecules, low thermal stability, and increased complexity emerging from molecule-molecule interactions. The usage of chiral metal surfaces promises to considerably reduce complexity and increase thermal stability. Such surfaces were created by cutting achiral single crystals along low-symmetry, *i.e.*, high Miller index, directions.[214,215] Although the resulting surfaces exhibit only low densities of chiral centers, enantioselective adsorption and decomposition of , *e.g.*, chiral tartaric and aspartic acid was reported on Cu$(643)^{R/S}$.[212,213]

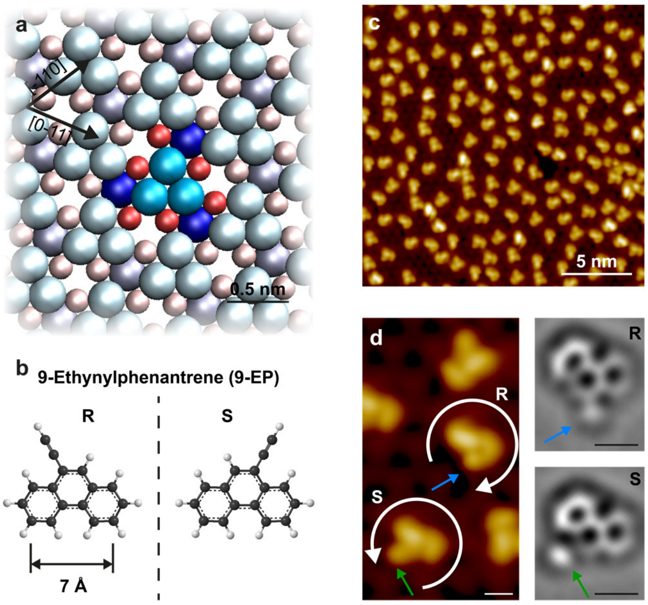

Figure 5.38 | Baseline of 9-EP on PdGa:A(-1-1-1)Pd$_3$

a Surface structure of PdGa:A(-1-1-1)Pd$_3$ with the chirality of the surface highlighted in saturated colors for one Pd trimer (top layer Pd$_3$ bright blue, z=0 nm) and its neighbors: second layer (Ga$_3$ red, z=-85 pm) and third layer (Pd$_1$ dark blue, z=-161 pm). **b** molecular structure of prochiral 9-Ethynylphenanthrene (9-EP), which appears in two distinguishable surface enantiomers R and S when restricted to a planar configuration. **c** STM image of 9-EP after room temperature deposition on PdGa:A(-1-1-1)Pd$_3$ (bias voltage $V_B = 20\ mV$, tunneling current $I_T = 1\ nA$). **d** STM image (left; $V_B = 20\ mV$, $I_T = 10\ nA$) and Gaussian-Laplace filtered nc-AFM images (right) of R and S enantiomers.

Low-index surfaces of intrinsically chiral metals offer the advantage of exhibiting orders of magnitude more chiral centers. However, today only surfaces of chiral PdGa have been sufficiently well characterized to allow the investigation of enantiospecific molecule-surface interactions, resultant molecular structure, and their formation kinetics.[22,54] Owing to its non-centrosymmetric nature,[25] PdGa exists as two enantiomorphs, PdGa:A and PdGa:B, and all its bulk truncated surfaces are chiral.[54] Here, we focus on the structurally dissimilar three-fold symmetric (111) and $(\bar{1}\bar{1}\bar{1})$ surfaces, one terminated by single, isolated Pd atoms, referred to as Pd$_1$, the other by isolated Pd trimers, accordingly denoted Pd$_3$ (Figure 5.38a).[48] Because of this difference in combination with similar electronic properties, identical symmetry group, and the same lattice parameters,[48] PdGa$\{111\}$ surfaces are ideal to disentangle the influence of geometric and electronic, *i.e.*, ensemble and ligand, effects in enantioselective heterogeneous catalysis.[264–266]

The chirality of Pd$_1$ manifests itself in enantioselective room temperature (RT) adsorption with an enantiomeric excess $ee = 100\% * \frac{|\#R-\#S|}{\#R+\#S} = 96\% \pm 2\%$ for prochiral 9-Ethynylphenanthrene (9-EP see Figure 5.38b).[27] However, no enantioselective reaction between molecules could be demonstrated on that surface.

Here, we study the near-enantiopure trimerization from an initial racemic mixture of 9-EP on the Pd$_3$-terminated PdGa$\{111\}$ surface by scanning tunneling probe microscopy (STM), CO-sensitized non-contact atomic force microscopy (nc-AFM), and density functional theory (DFT) calculations.

Deposition of sub-monolayer coverages of 9-EP onto the PdGa:A(-1-1-1)Pd$_3$ (A:Pd$_3$) surface kept at RT results in a homogeneous coverage of well isolated molecules when imaged at 5 K (Figure 5.38c). Analysis of adsorption site and molecule orientation reveals that the vast majority of 9-EP are present in two disparate configurations, each appearing in three symmetrically equivalent geometries. Combining high-resolution STM and nc-AFM images, the nature of these two distinct 9-EP configurations can be assigned to R and S surface enantiomorphs of the molecule (Figure 5.38d). The STM signature of the S configuration is an elongated protrusion (green arrows in Figure 5.38d) attributed to the alkyne group pointing towards the right of the phenanthrene backbone. Conversely, the adsorption configuration of the R surface-enantiomer leads to a dot like imaging of the alkyne group (blue arrows in Figure 5.38d).

Deposition at 100 K and 300 K substrate temperature results in basically identical adsorption configurations, as evidenced in Figure 5.39a-b. In both cases, the adsorbates are R and S enantiomers with equal abundance (100 K: $ee = 4\% \pm 5\%$; 300 K: $ee = 4\% \pm 4\%$). In some cases, S enantiomers seem to have some co-adsorbate, most likely CO, attached (labelled S$_{CO}$). Upon annealing to 350 K an $ee = 19\% \pm 5\%$ in favor of R evolves (Figure 5.39c). We therefore conclude that (i) the energy barrier for S to R interconversion cannot be overcome at 300 K, and (ii) R 9-EP is energetically preferred over S 9-EP on A:Pd$_3$. Concomitantly, the occurrence of S$_{CO}$ is reduced to virtually zero due to CO desorption,[45] and a new species labelled R' (Figure 5.40b), representing the same surface enantiomorph as R but being adsorbed on a different site, emerges in low numbers.

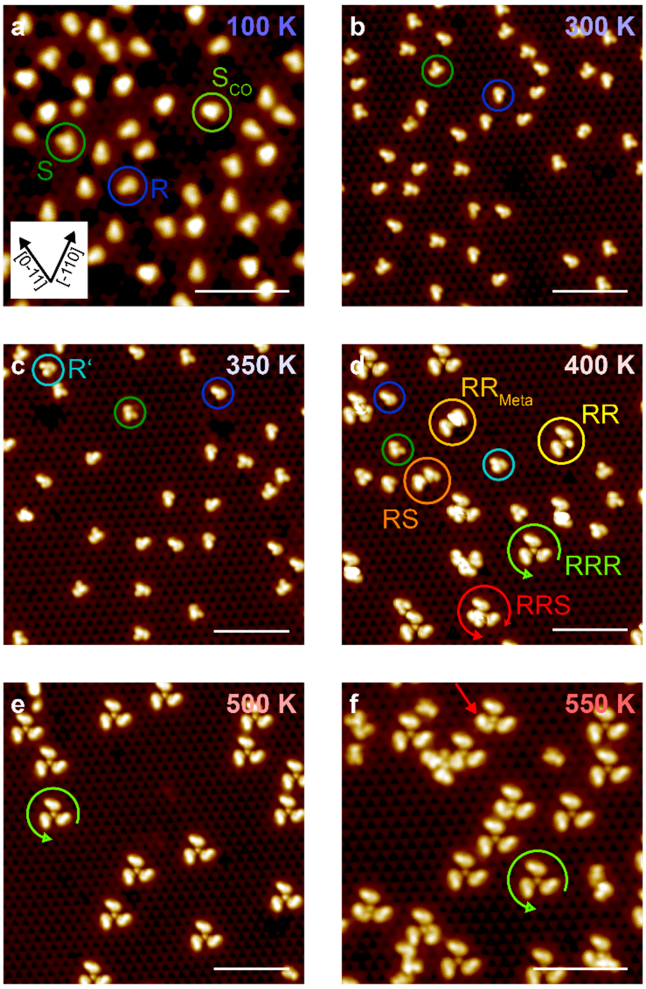

Figure 5.39 | Temperature evolution of 9-EP on PdGa:A(-1-1-1)Pd$_3$

STM images of 9-EP on PdGa:A(-1-1-1)Pd$_3$. As deposited at **a** 100 K and **b** 300 K. Annealing sereies of 9-EP on PdGa:A(-1-1-1)Pd$_3$ to **c** 350 K, **d** 400 K, **e** 500 K, and **f** 550 K. STM settings: **a** $V_B = 50\ mV, I_T = 50\ pA$; **b-f** $V_B = 20\ mV, I_T = 1\ nA$. 9-EP/PdGa:A(-1-1-1)Pd$_3$ structures are labelled according to the nomenclature in the text. The red arrow in **f** indicates an exemplary 9-EP integrated in a trimer, but with disintegrated alkyne group. All scale bars correspond to 5 nm.

We attribute the moderate R enantiomeric excess on A:Pd$_3$ to dissimilar lattice sites of the R and S alkyne groups, resulting in slight adsorption energy differences. Whereas the alkyne group peripherally overlaps with one Pd atom of the substrate trimer for R, it completely covers the Pd trimer for S. The phenanthrene backbone exhibits in both cases an identical adsorption configuration (Figure 5.40a). This difference in adsorption geometry will become decisive in the formation of chiral 9-EP oligomers, as we will show in the following.

Upon annealing at 400 K, 9-EP dimers and trimers are forming (Figure 5.39d), of which 92% exhibit well defined configurations that can be classified into the 5 species shown in Figure 5.40c-g. We will refer to 9-EP trimers as propellers based on their appearance. A common feature of all 9-EP oligomers is that they are linked with their alkyne group positioned on the same Pd trimer, facing each other. Additionally, several peculiarities related to the participation of R and S enantiomers in the oligomers are recognized. First, the R enantiomers in all coupled structures are on identical adsorption sites as the isolated R (except for one 9-EP contained in the RR$_{\text{Meta}}$ dimer in Figure 5.40d). Second, S' in a propeller exhibits a different positional and orientational configuration as the isolated S. Third, the entire absence of homochiral S or S' dimers and propellers. Without enantioselectivity, one expects a statistical propeller occurrence of $RRR{:}\,RRS'{:}\,RS'S'{:}\,S'S'S' = {}^{1}/_{8}{:}{}^{3}/_{8}{:}{}^{3}/_{8}{:}{}^{1}/_{8}$. Instead, we observe relative abundancies of ${}^{6}/_{8}{:}{}^{2}/_{8}{:}{}^{1}/_{100}{:}\,0$ (459 monomer units analyzed). This implies a strong bias towards the incorporation of R 9-EP in propellers, the probability amounts to roughly 90%, and yields an RRR enantiomeric excess of $ee_{RRR} = 100\% * \frac{\#RRR-\#RRS'-\#RS'S'-\#S'S'S'}{\#RRR+\#RRS'+\#RS'S'+\#S'S'S'} = 49\% \pm 4\%$ at 400 K.

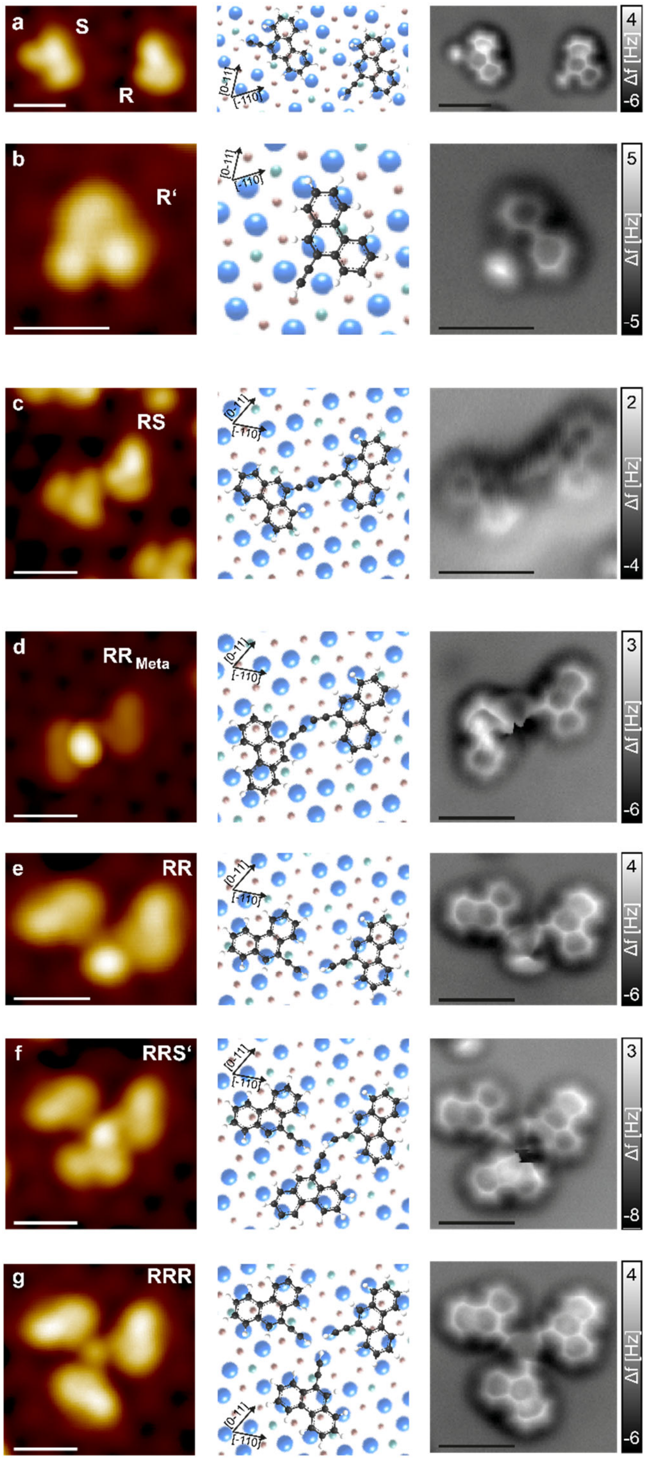

Figure 5.40 | Variety of 9-EP molecular structures on PdGa:A(-1-1-1)Pd$_3$

STM image (left) with the determined adsorption configuration (center) and the corresponding nc-AFM images (right) for **a** R, S and **b** R' monomer, the **c** RS, **d** RR$_{Meta}$ and **e** RR dimer, and the **f** RRS' and **g** RRR trimers. STM settings **a-b**, **d-g**: $V_B = 50\ mV$, $I_T = 10\ pA$; **c** $V_B = 20\ mV$, $I_T = 2\ nA$. All scale bars represent 1 nm.

By increasing the annealing temperature to 500 K (Figure 5.39e), raises the yield of propellers from around 50% to more than 86% with a corresponding decrease of dimers and monomers. The full temperature dependent development of 9-EP structures and their relative coverage, *i.e.*, the species' coverages normalized to the overall number of 9-EP units, is summarized in Figure 5.41. Besides propellers becoming the most abundant species at 500 K, they also evolve into homochiral, enantiopure RRR propellers (Figure 5.41b) with ee_{RRR} rising to staggering 97% ± 2%, which corresponds to a 99.5% probability of a 9-EP in the propeller being in form R. Moreover, RR and RR_{Meta} vanish at 500 K and only RS along with various other unidentified dimer structures with a collective yield of 6% remain.

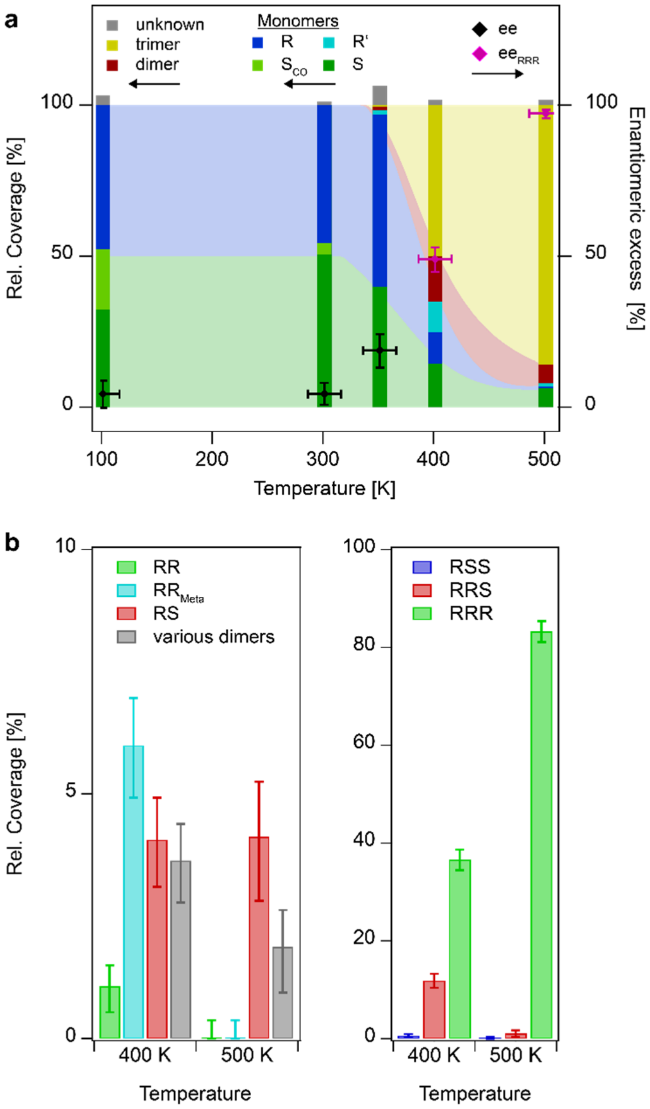

Figure 5.41 | From 9-EP racemic mixture to near-enantiopure, homochiral 9-EP trimer

a Color map of the relative coverage of 9-EP monomers, dimers, and trimers together with the enantiomeric excess as function of adsorption/annealing temperature on PdGa:A(-1-1-1)Pd_3. **b** Relative coverage of various 9-EP dimers and trimers at annealing temperatures 400 K and 500 K.

Annealing to 550 K initiates decomposition of 9-EP, presumably at the alkyl group, as evident from the emergence of propellers with one 9-EP unit closer to the connecting center (Figure 5.39f). Therefore, temperatures beyond 500 K have not been considered in our analysis.

Among all 9-EP oligomers, the structural identification of RS dimers presented in Figure 5.40c is most straightforward. Their R and S elements must be dehydrogenatively covalently coupled because pristine R and S enantiomers cannot be present in such close proximity due to steric hindrance of their alkyne group. Our interpretation is supported by the bond distances inferred from nc-AFM and their persistance upon annealing to 500 K (Figure 5.41b). This stability contrasts to that of the RR and RR_{Meta} dimers (Figure 5.40d-e), which are present at 400 K but vanish upon annealing to 500 K (Figure 5.41b). The depletion of RR and RR_{Meta} dimers suggests them to be precursors for 9-EP propellers (Figure 5.44). Both of the latter dimers are characterized by an apparent connection at the alkyne groups. This connection site shows up as bright protrusion in the STM images (bias dependent), indicating an extended connecting moiety, which, however, cannot be resolved by nc-AFM.

While RRS' exhibits a similarly strong protrusion in STM images as RR and RR_{Meta} dimers, the protrusion of RRR propellers is a less-pronounced, well-defined central dot (Figure 5.40f-g; for detailed STM characterization of RRR propellers, see Figure 5.42-Figure 5.43). The corresponding nc-AFM image of RRR (Figure 5.40g) is featureless in the center, but displays its R elements alike individual R monomers (Figure 5.40a). The near-complete absence of RRS' at 500 K implies that this species, alike RR and RR_{Meta} dimers, is a metastable precursor of RRR propellers. The conversion of RRS' into RRR requires the wrong-handed S' incorporated into a propeller to convert into the R configuration.

So far, only the dehydrogenative covalent coupling of RS dimers could be unambiguously deduced. Identification of the RR, RR_{Meta} and RRS' coupling is hampered by their presumably non-planar motif observed in nc-AFM (Figure 5.40d-f). For RRR, the central link exhibits a surprisingly featureless nc-AFM signature (Figure 5.40g), preventing elucidation of its atomic structure.

As 9-EP on A:Pd_3 is mobile at RT (Figure 5.45), the oligomers cannot be unspecifically bonded entities held together by weak interactions (*e.g.*, electrostatic). We rather postulate an activated oligomerization via strong bond formation which is supported by the fact that the trimers are impossible to separate by STM-tip induced manipulation. The likeliest mechanisms are either a [2+2+2] cyclization of alkynes, which has been reported for different molecules on Au(111)[267–269] and Cu(111)[270], or a coordination to individual Pd or Ga surface adatoms or to carbon-based fragments. The [2+2+2] cyclization as formation mechanism of the 9-EP propellers can be excluded due to the excessively large spatial separation of the phenanthrene moieties (Figure 5.46). Also the coordination of 9-EP molecules to Pd or Ga adatoms has to be discarded as direct evaporation of the respective metals does not aid the expected oligomer formation (Figure 5.47-Figure 5.48). Neither does co-adsorption of benzene stabilize the oligomers as they desorb below 350 K, just like other small carbon-based molecules such as acetylene, ethylene, and CO,[45,46] nor deliver simulated nc-AFM images of 9-EP coupled via additional central carbon species signatures comparable to the experimental ones (Figure 5.49). Therefore, the bonding motif of the 9-EP molecules building homochiral and highly enantioselective 9-EP propellers remains unresolved and thus limits our discussion of their synthesis to experimental observations.

We have presented a detailed study of the first asymmetric heterogeneous coupling reaction on an intrinsically chiral metal surface, which requires no enantiopure precursor or modifier molecules. Specifically, we investigated the oligomerization of 9-EP on PdGa:A(-1-1-1)Pd_3. The adsorption of 9-EP monomers as R and S enantiomorphs is governed by the identical configuration of the phenanthrene moiety and the energetic difference only resides in the interaction of the alkyne group with the substrate. This minor difference in the 9-EP adsorption configuration between R and S seems to be the origin of the enantioselective formation of homochiral 9-EP trimers at 500 K with an enantiomeric excess of 97% because the adsorption configuration of each 9-EP unit in the RRR trimers remains exactly the same as for an isolated R monomer.

Owing to the ensemble effect, the temperature evolution of the enantiomeric excess of 9-EP structures and reaction products on PdGa{111}Pd_3 are in stark contrast to those on PdGa{111}Pd_1.[27] Specifically, whereas on PdGa{111}Pd_3, 9-EP monomers occur in a racemic mixture at 300 K, they appear with an enantiomeric excess of 96% on PdGa{111}Pd_1 due to a lower energy barrier for the conversion between R and S monomers and the enantiospecific van der Waals interaction with the substrate's second layer Ga trimer.[230] At elevated temperatures, however, all 9-EP molecules form stable dimers on PdGa{111}Pd_1 without enantioselectivity, whereas dimers on PdGa{111}Pd_3 are metastable and primarily intermediates for the homochiral and virtually enantiopure trimerization.

The obvious disparities in reaction pathway, kinetics, and enantioselectivity for the two structurally different PdGa{111} surfaces underline the significance of the ensemble effect and the need for an understanding of molecule-substrate interaction at atomic scales. Moreover, the reported creation of near-enantiopure molecular structures from a racemic mixture of precursor constitutes a significant advancement towards enantioselective heterogeneous catalysis on chiral metallic surfaces.

5.4.1 Supporting Information for the publication "Near-enantiopure trimerization of 9-Ethynylphenanthrene on a chiral metal surface"

5.4.1.1 Methods

5.4.1.1.1 Experimental

All experiments were performed under ultra-high vacuum conditions with base pressures below 2x10^{-10} mbar with a commercial LT STM or QPlus from Scienta Omicron operated at 5 K if not mentioned differently. The sample preparation consisted of repeated sputtering and annealing cycles (sputtering: Ar^{+}, 1keV; annealing: 20 min at 870 K). 9-Ethynylphenanthrene (97%), Gallium (99.99999%), and benzene (anhydrous, 99.8%) were purchased from Sigma Aldrich, and the Palladium wire (99.95%) was bought from Alfa Aesar. All were used without further purification. Deposition of 9-Ethynylphenanthrene was performed by exposing the clean sample surface to the molecules from a crucible held at 300 K in a pumped glass tube separated by a gate valve from the preparation chamber to prevent contamination. Palladium and Gallium were dosed from a cold-lip evaporator with the crucible heated to 1320 K for Palladium (5 – 10 s) and 1015 K for Gallium (30 -120 s). Benzene molecules were dosed via a leak valve for about 10 s and a pressure of 1.5×10^{-8} mbar on the cold sample (T ≈ 100 K). Nc-AFM images were acquired in constant-height mode with an excitation voltage of 10 mV and a resonance frequency of 27,044 Hz (Figs. 1c, 3a-b, 3d-g) or 22'290 Hz (Figure 5.40c) and with CO functionalized tips. CO molecules were deposited on the cold sample (T < 15 K). In case of Figure 5.40c the sample contained bilayer NaCl(001) islands, with NaCl dosed for 3 min from a quartz crucible heated to 970 K, and CO functionalized tips were prepared by picking up individual CO molecules from NaCl islands. For all other nc-AFM measurements, CO functionalized tips were prepared by indentation of the QPlus tip into the CO covered Pd$_3$ surface. The data were processed with Wave Metrics' Igor Pro.

5.4.1.1.2 DFT Simulations

The equilibrium geometry of three 9-EP molecules with central Pd atom (Figure 7b,d) or connected via an additional C atom (Figure S5) was obtained with the CP2K[242] code implementing DFT within a mixed Gaussian plane waves approach.[251] The surface/adsorbate system was modeled within the repeated slab scheme,[271] with a simulation cell containing 23 atomic layers of PdGa along the [111] axis. 40 Å of vacuum was included in the simulation cell to decouple the system from its periodic replicas in the direction perpendicular to the surface. To account for van der Waals interactions, we used the D3 scheme proposed by Grimme.[272] The Pd$_3$ surface was modeled by a supercell of 34.75 × 36.11 Å^2 corresponding to 30 surface units. To obtain the equilibrium geometries, we kept the atomic positions of the bottom 7 layers of the slab fixed to the ideal bulk positions, and all other atoms were relaxed until forces were lower than 0.005 eV/Å.

The ProbeParticle model[273] was used to simulate AFM images. We used a 2-point implementation of the model where two probe particles represent the carbon and oxygen atoms in the CO molecule. The stiffness parameters of the ProbeParticle as well as the Lennard-Jones parameters of the tip were obtained by fitting to DFT calculations for an isolated PTCDA molecule and an isolated pentacene molecule. The charges of the tip atoms were assigned by the restrained electrostatic potential method[241] applied in the case of the pentacene molecule. For the tip sample electrostatic interactions the Hartree potential obtained from the CP2K calculations was used.

The calculations were performed via workflows based on the AiiDA platform.[274]

5.4.1.2 Bias voltage dependence STM imaging of 9-EP propeller

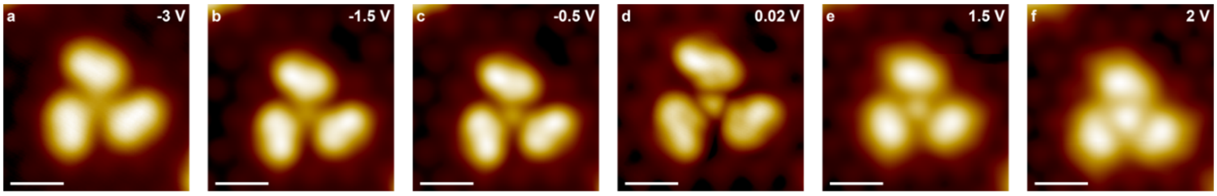

Figure 5.42 | Bias voltage dependence of 9-EP trimers

STM images of 9-EP trimers at **a** V_B = -3 V; I_T = 50 pA, **b** V_B = -1.5 V; I_T = 500 pA, **c** V_B = -0.5 V; I_T = 500 pA, **d** V_B = 0.02 V; I_T = 1'000 pA, **e** V_B = 1.5 V; I_T = 500 pA, and **f** V_B = 2 V; I_T = 500 pA.

For bias voltages larger than -0.5 V 9-EP trimers exhibit a pronounced central feature -0.5 V. At 0.02 V, the central part even appears separated from the three 9-EP molecules due to a sharp drop in intensity, which is indicative for an asymmetric wave function.

5.4.1.3 Deformation of 9-EP trimer

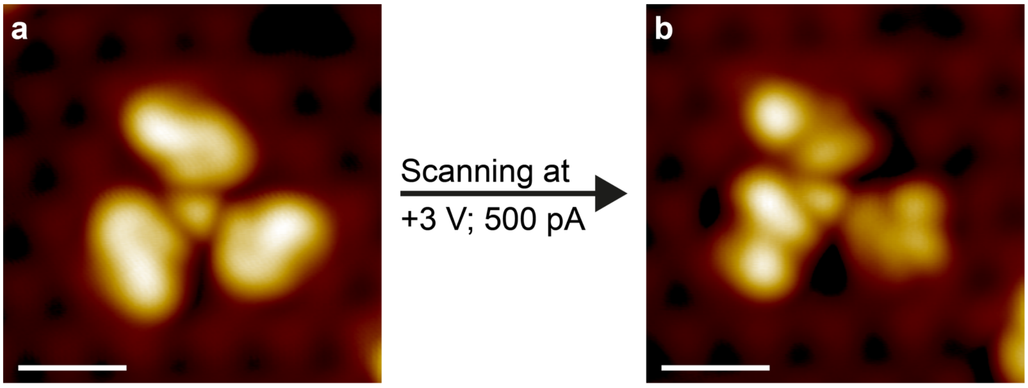

Figure 5.43 | Deformation of 9-EP trimers

a STM image of intact 9-EP trimer recorded with V_B = 0.02 V; I_T = 1 nA and **b** a deformed trimer after scanning with V_B = +3 V and I_T = 0.5 nA recorded with V_B = 0.02 V and I_T = 0.5 nA.

9-EP trimers can be "deformed" upon scanning at a bias voltage of +3 V. Although the individual 9-EP molecules building the trimer are barely recognizable after the deformation, the central protrusion of the trimer did not change and is still clearly visible, thus suggesting it to be a chemically stable structure.

5.4.1.4 Reaction scheme

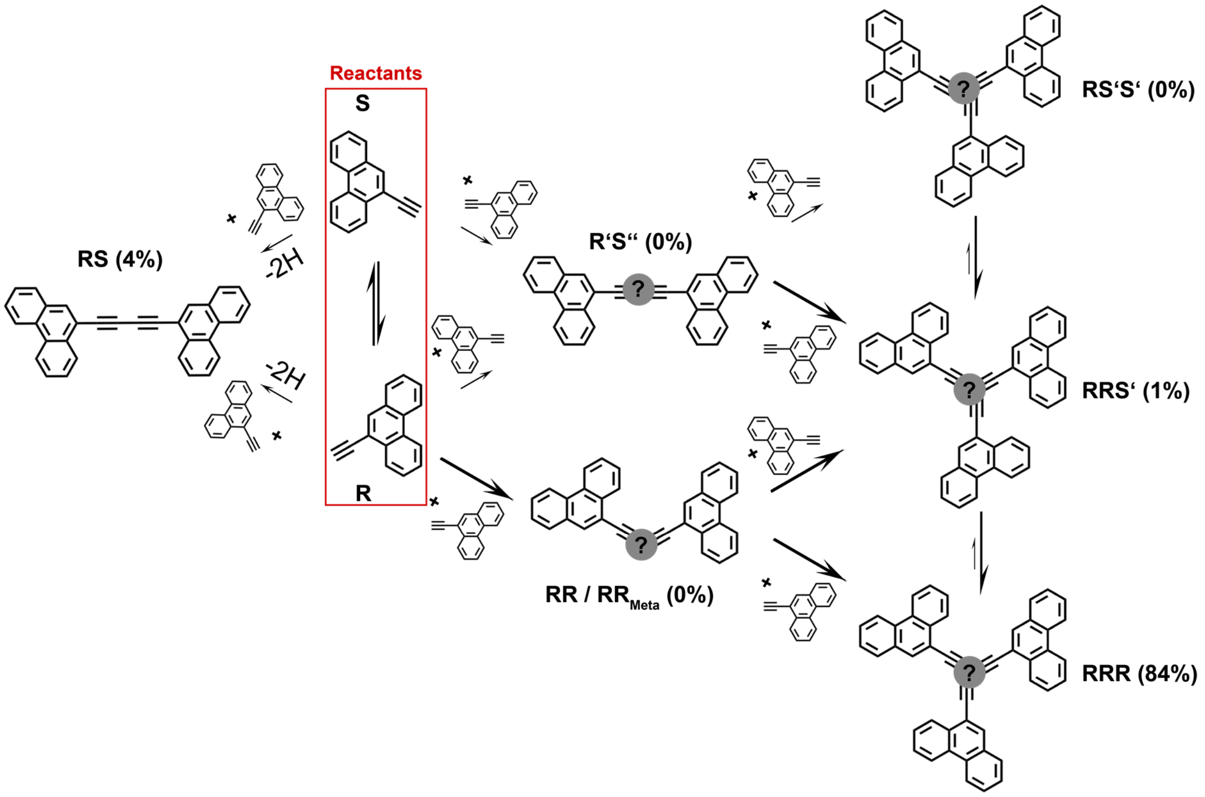

Figure 5.44 | Reaction pathway for the near-enantiopure, homochiral 9-EP trimerization

Reaction scheme of 9-EP dimerization and trimerization. In brackets, the yield of the synthesized molecular structure formed at 500 K is given.

In Figure 5.44, the formation of all 9-EP based structures as identified by STM, is summarized. In particular, starting from 9-EP R and S monomers (Figure 5.40a), the formation of stable 9-EP RS dimers (Figure 5.40c; low yield of 4%) and RRR trimers (Figure 5.40g; high yield of 84%) on the PdGa:A(-1-1-1)Pd_3 surface is outlined.

After depositing 9-EP molecules at 300 K, its R and S enantiomers appear as racemic mixture on the surface. The conversion of 9-EP R to S enantiomers starts to become significant between 300 and 350 K as we encounter a statistically significant enantiomeric excess of 9-EP R monomers at 350 K.

The R and the remaining S monomers then either form covalently bonded RS dimers via dehydrogenative coupling with a low yield of 4% at 500 K, or meta-stable RR or RR_{Meta} dimers which are bonded via an unidentified extended moiety that appears as a strong protrusion in STM images (Figure 5.40d-e, similar to the protrusion in the center of the RRR trimers as shown in Figure 5.42) and is indicated with a question mark in Figure 5.44. Another 9-EP monomer then bonds to the RR and RR_{Meta} dimers to form either RRS' or RRR trimers. RRS' trimers are then converted into RRR trimers via a conversion of the S' 9-EP moiety into a R moiety without detaching this 9-EP moiety from the trimer resulting in a 84% yield of RRR trimers at 500 K.

At lower temperatures (400 K), a very low number (1%) of RS'S' propellers are observed. Therefore, we have to assume the intermediate creation of R'S'' dimers, which, however, have not been observed experimentally. RS'S' trimers are then converted into RRS' by converting one S' 9-EP moiety into R, then into a RRR trimer by also converting the second S' moiety into R.

5.4.1.5 STM of 9-EP structures at room-temperature

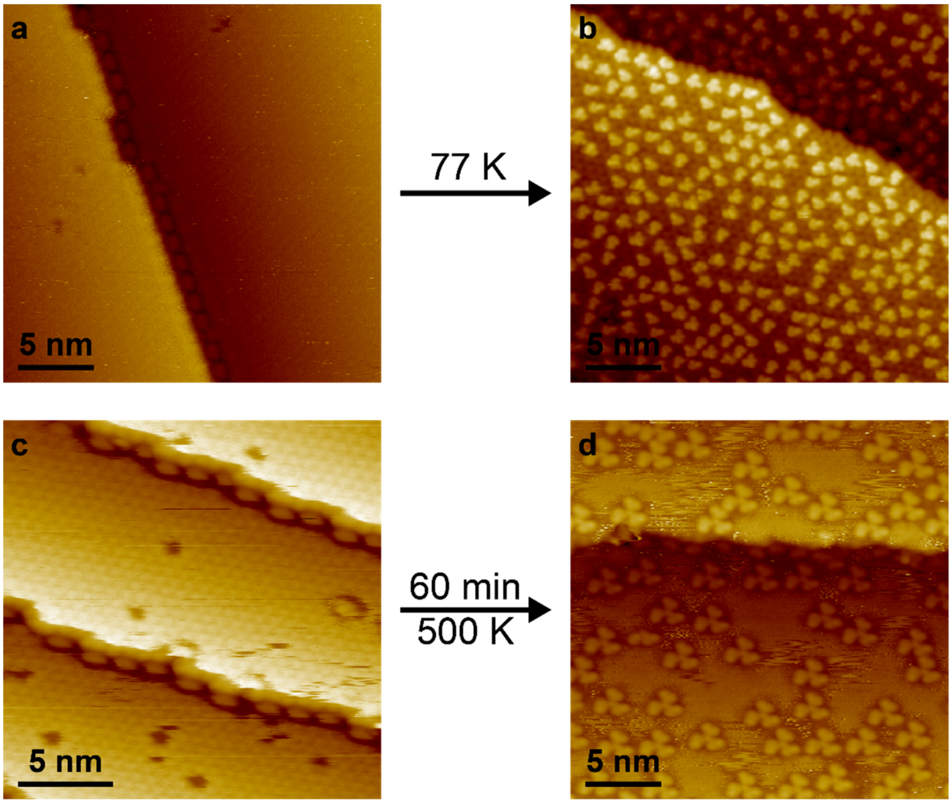

Figure 5.45 | Mobility of 9-EP structures

a, **c** RT-STM images of 9-EP monomers after RT deposition on PdGa:A(-1-1-1)Pd_3 (**a** V_B = -1 V; I_T = 20 pA, **c** V_B = -0.1 V; I_T = 100 pA). **b** STM image of sample **a** recorded at 77 K (V_B = 0.02 V; I_T = 100 pA). **d** RT-STM image of sample in **c** after annealing at 500 K (V_B = -1 V; I_T = 20 pA).

In order to elucidate the molecular dynamics, we performed STM at room-temperature (RT). Figure S4a and S4c show RT-STM images typical for molecules immobilized at step-edges, but mobile on the terraces. Cooling the sample to 77 K results in individual molecules in a near racemic mixture, analogous to the situation at 5 K (Figure 5.38b). In contrast, on a sample, which has been annealed to 500 K (Figure 5.45), immobilized propellers and a few dimers surrounded by mobile 9-EP monomers can be resolved by STM at RT.

This knowledge regarding the mobility of several 9-EP structures at 300 K allows us to rationalize the positional arrangement of individual 9-EP deposited at 300 K or below with the PdGa{111}Pd_3 surface shown in Figure 5.38b. We conclude that steric hindrance prevents the adsorption of a neighboring molecule on the nearest or, in most cases, even the next-nearest lattice site. Consequently, the molecules keep a minimum distance of 13.8 Å to each other, corresponding to twice the surface lattice constant of 6.9 Å, and accordingly appear well separated. Moreover, we conclude that neither dimerization nor trimerization is hindered by insufficient mobility for temperatures of 300 K or above and thus involves activation.

5.4.1.6 Exclusion of 9-EP [2+2+2] cyclotrimerization on Pd$_3$-terminated PdGa{111}

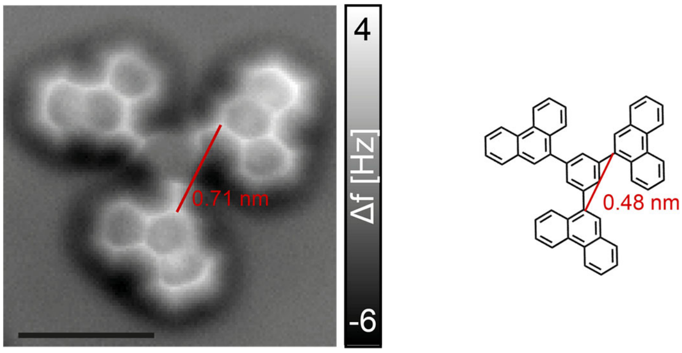

Figure 5.46 | 9-EP [2+2+2] cyclotrimerization

Left: nc-AFM image of a 9-EP RRR propeller based on which the distance between two phenanthrene moieties has been measured. Right: molecular structure of a [2+2+2] cyclotrimerized 9-EP propeller.

The experimentally determined distance between two phenanthrene moieties amounts to 0.71 nm, which is 50% larger than the distance expected if three 9-EP molecules undergo [2+2+2] cyclotrimerization on PGa:A(-1-1-1)Pd$_3$.

5.4.1.7 Adatoms as coordination center of 9-EP propellers

To test the possibility of 9-EP propeller formation via 9-EP coordination to central adatoms, we studied the formation of 9-EP structures in the presence of co-adsorbed Pd and Ga adatoms (Figure 5.47-Figure 5.48).

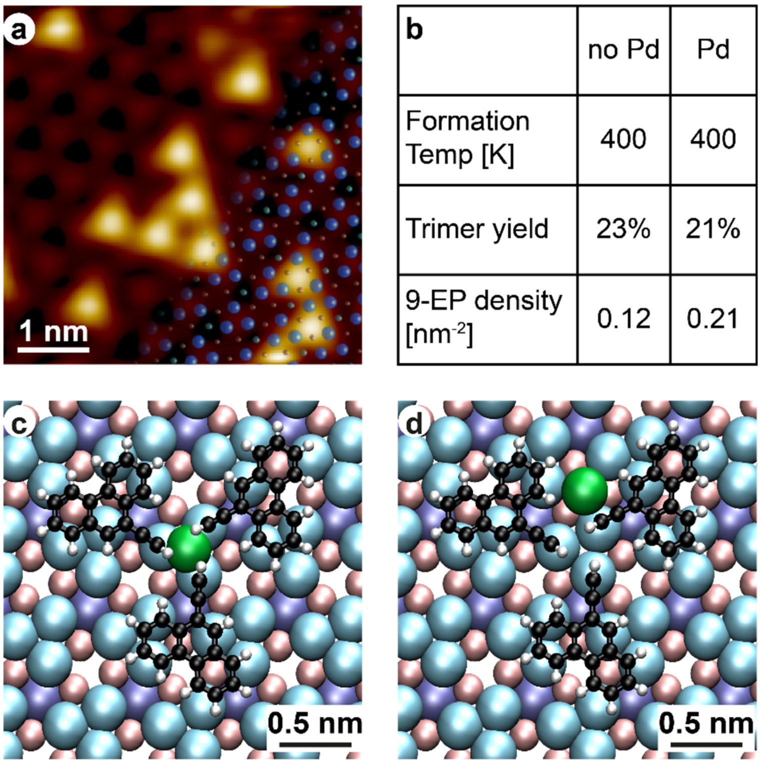

	no Pd	Pd
Formation Temp [K]	400	400
Trimer yield	23%	21%
9-EP density [nm^{-2}]	0.12	0.21

Figure 5.47 | Pd adatoms and their influence on 9-EP trimerization

a STM image of Pd adatoms on the PdGa:A(-1-1-1)Pd$_3$ surface partially overlaid with the atomic surface structure (V_B = 20 mV; I_T = 2 nA). **b** Statistical analysis of the propeller's formation temperature, propeller density and total 9-EP density with (Pd) and without (no Pd) co-deposited Pd adatoms. **c** Starting configuration for a DFT simulation of a 9-EP propeller with a central Pd adatom. This structure is unstable and the central Pd gets expelled upon relaxation of the atomic positions, shown in **d**.

For Pd adatoms, we determine the preferred low-temperature adsorption site not to be centered on the top layer Pd trimers, that coincide with the center of coupled 9-EP structures, but instead on the second layer Ga trimers as discernible in the structure overlay in Figure 5.47a. In DFT we find that a Pd adatom placed in the RRR propeller center (Figure 5.47c) is unstable. Upon relaxation of the atomic positions it is expelled from the 9-EP trimer center to the site atop of the second layer Ga trimer (Figure 5.47d) which were the experimentally the preferred adsorption site as shown in Figure 5.47a). Additionally, neither the propellers' formation kinetics nor their abundancy was influenced by the Pd adatoms (Figure 5.47b).

In case of Ga adatoms, the situation becomes more complex, since Ga adsorbs on different sites, preferably atop the Pd trimers and the third layer Pd atoms, as shown in Figure 5.48a,c. Co-adsorption of Ga adatoms and 9-EP at RT and subsequent annealing to 350 K already results in the formation of a variety of organometallic structures (Figure 5.48b). These 9-EP and Ga entities consist of achiral or enantiopure, homochiral Ga islands with mainly 9-EP/A:Pd_3 R enantiomers attached, but with the 9-EP in a 60° rotated configuration relative to the R monomer without the Ga adatoms (Figure 5.48d,e). The alkyne group of these attached 9-EP molecules presumably disintegrated, as upon formation of these 9-EP-Ga entities several Pd trimers appear darker with small central protrusions (blue arrow Figure 5.48b).

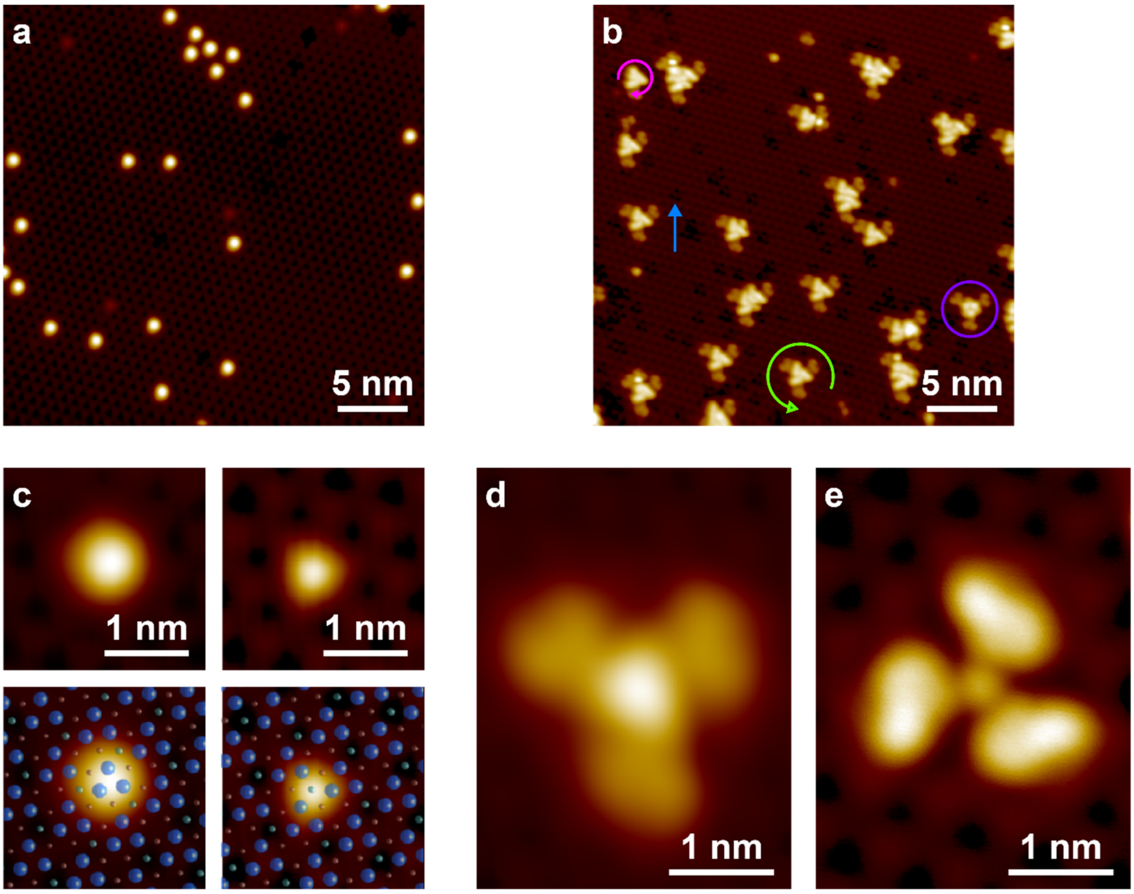

Figure 5.48 | Ga adatoms and their influence on 9-EP trimerization

STM images (V_B = 0.1 V; I_T = 10 pA) of **a** Ga adatoms adsorbed on PdGa:A(-1-1-1)Pd_3 with the two adsorption sites shown in **c**. **b** STM image of organometallic 9-EP-Ga entities consisting of either chiral (sense of rotation shown in pink circular arrow) or achiral (purple circle) Ga clusters and 9-EP/A:Pd_3 R enantiomers with disintegrated alkyne group (sense of rotation illustrated by green circular arrow). The detached molecular moieties are indicated by a blue arrow (V_B = 0.1 V; I_T = 10 pA). Comparison of the 9-EP-Ga entities (**d**, V_B = 0.1 V; I_T = 50 pA) with a regular RRR 9-EP propeller observed without addition of adatoms (**e** V_B = 0.05 V; I_T = 10 pA).

5.4.1.8 Single carbon atom or benzene as center of 9-EP trimers

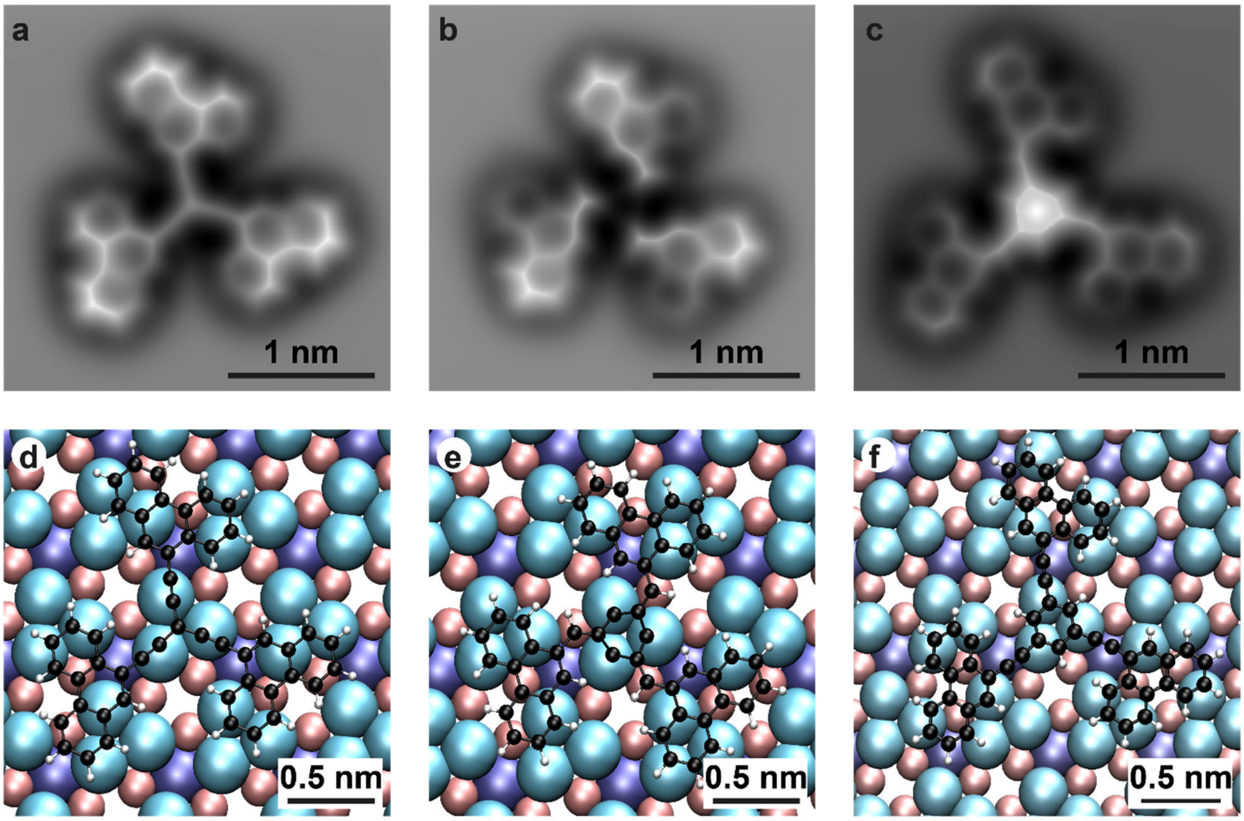

Figure 5.49 | carbon atoms as center of 9-EP trimers

a-c simulated nc-AFM images based on the molecular structures in **d-f**, respectively, which consisting of three 9-EP molecules bonded via **d** an additional central C atom, **e** three additional C atoms, s.t. a 6-membered ring is formed in the 9-EP trimer center, and **f** a central benzene.

For all three presented cases of simulated nc-AFM images, the signature of the phenanthrene moieties fits the experimentally recorded one, shown in Figure 5.40g, very well. However, the nc-AFM signature of none of the bonding motifs considered with DFT matches the experimental one in Figure 5.40g.

5.5 Publication (in preparation): "Asymmetric azide-alkyne Huisgen cycloaddition on chiral metal surfaces"

My contribution to this work consisted of the planning of the experiments, and of acquiring and analyzing all experimental data. I wrote the manuscript with input from all co-authors.

Asymmetric azide-alkyne Huisgen cycloaddition on chiral metal surfaces

Samuel Stolz[1,2], Harald Brune[2], Oliver Gröning[1], and Roland Widmer[1,*]

[1] *nanotech@surfaces Laboratory, Empa – Swiss Federal Laboratories for Materials Science and Technology, Überlandstrasse 129, CH -8600 Dübendorf, Switzerland*

[2] *Institute of Physics, École Polytechnique Fédérale de Lausanne, CH-1015 Lausanne, Switzerland*

* roland.widmer@empa.ch

Fundamental understanding of standard, and particularly enantioselective, heterogeneous synthesis is marred by the permanent presence of multitudinous dissimilar geometric environments in real world catalysts. Here, we address this problem by using the comparatively simple, yet chiral, three-fold symmetric, well-defined intermetallic PdGa{111} surfaces as catalytic substrates. We demonstrate the impact of chirality transfer and the so-called ensemble effect for the thermally activated azide-alkyne Huisgen cycloaddition between 3-(4-Azidophenyl)propionic azid and 9-Ethynylphenanthrene on these PdGa{111} surfaces under UHV conditions. Specifically, we encounter a dominating ensemble effect for the azide-alkyne Huisgen cycloaddition as on the Pd_3-terminated PdGa{111} surfaces no stable heterocoupled structures are created, while on the Pd_1-terminated PdGa{111} surfaces, the cycloaddition proceeds regioselectively. Moreover, we observe chirality transfer from the substrate to the reaction products, as they are formed enantioselectively on these Pd_1-terminated PdGa{111} surfaces. Our results evidence a determinant ensemble effect and the immense potential of PdGa in asymmetric heterogeneous catalysis.

Recently on-surface synthesis under ultra-high vacuum conditions (UHV) has emerged as a very successful method to produce extended, covalently bonded macro-molecules, which are inaccessible to classical wet-chemical synthesis due to insolubility or high reactivity.[219] On-surface synthesis is based on the controlled polymerization of dedicated precursor molecules on well-defined single crystal surfaces by thermal activation. Although in recent years the catalogue of on-surface reactions and successfully synthesized structures broadened extensively, the focus rarely lay on enantioselective synthesis, which is of immense importance for instance in pharmaceutical, agricultural or food industry.[3,4] This lack of enantioselective synthesis originates largely from the scarcity of intrinsically chiral, catalytically active, and well-characterized single-crystal surfaces needed for this task. The first option to circumvent this deficiency, where achiral surfaces are rendered chiral via the adsorption of enantiopure chiral molecules, is marred by low thermal stability, increased complexity due to the multitude of possible molecule-molecule interactions and the requirement of enantiopure molecular modifiers.[8–14] The second approach is the use of achiral crystals that are cut along non-symmetric directions, which, however, exhibit only a low density of chiral centers at kink sites of terrace step edges.[214,215] Despite the drawbacks of these two alternatives, enantioselective decomposition reactions were successfully performed with both approaches.[12,212,213]

In contrast to the approaches mentioned above, low Miller-index surfaces of intrinsically chiral bulk crystals possessa high density of well-defined and stable chiral centers. Currently, the only intrinsically chiral and catalytically active single-crystal whose low-index surfaces are well-characterized is the intermetallic compound PdGa. PdGa belongs to the non-centrosymmetric space-group $P2_13$,[25] and thus exists in two enantiomorphs, denoted as PdGa:A and PdGa:B.[54] Here, we focus on the two structurally dissimilar, bulk-truncated, three-fold symmetric PdGa:A($\bar{1}\bar{1}\bar{1}$) and PdGa:A(111) surfaces, of which the former is terminated by isolated Pd trimers, further referred to as A:Pd_3 (Figure 5.50a), while the top layer of the latter consists of single, isolated Pd atoms, and is denoted A:Pd_1 accordingly (Figure 5.50b).[48] Owing to their differing surface terminations, in combination with their equal lattice parameters, identical symmetry, and similar electronic properties, the PdGa{111} surfaces are ideally suited to disentangle ensemble and ligand effects, *i.e.*, the influence of the local geometric and electronic properties, in asymmetric heterogeneous catalysis.[45,46]

The chirality transfer from the PdGa{111} surfaces onto molecular processes has been demonstrated with achiral acetylene (C_2H_2) and prochiral 9-Ethynylphenanthrene (9-EP). Due to its prochirality, 9-EP appears in two distinguishable surface enantiomers R and

S when confined to a planar configuration. Specifically, the chirality of the Pd_3-terminated PdGa{111} surfaces manifests itself in the directed motion of C_2H_2[275] and the synthesis of almost enantiopure 9-EP trimers from an initial racemic mixture of monomers.[26] On the other hand, on the Pd_1-terminated PdGa{111} surfaces, 9-EP adsorbs enantioselectively 9-EP at room temperature (RT), but dimerization without enantioselectivity at elevated temperatures.[27]

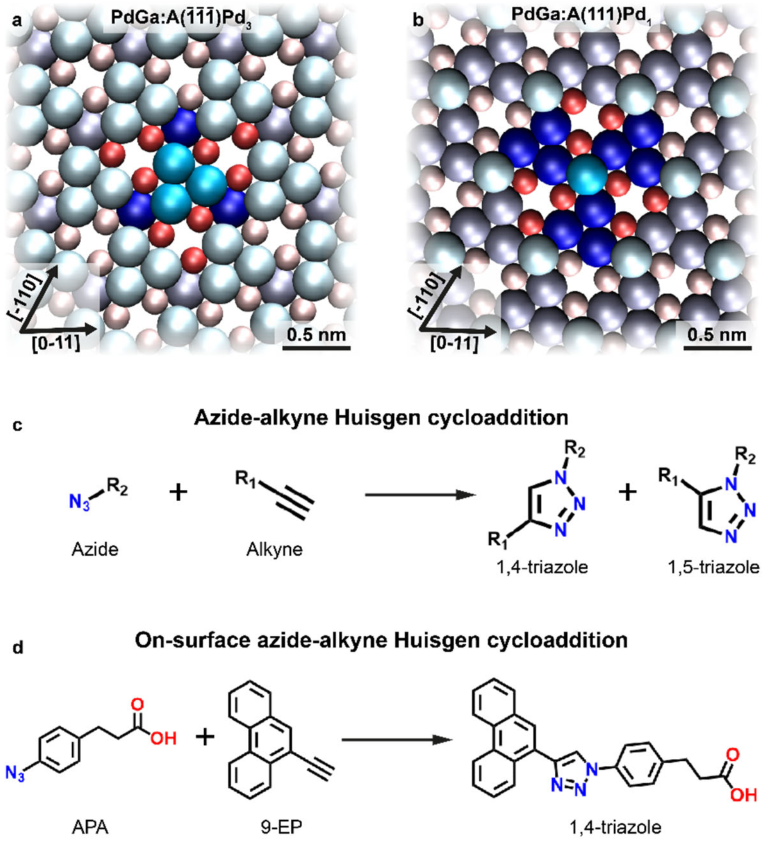

Figure 5.50 | Model system for enantioselective on-surface azide-alkyne Huisgen cycloaddition

The atomic surface structure of **a** PdGa:A(-1-1-1)Pd_3 (1st layer Pd_3 in bright blue: z = 0 pm; red 2nd layer Ga_3 in red: z = -85 pm; 3rd layer Pd_1 in dark blue: z = -161 pm) and **b** PdGa:A(111)Pd_1 (1st layer Pd_1 in bright blue: z = 0 pm; 2nd layer Ga_3 in red: -57.4 pm ; 3rd layer Pd_3 in dark blue: -149.8 pm) with their chirality highlighted by a top layer Pd trimer or a single top layer atom, respectively, and their neighbors in saturated colors. **c** General reaction scheme of the azide-alkyne Huisgen cycloaddition. **d** The investigated on-surface Huisgen cycloaddition between 9-Ethynylphenanthrene (9-EP) and 3-(4-Azidophenyl)propionic acid (APA) yielding 1,4-triazole regioisomers.

Therefore, 9-EP promotes itself as a molecular alkyne precursor for investigating enantioselective synthesis on the PdGa{111} surfaces. Moreover, on-surface alkyne-azide Huisgen cycloaddition (Figure 5.50c), without emphasis on enantioselectivity, has been successfully demonstrated using 9-EP as precursor on Cu(111) under UHV conditions by Bebensee *et al.*.[47] This catalytically activated reaction, which belongs to the field of Click Chemistry, selectively yields 1,4-triazole regioisomers and omits the formation of 1,5-triazoles. According to the d-band model introduced by Norskov *et al.*,[266] PdGa is expected to possess similar catalytic activity for the azide-alkyne Huisgen cycloaddition as copper. To perform the reaction, commercially available, prochiral 3-(4-Azidophenyl)propionic acid (APA) was chosen as azide reactant (Figure 5.50d).

Using scanning tunneling microscopy (STM), complemented with x-ray photoelectron spectroscopy (XPS), we demonstrate a significant ensemble effect on the PdGa{111} surface reactivity, manifested in the occurrence of the cycloaddition between APA and 9-EP on the Pd_1-terminated PdGa{111} surfaces, but its suppression on Pd_3-terminated PdGa{111}. Moreover, on the Pd_1-terminated PdGa{111} surfaces, the azide-alkyne Huisgen cycloaddition is not only regioselective, as it is on Cu(111)[47] or Au(111),[276] but also enantioselective.

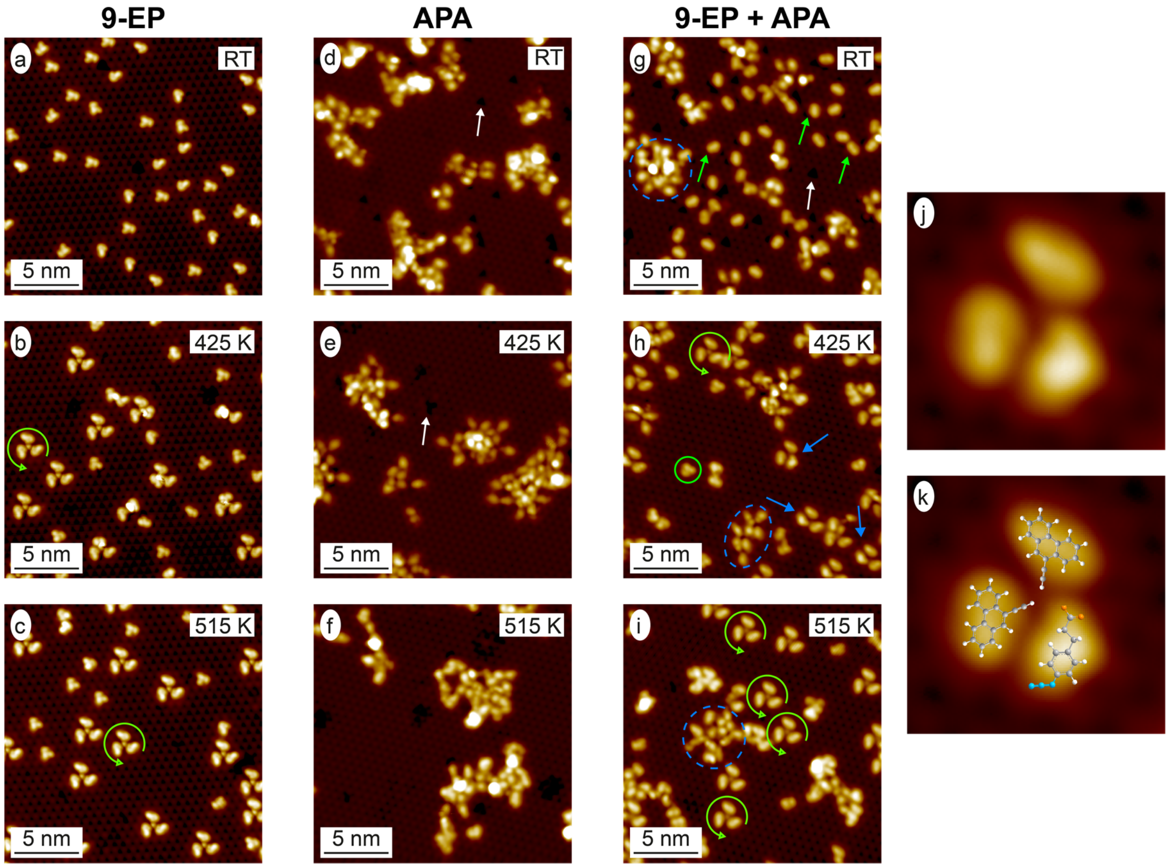

Figure 5.51 | Suppression of azide-alkyne Huisgen cycloaddition on PdGa:A(-1-1-1)Pd_3

STM images (V_B = 20 mV; I_T = 1 nA) of 9-EP **a** deposited on PdGa:A(-1-1-1)Pd_3 at RT, and after subsequent annealing to **b** 425 K and **c** 515 K. STM images (V_B = 200 mV; I_T = 0.1 nA) of APA molecules on the PdGa:A(-1-1-1)Pd_3 surface after **d** RT deposition, subsequent annealing to **e** 425 K and **f** 515 K. STM images (V_B = 200 mV; I_T = 0.1 nA) of APA co-adsorbed with 9-EP after **g** RT deposition, subsequent annealing to **h** 425 K and **i** 515 K. High-resolution STM image (3 × 3 nm^2; V_B = 20 mV; I_T = 0.2 nA) of the frequently observed molecular structure containing one APA and two 9-EP molecules, which is marked with a blue arrow in the **h**, is shown in **j** and overlaid with the molecular structure in **k**. The green circular arrow in **b, c, h, i** highlights the homochiral 9-EP propeller, the white arrow in **d, e, g** the depression caused by APA remnants, and the green arrow in **g** a 9-EP molecule interacting with an APA remnant. The blue dashed circles in **g, h, I** indicate APA agglomerations and the green circle in **h** a 9-EP monomer.

Figure 5.51 shows a series of STM images as a summary of the individual deposition of 9-EP and APA molecules and the co-deposition of both molecules on A:Pd_3 at RT and after subsequent annealing to 425 and 515 K. As previously reported,[26] 9-EP deposited at RT results in a homogeneous racemate of well isolated molecules (Figure 5.51a). Upon annealing to 425 K (Figure 5.51b), 9-EP dimers and trimers are formed with a strong enantiomeric excess (*ee*) of 49 ±4 % towards RRR homochiral enantiomorphs. By further increasing the annealing temperature to 515 K (Figure 5.51c), the yield of trimers increases from around 50% to more than 84% with a corresponding decrease of dimers and monomers and the corresponding *ee* of the RRR trimer rises up to 97 ± 2%. On the other hand, APA molecules deposited at RT on A:Pd_3 create large, unordered agglomerates (Figure 5.51d). Additionally, unusual depressions (absent on the pristine surface) are observed on the bare substrate, as indicated by the white arrow in Figure 5.51d, which we suspect to be small fragments of decomposed APA molecules. In this context, both functional groups of the APA molecule have been reported to disintegrate on other substrates; in particular the azide group at 300 K on Ag(111),[93] and the carboxylic acid at 430 K on Ag(111) and on Cu(111).[50] Due to the significantly lower temperature for the disintegration of the azide group on Ag(111) and distinct presence of COOH and COO- components in the XPS spectra of the C 1s core level (Figure 5.55), the depressions in the STM images are most likely remnants of the azide functional group. Subsequent annealing of the sample up to 515 K leads to a reduction of the depressions, as they most probably desorb, while agglomeration proceeds without ever forming discernible regular structures, *i.e.*, reoccurring structures of similar topographic signature in the STM images (Figure 5.51d-f).

When APA is co-deposited with 9-EP, no intermolecular reactions are observed at RT while APA again agglomerates and 9-EP mostly bonds to the previously mentioned molecular fragments potentially detached from APA molecules (depression), as pointed out by the green arrow in Figure 5.51g. Upon annealing to 425 K (Figure 5.51h), 9-EP appears in its pristine adsorption configuration, which means it detached from the molecular fragments, and new prochiral 9-EP/APA heterostructures are formed, in particular mixed trimers, where two 9-EP interact with one APA molecule (Figure 5.51j-k). The adsorption site of 9-EP molecules incorporated in these trimer heterostructures with respect to the PdGa substrate is identical with that reported in Ref.[26] for R enantiomers incorporated into pure 9-EP trimers. The heterostructure trimers exclusively appear in the enantiomeric form shown in Figure 5.51j-k on the A:Pd_3 termination. The incorporated APA is not covalently bonded to these heterostructure trimers, as upon further annealing to 515 K, these structures deplete and homostructural 9-EP trimers become the only regular motive (highlighted by a green circular arrow in Figure 5.51i). Therefore, even though PdGa is copper-like with regard to the catalytic reactivity according to the d-band model,[266] the azide-alkyne Huisgen cycloaddition cannot be triggered on the A:Pd_3 surface.

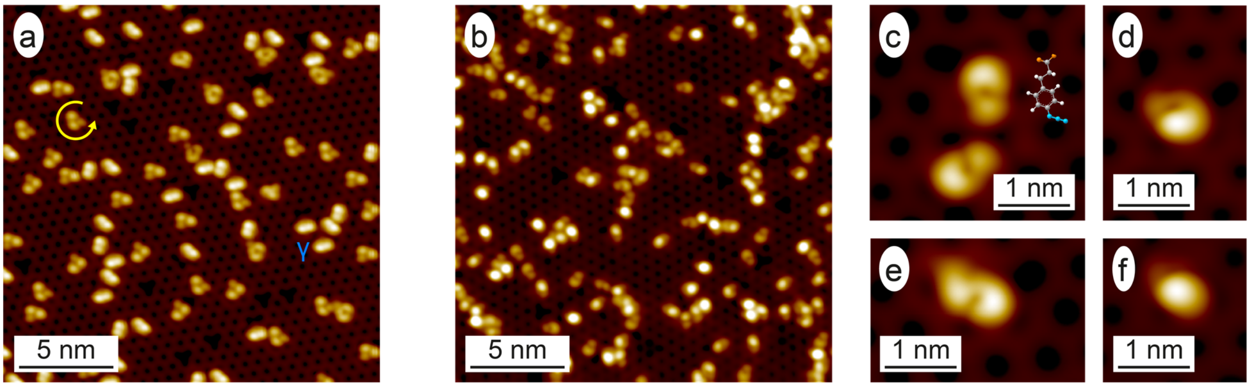

Figure 5.52 | Alkyne and azide on Pd_1-terminated PdGa{111} surfaces

Large-scale STM images of **a** 9-EP (V_B = 20 mV; I_T = 2 nA) and **b** APA (V_B = 100 mV; I_T = 0.4 nA) deposited at RT on PdGa:A(111)Pd_1. **b-e** high resolution STM images (V_B = 20 mV; I_T = 0.2 nA) of the different APA configurations on PdGa:A(111)Pd_1 with the molecular structure of APA in **b**.

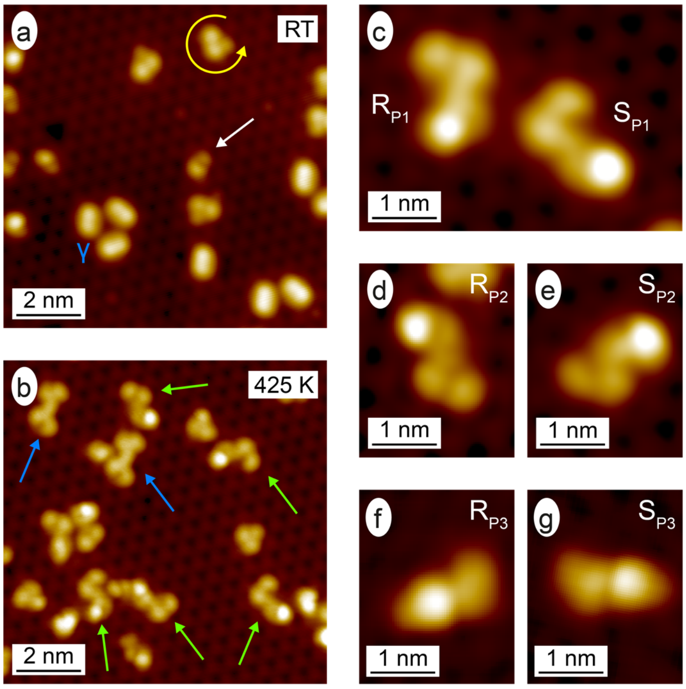

Figure 5.53 | Azide-alkyne Huisgen cycloaddition on Pd_1-terminated PdGa{111} surfaces

STM images (V_B = -200 mV; I_T = 0.05 nA) of **a** co-deposited APA (white arrow) and 9-EP (yellow arrow and γ-states marked) molecules on PdGa:B(-1-1-1)Pd_1, and after subsequent annealing to **b** 425 K. In **b**, the 9-EP dimers are pointed out with blue arrows, the 1,4-triazoles with green arrows. The different 1,4-triazoles are shown in detail in the high resolution STM images (V_B = -200 mV; I_T = 0.2 nA) in **c-g**. **d** and **g** have been rotated to highlight the relation of the shown 1,4-triazole to the one in e and f, respectively.

On the A:Pd_1 surface, 9-EP deposited at RT adsorbs with an *ee* of 98% in favor of the R enantiomer (cf. Figure 5.52a), as reported by Prinz *et al.*.[27] The adsorption behavior of APA on the Pd_1-terminated PdGa{111} surfaces is in stark contrast to that on A:Pd_3 , as the APA molecules barely agglomerate even at temperatures up to 415 K (Figure 5.52b for APA on A:Pd_1 and Figure 5.54a,b for PdGa:B(-1-1-1)Pd_1 (B:Pd_1)). The most common APA structures are shown in the four STM images in Figure 5.52c-f. Apparently, APA molecules seem smaller than expected in STM by comparing the molecular APA structure with its STM appearance. However, since i) APA is mainly resolved as single molecule, ii) no surface contamination due to APA disintegration is observed, iii) the azide group was reported to exhibit a weak STM signal on Ag(111),[93] we presume APA to remain intact.

After having clarified that the APA monomers remain structurally intact after RT deposition on the Pd_1-terminated PdGa{111} surfaces, APA was co-deposited with 9-EP (Figure 5.53). As shown in Figure 5.53a, both 9-EP and APA mainly appear as non-interacting monomers. The pronounced depression on this surface represent well known Pd vacancies in the Pd_1-termination[48] and the apparent trimer are 3 individual 9-EP molecules adsorbed on such a vacancy.[27] As expected, isolated 9-EP molecules exhibit an *ee* > 90% with a relative abundance between 40%-60%. Due to the lack of intermolecular interactions, also APA molecules occupy the same adsorption configurations as in the case when they are adsorbed without the 9-EP (cf. Figure 5.52).

Sample	1,4-triazoles						9-EP dimer	Others
	R_{P1} 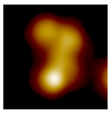	S_{P1} 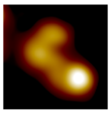	R_{P2} 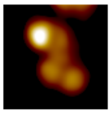	S_{P2} 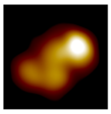	R_{P3} 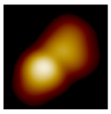	S_{P3} 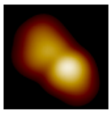		
A:Pd_1	5 ± 1%	21 ± 2%	13 ± 2%	14 ± 2%	30 ± 2%	6 ± 1%	6 ± 1%	5 ± 1%
B:Pd_1	18 ± 2%	3 ± 1%	10 ± 2%	10 ± 2%	12 ± 2%	36 ± 2%	5 ± 1%	6 ± 1%

Table 5.8 | Statistical analysis of the 1,4-triazoles on Pd_1-terminated PdGa{111} surfaces

Abundancies of the identified coupled molecular species on the PdGa:A(111)Pd_1 and PdGa:B(-1-1-1)Pd_1 surfaces.

The cycloaddition between APA and 9-EP can be triggered thermally on Pd_1-terminated PdGa{111} by annealing the co-deposited sample at 425 K. After this annealing, several new covalently coupled molecular structures are observed (Figure 5.53b) in high abundance (Figure 5.56, Figure 5.57), which cannot be decomposed with standard STM tip manipulations. The vast majority (90%, green arrows in Figure 5.53b) of all covalently coupled molecules exhibit one of the six different STM appearances presented in Figure 5.53c-g, which represent different configurations of 1,4-traizoles as identified by overlaying the molecular structure (Figure 5.58). About 5% of the covalently coupled molecules are the 9-EP dimers reported in Ref.[27], whereas the remaining 5% consist of one 9-EP molecule and some APA moiety, but are too small to be triazoles. We can therefore exclude the formation of 1,5-triazoles.

From first glance it becomes clear that the two molecules in Figure 5.53c, the two molecules in Figure 5.53d,e and the two molecules in Figure 5.53f,g are mirror images of each another, thus they represent complementary enantiomers, which will be discussed later in view of enantioselectivity. The distinctive feature in the STM signatures of the R, and S enantiomers is governed in all three cases by the prochiral arrangement of the phenylpropionic acid group with respect to the phenanthrene moiety. If the phenylpropionic acid unit is perpendicular (almost parallel) to the phenanthrene moiety the 1,4-triazoles appear L-shaped (Z-shaped) (Figure 5.53c-e, the triazoles are denoted P1 and P2, respectively), or I-shaped (P3) for an intermediate orientation (Figure 5.53f,g). The atomic resolution of the substrate in the STM images combined with the structure overlay allows to determine the adsorption configuration of these reaction products (Figure 5.58b,e,h), whereas the enantiospecific arrangement of the propionic acid moiety remains ambiguous. The relative abundance of the three product structures P1-P3 are summarized in Table 5.8 for the two enantiomeric forms R and S on the Pd_1-terminated surface (the products are correspondingly labeled R_{P1}, S_{P1}, R_{P2},..., S_{P3}). Enantioselectivity is clearly expressed for the L- and I-shaped products P1 and P3, where we find ratios between the different enantiomorphs of up to 4:1 and 5:1, respectively. As a consequence, they exhibit opposite handedness on the two crystal enantiomorphs. On the other hand, the Z-shaped products P2 do not experience any chirality transfer. Considering all 1,4-triazoles, the 9-EP moiety appear as racemic mixture, which implies that at the reaction temperature of 425 K, the chiral recognition of 9-EP by the Pd_1-terminated PdGa{111} surfaces has become insignificant. However, since about 70-76% of all 1,4-triazole occur as P2 and P3, this reaction proceed diastereoselectively.

Compared to investigation of the azide-alkyne Huisgen cycloaddition on Cu(111),[47] where the reaction yield is reported to be of the order of 2-10%, the formation of 1,4-triazoles on the Pd_1-terminated PdGa{111} surfaces reveals a much higher yield of up to 58%. It seems as if this yield depends mainly on the availability of intact APA molecules by comparing the ratio between APA/9-EP with the amount of 1,4-triazoles formed (Table 5.12).

In summary, we have shown that the azide-alkyne Huisgen cycloaddition between 9-EP and APA occurs region- and enantioselectively on the Pd_1-terminated PdGa{111} surfaces, forming exclusively 1,4-triazoles with an exceptionally high enantiospecifity of up to 5:1. In view of the d-band model, the Pd_1-terminated PdGa{111} surfaces therefore behave copper-like. On the other hand, the same reaction does not proceed on the Pd3-terminated PdGa{111} surfaces, even though these PdGa{111} surfaces exhibit similar electronic d-band structure. We therefore conclude that the vastly dissimilar catalytic properties of the Pd1- and Pd3-terminated PdGa{111} surfaces for the azide-alkyne Huisgen cycloaddition primarily arise from differences in the atomic arrangement in their terminating layers, *i.e.*, the ensemble effect.

5.5.1 Supporting Information for the publication "Asymmetric azide-alkyne Huisgen cycloaddition on chiral metal surfaces"

5.5.1.1 Methods

All experiments were performed under ultra-high vacuum conditions with a base pressure below 2x10-10 mbar with a commercial LT STM from Scienta Omicron operated at 5 K. XPS measurements were performed at room temperature in normal emission configuration using a monochromatized Al K_α source and a Scienta R3000 display analyzer operated at a pass energy of 100 eV. The sample was prepared by repeated sputtering and annealing cycles (sputtering: Ar^+, 1 keV; annealing: 20 min at 870 K). Both 9-Ethynylphenanthrene (97%) and 3-(4-Azidophenyl)propionic acid (≥97%) were purchased from Sigma Aldrich and were used without further purification. 9-Ethynylphenanthrene and 3-(4-Azidophenyl)propionic acid were deposited by exposing the clean sample surface to the molecules held at 300 K in a pumped glass tube separated by a gate valve from the preparation chamber to prevent contamination. 9-Ethynylphenanthrene and 3-(4-Azidophenyl)propionic acid were pumped via individual connections with the same turbo pump to minimize the risk of cross-contamination.

5.5.1.2 Temperature evolution of APA on PdGa:B(-1-1-1)Pd_1

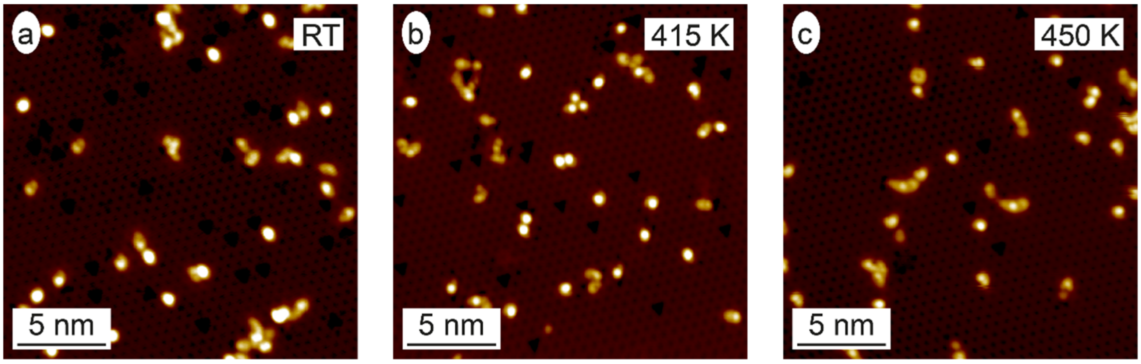

Figure 5.54 | Temperature evolution of APA on PdGa:B(-1-1-1)Pd_1

STM images of APA molecules after **a** room temperature deposition, subsequent annealing to **b** 415 K and **c** 450 K.

Between room temperature to 415 K, APA appears mostly isolated and in the four configurations shown in Figure 5.52b-e. Only upon annealing to 450 K agglomeration becomes more frequent and the configurations shown in Figure 5.52b,d completely disappear.

5.5.1.3 XPS of APA on PdGa:A(-1-1-1)Pd$_3$, PdGa:A(111)Pd$_1$, and Cu(111)

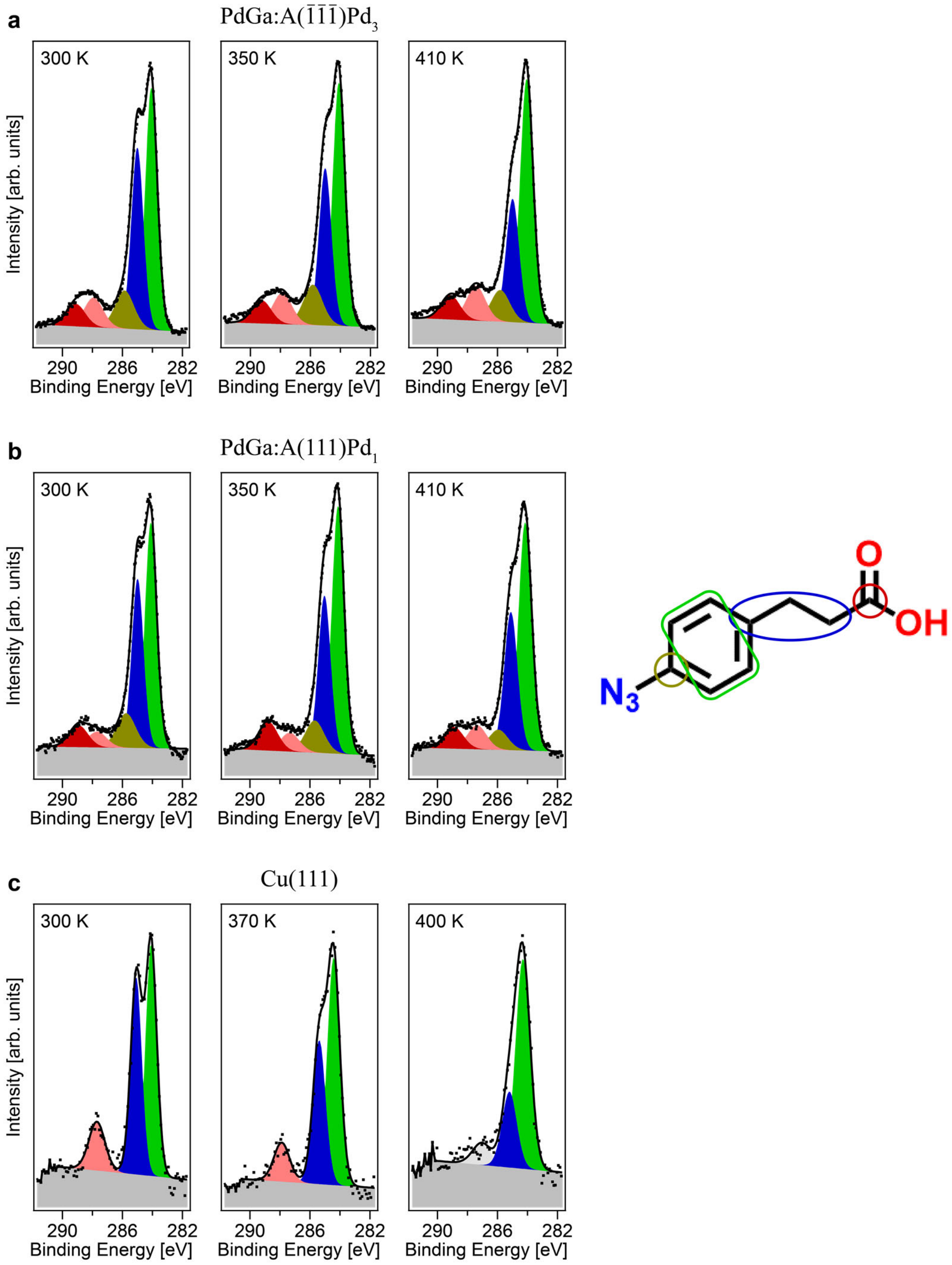

Figure 5.55 | XPS of APA on PdGa:A(-1-1-1)Pd$_3$, PdGa:A(111)Pd$_1$, and Cu(111)

C 1s XPS core level signal of APA on **a** PdGa:A($\bar{1}\bar{1}\bar{1}$)Pd$_3$, **b** PdGa:A(111)Pd$_1$, and **c** Cu(111) after deposition at 300 K (left) and after annealing to the temperature indicated in the top left corner of each XPS spectrum. On the right a sketch of the APA molecule is displayed with the carbon atoms contributing to each part of the XPS signal is colored according to the colors of the individual components in the XPS spectra.

5.5.1.3.1 PdGa:A(-1-1-1)Pd$_3$

	300 K		350 K		410 K	
	BE [eV]	Weighting	BE [eV]	Weighting	BE [eV]	Weighting
COOH	289.2	6.3	289.3	6.6	289.2	7.1
COO-	288	8.3	287.9	8.8	287.5	10.2
C-N	285.8	10.9	285.9	11.4	285.9	9.3
"C3"	285.1	32.8	285.1	28.8	285.1	24.7
"C4"	284.2	43.7	284.2	44.5	284.2	48.8

Table 5.9 | Fitting parameters for XPS of APA on PdGa:A(-1-1-1)Pd$_3$

Fitting parameters for the XPS spectra of APA on PdGa:A($\bar{1}\bar{1}\bar{1}$)Pd$_3$ for the temperatures indicated in Figure 5.55a. For each temperature the binding energy (BE) and weighting of all fitting components depicted in the molecular structure in Figure 5.55 are given.

5.5.1.3.2 PdGa:A(111)Pd$_1$

	300 K		350 K		410 K	
	BE [eV]	Weighting	BE [eV]	Weighting	BE [eV]	Weighting
COOH	289.0	7.0	288.9	8.5	289.0	6.7
COO-	287.8	5.1	287.4	5.5	287.5	7.5
C-N	285.9	11.0	285.8	9.4	286.0	9.3
"C3"	285.1	33.0	285.1	29.7	285.2	30.0
"C4"	284.2	44.0	284.2	46.8	284.3	49.5

Table 5.10 | Fitting parameters for XPS of APA on PdGa:A(-1-1-1)Pd$_1$

Fitting parameters for the XPS spectra of APA on PdGa:A(111)Pd$_1$ for the temperatures indicated in Figure 5.55b. For each temperature the binding energy (BE) and weighting of all fitting components depicted in the molecular structure in Figure 5.55 are given.

5.5.1.3.3 Cu(111)

	300 K		370 K		400 K	
	BE [eV]	Weighting	BE [eV]	Weighting	BE [eV]	Weighting
COOH	-	0	-	0	-	0
COO-	287.9	14.1	288	11.6	-	0
C-N	-	0	-	0	-	0
Unknown	-	0	-	0	287.2	8.9
"C3"	285.2	39.5	285.5	34.2	285.4	24.2
"C4"	284.2	46.4	284.6	54.1	284.5	66.9

Table 5.11 | Fitting parameters for XPS of APA on Cu(111)

Fitting parameters for the XPS spectra of APA on Cu(111) for the temperatures indicated in Figure 5.55c. For each temperature the binding energy (BE) and weighting of all fitting components depicted in the molecular structure in Figure 5.55 are given.

For reactivity investigations we are mainly interested in the two - out of the overall 9 - C atoms of the APA molecule (cf. Figure 5.55) that are either part of propionic acid or directly connected to the azide group. Each of these two C atoms in APA give rise to a component in C 1s core level signal with a chemical shift to higher binding energy with respect to the remaining 7 C atoms of the backbone with a theoretical weighting of 11%.

Because no information is found on the chemical shift in the XPS of the C 1s core level induced by azide functional groups,[47] we identify the contribution of the C atom attached to the azide group to the C 1s XPS signal by referring to Ref.[277], where they performed an XPS investigation of a molecule with a diazo group. The carbon atom attached to the diazo group has been reported to give rise to a C 1s component shifted by about 1 eV towards higher binding energy with respect to the C 1s component of aromatic carbon atoms. We therefore assign the components denoted with C-N in Table 5.9-Table 5.11 to originate from the carbon atom attached to the azide group.

For APA on the PdGa{111} surfaces this C-N XPS component is discernible in the expected amount (~11%), whereas it is lacking for APA on Cu(111). Based on the N 1s core level XPS signal, we estimate that only 25% of the expected N 1s signal for inert APA is detected, which indicates a large quantity of the azide groups to be detached from APA, in agreement with previous reports on Cu(111).[47] On the other hand, we could not resolve the N 1s signal for APA deposited on the PdGa{111} surfaces, because of the energy overlap with Ga LMM Auger peaks for Al K_α and Mg K_α, we cannot quantify the amount of intact azide groups for APA deposited on the PdGa{111} surfaces based on the N 1s XPS signal, but as the C-N component component in the C 1s signal amounts to 9-11% we have a further indication that APA is intact to a large extent on these surfaces.

Contrary to azide functional groups, detailed XPS investigations on carboxylic acids have been reported on Au(111), Ag(100), Ag(111), Cu(100), Cu(110) and Cu(111) surfaces.[50–52,278–281] In XPS, this functional group can be identified due to the large chemical shift in the

C 1s core level signal towards higher binding energy compared to aromatic carbon, resulting in a C 1s core level component at about 289.3 eV. Upon deprotonation of the COOH group, a new C 1s core level component emerges at around 288.1 eV.[281,52]

Applying these results to our XPS experiments, we find that the carboxylic acid of the APA molecules are deprotonated upon deposition at 300 K on the Cu(111) surface. Contrary to the PdGa{111} surfaces where more than 40% (Pd_3-terminated PdGa{111}) or even close to 60% (Pd_1-terminated PdGa{111}) of all carboxylic acids remain protonated. This ratio remains stable even upon annealing to 350 K. Moreover, while on Cu(111), the XPS signal originating from the carboxylic acid group vanishes upon annealing to 400 K, it persists on PdGa{111} up to temperatures of 410 K with a weighting of maximal 17%.

5.5.1.4 Abundance of reaction products

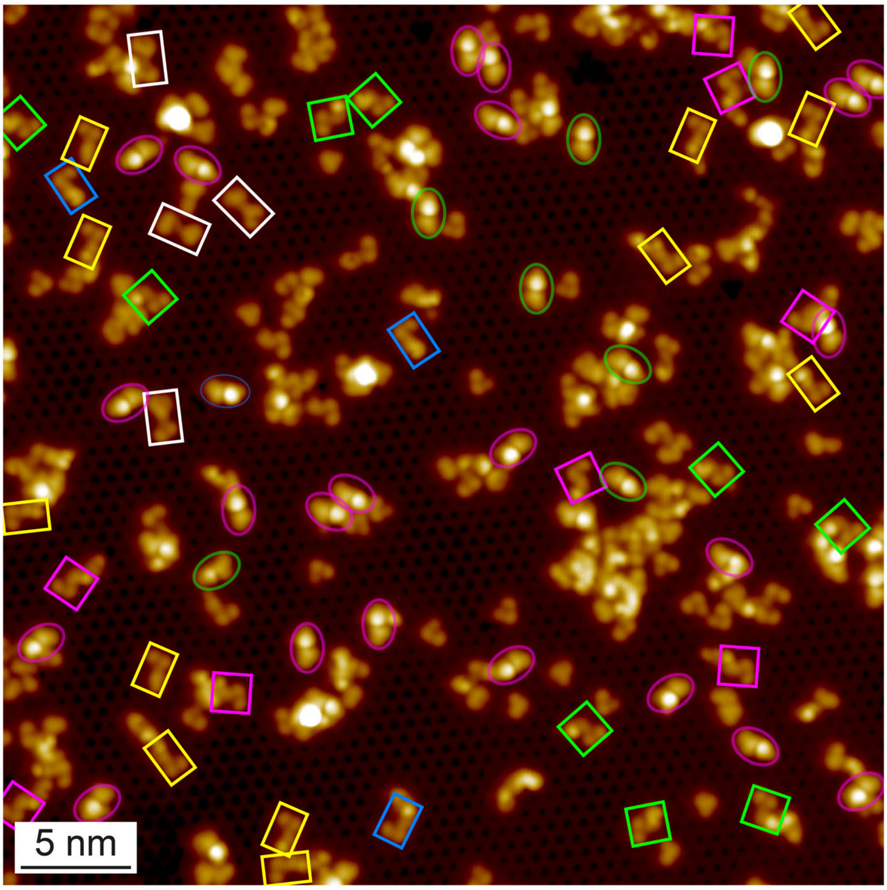

Figure 5.56 | Abundance of 1,4-triazoles on PdGa:B(-1-1-1)Pd_1
40 x40 nm^2 STM image after thermally triggering the azide-alkyne Huisgen cycloaddition on the PdGa:B(-1-1-1)Pd_1 ($V_G = 100\ mV$; $I_T = 100\ pA$). All 1,4-triazoles and 9-EP dimers are highlighted either by a colored area or circle.

The colors of the shaded areas and circles in Figure 5.56 and Figure 5.57 correspond to the same reaction product. In particular, the yellow shaded areas correspond to R_{P1}, the blue shaded ones to S_{P1}, the green ones to R_{P2}, the red ones to S_{P2} and the white ones to 9-EP dimers. The red circles highlight the S_{P3} and the green circles the R_{P3} 1,4-triazole, respectively. As can be seen from Figure 5.56 and Figure 5.57, we did not consider any structure which is part of a larger molecule agglomeration as reaction product for our statistical analysis.

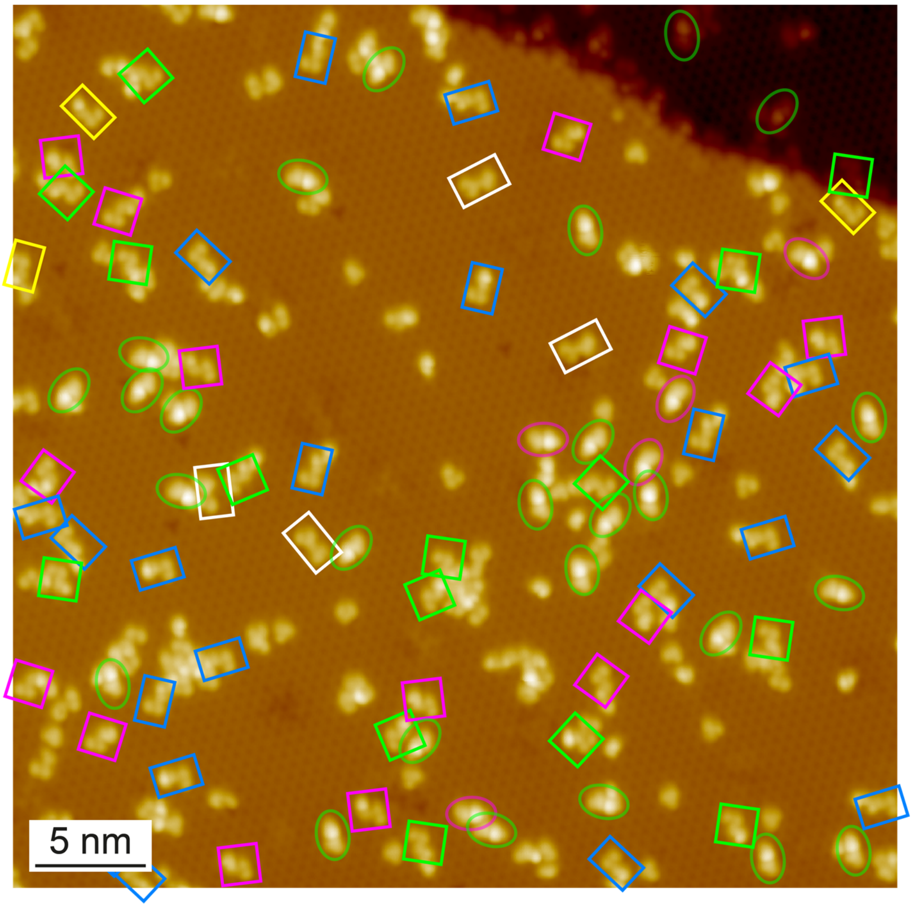

Figure 5.57 | Abundance of 1,4-triazoles on PdGa:A(111)Pd₁

40 x40 nm² STM image after thermally triggering the azide-alkyne Huisgen cycloaddition on the PdGa:A(111)Pd₁ ($V_G = 100\ mV$; $I_T = 100\ pA$). All 1,4-triazoles and 9-EP dimers are highlighted either by a colored area or circle.

5.5.1.5 *Adsorption configuration of the 1,4-triazoles*

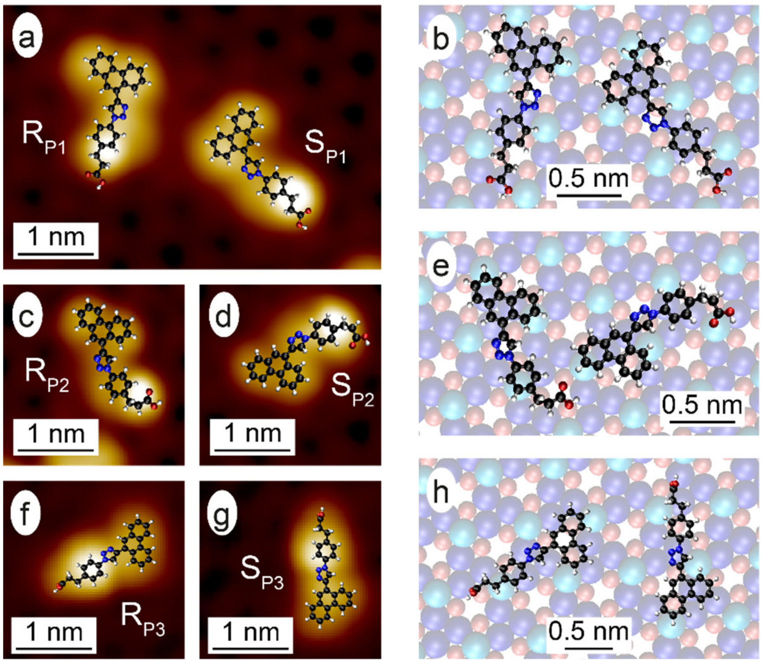

Figure 5.58 | Adsorption configuration of the 1,4-triazoles

STM images of the 1,4-triazoles on the PdGa:B(-1-1-1)Pd₁ surface overlaid with the molecular structure in **a**, **c**-**d**, **f**-**g** and the correspond adsorption configurations in **b**, **e**, **h**.

Substrate	#APA / 100 nm^2	#9-EP / 100 nm^2	#1,4-triazole / 100 nm^2	Yield
A:Pd$_1$	6.07	8.04	2.24	37%
B:Pd$_1$	8.75	6.10	3.57	58%

Table 5.12 | 1,4-triazole reaction yield

The number of APA and 9-EP molecules per 100 nm^2 after RT deposition on the A:Pd$_1$ and B:Pd$_1$ surfaces, respectively. The number of 1,4-triazoles per 100 nm^2 after subsequent annealing to 425 K. The percentage reaction yield is determined by the formula $Yield = \frac{actual\ yield}{theoretical\ yield} = \frac{\min(APA/100nm^2, 9-EP/100nm^2)}{1{,}4-triazole/100nm^2}$.

6. **Conclusion and outlook**

This thesis reports on the results of the investigation of physical and chemical effects connected to the special structural properties arising from the particular space group of intermetallic PdGa. Specifically, its chirality and the chirality transfer to the electronic surface structure, to the molecular dynamics, and to on-surface reaction processes have been studied. The main focus of this work was on gaining a deeper understanding on the surface reactivity and enantioselectivity of PdGa, which is so far very limited as compared to achiral surfaces employed in on-surface synthesis like Au(111), Cu(111), or Pd(111). Such deepened insight into asymmetric catalysis shall extend the field of on-surface synthesis towards the enantioselective formation of prochiral and chiral molecules. To achieve this goal, we investigated several surface-assisted intermolecular coupling reactions with regards to their enantioselectivity, the involved reaction steps going from adsorption, activation and chemical bonding with a particular emphasis on the ensemble effect.

Related to its unique properties, the effects of chirality of PdGa has been successfully evidenced and studied with regard to three different topics: (i) PdGa as a chiral topological material, for which it is predestined in the search of symmetry-protected fermionic quasiparticles, (ii) PdGa as a chiral stator, which can be used to enforce highly directed motion onto small achiral molecules, and (iii) PdGa as an ideal candidate to perform and investigate asymmetric heterogeneous catalytic processes on the atomic scale, thus allowing unprecedented insights into the chirality transfer of the substrate to the molecules during different phases of the on-surface reactions.

6.1 PdGa – chiral topological material

The chirality of PdGa is, for instance, expressed in highly exotic electronic surface states emerging with a Chern number of magnitude 4 on its (100) surface. Our results demonstrate that a fermionic topological state of matter, which is without counterpart in particle physics, hosted in PdGa and allow the control over the sign of the topological charge of this fermionic state by the specific selection of the crystal enantiomorph. Such multifold chiral fermionic states might be used to detect several optoelectronic effects predicted for this class of materials, among others the quantized photogalvanic optical response, or the chiral magnetic effect.[69] Moreover, superconducting pairing of the Fermi surface with non-zero Chern numbers have been proposed to give rise to a new type of topological superconducting phase, which could be investigated with STM-based spectroscopy.[282]

In terms of the chase for further exotic fermionic quasiparticles in solid-state systems, representatives of other chiral space groups could be investigated. In particular, members of space group 199, 214, or 220 are predicted to host three-fold band crossings, while representatives of space group 130, 135, 220, 222, 223, or 230 should possess eight-fold band crossing.[28] An extended catalogue of candidates for each space group is given in Ref.[283].

6.2 PdGa – stator for molecular machines

Apart from giving rise to chiral electronic surface states, the chirality of the Pd_3-terminated PdGa{111} surfaces has been shown to uniquely define the direction of rotation for single achiral acetylene molecules, which can be driven electronically with a directionality of 98%. In this context, the interesting question of how a single electron can induce molecular rotation is yet unresolved. It might be connected to structural differences of the ground state between the charged and neutral acetylene, similar to electron induced phonon excitation via the Franck-Condon principle. Therefore experimental determination of the vibrational and libration modes of acetylene molecules adsorbed on the Pd_3-terminated PdGa{111} surface with high-resolution electron energy loss spectroscopy in combination with DFT calculations might provide further insight on this aspect.

The persisting high directionality of the molecular motor even in the quantum tunneling regime seems to contradict the classical 2nd law of thermodynamics, according to which the entropy of a system cannot decrease under thermodynamic equilibrium and accordingly elastic tunneling and directional rotation are not compatible with each other . Therefore, this unexpected quantum tunneling behavior of our artificial molecular motor implicates the combination of quantum and non-equilibrium (*i.e.* inelastic) processes in this regime.[192]Consequently, this molecular motor might pave the way to experimentally investigate non-equilibrium dissipative quantum tunneling dynamics. One option to get further insight in this phenomena, is by investigating the same molecular motion on an identically terminated surface of another crystal belonging to the $P2_13$ space group, some of which are given in Ref.[29]. Most promising candidates in the context of the acetylene rotation are PtGa{111} or PdAl{111} surfaces. Ultimately, our molecular motor might also allow the testing of concepts to harvest energy at the smallest possible length scale by coupling the motion of isolated molecular motors such that they perform concerted motions upon triggering the rotation of one molecule.[166–168]

6.3 PdGa – template for enantioselective heterogeneous catalysis

The chirality transfer of the PdGa{111} surfaces to adsorbed molecules has not only been studied by observing the directed rotation of acetylene molecules, but also via the adsorption and reaction properties for several prochiral molecules. In this thesis, we have shown the chirality of the substrate to manifest itself in (i) the enantioselective debromination of 5-Bromo-7Methylbenz(a)Anthracene (BMA) with a temperature difference for the debromination of up to 46 K between the two enantiomers, (ii) the almost enantiopure formation of homochiral 9-Ethynylphenanthrene (9-EP) trimers on Pd_3-terminated PdGa{111} surfaces, and (iii) the enantioselective occurrence of 1,4-triazoles after the azide-alkyne Huisgen cycloaddition on the Pd_1-terminated PdGa{111} surfaces.

In conclusion, we could identify different mechanisms for the origin of the enantioselectivity in all three cases. In particular, (i) the debromination of BMA proceeds enantioselectively, because the interconversion between its two surface enantiomers ("flipping") is suppressed at the reaction temperature. This is in stark contrast to (ii) the formation of nearly enantiopure, homochiral 9-EP trimers, which only become homochiral and enantiopure due to the "flipping" of 9-EP molecules incorporated into the trimers. Finally, (iii) the 1,4-triazoles appear with enantioselective preferences, although the precursor molecules have the freedom of interconversion between their surface enantiomeric form at the reaction temperature.

Our investigations set the basis for further research on the reactivity of the PdGa(hkl) surfaces towards the extension of the field of asymmetric on-surface synthesis of novel organic materials by covalent bonding and towards the development of a general concept of enantioselective catalysis on intermetallic compounds. In this regard, an extension of the number of catalytically active, chiral intermetallic compounds which belong to the same space group as PdGa (*e.g.*, PtGa, PtAl, PdAl,…) and that can be prepared under UHV conditions to yield clean, atomically flat, bulk-truncated, and well-defined crystal surfaces would allow not only the investigation of the ensemble effect, but the ligand effect as well, in asymmetric on-surface synthesis.

After having achieved the formation of enantiopure prochiral molecular structures with the trimerization of 9-EP within this project, the investigation of the chirality transfer of the PdGa{111} surface to 'truly chiral' molecules with a 3-dimensional structure is the next logical step. However, due to their three dimensional character, chiral (as opposed to prochiral) molecules will be difficult to investigate with STM. Therefore, the enantioselectivity for chiral molecules on the PdGa{111} surfaces could first be demonstrated with a decomposition reaction, for instance the decomposition of tartaric- or aspartic acid, which is well-investigated on several Cu(hkl) surfaces under UHV conditions with a temperature-programmed desorption method. Among others, the decomposition reactions has been studied on kinked copper surfaces, which would allow a first comparison between the two approaches for enantioselective heterogeneous catalysis in terms of enantiospecifity.[212,213] The suggested decomposition reactions could be followed by a reaction process similar to the one performed in Ref.[92], where they reduced the complexity of the chirality from helical to prochiral. However, instead of initially deposit enantiopure chiral molecules, one would deposit a racemic mixture on PdGa{111} and evaluate for which of the two enantiomers the reaction proceeds first. As the reaction products would be planar, such a reaction could be tracked with STM. Finally, the on-surface synthesis of chiral molecules from prochiral precursors might be tackled. In case of high reaction selectivity, the exact structure and enantioselectivity could be determined with high resolution x-ray photoelectron diffraction (XPD), as has been demonstrated for tartaric acid on Cu(110).[284]

In the case of the BMA debromination, we showed a good correspondence between the experimentally determined adsorption configurations, and the one derived from DFT calculations. Also the simulated STM and nc-AFM images reproduce the experimentally measured ones very well. However, in terms of adsorption energies, experimental results can only be reproduced with difficulties, *e.g.*, the implementation of the van der Waals interaction needs to be adapted to the experiment, presumably because long distance interactions become determinant.[230] So far, there has been little experimental data to test non-local DFT corrections, hence limiting the overall predictive power of DFT. This might change with an increasing numbers of (pro-)chiral molecules being investigated on different chiral PdGa surfaces. Thereby, creating an extensive catalogue of adsorption configurations and their corresponding adsorption energies. The formidable challenge in this task is to obtain single-molecule interactions with an accuracy of 10 meV or better. Due to the further increased complexity of dynamic molecular processes on surfaces, which is challenging to accurately simulate even for small achiral molecules on well-studied single crystal surfaces like Pt(111),[285] the understanding of enantioselective dynamic processes is still in its very early infancy. Despite these challenges, the bulk-truncated PdGa (having a simple cubic structure and 8 atoms in the unit cell) surfaces might still constitute the simplest start to tackle real-world, heterogeneous enantioselective dynamic processes with DFT possible.

In view of the strong expression of PdGa bulk chirality on its surfaces, whether it is expressed in electronic chiral surface Fermi-arcs, or even in chirality transfer to molecules, we have demonstrated PdGa to be a very promising candidate to extend the field of on-surface synthesis by introducing enantioselective control for several different on-surface reactions forming exclusively prochiral products. The main challenge for future experiments will be to use this enantioselective control of prochiral molecules to form enantiopure extended prochiral molecular structures or even truly 3-dimensional chiral molecules.

7. References

1. Joyce, G. F. *et al.* Chiral selection in poly(C)-directed synthesis of oligo(G). *Nature* **310**, 602–603 (1984).
2. Avetisov, V. A., Goldanskii, V. I. & Kuz'min, V. V. Handedness, origin of life and evolution. *Phys. Today* **44**, 33 (1991).
3. Smith, S. W. Chiral Toxicology: It's the Same Thing... Only Different. *Toxicol. Sci.* **110**, 4–30 (2009).
4. Kasprzyk-Hordern, B. Pharmacologically active compounds in the environment and their chirality. *Chem. Soc. Rev.* **39**, 4466–4503 (2010).
5. Heitbaum, M., Glorius, F. & Escher, I. Asymmetric Heterogeneous Catalysis. *Angew Chem Int Ed* **45**, 4732–4762 (2006).
6. Bellemin-Laponnaz, S., Achard, T., Bissessar, D., Geiger, Y. & Maisse-François, A. Synthesis and application of dynamic self-supported enantioselective catalysts. *Coord. Chem. Rev.* **332**, 38–47 (2017).
7. Yun, Y. & Gellman, A. J. Adsorption-induced auto-amplification of enantiomeric excess on an achiral surface. *Nat. Chem.* **7**, 520–525 (2015).
8. Zaera, F. Chirality in adsorption on solid surfaces. *Chem. Soc. Rev.* **46**, 7374–7398 (2017).
9. Dutta, S. & Gellman, A. J. Enantiomer surface chemistry: conglomerate versus racemate formation on surfaces. *Chem. Soc. Rev.* **46**, 7787–7839 (2017).
10. Parschau, M., Romer, S. & Ernst, K.-H. Induction of Homochirality in Achiral Enantiomorphous Monolayers. *J Am Chem Soc* **126**, 15398–15399 (2004).
11. Stacchiola, D., Burkholder, L. & Tysoe, W. T. Enantioselective Chemisorption on a Chirally Modified Surface in Ultrahigh Vacuum: Adsorption of Propylene Oxide on 2-Butoxide-Covered Palladium(111). *J Am Chem Soc* **124**, 8984–8989 (2002).
12. Gao, F., Wang, Y., Li, Z., Furlong, O. & Tysoe, W. T. Enantioselective Reactions on a Au/Pd(111) Surface Allooy with Coadsorbed Chiral 2-Butanol and Propylene Oxide. *J Phys Chem C* **112**, 3362–3372 (2008).
13. Lee, I. & Zaera, F. Chiral Templating of Surfaces: Adsorption of (S)-2-Methylbutanoic Acid on Pt(111) Single-Crystal Surfaces. *J Am Chem Soc* **128**, 8890–8898 (2006).
14. Lawton, T. J. *et al.* Long Range Chiral Imprinting of Cu(110) by Tartaric Acid. *J Phys Chem C* **117**, 22290–22297 (2013).
15. Watson, D. J. *et al.* Heterogeneously Catalyzed Asymmetric Hydrogenation of C=C Bonds Directed by Surface-Tethered Chiral Modifiers. *J. Am. Chem. Soc.* **131**, 14584–14589 (2009).
16. Demers-Carpentier, V. *et al.* Direct Observation of Molecular Preorganization for Chirality Transfer on a Catalyst Surface. *Science* **334**, 776–780 (2011).
17. Hazen, R. M. & Sholl, D. S. Chiral selection on inorganic crystalline surfaces. *Nat. Mater.* **2**, 367–374 (2003).

18. Soai, K., Kawasaki, T. & Matsumoto, A. Role of Asymmetric Autocatalysis in the Elucidation of Origins of Homochirality of Organic Compounds. *Symmetry* **11**, 694 (2019).
19. Kovnir, K. *et al.* A new approach to well-defined, stable and site-isolated catalysts. *Sci. Technol. Adv. Mater.* **8**, 420–427 (2007).
20. Osswald, J. *et al.* Palladium–gallium intermetallic compounds for the selective hydrogenation of acetylene: Part I: Preparation and structural investigation under reaction conditions. *J. Catal.* **258**, 210–218 (2008).
21. Osswald, J. *et al.* Palladium–gallium intermetallic compounds for the selective hydrogenation of acetylene: Part II: Surface characterization and catalytic performance. *J. Catal.* **258**, 219–227 (2008).
22. Armbrüster, M. *et al.* Pd-Ga Intermetallic Compounds as Highly Selective Semihydrogenation Catalysts. *J. Am. Chem. Soc.* **132**, 14745–14747 (2010).
23. Armbrüster, M. *et al.* How to Control the Selectivity of Palladium-based Catalysts in Hydrogenation Reactions: The Role of Subsurface Chemistry. *ChemCatChem* **4**, 1048–1063 (2012).
24. Föttinger, K. & Rupprechter, G. In Situ Spectroscopy of Complex Surface Reactions on Supported Pd−Zn, Pd−Ga, and Pd(Pt)−Cu Nanoparticles. *Acc. Chem. Res.* **47**, 3071–3079 (2014).
25. Armbrüster, M. *et al.* Refinement of the crystal structure of palladium gallium (1:1), PdGa. *Z Krist. NCS* **225**, 617–618 (2010).
26. Prinz, J. Surface Science Investigations on Structure and Binding Centers of Intermetallic PdGa Surfaces. (EPFL, 2014).
27. Prinz, J., Gröning, O., Brune, H. & Widmer, R. Highly Enantioselective Adsorption of Small Prochiral Molecules on a Chiral Intermetallic Compound. *Angew. Chem. Int. Ed.* **54**, 3902–3906 (2015).
28. Bradlyn, B. *et al.* Beyond Dirac and Weyl fermions: Unconventional quasiparticles in conventional crystals. *Science* **353**, (2016).
29. Chang, G. *et al.* Unconventional Chiral Fermions and Large Topological Fermi Arcs in RhSi. *Phys. Rev. Lett.* **119**, 206401 (2017).
30. Tang, P., Zhou, Q. & Zhang, S.-C. Multiple types of topological fermions in transition metal silicides. *Phys. Rev. Lett.* **119**, 206402 (2017).
31. Chang, G. *et al.* Topological quantum properties of chiral crystals. *Nat. Mater.* **17**, 978–985 (2018).
32. Clair, S. & de Oteyza, D. G. Controlling a Chemical Coupling Reaction on a Surface: Tools and Strategies for On-Surface Synthesis. *Chem. Rev.* **119**, 4717–4776 (2019).
33. Hla, S.-W., Bartels, L., Meyer, G. & Rieder, K.-H. Inducing all steps of a chemical reaction with the scanning tunneling microscope tip: towards single molecule engineering. *Phys. Rev. Lett.* **85**, 2777 (2000).
34. Grill, L. *et al.* Nano-architectures by covalent assembly of molecular building blocks. *Nat. Nanotechnol.* **2**, 687–91 (2007).
35. Vasseur, G. *et al.* Quasi one-dimensional band dispersion and surface metallization in long-range ordered polymeric wires. *Nat. Commun.* **7**, 10235 (2016).
36. Di Giovannantonio, M. *et al.* On-Surface Synthesis of Indenofluorene Polymers by Oxidative Five-Membered Ring Formation. *J. Am. Chem. Soc.* **140**, 3532–3536 (2018).

37. Wang, W., Shi, X., Wang, S., Van Hove, M. A. & Lin, N. Single-Molecule Resolution of an Organometallic Intermediate in a Surface-Supported Ullmann Coupling Reaction. *J. Am. Chem. Soc.* **133**, 13264–13267 (2011).
38. Cai, J. *et al.* Atomically precise bottom-up fabrication of graphene nanoribbons. *Nature* **466**, 470–473 (2010).
39. Ruffieux, P. *et al.* On-surface synthesis of graphene nanoribbons with zigzag edge topology. *Nature* **531**, 489–492 (2016).
40. Gröning, O. *et al.* Engineering of robust topological quantum phases in graphene nanoribbons. *Nature* **560**, 209–213 (2018).
41. Rizzo, D. J. *et al.* Topological band engineering of graphene nanoribbons. *Nature* **560**, 204–208 (2018).
42. Shi, K. J. *et al.* Ullmann coupling reaction of aryl chlorides on Au(111) using dosed Cu as a catalyst and the programmed growth of 2D covalent organic frameworks. *Chem Commun* **52**, 8726–8729 (2016).
43. Steiner, C. *et al.* Hierarchical on-surface synthesis and electronic structure of carbonyl-functionalized one- and two-dimensional covalent nanoarchitectures. *Nat. Commun.* **8**, 14765 (2017).
44. Stolz, S. *et al.* Reversible dehalogenation in on-surface aryl-aryl coupling. *Angew Chem Int Ed* (2020) doi:doi.org/10.1002/ange.202005443.
45. Prinz, J. *et al.* Ensemble Effect Evidenced by CO Adsorption on the 3-Fold PdGa Surfaces. *J. Phys. Chem. C* **118**, 12260–12265 (2014).
46. Prinz, J. *et al.* Adsorption of Small Hydrocarbons on the Three-Fold PdGa Surfaces: The Road to Selective Hydrogenation. *J. Am. Chem. Soc.* **136**, 11792–11798 (2014).
47. Bebensee, F. *et al.* On-Surface Azide–Alkyne Cycloaddition on Cu(111): Does It “Click” in Ultrahigh Vacuum? *J. Am. Chem. Soc.* **135**, 2136–2139 (2013).
48. Prinz, J. *et al.* Isolated Pd sites on the intermetallic PdGa(111) and PdGa(-1-1-1) model catalyst surfaces. *Angew. Chem.* **124**, 9473–9477 (2012).
49. Bian, X. *et al.* Graphene layers on bimetallic Ni/Cu(111) surface and near surface alloys in controlled growth of graphene. *RSC Adv.* **6**, 74973 (2016).
50. Gao, H.-Y. *et al.* Decarboxylative Polymerization of 2,6-Naphthalenedicarboxylic Acid at Surfaces. *J Am Chem Soc* **136**, 9658–9663 (2014).
51. Morchutt, C. *et al.* Interplay of Chemical and Electronic Structure on the Single-Molecule Level in 2D Polymerization. *ACS Nano* **10**, 11511–11518 (2016).
52. Abyazisani, M., Bradford, J., Motta, N., Lipton-Duffin, J. & MacLeod, J. Adsorption, Deprotonation , and Decarboxylation of Isophthalic Acid on Cu(111). *Langmuir* **35**, 7112–7120 (2019).
53. Kovnir, K. *et al.* In situ surface characterization of the intermetallic compound PdGa – A highly selective hydrogenation catalyst. *Surf. Sci.* **603**, 1784–1792 (2009).
54. Rosenthal, D. *et al.* Surface investigation of intermetallic PdGa($\bar{1}\bar{1}\bar{1}$). *Langmuir* **28**, 6848–6856 (2012).
55. Horio, Y. Low-Energy Electron Diffraction. in *Compendium of Surface and Interface Analysis* (Springer, Singapore, 2018).

56. Andersen, J. N., Balasubramanian, T., Almbladh, C.-O., Johansson, L. I. & Nyholm, R. Strong Phonon Replicas in Be 1s Photoemission Spectra. *Phys. Rev. Lett.* **86**, 4398–4401 (2001).
57. Moulder, J. F. The impact of the scanning XPS microprobe on industrial applications of X-ray photoelectron spectroscopy. *J. Electron Spectrosc. Relat. Phenom.* **231**, 43–49 (2019).
58. Somorjai, G. A. *Chemistry in Two Dimensions: Surfaces*. (Cornell University Press, 1981).
59. Di Giovannantonio, M. *et al.* On-Surface Growth Dynamics of Graphene Nanoribbons: The Role of Halogen Functionalization. *ACS Nano* **12**, 74–81 (2018).
60. Di Giovannantonio, M. *et al.* On-Surface Synthesis of Antiaromatic and Open-Shell Indeno[2,1-b]fluorene Polymers and Their Lateral Fusion into Porous Ribbons. *J. Am. Chem. Soc.* **141**, 12346–12354 (2019).
61. Di Giovannantonio, M. *et al.* Insight into Organometallic Intermediate and Its Evolution to Covalent Bonding in Surface-Confined Ullmann Polymerization. *ACS Nano* **7**, 8190–8198 (2013).
62. Simonov, K. A. *et al.* Effect of Substrate Chemistry on the Bottom-Up Fabrication of Graphene Nanoribbons: Combined Core-Level Spectroscopy and STM Study. *J. Phys. Chem. C* **118**, 12532–12540 (2014).
63. Simonov, K. A. *et al.* From Graphene Nanoribbons on Cu(111) to Nanographene on Cu(110): Critical Role of Substrate Structure in the Bottom-Up Fabrication Strategy. *ACS Nano* **9**, 8997–9011 (2015).
64. Di Giovannantonio, M. *et al.* Mechanistic Picture and Kinetic Analysis of Surface-Confined Ullmann Polymerization. *J. Am. Chem. Soc.* **138**, 16696–16702 (2016).
65. Galeotti, G. *et al.* The role of halogens in on-surface Ullmann polymerization. *Faraday Discuss.* **204**, 453–469 (2017).
66. Simonov, K. A. *et al.* Synthesis of armchair graphene nanoribbons from the 10,10′-dibromo-9,9′-bianthracene molecules on Ag(111): the role of organometallic intermediates. *Sci. Rep.* **8**, (2018).
67. Galeotti, G. *et al.* An unexpected organometallic intermediate in surface-confined Ullmann coupling. *Nanoscale* **11**, 7682–7689 (2019).
68. Fritton, M. *et al.* The Role of Kinetics versus Thermodynamics in Surface-Assisted Ullmann Coupling on Gold and Silver Surfaces. *J Am Chem Soc* **141**, 4824–4832 (2019).
69. Sanchez, D. S. *et al.* Topological chiral crystals with helicoid-arc quantum states. *Nature* **567**, 500–505 (2019).
70. Rao, Z. *et al.* Observation of unconventional chiral fermions with long Fermi arcs in CoSi. *Nature* **567**, 496–499 (2019).
71. Schröter, N. B. M. *et al.* Chiral topological semimetal with multifold band crossings and long Fermi arcs. *Nat. Phys.* **15**, 759–765 (2019).
72. Binnig, G. & Rohrer, H. Scanning tunneling microscopy. *Surf. Sci.* **126**, 236–244 (1983).
73. Binnig, G., Rohrer, H., Gerber, Ch. & Weibel, E. 7 x 7 Reconstruction on Si(111) Resolved in Real Space. *Phys. Rev. Lett.* **50**, 120–123 (1983).

74. Nempkes, S. N. *et al.* Robust zero-energy modes in an electric higher-order topological insulator. *Nat. Mater.* **18**, 1292–1297 (2019).
75. Can We See an Atom? *Physics Forums Insights* https://www.physicsforums.com/insights/can-see-atom/ (2015).
76. Simmons, J. G. Electric Tunnel Effect between Dissimilar Electrodes Separated by a Thin Insulating Film. *J. Appl. Phys.* **34**, 2581–2590 (1963).
77. Chen, J. C. *Introduction to Scanning Tunneling Microscopy*. (Oxford Scholarship, 2007).
78. Wiesendanger, R. *Scanning Probe Microscopy and Spectroscopy: Methods and Applications*. (Cambridge University Press, 1994).
79. STM Manual. https://www.physik.uni-siegen.de/nanophysik/teaching/stm_manual.pdf.
80. Tersoff, J. & Hamann, D. R. Theory of the scanning tunneling microscope. *Phys. Rev. B* **31**, 805–813 (1985).
81. The Scanning Tunneling Microscope [IAP/TU Wien]. http://www.iap.tuwien.ac.at/www/surface/stm_gallery/stm_schematic.
82. Klein, M. & Schwitzgebel, G. An improved lamellae drop-off technique for sharp tip preparation in scanning tunneling microscopy. *Rev. Sci. Instrum.* **68**, 3099–3103 (1997).
83. Müller, A.-D. *et al.* Characterization of electrochemically etched tungsten tips for scanning tunneling microscopy. *Rev. Sci. Instrum.* **70**, 3970–3972 (1999).
84. Giessibl, F. J. Advances in atomic force microscopy. *Rev. Mod. Phys.* **75**, 949–983 (2003).
85. Pavliček, N. & Gross, L. Generation, manipulation and characterization of molecules by atomic force microscopy. *Nat. Rev. Chem.* **1**, 0005 (2017).
86. Gross, L., Mohn, F., Moll, N., Liljeroth, P. & Meyer, G. The Chemical Structure of a Molecule Resolved by Atomic Force Microscopy. *Science* **325**, 1110–1114 (2009).
87. Giessibl, F. J. Atomic resolution on Si(111)-(7×7) by noncontact atomic force microscopy with a force sensor based on a quartz tuning fork. *Appl. Phys. Lett.* **76**, 1470–1472 (2000).
88. Giessibl, F. J. The qPlus sensor, a powerful core for the atomic force microscope. *Rev. Sci. Instrum.* **90**, 011101 (2019).
89. Gross, L. *et al.* Bond-Order Discrimination by Atomic Force Microscopy. *Science* **337**, 1326–1329 (2012).
90. Schuler, B., Meyer, G., Peña, D., Mullins, O. C. & Gross, L. Unraveling the Molecular Structures of Asphaltenes by Atomic Force Microscopy. *J. Am. Chem. Soc.* **137**, 9870–9876 (2015).
91. Kaiser, K. *et al.* An sp-hybridized molecular carbon allotrope, cyclo[18]carbon. *Science* **365**, 1299–1301 (2019).
92. Stetsovych, O. *et al.* From helical to planar chirality. *Nat. Chem.* **9**, 213–218 (2017).
93. Hellerstedt, J. *et al.* Aromatic Azide Transformation on the Ag(111) Surface Studied by Scanning Probe Microscopy. *Angew Chem Int Ed* **58**, 2266–2271 (2019).
94. Wang, S. *et al.* On-surface synthesis and characterization of individual polyacetylene chains. *Nat. Chem.* **11**, 924–930 (2019).
95. Muntwiler, M. *et al.* Surface science at the PEARL beamline of the Swiss Light Source. *J. Synchrotron Radiat.* **24**, 354–366 (2017).

96. Strocov, V. N. *et al.* High-resolution soft X-ray beamline ADRESS at the Swiss Light Source for resonant inelastic X-ray scattering and angle-resolved photoelectron spectroscopies. *J. Synchrotron Radiat.* **17**, 631–643 (2010).
97. Hoesch, M. *et al.* A facility for the analysis of the electronic structure of solids and their surfaces by synchrotron radiation photoelectron spectroscopy. *Rev. Sci. Instrum.* **88**, 013106 (2017).
98. Pengzi, L., Williams, J. R. & Cha, J. J. Topological nanomaterials. *Nat. Rev. Mater.* **4**, 479 (2019).
99. Bernevig, B. A., Hughes, T. L. & Zhang, S.-C. Quantum Spin Hall Effect and Topological Phase Transition in HgTe Quantum Wells. *Science* **314**, 1757–1761 (2006).
100. König, M. *et al.* Quantum Spin Hall Insulator State in HgTe Quantum Wells. *Science* **318**, 766–770 (2007).
101. Yan, B. & Zhang, S.-C. Topological Materials. *Rep. Prog. Phys.* **75**, 096501 (2012).
102. Castro Neto, A. H., Guinea, F., Peres, N. M. R., Novoselov, K. S. & Geim, A. K. The electronic properties of graphene. *Rev. Mod. Phys.* **81**, 109–162 (2009).
103. Mourik, V. *et al.* Signatures of Majorana Fermions in Hybrid Superconductor-Semiconductor Nanowire Devices. *Science* **336**, 1003–1007 (2012).
104. Nadj-Perge, S. *et al.* Observation of Majorana fermions in ferromagnetic atomic chains on a superconductor. *Science* **346**, 602–607 (2014).
105. Lv, B. Q. *et al.* Experimental Discovery of Weyl Semimetal TaAs. *Phys. Rev. X* **5**, 031013 (2015).
106. Xu, S.-Y. *et al.* Discovery of a Weyl fermion semimetal and topological Fermi arcs. *Science* **349**, 613–617 (2015).
107. Xu, S.-Y. *et al.* Discovery of a Weyl fermion state with Fermi arcs in niobium arsenide. *Nat. Phys.* **11**, 748–754 (2015).
108. Liu, Z. K. *et al.* A stable three-dimensional topological Dirac semimetal Cd 3 As 2. *Nat. Mater.* **13**, 677–681 (2014).
109. Liu, Z. K. *et al.* Discovery of a Three-Dimensional Topological Dirac Semimetal, Na3Bi. *Science* **343**, 864–867 (2014).
110. Wan, X., Turner, A. M., Vishwanath, A. & Savrasov, S. Y. Topological semimetal and Fermi-arc surface states in the electronic structure of pyrochlore iridates. *Phys. Rev. B* **83**, 205101 (2011).
111. Thouless, D. J., Kohmoto, M., Nightingale, M. P. & den Nijs, M. Quantized Hall Conductance in a Two-Dimensional Periodic Potential. *Phys. Rev. Lett.* **49**, 405–408 (1982).
112. Kohmoto, M. Topological Invariant and the Quantization of the Hall Conductance. *Ann. Phys.* **160**, 343–354 (1985).
113. Burkov, A. A., Hook, M. D. & Balents, L. Topological nodal semimetals. *Phys. Rev. B* **84**, 235126 (2011).
114. Son, D. T. & Spivak, B. Z. Chiral anomaly and classical negative magnetoresistance of Weyl metals. *Phys. Rev. B* **88**, 104412 (2013).
115. Burkov, A. A. Chiral anomaly and transport in Weyl metals. *J. Phys. Condens. Matter* **27**, 113201 (2015).
116. de Juan, F., Grushin, A. G., Morimoto, T. & Moore, J. E. Quantized circular photogalvanic effect in Weyl semimetals. *Nat. Commun.* **8–15995**, (2017).
117. Flicker, F. *et al.* Chiral Optical Response of Multifold Fermions. *Phys. Rev. B* **98**, 155145 (2018).

118. de Juan, F. *et al.* Difference frequency generation in topological semimetals. *arXiv:1907.02537v1* (2019).

119. Hosur, P. & Qi, X. Recent developments in transport phenomena in Weyl semimetals. *Comptes Rendus Phys.* **14**, 857–870 (2013).

120. Armitage, N. P., Mele, E. J. & Vishwanath, A. Weyl and Dirac Semimetals in Three-Dimensioal Solids. *Rev. Mod. Phys.* **90**, 015001 (2018).

121. Chang, G. *et al.* Topological photocurrent responses from chiral surface Fermi arcs. *arXiv:1906.03207v1* (2019).

122. Fang, C., Gilbert, M. J., Dai, X. & Bernevig, B. A. Multi-Weyl Topological Semimetals Stabilized by Point Group Symmetry. *Phys. Rev. Lett.* **108**, 266802 (2012).

123. Tsirkin, S. S., Souza, I. & Vanderbilt, D. Composite Weyl nodes stabilized by screw symmetry with and without time-reversal invariance. *Phys. Rev. B* **96**, 045102 (2017).

124. Cano, J., Bradlyn, B. & Vergniory, M. G. Multifold nodal points in magnetic materials. *arXiv:1904.12867v2* (2019).

125. Takane, D. *et al.* Observation of Chiral Fermions with a Large Topological Charge and Associated Fermi-Arc Surface States in CoSi. *Phys. Rev. Lett.* **122**, 076402 (2019).

126. Lv, B. Q. *et al.* Observation of multiple types of topological fermions in PdBiSe. *Phys. Rev. B* **99**, 241104 (2019).

127. Rees, D. *et al.* Observation of Topological Photocurrents in the Chiral Weyl Semimetal RhSi. *arXiv:1902.03230v2* (2019).

128. Dyadkin, A. *et al.* Control of chirality of transition-metal monosilicides by the Czochralski method. *Phys. Rev. B* **84**, 014435 (2011).

129. Spence, J. C. H. & Zuo, J. M. On the minimum number of beams needed to distinguish enantiomorphs in X-ray and electron diffraction. *Acta Crystallogr. Sect. A* **A50**, 647–650 (1994).

130. Tanaka, M., Takayoshi, H., Masayoshi, I. & Endoh, Y. Crystal Chirality and Helicity of the Helical Spin Density Wave in MnSi. I. Convergent-Beam Electron Diffraction. *J Phys Soc Jpn* **54**, 2970–2974 (1985).

131. Strocov, V. N. *et al.* Soft-X-Ray ARPES facility at the ADRESS beamline of the SLS: concepts, technical realisation and scientific applications. *J. Synchrotron Radiat.* **21**, 32–44 (2014).

132. Strocov, V. N. *et al.* Three-Dimensional Electron Realm in VSe2 by Soft X-Ray Photoelectron Spectroscopy: Origin of Charge-Density Waves. *Phys. Rev. Lett.* **109**, 086401 (2012).

133. Kresse, G. & Furthmüller, J. Efficiency of *ab-initio* total energy calculations for metals and semiconductors using a plane-wave basis set. *Comput. Mater. Sci.* **6**, 15–50 (1996).

134. Kresse, G. & Furthmüller, J. Efficient iterative schemes for ab initio total-energy calculations using a plane-wave basis set. *Phys. Rev. B* **54**, 11169–11186 (1996).

135. P. K. S. Blaha, K. S. WIEN2k, An Augmented Plane Waves Local Orbitals Program for Calculating Crystal Properties. *Tech. Univ. Wien Wien* (2001).

136. Perdew, J. P., Burke, K. & Ernzerhof, M. Generalized Gradient Approximation Made Simple. *Phys. Rev. Lett.* **77**, 3865–3868 (1996).

137. Momma, K. & Izumi, F. VESTA 3 for three-dimensional visualization of crystal, volumetric and morphology data. *J Appl Cryst* **44**, 1272–1276 (2011).
138. Sheldrick, G. M. Crystal structure refinement with SHELXL. *Acta Crystallogr. Sect. C Struct. Chem.* **71**, 3–8 (2015).
139. Svoboda, K., Schmidt, C. F., Schnapp, B. J. & Block, S. M. Direct observation of kinesin stepping by obtical trapping interferometry. *Nature* **365**, 721–727 (1993).
140. Hoyt, M. A., Hyman, A. A. & Bähler, M. Motor proteins of the eukaryotic cytoskeleton. *PNAS* **94**, 12747–12748 (1997).
141. Schliwa, M. & Woehlke, G. Molecular motors. *Nature* **422**, 759–765 (2003).
142. Vale, R. D. & Milligan, R. A. The Way Things Move: Looking Under the Hood of Molecular Motor Proteins. *Science* **288**, 88–95 (2000).
143. Vale, R. D. The Molecular Motor Toolbox for Intracellular Transport. *Cell* **112**, 467–480 (2003).
144. Amos, L. A. Molecular motors: not quite like clockwork. *Cell. Mol. Life Sci.* **65**, 509–515 (2008).
145. Erbas-Cakmak, S., Leigh, D. A., McTernan, C. T. & Nussbaumer, A. L. Artificial Molecular Machines. *Chem. Rev.* **115**, 10081–10206 (2015).
146. Salma Kassern, T. van L., Anouk S. Lubbe, M. R. W. & Ben L. Feringa, D. A. L. Artificial molecular motors. *Chem Soc Rev* **46**, 2592–2621 (2017).
147. Astumian, R. D. Design principles for Brownian molecular machines: how to swim in molasses and walk in a hurricane. *Phys Chem Chem Phys* **9**, 5067–5083 (2007).
148. Hänggi, P. & Marchesoni, F. Articial Brownian motors: Controlling transport on the nanoscale. *Rev Mod Phys* **81**, 387–442 (2009).
149. Astumian, R. D., Mukherjee, S. & Warshel, A. The physics and physical chemistry of molecular machines. *ChemPhysChem* **17**, 1719–1741 (2016).
150. Bissell, R. A., Córdova, E., Kaifer, A. E. & Stoddart, J. F. A chemically and electrochemically switchable molecular shuttle. *Nature* **369**, 133–137 (1994).
151. Cheng, C. *et al.* An artificial molecular pump. *Nat. Nanotechnol.* **10**, 547–553 (2015).
152. Cárdenas, D. J., Livoreil, A. & Sauvage, J.-P. Redox Control of the Ring-Gliding Motion in a Cu-Complexed Catenane: A Process Involving Three Distinct Geometries. *J Am Chem Soc* **118**, 11980–11981 (1996).
153. Leigh, D. A., Wong, J. K. Y., Dehez, F. & Zerbette, F. Unidirectional rotation in a mechanically interlocked molecular motor. *Nature* **424**, 174–179 (2003).
154. José V. Hernández, E. R. K. & David A. Leigh. A Reversible Synthetic Rotary Molecular Motor. *Science* **306**, 1532–1537 (2004).
155. Wilson, M. R. *et al.* An autonomous chemically fuelled small-molecule motor. *Nature* **534**, 235–240 (2016).
156. Nagatoshi Koumura, R. W. J. Z., Richard A. van Delden, N. H. & Ben L. Feringa. Light-driven monodirectional molecular motor. *Nature* **401**, 152–155 (1999).

157. Koumura, N., Geertsema, E. M., Meetsma, A. & Feringa, B. L. Light-Driven Molecular Rotor: Unidirectional Rotation Controlled by a Single Stereogenic Center. *J Am Chem Soc* **122**, 12005–12006 (2000).
158. Vicario, J., Meetsma, A. & Feringa, B. L. Controlling the speed of rotation in molecular motors. Dramatic acceleration of the rotary motion by structural modification. *Chem Commun* **116**, 5910–5912 (2005).
159. Vicario, J., Walko, M., Meetsma, A. & Feringa, B. L. Fine Tuning of the Rotary Motion by Structural Modifications in Light-Driven Unidirectional Molecular Motors. *J Am Chem Soc* **128**, 5127–5135 (2006).
160. Faulkner, A., van Leeuwen, T., Feringa, B. L. & Wezenberg, S. J. Allosteric Regulation of the Rotational Speed in a Light-Driven Molecular Motor. *J Am Chem Soc* **138**, 13597–13603 (2016).
161. Ruangsupapichat, N., Pollard, M. M., Harutyunyan, S. R. & Feringa, B. L. Reversing the direction in a light-driven rotary molecular motor. *Nat. Chem.* **3**, 53–60 (2011).
162. Balzani, V. *et al.* Autonomous artificial nanomotor powered by sunlight. *PNAS* **103**, 1178–1183 (2006).
163. Cnossen, A. *et al.* Driving Unidirectional Molecular Rotary Motors with Visible Light by Intra- And Intermolecular Energy Transfer from Palladium Porphyrin. *J Am Chem Soc* **134**, 17613–17619 (2012).
164. Qu, D.-H. & Feringa, B. L. Controlling Molecular Rotary Motion with a Self-Complexing Lock. *Angew Chem Int Ed* **49**, 1107–1110 (2010).
165. Berná, J. *et al.* Macroscopic transport by synthetic molecular machines. *Nature* **4**, 704–710 (2005).
166. Eelkema, R. *et al.* Nanomotor rotates microscale objects. *Nature* **440**, 163 (2006).
167. Chen, J. *et al.* Artificial muscle-like function from hierarchical supramolecular assembly of photoresponsive molecular motors. *Nat. Chem.* **10**, 132–138 (2018).
168. Danowski, W. *et al.* Unidirectional rotary motion in a metal-organic framework. *Nat. Nanotechnol.* **14**, 488–494 (2019).
169. Tierney, H. L. *et al.* Experimental demonstration of a single-molecule electric motor. *Nat. Nanotechnol.* **6**, 625–629 (2011).
170. Kudernac, T. *et al.* Electrically driven directional motion of a four-wheeled molecule on a metal surface. *Nature* **479**, 208–211 (2011).
171. Zhang, Y. *et al.* A chiral molecular propeller designed for unidirectional rotations on a surface. *Nat. Commun.* **10**, 3742 (2019).
172. Heinrich, A. J., Lutz, C. P., Cupta, J. A. & Eigler, D. M. Molecule cascades. *Science* **298**, 1381–1387 (2002).
173. U. G. E. Perera, F. A., H. Kersell, Y. Z., G. Vives, J. E., M. Grisolia, G. R. & C. Joachim, S.-W. H. Controlled clockwise and anticlockwise rotational switching of a molecular motor. *Nat. Nanotechnol.* **8**, 46–51 (2013).
174. Simpson, G. J., García-López, V., Boese, A. D., Tour, J. M. & Grill, L. How to control single-molecule rotation. *Nat. Commun.* **10**, 4631 (2019).
175. Stipe, B. C., Rezaei, M. A. & Ho, W. Coupling of vibrational excitation to the rotational motion of a single adsorbed molecule. *Phys. Rev. Lett.* **81**, 1263–1266 (1998).

176. Lauhon, L. J. & Ho, W. Direct observation of the quantum tunneling of single hydrogen atoms with a scanning tunneling microscope. *Phys. Rev. Lett.* **85**, 4566–4569 (2000).
177. Stroscio, J. A. & Celotta, R. J. Controlling the dynamics of a single atom in lateral atom manipulation. *Science* **306**, 242–247 (2004).
178. Nacci, C. *et al.* Current versus temperature-induced switching in a single-molecule tunnel junction: 1,5 cyclooctadiene on Si(001). *Nano Lett.* **9**, 2996–3000 (2009).
179. Jethwa, S. J. *et al.* Supramolecular Corrals on Surfaces Resulting from Aromatic Interactions of Nonplanar Triazoles. *ACS Nano* **11**, 8302–8310 (2017).
180. Lin, C., Durant, E., Persson, M., Rossi, M. & Kumagai, T. Real-space observation of quantum tunneling by a carbon atom: flipping reaction of formaldehyde on Cu(110). *J. Phys. Chem. Lett.* **10**, 645–649 (2019).
181. Gimzewski, J. K. *et al.* Rotation of a Single Molecule Within a Supramolecular Bearing. *Science* **281**, 531–533 (1998).
182. Hahn, J. R. & Ho, W. Oxidation of a Single Carbon Monoxide Molecule Mainpulated and Induced with a Scanning Tunneling Microscope. *Phys Rev Lett* **87**, 166102 (2001).
183. Sainoo, Y. *et al.* Excitation of Molecular Vibrational Modes with Inelastic Scanning Tunneling Microscopy Processes: Examination through Action Spectra of cis-2-Butene on Pd(110). *Phys Rev Lett* **95**, 246102 (2005).
184. Zheng, C. Z., Yeung, C. K., Loy, M. M. T. & Xiao, X. Quantum diffusion of H on Pt(111): Step effects. *Phys. Rev. Lett.* **97**, 166101 (2006).
185. Fomin, E. *et al.* Vibrationally assisted diffusion of H2O and D2O on Pd(111). *Surf. Sci.* **600**, 542–546 (2006).
186. Kumagai, T., Hatta, S., Okuyama, H. & Aruga, T. Adsorbed states and scanning tunneling microscopy induced migration of acetylene on Cu(110). *J. Chem. Phys.* **126**, 234708 (2007).
187. CEMES - CNRS - Nanocar Race. http://www.cemes.fr/Molecule-car-Race?lang=fr.
188. Bauer, A. *et al.* Tip-Induced Inversion of the Chirality of a Molecule's Adsorption Potential Probed by the Switching Directionality. *Adv. Mater.* 1907390 (2020) doi:10.1002/adma.201907390.
189. Feynman, R. P. There's Plenty of Room at the Bottom. (1959).
190. Eigler, D. M. & Schweizer, E. K. Positioning single atoms with a scanning tunnelling microscope. *Nature* **344**, 524–525 (1990).
191. Pezzato, C., Cheng, C., Stoddart, J. F. & Astumian, R. D. Mastering the non-equilibrium assembly and operation of molecular machines. *Chem. Soc. Rev.* **46**, 5491 (2017).
192. Caldeira, A. O. & Leggett, A. J. Influence of Dissipation on Quantum Tunneling in Macroscopic Systems. *Phys. Rev. Lett.* **46**, 211–214 (1981).
193. Roke, D., Wezenberg, S. J. & Feringa, B. L. Molecular rotary motors: Unidirectional motion around double bonds. *PNAS* **115**, 9423–9431 (2018).
194. Hernández, J. V., Kay, E. R. & Leigh, D. A. A reversible synthetic rotary molecular motor. *Science* **306**, 1532–1537 (2004).

195. Erbas-Cakmak, S. *et al.* Rotary and linear molecular motors driven by pulses of a chemical fuel. *Science* **358**, 340–343 (2017).

196. Gao, S., Persson, M. & Lundqvist, B. I. Theory of atom transfer with a scanning tunneling microscope. *Phys. Rev. B* **55**, 4825 (1997).

197. Schreiner, P. R. Tunneling control of chemical reactions: The third reactivity paradigm. *J Am Chem Soc* **139**, 15276–15283 (2017).

198. Klinman, J. P. & Kohen, A. Hydrogen tunneling links protein dynamics to enzyme catalysis. *Annu. Rev. Biochem.* **82**, 471–496 (2013).

199. Tikhodeev, S. G. & Ueba, H. How vibrationally assisted tunneling with STM affects the motions and reactions of single adsorbates. *Phys. Rev. Lett.* **102**, 246101 (2009).

200. Kim, Y., Motobayashi, K., Frederiksen, T., Ueba, H. & Kawai, M. Action spectroscopy for single-molecule reactions - Experiments and theory. *Prog. Surf. Sci.* **90**, 85–143 (2015).

201. Prager, M. & Heidemann, A. Rotational tunneling and neutron spectroscopy: A compilation. *Chem. Rev.* **97**, 2933–2966 (1997).

202. Bonner, W. A. The origin and amplification of biomolecular chirality. *Orig. Life Evol. Biosph.* **21**, 59–111 (1991).

203. Bada, J. L. Origins of homochirality. *Nature* **374**, 594–595 (1995).

204. Ernst, K.-H. Molecular chirality at surfaces. *Phys. Status Solidi B* **11**, 2057–2088 (2012).

205. Minyoung, Y., Renganathan, S. & Kimoon, K. Homochiral Metal-Organic Frameworks for Asymmetric Heterogeneous Catalysis. *Chem. Rev.* **112**, 1196–1231 (2012).

206. Ohtani, B., Shintani, A. & Uosaki, K. Two-Dimensional Chirality: Self-Assembled Monolayer of an Atropisomeric Compound Covalently Bound to a Gold Surface. *J Am Chem Soc* **121**, 6515–6516 (1999).

207. Balandina, T. *et al.* Self-assembly of an asymmetrically functionalized [6]helicene at liquid/solid interfaces. *Chem Commun* **49**, 2207–2209 (2013).

208. Chen, T., Yang, W.-H., Wang, D. & Wan, L.-J. Globally homochiral assembly of two-dimensional molecular networks triggered by co-absorbers. *Nat. Commun.* **4**, 1389 (2013).

209. Ghijsens, E. *et al.* Towards enantioselective adsorption in surface-confined nanoporous systems. *Chem. Commun.* **51**, 4766–4769 (2015).

210. Somorjai, G. A. Surface Science and Catalysis. *Science* **227**, 902–908 (1985).

211. Ertl, G. & Freund, H.-J. Catalysis and Surface Science. *Phys. Today* **52**, 32–38 (1999).

212. Gellman, A. J. *et al.* Superenantioselective Chiral Surface Explosions. *J. Am. Chem. Soc.* **135**, 19208–19214 (2013).

213. Mhatre, B. S., Dutta, S., Reinicker, A., Karagoz, B. & Gellman, A. J. Explosive enantiospecific decomposition of aspartic acid on Cu surfaces. *Chem Commun* **52**, 14125–14128 (2016).

214. McFadden, C. F., Cremer, P. F. & Gellman, A. J. Adsorption of Chiral Alcohols on ‘Chiral’ Metal Surfaces. *Langmuir* **12**, 2483–2487 (1996).

215. Sholl, D. S. & Gellman, A. J. Developing Chiral Surfaces for Enantioselective Chemical Processing. *AIChE J.* **55**, 2484–2490 (2009).

216. Han, P. *et al.* Bottom-Up Graphene-Nanoribbon Fabrication Reveals Chiral Edges and Enantioselectivity. *ACS Nano* **8**, 9181–9187 (2014).
217. Oteyza, D. G. *et al.* Substrate-Independent Growth of Atomically Precise Chiral Graphene Nanoribbons. *ACS Nano* **10**, 9000–9008 (2016).
218. Wang, X.-Y. *et al.* Bottom-Up Synthesis of Heteroatom-Doped Chiral Graphene Nanoribbons. *J. Am. Chem. Soc.* **140**, 9104–9107 (2018).
219. Clair, S. & de Oteyza, D. G. Controlling a Chemical Coupling Reaction on a Surface: Tools and Strategies for On-Surface Synthesis. *Chem. Rev.* **119**, 4717–4776 (2019).
220. Shi, K.-J. *et al.* On-Surface Heck Reaction of Aryl Bromides with Alkene on Au(111) with Palladium as Catalyst. *Org. Lett.* **19**, 2801–2804 (2017).
221. Kanuru, V. K. *et al.* Sonogashira Coupling on an Extended Gold Surface in Vacuo: Reaction of Phenylacetylene with Iodobenzene on Au(111). *J. Am. Chem. Soc.* **132**, 8081–8086 (2010).
222. Sánchez-Sánchez, C. *et al.* The Flexible Surface Revisited: Adsorbate-Induced Reconstruction, Homocoupling, and Sonogashira Cross-Coupling on the Au(100) Surface. *J. Phys. Chem. C* **118**, 11677–11684 (2014).
223. Vasseur, G. *et al.* Quasi one-dimensional band dispersion and surface metallization in long-range ordered polymeric wires. *Nat. Commun.* **7**, 10235 (2016).
224. Ruffieux, P. *et al.* On-surface synthesis of graphene nanoribbons with zigzag edge topology. *Nature* **531**, 489–492 (2016).
225. Shi, K. J. *et al.* Ullmann coupling reaction of aryl chlorides on Au(111) using dosed Cu as a catalyst and the programmed growth of 2D covalent organic frameworks. *Chem Commun* **52**, 8726–8729 (2016).
226. Steiner, C. *et al.* Hierarchical on-surface synthesis and electronic structure of carbonyl-functionalized one- and two-dimensional covalent nanoarchitectures. *Nat. Commun.* **8**, 14765 (2017).
227. Rampulla, D. M., Francis, A. J., Knight, K. S. & Gellman, A. J. Enantioselective Surface Chemistry of R-2-bromobutane on Cu(643)R&S and Cu(531)R&S. *J Phys Chem B* **110**, 10411–10420 (2006).
228. Rampulla, D. M. & Gellman, A. J. Enantioselective decomposition of chiral alkyl bromides on Cu(643)R&S: Effects of moving the chiral center. *Surf. Sci.* **600**, 2823–2829 (2006).
229. Prinz, J. *et al.* Isolated Pd Sites on the Intermetallic PdGa(111) and PdGa($\bar 1$$\bar 1$$\bar 1$) Model Catalyst Surfaces. *Angew. Chem.* **124**, 9473–9477 (2012).
230. Yakutovich, A. V., Hoja, J., Passerone, D., Tkatchenko, A. & Pignedoli, C. A. Hidden Beneath the Surface: Origin of the Observed Enantioselective Adsorption on PdGa(111). *J. Am. Chem. Soc.* **140**, 1401–1408 (2018).
231. Simonov, K. A. *et al.* From Graphene Nanoribbons on Cu(111) to Nanographene on Cu(110): Critical Role of Substrate Structure in the Bottom-Up Fabrication Strategy. *ACS Nano* **9**, 8997–9011 (2015).

232. Nørskov, J. K., Bligaard, T., Rossmeisl, J. & Christensen, C. H. Towards the computational design of solid catalysts. *Nat. Chem.* **1**, 37–46 (2009).

233. Giessibl, F. J. Atomic resolution on Si(111)-(7×7) by noncontact atomic force microscopy with a force sensor based on a quartz tuning fork. *Appl Phys Lett* **76**, 1470–1472 (2000).

234. Fletcher, R. & Reeves, C. M. Function minimization by conjugate gradients. *Comput. J.* **7**, 149–154 (1964).

235. Pizzi, G., Cepellotti, A., Sabatini, R., Marzari, N. & Kozinsky, B. AiiDA: automated interactive infrastructure and database for computational science. *Comput. Mater. Sci.* **111**, 218–230 (2016).

236. Jónsson, H., Mills, G. & Jacobsen, K. W. Nudged Elastic Band Method for Finding Minimum Energy Paths of Transitions. in *Classical and Quantum Dynamics in Condensed Phase Simulations* 385–404 (World Scientific, 1998).

237. Henkelman, G., Uberuaga, B. P. & Jónsson, H. A climbing image nudged elastic band method for finding saddle points and minimum energy paths. *J. Chem. Phys.* **113**, 9901–9904 (2000).

238. Tersoff, J. D. & Hamann, D. R. Theory of the scanning tunneling microscope. *Phys. Rev. B* **31**, 805–813 (1985).

239. Tersoff, J. D. Method for the calculation of scanning tunneling microscope images and spectra. *Phys. Rev. B* **40**, 11990–11993 (1989).

240. Hapala, P. *et al.* Mechanism of high-resolution STM/AFM imaging with functionalized tips. *Phys. Rev. B* **90**, 085421 (2014).

241. Bayly, C. I., Cieplak, P., Cornell, W. & Kollman, P. A. A well-behaved electrostatic potential based method using charge restraints for deriving atomic charges: the RESP model. *J. Phys. Chem.* **97**, 10269–10280 (1993).

242. Hutter, J., Iannuzzi, M., Schiffmann, F. & Vandevondele, J. Cp2k: Atomistic simulations of condensed matter systems. *Wiley Interdiscip. Rev. Comput. Mol. Sci.* **4**, 15–25 (2014).

243. Hohenberg, P. & Kohn, W. Inhomogeneous Electron Gas. *Phys. Rev.* **136**, B864–B871 (1964).

244. Kohn, W. & Sham, L. J. Self-Consistent Equations Including Exchange and Correlation Effects. *Phys. Rev.* **140**, A1133–A1138 (1965).

245. Perdew, J. P. & Wang, Y. Accurate and simple density functional for the electronic exchange energy: Generalized gradient approximation. *Phys. Rev. B* **33**, 8800–8802 (1986).

246. Grimme, S., Antony, J., Ehrlich, S. & Krieg, H. A consistent and accurate ab initio parametrization of density functional dispersion correction (DFT-D) for the 94 elements H-Pu. *J. Chem. Phys.* **132**, 154104 (2010).

247. Barth, U. von & Hedin, L. A local exchange-correlation potential for the spin polarized case. i. *J. Phys. C Solid State Phys.* **5**, 1629–1642 (1972).

248. Gunnarsson, O. & Lundqvist, B. I. Exchange and correlation in atoms, molecules, and solids by the spin-density-functional formalism. *Phys. Rev. B* **13**, 4274–4298 (1976).

249. Rajagopal, A. K. & Callaway, J. Inhomogeneous Electron Gas. *Phys. Rev. B* **7**, 1912–1919 (1973).

250. Goedecker, S., Teter, M. & Hutter, J. Separable dual-space Gaussian pseudopotentials. *Phys. Rev. B* **54**, 1703–1710 (1996).

251. VandeVondele, J. *et al.* Quickstep: Fast and accurate density functional calculations using a mixed Gaussian and plane waves approach. *Comput. Phys. Commun.* **167**, 103–128 (2005).
252. Genovese, L., Deutsch, T., Neelov, A., Goedecker, S. & Beylkin, G. Efficient solution of Poisson's equation with free boundary conditions. *J. Chem. Phys.* **125**, 074105 (2006).
253. Ullmann, F. & Bielecki, J. Ueber Synthesen in der Biphenylreihe. *Berichte Dtsch. Chem. Ges.* **34**, 2174–2185 (1901).
254. Lackinger, M. Surface-assisted Ullmann coupling. *Chem. Commun.* **53**, 7872–7885 (2017).
255. Lafferentz, L. *et al.* Controlling on-surface polymerization by hierarchical and substrate-directed growth. *Nat Chem* **4**, 215–220 (2012).
256. Basagni, A. *et al.* Molecules–Oligomers–Nanowires–Graphene Nanoribbons: A Bottom-Up Stepwise On-Surface Covalent Synthesis Preserving Long-Range Order. *J. Am. Chem. Soc.* **137**, 1802–1808 (2015).
257. Blanksby, S. J. & Ellison, G. B. Bond Dissociation Energies of Organic Molecules. *Acc. Chem. Res.* **36**, 255–263 (2003).
258. King, D. A. Thermal Desorption from Metal Surfaces: A review. *Surf. Sci.* **47**, 384–402 (1975).
259. Björk, J., Hanke, F. & Stafström, S. Mechanisms of Halogen-Based Covalent Self-Assembly on Metal Surfaces. *J. Am. Chem. Soc.* **135**, 5768–5775 (2013).
260. Dienstmaier, J. F. *et al.* Synthesis of Well-Ordered COF Monolayers: Surface Growth of Nanocrystalline Precursors *versus* Direct On-Surface Polycondensation. *ACS Nano* **5**, 9737–9745 (2011).
261. Guan, C.-Z., Wang, D. & Wan, L.-J. Construction and repair of highly ordered 2D covalent networks by chemical equilibrium regulation. *Chem. Commun.* **48**, 2943 (2012).
262. Liu, X.-H. *et al.* On-Surface Synthesis of Single-Layered Two-Dimensional Covalent Organic Frameworks via Solid–Vapor Interface Reactions. *J. Am. Chem. Soc.* **135**, 10470–10474 (2013).
263. Drost, R., Ojanen, T., Harju, A. & Liljeroth, P. Topological states in engineered atomic lattices. *Nat. Phys.* **13**, 668–671 (2017).
264. Sachtler, W. M. H. Chemisorption Complexes on Alloy Surfaces. *Catal. Rev. - Sci. Eng.* **14**, 193–210 (1976).
265. Liu, P. & Nørskov. Ligand and ensemble effects in adsorption on alloy surfaces. *Phys Chem Chem Phys* **3**, 3814–3818 (2001).
266. Nørskov, J. K. *et al.* The nature of the active site in heterogeneous metal catalysis. *Chem Soc Rev* **37**, 2163–2171 (2008).
267. Zhou, H. *et al.* Direct Visualization of Surface-Assisted Two-Dimensional Diyne Polycyclotrimerization. *J. Am. Chem. Soc.* **136**, 5567–5570 (2014).
268. Liu, J., Ruffieux, P., Feng, X., Müllen, K. & Fasel, R. Cyclotrimerization of arylalkynes on Au(111). *Chem. Commun.* **50**, 11200 (2014).
269. Xiang, F. *et al.* Cyclotrimerization-Induced Chiral Supramolecular Structures of 4-Ethynyltriphenylamine on Au(111) Surface. *Chem. – Eur. J.* **21**, 12978–12983 (2015).
270. Eichhorn, J., Heckl, W. M. & Lackinger, M. On-surface polymerization of 1,4-diethynylbenzene on Cu(111). *Chem. Commun.* **49**, 2900 (2013).

271. Pickett, W. E. Pseudopotential methods in condensed matter applications. *Comput. Phys. Rep.* **9**, 115–197 (1989).

272. Grimme, S., Antony, J., Ehrlich, S. & Krieg, H. A consistent and accurate ab initio parametrization of density functional dispersion correction (DFT-D) for the 94 elements H-Pu. *J. Chem. Phys.* **132**, 154104 (2010).

273. Hapala, P. *et al.* Mechanism of high-resolution STM/AFM imaging with functionalized tips. *Phys. Rev. B* **90**, 085421 (2014).

274. Pizzi, G., Cepellotti, A., Sabatini, R., Marzari, N. & Kozinsky, B. AiiDA: automated interactive infrastructure and database for computational science. *Comput. Mater. Sci.* **111**, 218–230 (2016).

275. Stolz, S., Gröning, O., Prinz, J., Brune, H. & Widmer, R. Molecular motor crossing the frontier of classical to quantum tunneling motion. *Proc. Natl. Acad. Sci. U. S. A.* (2020).

276. Arado, O. D. *et al.* On-surface Azide-Alkyne Cycloaddition on Au(111). *ACS Nano* **7**, 8509–8515 (2013).

277. Liu, L. *et al.* α-Diazo Ketones in On-Surface Chemistry. *J Am Chem Soc* **140**, 6000–6005 (2018).

278. Wasio, N. A. *et al.* Self-assembly of hydrogen-bonded two-dimensional quasicrystals. *Nature* **507**, 86–89 (2014).

279. Franke, M. *et al.* Temperature-dependent reaction of phthalic acid on Ag(100). *J. Phys. Chem. C* **119**, 23580–23585 (2015).

280. Lipton-Duffin, J., Abyazisani, M. & MacLeod, J. Periodic and nonperiodic chiral self-assembled networks from 1,3,5-benzenetricarboxylic acid on Ag(111). *Chem. Commun.* **54**, 8316–8319 (2018).

281. Abyazisani, M., Bradford, J., Motta, N., Lipton-Duffin, J. & MacLeod, J. Adsorption and Reactivity of Pyridine Dicarboxylic Acid on Cu(111). *J Phys Chem C* **122**, 17836–17845 (2018).

282. Li, Y. & Haldane, F. D. M. Topological Nodal Cooper Pairing in Doped Weyl Metals. *Phys. Rev. Lett.* **120**, 067003 (2018).

283. Vergniory, M. G. *et al.* A complete catalogue of high-quality topological materials. *Nature* **566**, 480–485 (2019).

284. Fasel, R., Wider, J., Quitmann, C., Ernst, K.-H. & Greber, T. Determination of the Absolute Chirality of Adsorbed Molecules. *Angew. Chem. Int. Ed.* **43**, 2853–2856 (2004).

285. Sugiyama, K., Sumiya, Y., Takagi, M., Saita, K. & Maeda, S. Understanding CO oxidation on the Pt(111) surface based on a reaction route network. *Phys. Chem. Chem. Phys.* **21**, 14366–14375 (2019).

Curriculum Vitae

Samuel Stolz

stolzsamuel@gmail.com
Date of Birth: 10.11.1989
Nationality: Swiss

EMPLOYMENT HISTORY

Nov. 2015 – Apr 2020	**Empa Dübendorf, nanotech@surfaces laboratory** in collaboration with **EPF Lausanne**, Switzerland *PhD studies in Physics: "Exploration of electronic, dynamic and chemical properties of the chiral intermetallic PdGa"*
Jul. 2014 – Oct. 2015	**various civil services** among others at SLF in Davos in the mountain ecosystem group, "Projekt Werkstatt" in St.Gallen, rehabilitation clinic of Kispi USZ in Affoltern a. A., Niklaus Hari's farm in Reichenbach i. K. and "Heilsarmee Wohnheime" in Zurich
2011-2018	**Fitness instructor at update Fitness**

EDUCATION

Sept. 2009 – June 2015	**Bsc and Msc Physics at ETH Zurich** Switzerland *Msc thesis in the groups of Prof. T. Lomax (PSI) and Prof. U. Schneider (UZH): "The impact of range adjusted ITV on organ equivalent dose in proton therapy"* *Semester thesis in the group of Prof. M. Sigrist (ETHZ): "Impact of a coupling between order parameter and strain on the superconducting electric properties"* *Semester thesis in the group of Prof. J. Faîst (ETHZ): "Influence of monolithic extractors on the performance of terahertz quantum cascade laser"*

PUBLICATIONS

Di Giovannantonio M., Deniz O., Urgel J. I., Widmer R., Dienel T., Stolz S., Sánchez-Sánchez C., Muntwiler M., Dumslaff T., Berger R., Narita A., Feng X., Müllen K., Ruffieux P., Fasel R. "On-Surface Growth Dynamics of Graphene Nanoribbons: The Role of Halogen Functionalization" *ACS Nano* **2018**, 12, 74-81

Wang X.-Y., Dienel T., Di Giovannantonio M., Borin Barin G., Kharche N., Deniz O., Urgel J. I., Widmer R., Stolz S., De Lima L. H., Muntwiler M., Tommasini M., Meunier V., Ruffieux P., Feng X., Fasel R., Müllen K., Narita A. "Heteroatom-Doped Perihexacene from a Double Helicene Precursor: On-Surface Synthesis and Properties" *J. Am. Chem. Soc.* **2017**, 139, 13, 4671-4674

Stolz S., Di Giovannantonio M., Urgel J. I., Sun Q., Kinikar A., Borin Barin G., Bommert M., Fasel R., Widmer R. "Reversibility in on-surface dehalogenative aryl-aryl coupling", *accepted in Angew. Chem. Int. Ed. (**2020**)*

Urgel J. I., Di Giovannantonio M., Eimre K., Lohr T. G., Liu J., Mishra S., Sun Q. Kinikar A., Widmer R., Stolz S., Bommert M., Berger R., Ruffieux P., Pignedoli C. A., Müllen K., Feng X., Fasel R. "On-surface synthesis of cumulene-like polymers via two-step dehalogenative homocoupling of dibromomethylenes", *accepted in Angew. Chem. Int. Ed. (**2020**)*

Schröter N. B. M., Stolz S., Manna K., de Juan F., Vergniory M. G., Krieger J. A., Pei D., Schmitt T., Dudin P. Kim T. K., Cacho C., Bradlyn B., Borrmann H., Schmidt M., Widmer R., Strocov V. N., Felser C. "Observation and control of maximal Chern numbers in a chiral topological semimetal, *accepted in Science (**2020**)*

Stolz S., Gröning O., Prinz J., Brune H., Widmer R. "Molecular motor crossing the frontier of classical to quantum tunneling motion", *accepted in PNAS (**2020**)*

SUBMITTED MANUSCRIPTS

Stolz S., Yakutovich A. V., Prinz J., Dienel T., Passerone D., Pignedoli C. A., Brune H., Gröning O., Widmer R. "Near-enantiopure trimerization of 9-Ethynylphenanthrene on a chiral metal surface", *under Review in Angew. Chem. Int. Ed. (**2020**)*

Sessi P., Fan F.-R., Küster F., Manna K., Schröter N. B.M., Ji J.-R., Stolz S., Krieger J. A., Pei D., Kim T. K., Dudin P., Cacho C. Widmer R., Borrmann H., Shi W., Chang K., Sun Y., Felser C., Parkin S. S.P. "Direct observation of handedness-dependent quasiparticle interference in the two enantiomers of topological chiral semimetal PdGa", *submitted to Nat. Commun. (**2020**)*

Schröter N. B. M., Robredo I., Klemenz S., Kirby R. J., Krieger J. A., Pei D., Yu T., Stolz S., Schmitt T., Dudin P., Kim T. K., Cacho C., Schnyder A., Bergara A., Strocov V. N., de Juan F., Vergniory M. G., Schoop L. M. "Weyl-fermions, Fermi-arcs, and minority-spin carriers in ferromagnetic CoS_2", *submitted to Nature Materials (**2020**)*

MANUSCRIPTS IN PREPARATION

Stolz S., Gröning O., Brune H., Widmer R., "Asymmetric azid-alkyne Huisgen cycloaddition on chiral metal surfaces", *in preparation for submission to J. Am. Chem. Soc. (**2020**)*

Stolz S., Danese M., Di Giovannantonio M. Urgel J. I., Sun Q., Kinikar A., Bommert M., Mishra S., Brune H., Passerone D., Gröning O., Widmer R. "Enantioselective dehalogenative aryl-aryl coupling on chiral metal surfaces", *in preparation for submission to Advanced Materials (**2020**)*

SCIENTIFIC PRESENTATIONS

"Does it «click»? – Asymmetric coupling reactions on the chiral PdGa{111} surfaces", *Invited talk*, ECMetAC Days, Poznań (Poland), **2018**

"Does it «click»? – Asymmetric coupling reactions on the chiral PdGa{111} surfaces", *Oral contribution*, ECOSS34, Aarhus (Denmark), **2018**

"Click reaction on the chiral PdGa{111} surfaces", Poster presentation, ECSCD – 13, Donostia San Sebastián (Spain), **2017**

"Asymmetric reaction on a chiral surface – Does it «click»?", *invited talk*, MolCH meeting, Bern (Switzerland), **2017**

"Click reaction on the PdGa:A(111)Pd_1 surface", *Poster presentation*, Symposium on Surface Science, St. Moritz (Switzerland), **2017**

"Does it click", *Oral contribution*, CMAC days, Bratislava (Slovakia), **2016**

"Enantioselective formation of molecular structures on the PdGa:A(-1-1-1)Pd_3 surface", *Poster presentation*, Trends in NanoTechnology Conference, Fribourg (Switzerland), **2016**

Acknowledgements

The submission of this thesis marks the approaching end an instructive, delightful, and eventful four and a half years in the nanotech@surfaces laboratory at Empa, the Swiss Federal Laboratories for Materials Science and Technology. I could not have these four and a half years spent in such an inspiring scientific environment, if Roland Widmer and Harald Brune had not given me the chance to carry out this PhD work; even though I had absolutely no background in surface science.

First and foremost, I want to express my gratitude to Roland for all the time he spent on scientific discussions, for teaching me the proper handling and maintenance of the scientific instruments, and for the opportunities he provided me, for instance to perform new and exciting experiments at numerous beamlines or to participate at several conferences and meetings. I also enjoyed our countless non-scientific discussions and the days we spent exploring Bratislava, Poznań, and Warsaw.

I appreciate a lot, that, despite the long (in Swiss standards) physical distance between EPFL and EMPA, Harald was willing to meet several times a year in Bern or even in Dübendorf to discuss my latest results, future plans, and past or upcoming sport activities. Harald, I valued your interest and input a lot.

I would like to thank Oliver Gröning for all the hours he spent with me to discuss my experimental results, to devise new approaches for data analysis and simulations, to perform several simulations for me, and to help me getting started in Igor programming; and of course the exchange of biking experience.

I would like to thank Tibor Kudernac, Karl-Heinz Ernst, Rainer Beck, and Henrik M. Rønnow for kindly agreeing to read and evaluate my work.

I would like to thank Niels Schröter for taking me to several beamlines and introducing me to the fascinating field of topological materials

Further gratitude is devoted to all present and a couple of former members of the nanotech@surfaces laboratory for creating a pleasant and inspiring environment. I enjoyed a lot the discussions and events, scientific or non-scientific, during coffee or lunch breaks, official meetings or leisure time. Special thanks go to:

Daniele Passerone, Carlo Pignedoli, Martina Danese, and Aliaksandr Yakutovich, who all struggled a lot with ab-initio calculations on PdGa, but never gave up and could in the end often provide valuable insight into the interpretation of experimental results.

Carlo again, for enduring all the hiking and climbing weekends, for the beautiful flight over the Swiss Alps, and of course for the excellent olive oil supply.

Roman Fasel, for revising some of the manuscripts, for his advice and opinion on my project, and for being reference when I started looking for future positions.

Thomas Dienel, Shantanu Mishra, Amogh Kinikar, Julia Dshemuchadse, Wei Ruan, and Michael F. Crommie for their support and inputs on my proposal for a SNSF Early Postdoc.Mobility fellowship.

Lukas Rotach, for always being available to immediately solve technical problem in the laboratory.

In no particular order, I would like to thank Marco Di Giovannantonio for his company during many climbing and bouldering sessions; Guido Gandus for the unforgettable biking ride Zurich → Haslen LU →× Bern; and my current and former office- and floor-mates Gabriela Borin Barin, José I. Urgel, Max Bommert, Okan Deniz, Qiang Sun, Rimah Darawish, and Shiyong Wang for the pleasant and cordial atmosphere, and the lively conversations and discussions.

Finally, I would like to thank all my friends and my family. My deepest thanks go to my partner Svenja Mittelmeijer and my mother, Monika Stolz, who unconditionally loved, supported and motivated me in every situation.